5-2015

CHARACTERIZATION OF LOW DENSITY INTRACRANIAL LESIONS USING DUAL-ENERGY COMPUTED TOMOGRAPHY

Jessica L. Nute

CHARACTERIZATION OF LOW DENSITY INTRACRANIAL LESIONS USING DUAL-ENERGY COMPUTED TOMOGRAPHY

by

Jessica Nute, M.S.

APPROVED:

_____
Dianna Cody, Ph. D., Supervisory Professor

_____
Dawid Schellingerhout, M.D.

_____
Lucia LeRoux, Ph.D.

_____
John Rong, Ph.D.

_____
Donna Reeve, M.S.

_____
Veera Baladandayuthapani, Ph.D.

APPROVED:

_____
Dean, The University of Texas
Graduate School of Biomedical Sciences at Houston

CHARACTERIZATION OF LOW DENSITY INTRACRANIAL LESIONS USING DUAL-ENERGY COMPUTED TOMOGRAPHY

A

DISSERTATION

Presented to the Faculty of

The University of Texas
Health Science Center at Houston

and

The University of Texas
MD Anderson Cancer Center
Graduate School of Biomedical Sciences

in Partial Fulfillment
of the Requirements
for the Degree of

DOCTOR OF PHILOSOPHY

by

Jessica Nute, M.S.

Houston, Texas
May, 2015

To my parents, Marshall and Lorraine. They taught me through garage experiments to love science, they taught me through afternoon talks after school the importance of kindness and confidence, they taught me through their encouragement to reach for the stars, and they taught me through their love that though we may stumble, it's what we do after that makes us who we are. They are responsible for the person I am today and I owe them more than I can express in words.

And to Marty, for his loving companionship and support through the good times and the bad, for making me laugh when I need it most of all, and for always believing in me. And, of course, for the LEGO.

Acknowledgements

It is difficult to acknowledge all the people who have, over the past five years, made this research possible. Research is not performed in a vacuum and, as much as one would like to think that one's dissertation represents their personal contribution to the field, not one page of this document would have been possible without these people.

First and foremost I would like to thank my advisor, Dianna Cody. Regardless of her schedule, she always made time for me to discuss the research, give her thoughts, and help me through, and sometimes around, the quagmires of research. While she was always there to listen and help, she also provided me with something invaluable: a certain amount of autonomy. Whether it was through leading meetings, making research decisions, writing grants and papers or interacting with manufacturers, this independence has led to a greater appreciation for the research process and a level of confidence and comfort that will serve me well beyond my time at MDA.

I'd like to acknowledge the generous financial support of the Center for Advanced Biomedical Imaging and GE Healthcare, as well as the faculty and staff who provided support for this work. I'd like to especially thank Anne Fisher and Dr. John Hazle for their tireless commitment to the CABI program and to our continued research endeavors.

I would also like to say a special thank you to my lab member Megan Jacobsen, who has sacrificed her time, and at some points, her health, to ensure this research got done. She has served as a sounding board, a team mate, and a friend. So much of what is shown here would not have been possible without her unwavering and generous assistance.

I'd like to thank my committee for their time and commitment. To Donna Reeve and John Rong, I owe a tremendous debt of thanks for their support, both professionally and

personally. I owe special thanks to Dawid Schellingerhout and Lucia LeRoux, who have been both fantastic advisors and true mentors. Dawid has provided invaluable direction on both the physics and clinical aspects of this work. His direction and council have been absolutely critical in readying this work for clinical implementation. He also asks the absolute best, and sometimes most frustrating, questions that, while difficult, always lead the project in a better direction. I owe so much to Lucia who, with endless kindness and generosity, has been a steadfast supporter and voice of reason in my time here at MDA. She has always made the time to help me, be it through brainstorming agar gel mixing techniques, providing advice on surviving as a female scientist, or even a simple word or two of encouragement.

In my notes for my acknowledgements I have written “To Kathy… for everything” and, try as I might, I cannot characterize my debt to her any better. All the meetings to discuss projects, the telephone conferences with manufacturers, the national conferences: none would have happened without her constant and expert assistance. She has always been ready with a smile, or a mocking glare, that never fails to make my day.

I’d like to thank Jiang Hsieh, Imai Yasuhiro and especially Adam Chandler for their unwavering support and assistance with these projects. They have made the time to attend countless meetings and answer numerous technical inquiries that have benefited this work. I owe Adam Chandler a special thanks for teaching me how to use the GE 750HD scanner and GSI software, as well as serving as a very vital sounding board for any number of dual-energy related questions.

I’d like to thank our partners at Gammex for providing such high quality materials for both our DEQC and biologically relevant phantom systems. Cristel Baiu has put in significant effort to ensure the quality of these materials and has really allowed us to take our research to the next level.

I'd like to thank Veera Baladandayuthapani, Wei "Auston" Wei, and Brian Hobbs for their statistical support of this project and their patience for those of us who haven't quite mastered statistics. A special thank you goes to Auston for his data analysis and for working hard to always ensure we had what we needed in time for every conference.

I'd like to thank David Fuentes for his help with the coding, organization and management of the SQL databases used to analyze the wealth of data collected in these projects; and Wolfgang Stefan for setting up and maintaining the AutoQC tool which enabled us to access and analyze our DEQC data. They are some of the smartest people I know and we would be lost without them.

Although he is now retired, I owe a lot of thanks to Jim Pennington. Not only did he build the DEQC body and DEQC head phantoms but contributed directly to their design. He also offered me workspace and an extra set of hands during the construction of the biologically relevant brain phantom. With his help I learned to use a belt sander, a hot wire cutter, a dremmel tool and a die grinder, all without losing any fingers.

Finally I'd like to extend my thanks to all those I have shared an office with: Ryan Bosca, Hua Ai, Kelsey Mathieu, Josh Yung, Jonathan Lin, Megan Jacobsen, Chris MacLellan and Sam Fahrenholtz. Thank you for being there through the research highs and lows. Thank you for making me laugh, letting me vent, and providing your advice. You have each been excellent companions on this journey, and I wouldn't have finished, or at least finished with any semblance of sanity, without your help.

Research is not performed in a vacuum. Although this acknowledgement may seem overly long, it would probably take another 5 pages to simply name all those who have had an impact on this work and my time here. Therefore I will simply say thank you. Thank you to the faculty who educated me, the administrative assistants who got me where I needed to be, the graduate school administrators who ensured I was completing what I needed to complete, and the mentors and advisors that got me where I am today. Thank you all.

CHARACTERIZATION OF LOW DENSITY INTRACRANIAL LESIONS USING DUAL-ENERGY COMPUTED TOMOGRAPHY

Jessica Nute, M.S.

Supervisory Professor: Dianna Cody, Ph.D.

Calcific and hemorrhagic foci of susceptibility are frequently encountered on routine brain MR studies. Both etiologies cause variations in local magnetic field strength, leading to dark regions on the MR images that cannot be classified. Single-energy CT (SECT) can be used to identify lesions with attenuation over 100 HU as calcific, however lesions with lower attenuation cannot be reliably identified. While calcific lesions are unlikely to cause harm, hemorrhagic lesions carry a risk of subsequent intracranial bleeding; as such, identification of hemorrhage is vital in preventing the inappropriate use of anticoagulant medications in patients with hemorrhagic lesions.

Given there currently exists no clinically available means of differentiating between these two lesions over their full biological attenuation ranges, there is a clear need for a reliable imaging method to differentiate low intensity calcification and hemorrhage. Recently, several vendors have released new computed tomography (CT) scanner models with dual-energy capabilities, which may be successfully applied to this issue. By acquiring data at two different energies, dual-energy CT (DECT) collects information about the energy-dependent attenuation changes in a material and may help distinguish between two materials with similar linear attenuation measurements which would be impossible to differentiate using SECT.

This work applies the unique capabilities of DECT to the characterization of intracranial hemorrhage and calcification using biologically-relevant and spectrally-

equivalent models. Lesion and acquisition parameters were varied to elucidate their impact on DECT's ability to differentiate and subsequently classify intracranial lesions. DECT's characterization ability was shown to improve with increasing $CTDI_{vol}$, image thickness and lesion size. Using an optimized protocol, intracranial lesions were correctly classified with over 90% confidence down to a minimum attenuation of 56 HU, representing a significant improvement beyond the 100 HU limit imposed by the current standard. Since this data collection spanned several years, a dual-energy quality control program was designed to validate the comparison of collected data. The added characterization ability of DECT will assist physicians in the correct prescription of anticoagulant medications, hopefully sparing hemorrhagic patients from prophylaxis that might cause them harm.

Table of Contents

Acknowledgements iv

Abstract vii

Table of Contents ix

List of Figures xiv

List of Tables xxvii

List of Equations xxxvii

List of Abbreviations xxxix

1 Introduction 1

1.1 Objectives and Hypothesis 2

1.2 Specific Aims 2

1.3 Dissertation Organization 4

2 Background 5

2.1 Basics of DECT 9

2.2 DECT Implementations 10

2.3 Dual-Energy Image Reconstruction 12

2.4 Tissue Differentiation using Dual-Energy CT 17

2.5 MR for the Differentiation of Calcification and Hemorrhage 17

3 Lesion Differentiation using an Agar-Gel Based Phantom 19

3.1 Introduction 19

3.2 Materials and Methods 21
3.2.1 Calcification and Hemorrhage Phantom Models 21
3.2.2 Imaging and Region-of-Interest Analysis 23
3.2.3 Fabrication of Matched Hemorrhage and Calcification Gel Models 24
3.2.4 Dual-Energy Data Processing 25
3.2.5 Matched Model Pair Data Analysis 26
3.3 Results 29
3.3.1 Calcification and Hemorrhage Phantom Models 29
3.3.2 Fabrication of Matched Hemorrhage and Calcification Gel Models 29
3.3.3 Matched Model Pair Data Analysis 30
3.4 Discussion 35
4 Lesion Differentiation using a Biologically-Relevant Phantom 39
4.1 Materials and Methods 39
4.1.1 Phantom Preparation 39
4.1.2 Spectrally Equivalent Brain Material 41
4.1.3 Lesion Models 42
4.1.4 Selection of optimal keV level for simulated SECT scanning 44
4.1.5 Collection of Lesion Differentiation Data 46
4.1.6 Data Organization and Structure 48
4.1.7 Determination of Differentiation Accuracy 53
4.1.8 Inter-Scanner and Intra-Scanner Correlation 57
4.1.9 Validation of Lesion Attenuation 57
4.2 Results 58
4.2.1 Spectrally Equivalent Brain Material 58

4.2.2 Lesion Models 62
4.2.3 Selection of Optimal keV Level for Simulated SECT Scanning 65
4.2.4 Validation of Lesion Attenuation 66
4.2.5 Determination of Differentiation Accuracy 70
4.2.6 Inter-Scanner and Intra-Scanner Correlation 106

4.3 Discussion 118
4.3.1 Gaussian Mixture Model (GMM) Analysis 118
4.3.2 Support Vector Machine and Geometric Bisector Analyses 118
4.3.3 Inter- and Intra-Scanner Correlation 120
4.3.4 Validation of Optimal keV Level for Simulated SECT Scanning 122
4.3.5 Power Fits for 90% Differentiation Accuracy 123
4.3.6 Limitations 124

5 Lesion Classification using Unknown Lesion Models 125

5.1 Materials and Methods 125
5.1.1 Fabrication and Evaluation of Unknown Lesion Models 125
5.1.2 Unknown Lesion Data Acquisition 127
5.1.3 Unknown Lesion Classification Methods 128
5.1.4 Inter-Method correlation 132

5.2 Results 133
5.2.1 Fabrication and Evaluation of Unknown Lesion Models 133
5.2.2 Probability Distribution Definition 133
5.2.3 Classification of Unknown Lesions 137
5.2.4 Inter-Method Correlations 149

5.3 Discussion 154

5.3.1 Effect of Lesion Parameters on Classification Confidence 154
5.3.2 Effect of $CTDI_{vol}$ on Classification Confidence 159
5.3.3 Generalizability of the Geometric Bisector Plane Solution 160
5.3.4 Protocol Recommendations for Optimal Classification Confidence 162
5.3.5 Limitations 163
6 Dual-Energy CT Quality Control Program Development 165
6.1 Introduction 165
6.2 Materials and Methods 168
6.2.1 Phantom Design 168
6.2.2 Test Metrics 173
6.2.3 Protocol Development 176
6.2.4 Data Collection 181
6.3 Results 184
6.3.1 Determination of Relevant Acquisition Parameters 184
6.3.2 DECT Response by Test Metric 185
6.3.3 Recommendations on Clinical Implementation of DEQC Program.211
6.4 Discussion 212
6.4.1 Iodine Accuracy 213
6.4.2 Uniformity 213
6.4.3 Monoenergetic HU Stability 215
6.4.4 Noise 216
6.4.5 Differences in DEQC Body and DEQC Head Phantom Results 216
6.4.6 Impact of Results on Intracranial Lesion Characterization 217
6.4.7 Limitations 220

6.4.8 Future Work....221
7 Conclusions....222
7.1 Summary of Major Findings....222
7.2 Comments on Clinical Implementation....225
7.3 Limitations and Future Directions....226
8 Appendix....228
8.1 Gaussian Mixture Model Formulation....228
8.2 GMM Fitting and Analysis....229
References....232
Vita....243

List of Figures

Figure 2.1: Increase in DECT publications from January 1, 2000 to December 31, 2014 based on occurrence of “Dual-Energy CT” or “Spectral CT” using the Web of Science database tool (34). 8

Figure 3.1: Anthropomorphic head phantom. 22

Figure 3.2: (a) Custom water-filled insert for the anthropomorphic head phantom. The lateral view (top), the axial view (bottom left), and the relative position of the insert in the head phantom (bottom right) are shown. The orientation of the imaging volume is represented by the yellow shaded region. (b) A lateral scout image of the anthropomorphic head phantom with custom water-filled insert and gel models in place. 23

Figure 3.3: 3D plot of voxel data from all calcification and hemorrhage gel models used in this study, rotated to show the full distribution of the data (a) or the planar nature of these data in the 3D coordinate space (b). Hemorrhage gel model voxel data are shown in red; calcification gel model voxel data are shown in blue. 28

Figure 3.4: SECT attenuation (HU) for the concentration of iron oxide in the hemorrhage gel models and the hydroxyapatite in the calcification gel models. Linear regression equations and correlation coefficients are shown for each data set. 29

Figure 3.5: GMM assignment results for the 62-HU matched gel model pair (1 of 16 pairs). Each point represents a voxel within the 6,032-voxel volume of interest in one of the two gel models. 32

Figure 3.6: Accuracy of hemorrhage and calcification differentiation using the GMM and threshold plane analysis method for all attenuation-matched model pairs. For the GMM

series, each point represents 1,000 iteratively filtered runs of the analysis. A third-order polynomial (Poly.) was fit to each series to facilitate visual interpretation of the data.....33
Figure 3.7: 3D plot of all voxel data (n = 193,024) from all 16 hemorrhage/calcification matched model pairs. Hemorrhage gel model voxel data are shown in red; calcification gel model voxel data are shown in blue. (a) Threshold plane viewed edge on as black line [equation: -0.93x + 0.31y - 0.20z = -929.20]. (b) Voxel data viewed from an angle showing hemorrhage and calcification data falling on the hemorrhage side of the threshold plane. Bright blue calcification data would be incorrectly identified as belonging to the hemorrhage population, with greyed-out blue data being correctly classified. (c) Voxel data viewed from an angle showing hemorrhage and calcification data falling on the calcification side of the threshold plane. Bright red hemorrhage data would be incorrectly identified as belonging to the calcification population, with greyed-out red data being correctly classified. 35
Figure 4.1: Interior of anthropomorphic nuclear medicine phantom. 39
Figure 4.2: Intracranial lesion phantom plan showing brain slabs in tan, hemorrhage lesion models in red and calcification lesion models in blue. (a) sagittal view showing position of cerebrum and skull base brain slabs. (b) axial view of cerebrum brain slab showing position of hemorrhage and calcification lesion models. (c) axial view of skull base slab showing position calcification and hemorrhage model. 40
Figure 4.3: Gammex validation phantom. Water balloons are positioned in insert holes covered by tape. Target lesion was positioned at 12 o'clock. 43
Figure 4.4: Artifact caused by phantom discontinuity.....50
Figure 4.5: Support vector machine plane (gray) based on identified support vectors (green) for the hemorrhage (red) and calcification (blue) distributions. 54
Figure 4.6: Geometric bisector plane (gray) shown separating the hemorrhage (red) and calcification (blue) distributions. Three dimensional linear regressions of the two distributions and the resulting bisector are shown in as color-matched lines. 55

Figure 4.7: Results of dual-energy analysis for potential spectrally equivalent brain materials. Spectral data from a clinical brain study (GE, Waukesha, WI; personal contact) is shown in black. 59
Figure 4.8: Sagittal reformat of intracranial lesion phantom showing potential positioning of cerebrum and skull base slabs. Red lines show the relative thickness of the cerebrum vs the skull base brain slabs while the blue dotted line represents the upper bound of the imaging area affected by the bony anatomy of the skull base. 60
Figure 4.9: Simplified structure of cerebrum slab based on upper and lower curvatures with arrow showing mismatch between phantom base and crown interiors. 61
Figure 4.10: Error in attenuation (HU) measurement between SECT and 68 keV reconstructions for both calcification and hemorrhage models. Error bars represent one standard deviation (SD) of the distribution accounting for all image thickness, $CTDI_{vol}$ and reconstruction filter protocol variations. 67
Figure 4.11: Bland-Altman and Correlation graphs for the correlation of SECT attenuation (HU) to 68 keV HU. Data includes all protocol variations and lesion models. 67
Figure 4.12: Lesion matching results based on SECT and 68 keV attenuation evaluation. Values represent mean difference in calcification and hemorrhage models across all available protocol variations. Error bars represent one SD of this distribution. 69
Figure 4.13: Accuracy of 3D GMM differentiation for intracranial lesion pairs based on lesion model size and location. Displayed values represent mean of accuracy across the three studies and all protocol variations: $CTDI_{vol}$, image thickness and reconstruction filter. Error bars represent one SD of the distribution. 71
Figure 4.14: Differentiation Accuracy using Gaussian Mixture Model (GMM) method analyzed by $CTDI_{vol}$. Displayed values represent mean of accuracy across the three studies and additional protocol variations: image thickness and reconstruction filter. Error bars represent one SD for each distribution. 72

Figure 4.15: Differentiation Accuracy using Gaussian Mixture Model (GMM) method analyzed by image thickness. Displayed values represent mean of accuracy across the three studies and additional protocol variations: $CTDI_{vol}$ and reconstruction filter. Error bars represent one SD for each distribution. 73
Figure 4.16: Differentiation Accuracy using Gaussian Mixture Model (GMM) method analyzed by reconstruction filter. Displayed values represent mean of accuracy across the three studies and additional protocol variations: $CTDI_{vol}$ and image thickness. Error bars represent one SD for each distribution 74
Figure 4.17: Distribution of differentiation accuracy results from 7,000 GMMs (1,000 per lesion pair) graphed versus the attenuation of lesion pair. Data represents 67 mGy $CTDI_{vol}$, 3.75 mm image thickness, standard filter acquisition of 1 cm cerebrum matched lesion pairs. 75
Figure 4.18: Differentiation accuracy results for calcification model, hemorrhage model and combined matched model pair. Error bars represent standard deviation in accuracy value over the 1,000 GMM repetitions. Data represents 67 mGy $CTDI_{vol}$, 3.75 mm image thickness, standard filter acquisition of 1 cm cerebrum matched lesion pairs. 76
Figure 4.19: Top: Raw voxel data from a $CTDI_{vol}$, 3.75 mm image thickness, standard filter acquisition of 1 cm cerebrum matched lesion pairs at 80 HU. Lower Left: GMM solution resulting in high calcification model and overall matched model pair accuracies. Lower Right: GMM solution resulting in low calcification model and overall matched model pair accuracies. 77
Figure 4.20: Differentiation accuracy using support vector machine method. Displayed values represent mean of accuracy across the three studies and all protocol variations: $CTDI_{vol}$, image thickness and reconstruction filter. Error bars represent one SD of the distribution. 79

Figure 4.21: Differentiation accuracy using support vector machine method analyzed by $CTDI_{vol}$. Displayed values represent mean of accuracy across the three studies and additional protocol variations: image thickness and reconstruction filter. Error bars represent one SD for each distribution. 80
Figure 4.22: Differentiation accuracy using support vector machine method analyzed by image thickness. Displayed values represent mean of accuracy across the three studies and additional protocol variations: $CTDI_{vol}$ and reconstruction filter. Error bars represent one SD for each distribution. 81
Figure 4.23: Differentiation accuracy using support vector machine method analyzed by reconstruction filter. Displayed values represent mean of accuracy across the three studies and additional protocol variations: $CTDI_{vol}$ and image thickness. Error bars represent one SD for each distribution. 82
Figure 4.24: Surface plots for SVM differentiation accuracy (z-axis) for 0.5 cm and 1.0 cm cerebrum matched model pairs based on the attenuation (HU) of the lesion pair (x-axis, right) and the $CTDI_{vol}$ of the acquisition (y-axis, left) for all image thicknesses. Standard filter used for all visualizations. Color bar provided to assist in visualization of higher accuracy results (warmer colors correspond with higher accuracies). The gray plane is fixed at 90% differentiation accuracy. 83
Figure 4.25: Surface plots for SVM differentiation accuracy (z-axis) for 1.5 cm cerebrum and 1.5 cm skull base matched model pairs based on the attenuation (HU) of the lesion pair (x-axis, right) and the $CTDI_{vol}$ of the acquisition (y-axis, left) for all image thicknesses. Standard filter used for all visualizations. Color bar provided to assist in visualization of higher accuracy results (warmer colors correspond with higher accuracies). The gray plane is fixed at 90% differentiation accuracy. 84
Figure 4.26: Graphical representation of lesion attenuation (HU) necessary for 90% SVM differentiation accuracy by acquisition parameters (Table 4.13). The un-shaded region

represents $CTDI_{vol}$ and image thickness values allow 90% differentiation accuracy under the current clinical limit of 100 HU imposed by SECT. 89
Figure 4.27: Differentiation accuracy using geometric bisector method. Displayed values represent mean of accuracy across the three studies and all protocol variations: $CTDI_{vol}$, image thickness and reconstruction filter. Error bars represent one SD of the distribution..90
Figure 4.28: Differentiation accuracy using geometric bisector method analyzed by $CTDI_{vol}$. Displayed values represent mean of accuracy across the three studies and additional protocol variations: image thickness and reconstruction filter. Error bars represent one SD for each distribution. 91
Figure 4.29: Differentiation accuracy using geometric bisector method analyzed by image thickness. Displayed values represent mean of accuracy across the three studies and additional protocol variations: $CTDI_{vol}$ and reconstruction filter. Error bars represent one SD for each distribution. 92
Figure 4.30: Differentiation accuracy using geometric bisector method analyzed by reconstruction filter. Displayed values represent mean of accuracy across the three studies and additional protocol variations: $CTDI_{vol}$ and image thickness. Error bars represent one SD for each distribution. 93
Figure 4.31: Surface plots for GB differentiation accuracy (z-axis) for 0.5 cm and 1.0 cm cerebrum matched model pairs based on the attenuation (HU) of the lesion pair (x-axis, right) and the $CTDI_{vol}$ of the acquisition (y-axis, left) for all image thicknesses. Standard filter used for all visualizations. Color bar provided to assist in visualization of higher accuracy results (warmer colors correspond with higher accuracies). The gray plane is fixed at 90% differentiation accuracy. 94
Figure 4.32: Surface plots for GB differentiation accuracy (z-axis) for 1.5 cm cerebrum and 1.5 cm skull base matched model pairs based on the attenuation (HU) of the lesion pair (x-axis, right) and the $CTDI_{vol}$ of the acquisition (y-axis, left) for all image thicknesses.

Standard filter used for all visualizations. Color bar provided to assist in visualization of higher accuracy results (warmer colors correspond with higher accuracies). The gray plane is fixed at 90% differentiation accuracy. 95

Figure 4.33: Graphical representation of lesion attenuation (HU) necessary for 90% GB differentiation accuracy by acquisition parameters (Table 4.15). The un-shaded region represents $CTDI_{vol}$ and image thickness values allow 90% differentiation accuracy under the current clinical limit of 100 HU imposed by SECT. 100

Figure 4.34: Bland-Altman and Correlation graphs for inter-method correlation between SVM and GB methods. Top: Full data results including all protocol variations and lesion models. Middle: Results for 0.5 cm cerebrum matched model pair, identified as a major source of variability in Table 4.18. Bottom: Results for full data excluding 0.5 cm cerebrum matched model pair values. 105

Figure 4.35: Bland-Altman and correlation graphs for SVM inter-scanner correlation. Upper Left: Analysis of full data. Right: Analysis of major sources of variability based on results in Table 4.19. Lower Left: Analysis of full data with the data associated with these major sources of variability removed. 108

Figure 4.36: Bland-Altman and correlation graphs for GB inter-scanner correlation. Upper Left: Analysis of full data. Right: Analysis of major sources of variability based on both CV and R^2 cutoff criteria (Table 4.20). Sources of variability identified solely by R^2 criteria were excluded for simplicity of visualization. Lower Left: Analysis of full data with the data associated with these major sources of variability removed 111

Figure 4.37: Bland-Altman and correlation graphs for SVM intra-scanner correlation. Upper Left: Analysis of full data. Right: Analysis of major sources of variability based on results in Table 4.21. Lower Left: Analysis of full data with the data associated with these major sources of variability removed. 114

Figure 4.38: Bland-Altman and correlation graphs for GB intra-scanner correlation. Upper Left: Analysis of full data. Right: Analysis of major sources of variability based on results in Table 4.22. Lower Left: Analysis of full data with the data associated with these major sources of variability removed 117
Figure 5.1: Application of lesion and acquisition specific geometric bisector plane (gray) to an example unknown lesion model. The lesion model mean is shown as a black diamond to the left of the plane. The voxel data also on the left of the plane (and thus contributing to the classification confidence) is shown in red, while the voxel data on the right side of the plane (and thus counting against the classification confidence) is shown in blue. 129
Figure 5.2: Classification confidence results for all unknown lesion models using the geometric bisector method. Calcification lesion models are shown in blue while hemorrhage models are shown in red. 137
Figure 5.3: Classification confidence results for all unknown lesion models using the generalized geometric bisector method. Calcification lesion models are shown in blue while hemorrhage models are shown in red. 138
Figure 5.4: Classification confidence results for all unknown lesion models using the probability distribution method. Calcification lesion models are shown in blue while hemorrhage models are shown in red. 140
Figure 5.5: Geometric bisector confidence in classification of hemorrhage unknown lesions. Darker shades of red indicate higher $CTDI_{vol}$ levels.....141
Figure 5.6: Geometric bisector confidence in classification of calcification unknown lesions. Darker shades of blue indicate higher $CTDI_{vol}$ levels. 141
Figure 5.7: Generalized geometric bisector confidence in classification of hemorrhage unknown lesions. Darker shades of red indicate higher $CTDI_{vol}$ levels.....144
Figure 5.8: Generalized geometric bisector confidence in classification of calcification unknown lesions. Darker shades of red indicate higher $CTDI_{vol}$ levels.....144

Figure 5.9: Probability distribution confidence in classification of hemorrhage unknown lesions. Darker shades of red indicate higher $CTDI_{vol}$ levels. 147
Figure 5.10: Probability distribution confidence in classification of calcification unknown lesions. Darker shades of blue indicate higher $CTDI_{vol}$ levels. 147
Figure 5.11: Bland-Altman and Correlation graphs for inter-method correlation between GB and PD methods. Top: Full data results including all lesion/acquisition combinations. Middle: Results for hemorrhage lesion models, identified as a major source of variability in Table 5.11. Bottom: Results for full data excluding hemorrhage lesion model values. 151
Figure 5.12: Bland-Altman and Correlation graphs for inter-method correlation between GB and GGB methods. Top: Full data results including all lesion/acquisition combinations. Middle: Results for 0.5 cm cerebrum lesion models, identified as a major source of variability in Table 5.12. Bottom: Results for full data excluding 0.5 cm cerebrum lesion model values. 153
Figure 5.13: Summary of GB (solid lines) and PD (dashed lines) classification confidence based on lesion size and location. Error bars represent one SD of the $CTDI_{vol}$ levels investigated. Hemorrhage data is shown in red while calcification data is shown in blue. 155
Figure 5.14: Distance between unknown lesion mean value and parameter-specific GB plane. Error bars represent one SD of the $CTDI_{vol}$ levels investigated. Hemorrhage model data is shown in red while calcification model data is shown in blue. 156
Figure 5.15: Visualization of unknown lesion and prior differentiation lesion mean values for a 1.0 cm cerebrum lesion imaged using 105.6 mGy, 3.75 mm image thickness, and Standard reconstruction filter. Acquisition matched GB plane and hemorrhage and calcification line fits shown. 157
Figure 5.16: Visualization of unknown lesion and prior differentiation lesion mean values for a 0.5 cm cerebrum lesion imaged using 105.6 mGy, 3.75 mm image thickness, and

Standard reconstruction filter. Acquisition matched GB plane and hemorrhage and calcification line fits shown. 157
Figure 5.17: Summary of geometric bisector results for hemorrhage lesions by availability of prior knowledge. GB (dotted line) is lesion and acquisition parameter-specific and thus requires prior knowledge of the lesion size and location and acquisition to be used. GGB (dashed line) requires knowledge of only the lesion size and location. SGGB (solid line) assumes no prior knowledge of either the lesion or acquisition. 161
Figure 5.18: Summary of geometric bisector results for calcification lesions by availability of prior knowledge. GB (dotted line) is lesion and acquisition parameter-specific and thus requires prior knowledge of the lesion size and location and acquisition to be used. GGB (dashed line) requires knowledge of only the lesion size and location. SGGB (solid line) assumes no prior knowledge of either the lesion or acquisition. 162
Figure 6.1: Basic structure and measurements of DEQC phantom. Solid water components are shown in dark brown, HDPE components in tan and PVC in light gray. 169
Figure 6.2: DEQC insert layout with average 120kVp HU level of inserts labeled. 170
Figure 6.3: a) Polycarbonate plate attached to back of phantom with solid water bolts visible at the bottom and side periphery of the phantom (white arrows). b) Detail of lower solid water bolt as well as the orientation plug (red arrow) used to ensure proper alignment of the head phantom within the body phantom. 171
Figure 6.4: DEQC body phantom results for iodine accuracy. Left: Iodine accuracy trends sorted primarily by mAs and secondarily by $CTDI_{vol}$ for 2 mg/mL, 5 mg/mL, and 15 mg/mL iodine rods displayed by scanner. Right: Iodine accuracy inter- and intra-scanner variance trends sorted primarily by $CTDI_{vol}$ and secondarily by mAs for 2 mg/mL, 5 mg/mL, and 15 mg/mL iodine rods.....187
Figure 6.5: DEQC head phantom results for iodine accuracy. Left: Iodine accuracy trends sorted primarily by mAs and secondarily by $CTDI_{vol}$ for 2 mg/mL and 5 mg/mL iodine rods

displayed by scanner. Right: Iodine accuracy inter- and intra-scanner variance trends sorted primarily by mAs and secondarily by $CTDI_{vol}$ for 2 mg/mL and 5 mg/mL iodine rods. 189
Figure 6.6: DEQC body phantom results for uniformity. Left: Uniformity trends sorted primarily by rotation time and secondarily by $CTDI_{vol}$ for 50, 70, 110 and 140 keV monoenergetic reconstructions and displayed by scanner. Right: Uniformity inter- and intra-scanner variance trends sorted primarily by $CTDI_{vol}$ and secondarily by mAs for 50, 70, 110, and 140 keV monoenergetic reconstructions.....192
Figure 6.7: DEQC body phantom results for uniformity. Left: Uniformity trends sorted primarily by rotation time and secondarily by $CTDI_{vol}$ for Water(Iodine) and Iodine(Water) material density reconstructions and displayed by scanner. Right: Uniformity inter- and intra-scanner variance trends sorted primarily by $CTDI_{vol}$ and secondarily by mAs for Water(Iodine) and Iodine(Water) material density reconstructions. 193
Figure 6.8: DEQC body phantom results for uniformity sorted primarily by rotation time and secondarily by mAs for 50, 70, 110 and 140 keV monoenergetic reconstructions. 195
Figure 6.9: DEQC head phantom results for uniformity. Left: Uniformity trends sorted primarily by mAs and secondarily by $CTDI_{vol}$ for 50, 70, 110 and 140 keV monoenergetic reconstructions and displayed by scanner. Right: Uniformity inter- and intra-scanner variance trends sorted primarily by CTDIvol and secondarily by mA for 50, 70, 110, and 140 keV monoenergetic reconstructions. 197
Figure 6.10: DEQC head phantom results for uniformity. Left: Uniformity trends sorted primarily by mAs and secondarily by $CTDI_{vol}$ for Water(Iodine) and Iodine(Water) material density reconstructions and displayed by scanner. Right: Uniformity inter- and intra-scanner variance trends sorted primarily by $CTDI_{vol}$ and secondarily by mA for Water(Iodine) and Iodine(Water) material density reconstructions. 198

Figure 6.11: DEQC head phantom results for uniformity sorted primarily by mAs and secondarily by rotation time for 50, 70, 110 and 140 keV monoenergetic reconstructions. 199
Figure 6.12: DEQC body phantom results for monoenergetic HU stability. Left: Monoenergetic HU stability trends sorted primarily by mAs and secondarily by $CTDI_{vol}$ for 50, 70, 110 and 140 keV monoenergetic reconstructions and displayed by scanner. Calculated attenuations (using NIST values) based on vendor-provided elemental composition and true monoenergetic acquisition are shown in black. Right: Monoenergetic HU stability inter- and intra-scanner variance trends sorted primarily by $CTDI_{vol}$ and secondarily by mAs for 50, 70, 110, and 140 keV monoenergetic reconstructions. 202
Figure 6.13: DEQC body phantom results for monoenergetic HU stability trends sorted primarily by mAs and secondarily by $CTDI_{vol}$ for 50, 70, 110 and 140 keV monoenergetic reconstructions. The dashed red line indicates a potential mAs cutoff for optimum efficiency of monoenergetic visualizations. 203
Figure 6.14: DEQC head phantom results for monoenergetic HU stability. Left: Monoenergetic HU stability trends sorted primarily by mA and secondarily by $CTDI_{vol}$ for 50, 70, 110 and 140 keV monoenergetic reconstructions and displayed by scanner. Calculated attenuations (using NIST values) based on vendor-provided elemental composition and true monoenergetic acquisition are shown in black. Right: Monoenergetic HU stability inter- and intra-scanner variance trends sorted primarily by mA and secondarily by $CTDI_{vol}$ for 50, 70, 110, and 140 keV monoenergetic reconstructions.....206
Figure 6.15: DEQC head phantom results for monoenergetic HU stability trends sorted primarily by mA and secondarily by $CTDI_{vol}$ for 50, 70, 110 and 140 keV monoenergetic reconstructions.....207
Figure 6.16: DEQC body phantom results for noise trends sorted by $CTDI_{vol}$ for 50, 70, 110 and 140 keV monoenergetic reconstructions.....208

Figure 6.17: DEQC body phantom results for noise trends sorted by $CTDI_{vol}$ for Water(Iodine) and Iodine(Water) material density reconstructions. 208
Figure 6.18: DEQC head phantom results for noise trends sorted by $CTDI_{vol}$ for 50, 70, 110 and 140 keV monoenergetic reconstructions.....210
Figure 6.19: DEQC head phantom results for noise trends sorted by $CTDI_{vol}$ for Water(Iodine) and Iodine(Water) material density reconstructions. 210
Figure 7.1: Graphical representation of lesion attenuation (HU) necessary for 90% GB differentiation accuracy by acquisition parameters (Table 4.15). The un-shaded region represents $CTDI_{vol}$ and image thickness values allow 90% differentiation accuracy under the current clinical limit of 100 HU imposed by SECT. 223
Figure 7.2: Accuracy of intracranial lesion differentiation using geometric bisector method with 132.6 mGy $CTDI_{vol}$, 5 mm image thickness and standard filter. Error bars represent one SD of the variation over the three studies collected. 224
Figure 8.1: Posterior probabilities for the calcification cluster based on the GMM results of the 50 HU matched model pair. Red indicates a very high probability the voxel is calcification, while blue indicates a very low probability. 231

List of Tables

Table 3.1: Imaging parameters for the single- and dual-energy CT protocols used in the study. For both protocols: Image thickness: 3.75 mm, Table Speed: 10.62 mm/rotation, Pitch: 0.531, Interval: 3 mm, Scan Field of View (SFOV): Head, Display Field of View (DFOV): 12 cm, Reconstruction Algorithm: Soft. 24

Table 3.2: Concentrations and weights of iron oxide and hydroxyapatite needed to create hemorrhage and calcification models of specific SECT attenuation (HU). 30

Table 3.3: Average SECT attenuation (HU) of each matched pair and mean SECT attenuations (HU) for the hemorrhage gel model and the calcification gel model in each pair.....31

Table 4.1: Imaging Technique for basic single-energy and matched dual-energy data collection.....41

Table 4.2: Imaging technique for validation of lesion model inserts. Bold line indicates break in protocol where insert was repositioned to allow imaging of second half of insert extent. Series 2 and 4 were not repeated since their relation to series 3 was already evaluated in the first imaging setting. For all series: SFOV: Head, DFOV: 25 cm, Filter: Standard. 43

Table 4.3: Imaging technique for intracranial lesion phantom scanning. For all series and groups (except series 1): SFOV: Head, DFOV: 25 cm, Scan Type: Helical, Beam Width: 20 mm.....46

Table 4.4: Dual-energy reconstructions for intracranial lesion phantom protocol (detailed in Table 4.3). Prospective recons are listed first and labeled with a P, followed by retrospective recons labeled with an R.....47

Table 4.5: ROI diameters and associated number of voxels based on lesion model size and location. 49
Table 4.6: Number of images and extent analyzed for both the cerebrum and skull base brain slabs. 51
Table 4.7: Total number of voxels included in analysis for both cerebrum and skull base brain slabs based on image thickness and lesion diameter. Note: This total includes multiple image locations as defined by Table 4.6. 52
Table 4.8: Results of lesion rod imaging and ROI analysis using a SECT acquisition. Green fields represent a matched model pair with < 1 HU difference between the calcification and hemorrhage model while orange represents a difference > 1 HU but < 2 HU. Gray regions represent data that is not applicable given the skull base contained only 1.5 cm lesion models. 63
Table 4.9: Initial SECT attenuation (HU) matching of milled lesion model pairs (calcification and hemorrhage). Green denotes matching < 2 HU, orange denotes matching < 3 HU and red denotes matching out of tolerance > 3 HU. 64
Table 4.10: Final SECT attenuation (HU) matching of lesion model pairs (calcification and hemorrhage). Green denotes matching < 2 HU, orange denotes matching < 3 HU and red denotes matching out of tolerance > 3 HU. Note the improved lesion matching of the 50 HU, 0.5 cm cerebrum and 100 HU, 1.5 cm skull base lesion pairs. 65
Table 4.11: Sorted results of Bland-Altman analysis of the correlation of attenuation (HU) from 68 keV and SECT acquisitions organized for subsets of the data based on available protocol and lesion parameters. Parameters and values above the double line indicate worse correlation or linearity than the analysis of the full data set while those below the double line indicate improved correlation or linearity. 68
Table 4.12: $CTDI_{vol}$ (mGy) necessary for 90% SVM differentiation accuracy by HU of matched model pair based on a second order power fit of available data from studies 1-3.

Areas in gray indicate 90% SVM differentiation accuracy was not possible at any dose level investigated. Areas in green indicate 90% SVM differentiation accuracy was achieved at all dose levels investigated (minimum dose investigated shown). Remaining areas in white indicate 90% SVM differentiation accuracy was reached within the investigated dose range and show the minimum $CTDI_{vol}$ required for this level of accuracy. Values in red indicate a fit with an R^2 value of less than 0.8.....87

Table 4.13: Lesion attenuation (HU) necessary for 90% SVM differentiation accuracy by acquisition parameters based on a second order power fit of available data from studies 1-3. Areas in gray indicate 90% SVM differentiation accuracy was not possible under 100 HU. Attenuation (HU) values in red indicate a fit with an R^2 values less than 0.8. 88

Table 4.14: $CTDI_{vol}$ (mGy) necessary for 90% GB differentiation accuracy by HU of matched model pair based on a second order power fit of available data from studies 1-3. Areas in gray indicate 90% GB differentiation accuracy was not possible at any dose level investigated. Areas in green indicate 90% GB differentiation accuracy was achieved at all dose levels investigated (minimum dose investigated shown). Remaining areas in white indicate 90% GB differentiation accuracy was reached within the investigated dose range and show the minimum $CTDI_{vol}$ required for this level of accuracy. Values in red indicate a fit with an R^2 value of less than 0.8.....98

Table 4.15: Lesion attenuation (HU) necessary for 90% GB differentiation accuracy by acquisition parameters based on a second order power fit of available data from studies 1-3. Areas in gray indicate 90% GB differentiation accuracy was not possible under 100 HU. Attenuation (HU) values in red indicate a fit with an R^2 values less than 0.8. 99

Table 4.16: Results of parameter-specific geometric bisector plane calculations. Both raw accuracy and accuracy difference (relative to all data solution) are shown. Plane coefficients follow the equation form Ax+By+Cz+D = 0, where x is water density, y is calcium density and z is measured attenuation (HU) at 68 keV. Those parameters

identified as major sources of variability based on their accuracy difference are shown in red. Note: Location (Skull Base) and Lesion Model (1.5 cm Skull Base) represent identical analysis because only 1.5 cm lesions were evaluated in the skull base. 101
Table 4.17: Generalized geometric bisector plane results assuming prior knowledge of lesion location and size. Plane coefficients follow the equation form Ax+By+Cz+D = 0, where x is water density, y is calcium density and z is measured attenuation (HU) at 68 keV. 103
Table 4.18: Sorted results of Bland-Altman analysis for inter-method correlation between SVM and GB methods for subsets of data based on available protocol and lesion parameters. Parameters and values above the double line indicate worse correlation or linearity than the full data set while those below the double line indicate improved correlation or linearity. Text in red indicates a major source of variability based on CV or R^2 cutoff criteria. 104
Table 4.19: Sorted results of Bland-Altman analysis of SVM inter-scanner correlation for subsets of data based on available protocol and lesion parameters. Parameters and values above the double line indicate worse correlation or linearity than the full data set while those below the double line indicate improved correlation or linearity. Text in red indicates a major source of variability based on CV or R^2 cutoff criteria. 107
Table 4.20: Sorted results of Bland-Altman analysis of GB inter-scanner correlation for subsets of data based on available protocol and lesion parameters. Parameters and values above the double line indicate worse correlation or linearity than the full data set while those below the double line indicate improved correlation or linearity. Text in red indicates a major source of variability based on CV or R^2 cutoff criteria. 110
Table 4.21: Sorted results of Bland-Altman analysis of SVM intra-scanner correlation for subsets of data based on available protocol and lesion parameters. Parameters and values above the double line indicate worse correlation or linearity than the full data set while those

below the double line indicate improved correlation or linearity. Text in red indicates a major source of variability based on CV or R^2 cutoff criteria. 113
Table 4.22: Sorted results of Bland-Altman analysis of GB intra-scanner correlation for subsets of data based on available protocol and lesion parameters. Parameters and values above the double line indicate worse correlation or linearity than the full data set while those below the double line indicate improved correlation or linearity. Text in red indicates a major source of variability based on CV or R^2 cutoff criteria. 116
Table 4.23: Summary of inter-scanner (Study 1 versus Study 3) and intra-scanner (Study 1 versus Study 2) correlations based on both SVM and GB methods. Parameters identified as major sources of variability are listed along with the initial CV and R^2 for the full data, as well as, the final CV and R^2 with the sources of variability removed from analysis. 121
Table 5.1: Unknown lesion material verification and evaluation protocol. Both series were acquired in helical mode, using a 20 mm beam width, 25 cm DFOV and Head SFOV. Images were evaluated visually to confirm the lesion models were homogeneous and free of defects. 126
Table 5.2: Unknown lesion validation protocol. For all acquisitions: helical, 20 mm beam width, 25 cm DFOV, Head SFOV. 128
Table 5.3: Summary of multivariate logistic regression model results correlating water, calcium, and 68 keV measurements with probability of the unknown lesion being calcification. Odds ratio is for each unit increase in the measurement. Odds ratio greater than 1 means an increased probability of being calcification. LCL and UCL refer to the lower and upper confidence limits, respectively. 135
Table 5.4: Summary of logistic regression model coefficients based on analysis of Study 1 differentiation data (Chapter 4). These coefficients work with Equations 12-14 to calculate the probability of being calcification based on an unknown lesion's mean 3D-DECT measurement. 136

Table 5.5: SECT attenuation (HU) necessary for 90% classification confidence using the GB method. Gray regions represent lesion/acquisition combinations that would only be classified with 90% confidence above the 100 HU limit imposed by SECT. Green regions represent lesion/acquisition combinations that would be classified with 90% confidence below the minimum SECT investigated. White regions represent lesion/acquisition combinations that would be classified with 90% confidence within the investigated lesion attenuation range. Text in red indicates a curve fit R^2 with less than 0.8. 142
Table 5.6: SECT attenuation (HU) necessary for 80% classification confidence using the GB method. Gray regions represent lesion/acquisition combinations that would only be classified with 80% confidence above the 100 HU limit imposed by SECT. Green regions represent lesion/acquisition combinations that would be classified with 80% confidence below the minimum SECT investigated. White regions represent lesion/acquisition combinations that would be classified with 80% confidence within the investigated lesion attenuation range. Text in red indicates a curve fit R^2 with less than 0.8. 143
Table 5.7: SECT attenuation (HU) necessary for 90% classification confidence using the GGB method. Gray regions represent lesion/acquisition combinations that would only be classified with 90% confidence above the 100 HU limit imposed by SECT. Green regions represent lesion/acquisition combinations that would be classified with 90% confidence below the minimum SECT investigated. White regions represent lesion/acquisition combinations that would be classified with 90% confidence within the investigated lesion attenuation range. Text in red indicates a curve fit R^2 with less than 0.8. 145
Table 5.8: SECT attenuation (HU) necessary for 80% classification confidence using the GGB method. Gray regions represent lesion/acquisition combinations that would only be classified with 90% confidence above the 100 HU limit imposed by SECT. Green regions represent lesion/acquisition combinations that would be classified with 90% confidence below the minimum SECT investigated. White regions represent lesion/acquisition

combinations that would be classified with 90% confidence within the investigated lesion attenuation range. Text in red indicates a curve fit R^2 with less than 0.8. 146
Table 5.9: SECT attenuation (HU) necessary for 90% classification confidence using the PD method. Gray regions represent lesion/acquisition combinations that would only be classified with 90% confidence above the 100 HU limit imposed by SECT. Green regions represent lesion/acquisition combinations that would be classified with 90% confidence below the minimum SECT investigated. White regions represent lesion/acquisition combinations that would be classified with 90% confidence within the investigated lesion attenuation range. Text in red indicates a curve fit R^2 with less than 0.8. 148
Table 5.10: SECT attenuation (HU) necessary for 80% classification confidence using the PD method. Gray regions represent lesion/acquisition combinations that would only be classified with 80% confidence above the 100 HU limit imposed by SECT. Green regions represent lesion/acquisition combinations that would be classified with 80% confidence below the minimum SECT investigated. White regions represent lesion/acquisition combinations that would be classified with 80% confidence within the investigated lesion attenuation range. Text in red indicates a curve fit R^2 with less than 0.8. 149
Table 5.11: Sorted results of GB vs PD inter-method Bland-Altman analysis for subsets of data based on available protocol and lesion parameters. Parameters and values above the double line indicate worse correlation or linearity than the full data set while those below the double line indicate improved correlation or linearity. Text in red indicates a major source of variability based on CV or R^2 cutoff criteria. 150
Table 5.12: Sorted results of GB vs GGB inter-method Bland-Altman analysis for subsets of data based on available protocol and lesion parameters. Parameters and values above the double line indicate worse correlation or linearity than the full data set while those below the double line indicate improved correlation or linearity. Text in red indicates a major source of variability based on CV or R^2 cutoff criteria. 152

Table 6.1: List of DEQC phantom insert types.....170
Table 6.2: DEQC insert validation protocol. For all series: SFOV: Head, DFOV: 25 cm, Filter: Standard. 172
Table 6.3: Reconstructions created from DEQC validation data and quantitative data acquired. 173
Table 6.4: List of test metrics included in DEQC program and their application to various image reconstruction types, as well as the composition and position of the rods used to evaluate the metric.....176
Table 6.5: Head Phantom DEQC Protocol Version 1. All acquisitions used helical acquisition mode, beam width of 20 mm, Head SFOV, DFOV of 25 cm, and Standard reconstruction algorithm. A total of 5 images were acquired per group.....177
Table 6.6: Body Phantom DEQC Protocol Version 1. All acquisitions used helical acquisition mode, beam width of 40 mm, Large Body SFOV, 42 cm DFOV, and Standard reconstruction algorithm. A total of 5 images were acquired per group.....178
Table 6.7: Dual-energy reconstructions applied to all dual-energy acquisitions in both the version 1 DEQC Body and Head protocols. The number of images reconstructed was based on the minimum setting for each reconstruction type: five for monoenergetic and one for material density.....179
Table 6.8: DEQC Head Phantom Protocol Version 2. All acquisitions used helical scan mode, 20 mm beam width, Head SFOV, 25 cm DFOV, and Standard reconstruction algorithm. 180
Table 6.9: DEQC Body Phantom Protocol Version 2. All acquisitions used helical scan mode, 40 mm beam width, Large Body SFOV, 42 cm DFOV, and Standard reconstruction algorithm. 180
Table 6.10: Dual-energy reconstructions applied to all dual-energy acquisitions in both the version 2 DEQC body and head protocols. The number of images reconstructed was based

on the minimum setting for each reconstruction type: five for monoenergetic and one for material density. 181
Table 6.11: Results of DEQC protocol 1 for the DEQC Body phantom showing which factors were found to influence the test metrics investigated. Marked cells indicate that the acquisition parameter was found to have an effect on the test metric. Empty cells indicate no effect was identified. 185
Table 6.12: Results of DEQC protocol 1 for the DEQC head phantom showing which factors were found to influence the test metrics investigated. Marked cells indicate that the acquisition parameter was found to have an effect on the test metric. Empty cells indicate no effect was identified. 185
Table 6.13:DEQC body phantom results for the effect of mAs on iodine accuracy based on linear mixed model analysis. 188
Table 6.14: DEQC head phantom results for the effect of mAs on iodine accuracy based on linear mixed model analysis. 190
Table 6.15: DEQC body phantom results for the effect of rotation time on uniformity based on linear mixed model analysis. 194
Table 6.16: DEQC head phantom results for the effect of mAs on Uniformity based on linear mixed model analysis. 199
Table 6.17: DEQC body phantom results for the effect of mAs on monoenergetic HU stability based on linear mixed model analysis. 202
Table 6.18: DEQC head phantom results for the effect of mA on monoenergetic HU stability based on linear mixed model analysis. 206
Table 6.19: DEQC body phantom results for the effect of $CTDI_{vol}$ on noise based on linear mixed model analysis. 209
Table 6.20: DEQC head phantom results for the effect of $CTDI_{vol}$ on noise based on linear mixed model analysis. 211

Table 6.21: Final recommendations for the clinically implementable dual-energy quality control protocol. All acquisitions performed in helical mode, using a 40 mm beam width, Large Body SFOV, 42 cm DFOV and standard reconstruction filter. 212

List of Equations

Equation 1 $\boldsymbol{\mu}(E) = \boldsymbol{\alpha} f_{pe}(E) + \boldsymbol{\beta} f_c(E)$ 13

Equation 2 $\mu_1(E) = \alpha_1 f_{pe}(E) + \beta_1 f_c(E)$ 13

Equation 3 $\mu_2(E) = \alpha_2 f_{pe}(E) + \beta_2 f_c(E)$ 13

Equation 4 $f_{pe}(E) = \frac{\beta_2 \mu_1(E) - \beta_1 \mu_2(E)}{\alpha_1 \beta_2 - \alpha_2 \beta_1}$ 14

Equation 5 $f_c(E) = \frac{\alpha_2 \mu_1(E) - \alpha_1 \mu_2(E)}{\beta_1 \alpha_2 - \beta_2 \alpha_1}$ 14

Equation 6 $\mu_{voxel}(E) = \alpha\, f_{pe}(E) + \beta\, f_c(E)$ 14

Equation 7 $\mu_{voxel}(E) = \alpha\left(\frac{\beta_2 \mu_1(E) - \beta_1 \mu_2(E)}{\alpha_1 \beta_2 - \alpha_2 \beta_1}\right) + \beta\left(\frac{\alpha_2 \mu_1(E) - \alpha_1 \mu_2(E)}{\beta_1 \alpha_2 - \beta_2 \alpha_1}\right)$ 14

Equation 8 $\mu_{voxel}(E) = \left(\frac{\alpha\beta_2 - \beta\alpha_2}{\alpha_1 \beta_2 - \alpha_2 \beta_1}\right)\mu_1(E) + \left(\frac{\beta\alpha_1 - \alpha\beta_1}{\beta_2 \alpha_1 - \alpha_2 \beta_1}\right)\mu_2(E)$ ...14

Equation 9 $\mu_{voxel}(E) = a_1 \mu_1(E) + a_2 \mu_2(E) \quad where$ 15

$a_1 = \left(\frac{\alpha\beta_2 - \beta\alpha_2}{\alpha_1 \beta_2 - \alpha_2 \beta_1}\right) \quad and \quad \alpha_2 = \left(\frac{\beta\alpha_1 - \alpha\beta_1}{\beta_2 \alpha_1 - \alpha_2 \beta_1}\right)$

Equation 10 $\mu_{voxel}(E_{high}) = a_1 \mu_1(E_{high}) + a_2 \mu_2(E_{high})$ 15

Equation 11 $\mu_{voxel}(E_{low}) = a_1 \mu_1(E_{low}) + a_2 \mu_2(E_{low})$ 15

Equation 12 $Lesion\ Probability\ Coefficient\ (LPC) =$ .131

$b_0 + b_1(Water\ density) + b_2(Calcium\ density) + b_3(68keV\ HU)$

Equation 13 $Probability(Calcification) = \frac{e^{LPC}}{(1+e^{LPC})}$ 131

Equation 14 $Probability(Hemorrhage) = 1 - Probability(Calcification)$ 131

Equation 15 $P(X) = \sum_{k=1}^{K} p_k \, N(\mu_k, \Sigma_k)$ 229

Equation 16 $P = Prob(Voxel|Cluster) = Prob(Cluster|Voxel)Prob(Voxel)$ 230

List of Abbreviations

3D	Three Dimensional
AW	Advantage Workstation
CNR	Contrast-To-Noise Ratio
CT	Computed Tomography
$CTDI_{vol}$	Computed Tomography Dose Index Volumetric
CV	Coefficient of Variation
DECT	Dual-Energy CT
DEQC	Dual-Energy Quality Control
DFOV	Display Field of View
DICOM	Digital Imaging and Communications in Medicine
EM	Expectation Maximization
GB	Geometric Bisector
GE	General Electric
GGB	Generalized Geometric Bisector
GMM	Gaussian Mixture Model
GRE	Gradient Echo
GSI	Gemstone Spectral Imaging
HDPE	High Density Polyethylene
HU	Hounsfield Unit
keV	Kilo-Electron Volt
kVp	Kilo-Voltage Peak
LCL	Lower Confidence Limit
mA	Milliamperes

mAs	Milliampere-Second
MR	Magnetic Resonance
NPS	Noise Power Spectrum
PD	Probability Distribution
PVC	Polyvinyl Chloride
QC	Quality Control
QSM	Quantitative Susceptibility Mapping
R^2	Squared Pearson R-Value
ROI	Region of Interest
SD	Standard Deviation
SECT	Single-Energy CT
SFOV	Scan Field of View
SGGB	Super Generalized Geometric Bisector
SVM	Support Vector Machine
SWI	Susceptibility Weighted Imaging
UCL	Upper Confidence Limit
VMS	Virtual Monoenergetic Spectral

Chapter 1

Introduction

Calcific and hemorrhagic foci of susceptibility are frequently encountered in routine brain Magnetic Resonance (MR) studies. Both etiologies cause variations in magnetic field strength leading to dark regions on the MR images that cannot be classified (1). Single-energy computed tomography (SECT) can be used to identify lesions with attenuation over 100 Hounsfield Units (HU) as calcific (2), however lesions with lower attenuation cannot be reliably identified. While calcific lesions are unlikely to cause harm (3), hemorrhagic lesions carry a risk of subsequent intracranial bleeding (4,5); as such, identification of hemorrhage is vital in preventing the inappropriate use of anticoagulant medications in patients with hemorrhagic lesions. The relatively high incidence of deep vein thrombosis and pulmonary embolism in cancer patients (6–10) has led many practitioners to treat prophylactically for these conditions. The proper differentiation of calcification and hemorrhage will allow physicians to guide therapy for patients with hemorrhagic lesions away from therapy or prophylaxis that might cause them harm (11,12). Given that there currently exists no clinically available means of differentiating between these two lesion types over their full biological attenuation ranges, there is a clear need for a reliable imaging method to differentiate low intensity calcification and hemorrhage. A novel computed tomography (CT) modality has been developed which collects temporally and anatomically registered CT scans at two different tube voltages. By collecting data at two different energies, dual-energy CT (DECT) identifies energy-dependent attenuation changes which can be used to gain information about the material characteristics within a specific voxel. The rationale behind this research is that the difference in the energy-dependent attenuation characteristics of calcium, found in calcification, and iron, found in hemorrhage should

result in unique signatures using DECT, permitting the differentiation of the two lesion types.

1.1 Objectives and Hypothesis

Therefore, the objective of this project is to model intracranial calcification and hemorrhage over a wide range of biological conditions and image using DECT in order to determine if material characteristic information derived from DECT images can be used to differentiate between calcification and hemorrhage. **The central hypothesis is that DECT can be used to differentiate between intracranial calcium associated with calcification and iron associated with hemorrhage below the attenuation level possible using traditional SECT.**

1.2 Specific Aims

To test this central hypothesis, four specific aims were constructed:

Specific Aim 1: Determine the SECT attenuation (HU) level at which hemorrhage and calcification models can be differentiated on DECT images to within 90% accuracy using an agar gel-based phantom.

Specific Aim 2:

A: Design and create a biologically relevant phantom that more realistically replicates the attenuation characteristics of the human brain, and includes various intracranial lesion sizes and locations.

B: Determine the DECT technique that provides optimal differentiation of calcification and hemorrhage models based on the lesion pair's size and location within the biologically relevant phantom (Specific Aim 2A).

Specific Aim 3: Assess the ability of DECT to classify unknown intracranial lesions with SECT attenuation levels under 100 HU as either calcific or hemorrhagic using the biologically relevant phantom model described in Specific Aim 2.

Specific Aim 4: Develop a dual-energy CT quality control phantom and program to provide inter- and intra-scanner quality assurance data for long term clinical DECT applications.

To achieve these specific aims, models of calcification and hemorrhage will be designed and fabricated. The models will be imaged in anthropomorphic phantoms using both single-energy and dual-energy techniques. Calcification and hemorrhage models will be organized into pairs consisting of a calcification model and a hemorrhage model that display equivalent single-energy attenuation. The material characteristic information for all matched attenuation pairs will be derived from the dual-energy images. The accuracy of the differentiation between calcification and hemorrhage model will be calculated for each matched model pair and the SECT attenuation (HU) level at which the accuracy exceeds 90% will be determined. In specific aim 2, the models of calcification and hemorrhage will be improved to better mimic the typical biology as well as to simulate a range of lesion sizes, intracranial locations and imaging parameters. The resulting material characteristic information from the dual-energy images will be compared to the results in specific aim 1 and used to determine the imaging technique, patient population constraints and analysis methods for a prospective human trial. These conclusions will be verified using unknown lesion models of varying attenuation, size and intracranial location in the biologically relevant phantom system designed in Specific Aim 2. Given that this work will span several years, verification that the results are intercomparable is necessary. Unfortunately, since DECT is a novel and emerging modality, a true quality control standard has yet to be determined. Specific Aim 4 will strive to develop a quality control phantom and program designed specifically to verify the dual-energy capabilities of the scanners used in this study. Through the completion of Specific Aims 1-4 we propose to develop a clinically

feasible method for the differentiation, and hopefully correct classification, of intracranial hemorrhage and calcification.

1.3 Dissertation Organization

The remaining chapters of this dissertation are organized as follows: Chapter 2 introduces background concepts specific to DECT as well as competing modalities. Chapter 3 addresses Specific Aim 1 and presents the results of a simple agar-gel based phantom for the differentiation of calcification and hemorrhage. Chapter 4 addresses Specific Aim 2 and covers the development of the biologically relevant phantom model and the determination of optimal DECT techniques based on lesion size and location within the phantom. Chapter 5 addresses Specific Aim 3 and includes preliminary results on unknown lesion characterization. Chapter 6 addresses Specific Aim 4 and covers the design and development of the DECT quality control phantom and protocol as well as preliminary results and clinical insights. Finally, Chapter 7 summarizes the dissertation and comments on future work.

Chapter 2

Background

Intracranial hemorrhagic and calcific lesions are associated with very different outcomes and may require different management strategies. Intracranial calcifications are relatively common but in general are benign and have little clinical importance (3). They can be caused by a number of conditions and treatments including radiation therapy and chemotherapy (13) and are typically found in the pineal gland, choroid plexus, habenula, and blood vessels. Their size and structure can range from small and punctuate to large and more laminar (2) and typically consist of a combination of calcium phosphorus, silicon, potassium, magnesium and zinc (14).

Intracranial hemorrhagic lesions due to cavernomata, however, carry a risk of subsequent intracranial bleeding, with rehemorrhage rates as high as 4-10% per lesion per year (4,5). The lesions range in size from 1 mm up to several centimeters (4) and can be found throughout the nervous system, but are most commonly found in the cerebrum (15). They present in approximately 0.1 to 0.5% of the population and comprise roughly 5-13% of all vascular lesions (4).

Due to the risk of brain hemorrhage, the use of anticoagulants in patients with intracranial cavernomata or hemorrhagic lesions is contraindicated (11,12). However, driven by the high incidence of deep vein thrombosis and pulmonary embolism in cancer patients (6–10) and other high risk populations, many practitioners are prescribing prophylactic anticoagulants (16). Cohen et al. investigated the risk for venous thromboembolism (VTE) and the application of anticoagulant prophylaxis based on all hospital impatients over the age of 40 admitted to the medical ward, or over the age of 18 admitted to the surgical ward over 358 hospitals spanning 32 countries (17). They found

that of the 68,183 patients admitted, 64% of surgical patients and 42% of medical patients were at risk of VTE. Of the at risk population, 59% of at risk surgical patients and 40% of at risk medical patients were administered anticoagulants. Zwicker et al. investigated cancer patients specifically and found that of the 775 patients at risk of VTE, 68% had no contraindication for prophylaxis and of those a full 75% were administered anticoagulants (18). Beyond inpatients, a recent study has shown that approximately 5% of people between the ages of 65 and 74, and 10% of people over the age of 75 have been prescribed prophylactic anticoagulants (19). Based on these facts it is evident that accurate differentiation of intracranial calcification and hemorrhage would benefit a large patient population by allowing physicians to steer patients with hemorrhagic lesions away from common anticoagulant prophylaxis that might harm them.

Accurate differentiation of intracranial calcification and hemorrhage would allow physicians to steer patients with hemorrhagic lesions away from anticoagulation that might harm them.

Currently there exists no clinically available means of differentiating calcification and hemorrhage over their full biological ranges. Traditional SECT is considered the gold standard modality for the identification of calcification. Generally, any lesion with SECT attenuation levels >100 HU is classified as a calcification (2). However, lesions with SECT attenuation levels <100 HU present a clinical problem, since hemorrhage and calcifications overlap in this attenuation range, making classification difficult.

Magnetic Resonance (MR) has long been the gold standard for hemorrhage detection where the characteristic appearance is a ring of hypo-intensity due to susceptibility artifacts caused by the iron-rich hemosiderin deposits in the lesion (15). However, calcifications also induce this susceptibility artifact which leads to a similar hypo-intense region within the image.

Susceptibility artifacts occur due to variations in magnetic field strength which are caused by paramagnetic materials, diamagnetic materials or interfaces between regions of very different magnetic susceptibility. These intra-voxel variations in the magnetic field strength result in variations in the protons' precession frequency and thus phase shifts. Secondly, intra-voxel variations create spin incoherence resulting in a hypo-intense or signal void region on the image (20,21). Since foci of susceptibility can be caused by either calcification or hemorrhage, conventional MR is of little help in differentiating these two lesion types.

Given that at this time there are no clinically available means of differentiating between these two lesions over their full biological attenuation ranges, there is a clear need for a reliable imaging method to differentiate low intensity calcification and hemorrhage. Recently, several vendors have released new CT scanner models with dual-energy capabilities, which may be successfully applied to this issue. By collecting data at two different energies, DECT provides information about energy-dependent changes in linear attenuation which can be used to derive information about the material characteristics within a specific voxel. This information may help distinguish between two materials with similar linear attenuation measurements which would be impossible to differentiate using SECT (22).

Although the technique of dual-energy Computed Tomography (DECT) has been known since the 1970s (23–25), the application of the technique has been hampered by a range of issues including high image noise, motion misregistration and long acquisition times resulting in excessive patient dose (26). Only recently have advances in scanner hardware helped overcome these issues and allowed DECT to enter the realm of clinical applications. With the release of the first clinical DECT scanner by Siemens (SOMATOM Flash) in 2005 (27), and the subsequent release of the General Electric (GE) Discovery 750HD and Siemens SOMATOM Definition Flash in 2008 (28,29), dual-energy CT (or

spectral CT) research and applications have grown at an increasing rate (Figure 2.1). Given the recent release of the Siemens SOMATOM Force, as well as the scheduled release of the dual-energy package on the GE Revolution CT within the next year, it can be expected that this trend will continue as new hardware and software advance the capabilities of material decomposition. The Siemens SOMATOM Force x-ray tube is capable a generating peak kilovoltage (kVp) beams from 70kVp to 150kVp and has higher milliampere (mA) limits, both hopefully leading to better characterized material decomposition (30–32). The GE Revolution CT, once equipped with dual-energy software, will provide a much larger beam width of 16 cm (33), opening up a wealth of applications in cardiac imaging and perfusion measurements. These advances in dual-energy data collection are sure to lead to further research into the expanding clinical applications of dual-energy CT.

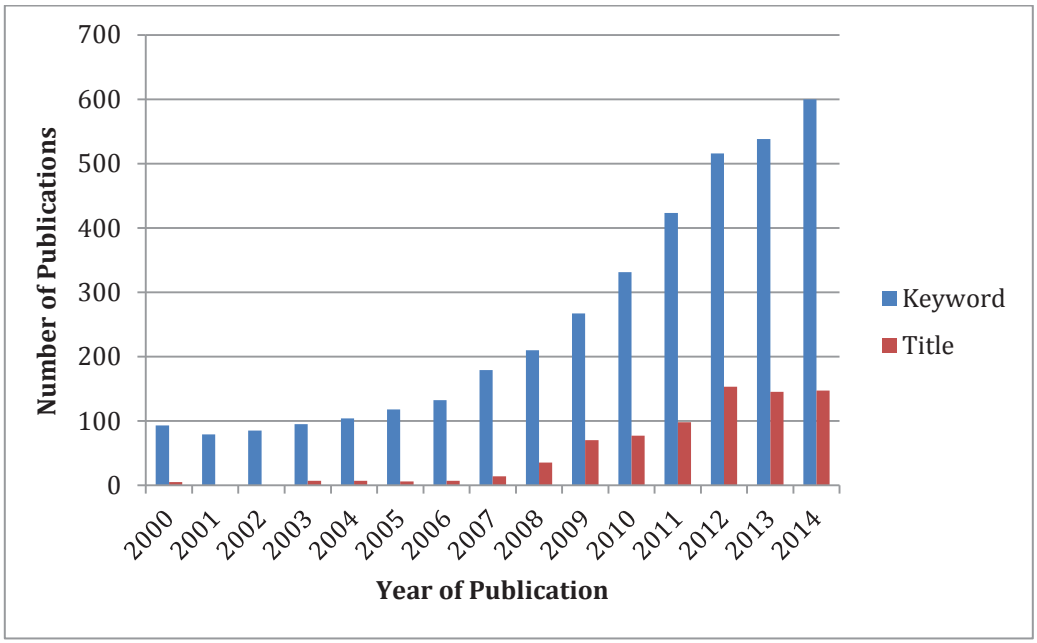

Figure 2.1: Increase in DECT publications from January 1, 2000 to December 31, 2014 based on occurrence of "Dual-Energy CT" or "Spectral CT" using the Web of Science database tool (34).

2.1 Basics of DECT

In traditional single-energy CT (SECT), the x-ray absorption through the patient is expressed as an attenuation value normalized to the linear attenuation of water. The resulting CT numbers, measured in Hounsfield units (HU), are displayed in shades of gray on the CT image. While intuitive to view, these Hounsfield units do not accurately represent material composition within the voxel. First, linear attenuation is dependent on the effective energy of the X-ray beam. Since the effective energy of the beam varies with location due to X-ray beam hardening and scatter, the same material could have different CT numbers at two different locations within the scan field of view. Second, two very different materials could have the same CT number by having the same linear attenuation coefficient even though they possess very different elemental composition, mass attenuation coefficient and density.

Dual-energy CT is based on the premise that by measuring the attenuation of a voxel at two different energies, energy-dependent attenuation characteristics can be derived allowing for material-specific information to be deduced. This information would then help distinguish between two materials with similar linear attenuation measurements which would be impossible to differentiate using single energy CT (22,35,36). The energy-dependent changes in attenuation are relatively specific for every material. Materials with high atomic number, such as iodine, display much larger changes in attenuation over diagnostic CT energies than low atomic number materials, such as water, due to the higher relative dominance of the photoelectric effect. By obtaining attenuation information at two different energies, material specific information can be deduced and images can be created that highlight the distribution of selected materials within the body. Useful dual-energy attenuation data relies on an adequate separation between the high and low energy, accurate temporal registration and accurate spatial registration (22).

2.2 DECT Implementations

Three vendors have developed dual-energy CT systems which use different methods for obtaining dual-energy attenuation data. Siemens has implemented a dual-source dual-energy CT design (SOMATOM FLASH®, Siemens AG, Forchheim, Germany) that employs two X-ray tubes mounted 90 to 95 degrees apart, operating at two different tube potentials (27,35). Generally, 80 and 140 peak kilovoltage (kVp) are used; however, 100 and 140 kVp may be employed for larger patients to help with X-ray penetration (35). The two separate tubes allow for the tube current associated with each energy in dual-energy mode to be modified based on the patient size and anatomy to be imaged. It also allows for an additional filter to be inserted to constrain the energy spread of the X-ray spectra and achieve better spectral separation between the two energies (37). While using two tubes can improve the spectral separation, it can also lead to registration issues as the data is collected at slightly different times. Siemens has resolved this issue by minimizing the temporal related offset by using two sets of 64-row detectors in conjunction with a moving focal spot which can collect 128 isotropic 0.6-mm slices in 0.4ms (38). The use of two tubes can also lead to cross scatter from tube A into the detector associated with tube B. The effect of the cross scatter is reduced through the use measurement based scatter correction using scatter sensors positioned close to the detectors but outside the fan beam penumbra (39). Additionally, in order to fit two x-ray tubes and two sets of detectors in the scanner, one of the detectors had to be reduced in size. Due to this, the dual-energy capabilities of the system are currently limited to a 33 cm field of view (26).

General Electric has designed a fast kilovoltage switching dual-energy CT scanner (Discovery CT 750HD, GE Healthcare, Milwaukee, USA) that uses a single X-ray tube that quickly switches between 80 and 140 kVp every 0.5ms as it rotates around the patient (40). To capture the alternating high and low energy projections individually, the scanner is equipped with a garnet crystal scintillator detector. The detector has a 100 times faster

response time than the typical gadolinium oxysulfide scintillator detector and four times less afterglow. The data acquisition system is also enhanced with fast sampling capabilities which enables 2.5 times the data sampling possible in a conventional 64-channel CT scanner (40–42).

Unlike the Siemens system where the current for each X-ray tube can be adjusted, the single tube on the GE system is forced to maintain a constant tube current since it is not possible to alternate the mA as rapidly as the tube voltage (37). The exposure time ratio is adjusted to 60% at 80 kVp and 40% at 140kVp to help account for the higher tube output at the higher energy (43). A number of preset protocols are available on the scanner with varying bowtie filters, beam widths, rotation times and dose levels depending on the anatomy to be imaged and the patient size. By utilizing a single fast switching X-ray tube, both axial and helical scanning are possible, and dual-energy analysis is available over the full 50 cm field of view. The close timing of the alternating high- and low-kVp projections provides excellent temporal resolution (40,41).

Similar to the GE fast-kilovoltage switching system, Toshiba offers a single-source dual-energy scanner based on kV switching (Aquilion ONE; Toshiba Medical Systems, Otawara, Japan). The system contains 320 detector rows covering 160 mm in the z-direction allowing volumetric data collection (44,45). The system switches from 80 to 135kV between rotations rather than between projections like the GE variant (44,45). This rotation-based kV switching allows for different tube currents to be used for the high and low kV rotations, as well as the application of tube current modulation (46). It also allows for perfect spatial matching between the initial high-kV tube rotation and the subsequent low-kV tube rotation. However, the time difference between the high and low kV data collection results in spatial misregistration of the two data sets which may adversely affect the dual-energy processing (45). The extent of spatial misregistration will depend on patient motion, the rotation time, and the time interval between the high and low kV data

collection (44,45). This interval subsequently depends on the difference in the tube currents in the two rotations and can vary from 180 to 800 milliseconds (45).

The last vendor to develop a dual-energy CT system, Phillips, has designed a scanner (Brilliance CT, Phillips Healthcare) that uses a single X-ray tube and a modified detector with two scintillation layers. The top layer of the detector captures low energy data, while the bottom layer captures high energy data. The low and high energy data are then reconstructed to allow for dual-energy analysis. While anticipated for multiple years, the scanner was just officially released at the Radiologic Society of North America 2015 conference in Chicago. At the time of this publication however, no publications can be found based on clinical use of this system.

2.3 Dual-Energy Image Reconstruction

Given the prevalence of the Siemens and GE scanners over the Toshiba and Phillips variants, discussion of image reconstruction processes will be limited to the two major vendors, Siemens and GE.

Processing of the dual-energy data from the Siemens SOMATOM FLASH® system is performed in the imaging domain after the independent reconstruction of the high and low energy images. Three data sets are automatically produced: a pure 140 kVp image, a pure 80 kVp image and a “blended” set combining partial contributions of the 140 and 80 kVp images. The percent contribution of the two energies can be customized for the desired application. The combination can be linear, where the intensity of each pixel is weighed equally, or non-linear sigmoidal, where the intensity of each pixel is weighed by its CT number. Non-linear sigmoidal blending is particularly useful for iodine signal enhancement (35,47). Material specific information is generated using a “three-material decomposition algorithm” which is based on the fixed attenuation values of two fixed materials, soft tissue

and fat, at both the high and low energy as well as a third varied material (35,36). This third material, usually iodine, can be selectively mapped or removed from the images (37).

Unlike Siemens systems, the GE Discovery CT 750HD system processes dual-energy data in the projection domain before the images are reconstructed. This allows for greater flexibility in material decomposition as well as the reduction of beam hardening artifacts (48–51). Reducing beam hardening can provide images with improved CT attenuation linearity, lower image noise and improved contrast-to-noise ratio (CNR) compared to their single-energy counterparts (35,52). Because the processing of the dual-energy data takes time to complete, the 140 kVp projections are reconstructed and immediately displayed to allow for a quick anatomic coverage check. These images should not be used for analysis, however, since they are not fully corrected for scanner calibration (52).

Material specific information is generated using a "basis material decomposition algorithm" which proposes that the attenuation coefficients of a material can be characterized as a weighted sum of the attenuation coefficients of two basis materials (35,36). This idea is based on the concept that any material can be characterized as the linear combination of its photoelectric and Compton scatter properties (Equation 1) (22,51)

.

Equation 1 $$\boldsymbol{\mu}(E) = \boldsymbol{\alpha} f_{pe}(E) + \boldsymbol{\beta} f_{c}(E)$$

Equation 2 $$\mu_1(E) = \alpha_1 f_{pe}(E) + \beta_1 f_{c}(E)$$

Equation 3 $$\mu_2(E) = \alpha_2 f_{pe}(E) + \beta_2 f_{c}(E)$$

Applying the concept described in Equation 1 to two materials (Equation 2, Equation 3), one can derive equations that express the photoelectric and Compton components of attenuation in terms of the two basis materials (Equation 4, Equation 5).

Equation 4 $$f_{pe}(E) = \frac{\beta_2\mu_1(E) - \beta_1\mu_2(E)}{\alpha_1\beta_2 - \alpha_2\beta_1}$$

Equation 5 $$f_c(E) = \frac{\alpha_2\mu_1(E) - \alpha_1\mu_2(E)}{\beta_1\alpha_2 - \beta_2\alpha_1}$$

The algorithm then selects a target voxel of unknown composition. This voxel can also be expressed as a linear combination of photoelectric and Compton scatter properties (Equation 6).

Equation 6 $$\mu_{voxel}(E) = \alpha\, f_{pe}(E) + \beta\, f_c(E)$$

Equations 4 and 5, which express photoelectric and Compton scatter properties in terms of the two basis materials, can then be substituted into Equation 6 resulting in Equation 7.

Equation 7 $$\mu_{voxel}(E) = \alpha\left(\frac{\beta_2\mu_1(E) - \beta_1\mu_2(E)}{\alpha_1\beta_2 - \alpha_2\beta_1}\right) + \beta\left(\frac{\alpha_2\mu_1(E) - \alpha_1\mu_2(E)}{\beta_1\alpha_2 - \beta_2\alpha_1}\right)$$

This equation can be further rearranged (Equation 8) and simplified into an expression that characterizes the attenuation of the target voxel in terms of the weighted sum of the attenuation coefficients of the two basis materials (Equation 9).

Equation 8 $$\mu_{voxel}(E) = \left(\frac{\alpha\beta_2 - \beta\alpha_2}{\alpha_1\beta_2 - \alpha_2\beta_1}\right)\mu_1(E) + \left(\frac{\beta\alpha_1 - \alpha\beta_1}{\beta_2\alpha_1 - \alpha_2\beta_1}\right)\mu_2(E)$$

Equation 9

$$\mu_{voxel}(E) = a_1\mu_1(E) + a_2\mu_2(E) \quad where$$

$$a_1 = \left(\frac{\alpha\beta_2 - \beta\alpha_2}{\alpha_1\beta_2 - \alpha_2\beta_1}\right) \quad and \quad \alpha_2 = \left(\frac{\beta\alpha_1 - \alpha\beta_1}{\beta_2\alpha_1 - \alpha_2\beta_1}\right)$$

Since the attenuation coefficients of the two basis materials would be known, the equation contains two unknown factors: the weighting factor of basis material 1 and the weighting factor of basis material 2. By collecting attenuation data on the target voxel at two separate energies, two equations can be written (Equation 10, Equation 11). This system of equations can then be solved for the factors for the two material basis pairs (22,51). These factors, expressed in material density, are then displayed in shades of gray to produce two material density images of the object.

Equation 10

$$\mu_{voxel}(E_{high}) = a_1\mu_1(E_{high}) + a_2\mu_2(E_{high})$$

Equation 11

$$\mu_{voxel}(E_{low}) = a_1\mu_1(E_{low}) + a_2\mu_2(E_{low})$$

The two materials used as the basis material pair can be selected by the user. A range of materials are included in the GE Discovery CT 750HD software package; however, additional materials may be added to the software database by the user using published attenuation coefficients. Care should be taken in the selection of the basis material pair, as the two materials must have sufficiently different atomic numbers and thus sufficiently different attenuation properties (22,51). Water and Iodine are currently the most common pair in use. The atomic numbers of the materials adequately frame the range of atomic numbers of materials commonly found in medical imaging thus allowing for optimal separation of tissues, bone and iodinated contrast (53). Measurements of iodine density from the material density image can also be used to detect iodinated contrast enhancement (54). Iodine material density images have proven to be semi-quantitative and thus may be

used to measure relative iodine concentrations in the body (53,55). The water material density image produced from a water/Iodine material decomposition of a contrast scan has its own unique use as a virtual non-contrast image. This approach reduces patient dose by eliminating the need for a true non-contrast image and can improve image quality of the non-contrast image due to the inherent reductions in beam hardening from a dual-energy scan (56–59).

In addition to the material density images, the GE system also supports a virtual monoenergetic spectral (VMS) image output. The VMS images depict an object as if it were imaged not by a polychromatic kVp beam but by a single monoenergetic kilo-electron volt (keV) beam (50,60). VMS images are derived from the material density images by applying the known energy-specific attenuation of each basis material to the image, converting the material density values into attenuation values. The resulting attenuation images, one for each basis material, are then summed to create the final VMS image.

Using this method, VMS images can be created at any specific energy level between 40 and 140 keV (61). Low-energy VMS images have been shown to provide excellent contrast for iodinated structures due to higher attenuation closer to Iodine's k-edge, allowing for a 50% reduction in the required amount of iodinated contrast delivered to the patient (54,62). Several studies have also shown that VMS images in the range of 65-70 keV have less noise, decreased beam hardening artifact and higher contrast-to-noise ratio (CNR) than traditional 120 kVp single-energy CT images acquired using the same dose (41,48,63)(41),(48) (63). In fact, both the "blended" images produced by Siemens systems and the VMS images produced by GE have been shown to "provide equivalent structural information" as compared to single-energy scans using the same dose over a wide range of patient sizes (41,64).

2.4 Tissue Differentiation using Dual-Energy CT

Although no other studies to our knowledge have explored the potential of applying dual-energy CT to differentiate calcific and hemorrhagic lesions, the differentiating power of dual-energy CT has been shown in many previously published studies. Dual-energy CT has been used to distinguish between non-enhancing and enhancing renal lesions (54) as well as benign and malignant tumors in the liver, thyroid and adrenal glands (53,55,65). It has also been shown useful in the detection and characterization of endoleaks, pulmonary embolism, liver metastases, urinary stones, myocardial ischemia and renal corticomedullary sodium gradients(57,58,63,66–71). In two studies using Siemens dual-source dual-energy CT scanners and a three-material decomposition algorithm, hemorrhage was distinguished from iodinated contrast on the basis of the pattern of hyper-attenuation on the virtual unenhanced image relative to the iodine overlay image (72,73).

2.5 MR for the Differentiation of Calcification and Hemorrhage

Data derived from the phase component of magnetic resonance imaging has been investigated in the differentiation of intracranial calcification from hemorrhage for several years. Corrected gradient echo (GRE) phase imaging (20,74,75), susceptibility-weighted imaging (SWI) (21,76,77), and quantitative susceptibility mapping (QSM) (78–81), have each been proposed, however none has found wide clinical acceptance at this point in time. GRE-based approaches are prone to errors due to either low T2* decay signal or low proton density, noise, lesion orientation, the influence of non-local susceptibility effects and differences in vendor phase sign conventions (74,75,82–87). However, techniques such as SWI have been found to improve calcification and hemorrhage detection and characterization compared to these earlier techniques (88–90). Although these phase based methods have provided positive results in the differentiation of these two lesion

types, SECT was employed as the criterion standard for calcification detection. As such, the usefulness of these methods can only be applied to intracranial hemorrhage and calcification above 100 HU. Preliminary work by Berberat, et al suggests that calcification and hemorrhage in glioma could be differentiable under 100 HU using SWI (77), however further work is needed to confirm these results for low density lesions. While these methods for the differentiation of calcification and hemorrhage are of note, the transition of phase dependent MR techniques from research to clinical use has traditionally proved difficult due the sensitivity of these techniques to commonly encountered magnetic field inhomogeneities (83,91).

Chapter 3

Lesion Differentiation using an Agar-Gel Based Phantom

This chapter investigates the differentiation of calcium, present in calcification, and iron, present in hemorrhage, using dual-energy CT. A simplified physics approach based on agar get models was developed. SECT attenuation (HU) matched model pairs, consisting of a hemorrhage and a calcification model, were evaluated using an anthropomorphic phantom and the SECT attenuation (HU) necessary for 90% differentiation accuracy were determined.

This chapter is taken from:
JL Nute, LG Le Roux, AG Chandler, V Baladandayuthapani, D Schellingerhout, DD Cody. Differentiation of low-attenuation intracranial hemorrhage and calcification using dual-energy computed tomography in a phantom system. Invest Radiol. 2015; 50(1): 9-16. doi: 10.1097/RLI.0000000000000089

3.1 Introduction

The ability to characterize cerebral lesions in terms of material composition, especially at low Hounsfield values, has many important clinical applications, such as the distinction of hemorrhagic from calcific lesions. There is overlap in the Hounsfield densities of blood and calcium on conventional CT, particularly below 100 Hounsfield Units (HU). This difference is clinically important, for example in differentiating benign cerebral

calcifications, which require no treatment (3), from cavernous angiomata which carry a risk of bleeding and are a contra-indication for anticoagulant therapy (4,5). Oligodendrogliomas are commonly calcified, and need to be distinguished from glioblastomas, which commonly contain intratumoral hemorrhages. The treatment strategies for these tumors are completely different, and would be better informed if calcification and hemorrhage could be reliably separated.

Currently, conventional single-energy computed tomography (SECT) is considered the gold standard modality for the identification of calcification. In general, any lesion with SECT attenuation levels >100 HU is classified as a calcification (2). However, this gold standard fails for lesions with SECT attenuation levels <100 HU, where blood and calcifications overlap in attenuation.

In clinical practice, MR is often used as a characterizing modality to add to the information derived from CT. However, conventional MR is of little help in distinguishing hemorrhagic from calcific lesions. Both types of lesion manifest as signal voids on Gradient Echo images, with little characterizing information available without the use of specialized experimental phase contrast MR techniques (1). There is a significant clinical need for an imaging technology to distinguish hemorrhage from calcification at low Hounsfield values, and dual-energy CT is a strong candidate to fill this gap in our imaging armamentarium.

Dual-energy CT is based on the knowledge that the relationship between attenuation and x-ray energy is material dependent. By collecting attenuation information at two distinct energies, assumptions can be made about the shape of the energy-dependent attenuation curve for a given tissue, and thus about its material characteristics. This represents a significant advance from SECT, where only a single attenuation value is derived, with no further information available on the material characteristics of the tissue(35,36,51).

Dual-energy CT has already been used with success in distinguishing blood from iodinated contrast staining in patients after intra-arterial stroke therapies (72,73,92), in distinguishing iodine enhancement from calcification in artificial pulmonary nodules (93), and in distinguishing complimentary contrast media (iodine and tungsten, or iodine and bismuth subsalicylate) (94). All are clinically significant problems where the attenuations of the two main differential diagnostic possibilities have significant overlap on conventional SECT. Dual-energy CT's success has also been shown in the characterization of renal calculi (26,95,96), distinguishing non-enhancing and enhancing renal lesions(54), distinguishing benign and malignant tumors in the liver (53), thyroid (53) and adrenal glands (55,97,98). It has also been shown useful in the detection and characterization of endoleaks, pulmonary embolism, liver metastases, urinary stones, myocardial ischemia and renal corticomedullary sodium gradients (57,58,63,66–69,71).

In this study, we apply dual-energy CT to the more subtle problem of distinguishing calcification and hemorrhage. We provide a phantom-based proof-of-concept that the differentiation of these two intracranial lesion types below 100 HU is both possible and clinically feasible using dual-energy CT.

3.2 Materials and Methods

3.2.1 Calcification and Hemorrhage Phantom Models

Powdered ferric oxide (#529311; Sigma-Aldrich, St. Louis, MO) and hydroxyapatite (#289396; Sigma-Aldrich) were used to model hemorrhage and calcification, respectively. Ferric oxide and hydroxyapatite were added to separate sets of 1.8-mL cryo-vials (#375418; Thermo Scientific, Waltham, MA), and 500 µL of 0.01% Tween-20 (#P9416; Sigma-Aldrich) solution was added to each vial as an emulsificant to promote a uniform mixture. The hydroxyapatite vials were agitated for 24 hours using a Max Q2000 shaker (#4314; Thermo Scientific). The iron oxide particles used to model hemorrhage were not

adequately emulsified by Tween alone, and required the addition of small 7 mm × 2 mm magnetic stir bars (#14-513-63; Fisher Scientific, Waltham, MA) to provide mechanical agitation. Iron oxide vials were agitated for 24 hours using a PC-220 stirrer plate (Corning, Corning, NY).

The stirrer bars were removed from the iron oxide vials using a strong magnet, and both sets of vials were moved to a water bath, where they were heated to 75°C. Heated 1% agar gel solution (2 mL) (#0710; Amresco, Solon, OH) was added to both sets, and the vials were tightly capped. The warm vials were then manually agitated by vigorous shaking for approximately 10 minutes until the solution cooled into a gel with uniform compound distribution. These gel models were stored at 4°C prior to scanning.

An anthropomorphic head phantom (The Phantom Laboratory, Salem, NY) (Figure 3.1) consisting of a human skull cast in tissue-equivalent Alderson material with anatomical airways was obtained from the Radiological Physics Center (Houston, TX). A cylindrical insert was placed in the cranium, and a custom insert was fabricated that allowed for simultaneous imaging of six agar gels (Figure 3.2).

Figure 3.1: Anthropomorphic head phantom.

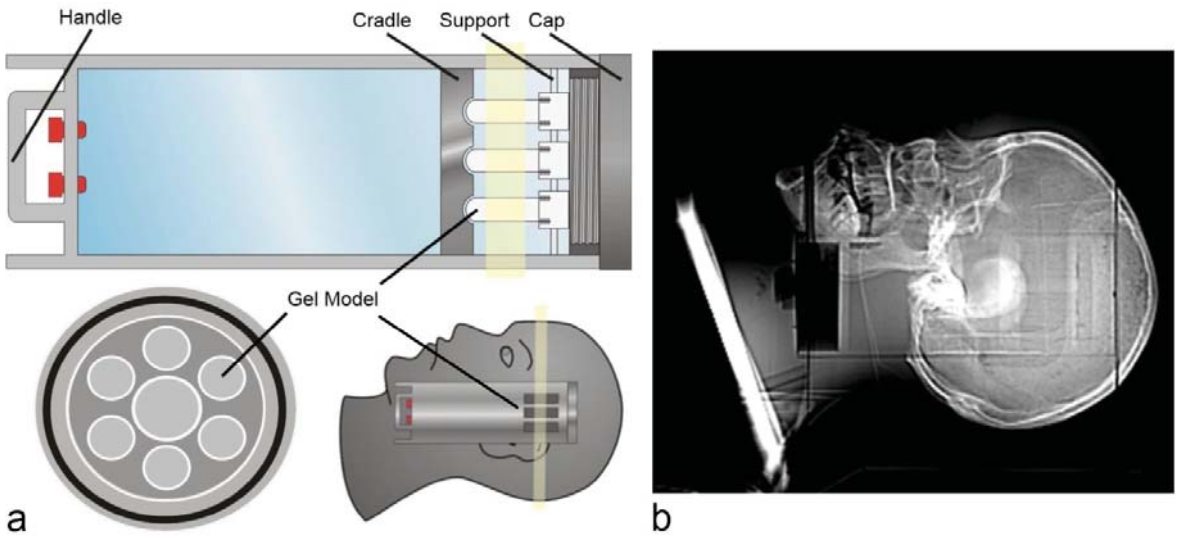

Figure 3.2: (a) Custom water-filled insert for the anthropomorphic head phantom. The lateral view (top), the axial view (bottom left), and the relative position of the insert in the head phantom (bottom right) are shown. The orientation of the imaging volume is represented by the yellow shaded region. (b) A lateral scout image of the anthropomorphic head phantom with custom water-filled insert and gel models in place.

3.2.2 Imaging and Region-of-Interest Analysis

The calcification and hemorrhage gel model were scanned in the phantom on a Discovery CT750 HD CT scanner (GE Healthcare, Waukesha, WI) using two protocols: a) a single-energy in-house routine brain protocol and b) a dual-energy protocol designed to match the imaging parameters and dose of the single-energy protocol (Table 3.1). To improve the spatial resolution of the gel images, the display field of view was reduced to the minimum of 12 cm. Images were viewed with Gemstone Spectral Imaging (GSI) viewer software (version 2; GE Healthcare), and data were collected on eight consecutive images using a circular 39-mm^2 (7 mm diameter) region of interest covering approximately two-thirds of the vial diameter. The total number of voxels per region of interest was 754, for a total of 6,032 voxels in a volume of interest per vial. The 6,032-voxel volume of interest covered 952 mm^3 and constituted 37% of the total gel volume of approximately 2.5 mL. For

each voxel in the volume of interest, the following data were recorded: a) SECT attenuation (HU), b) calcium density from a water/calcium material decomposition based on the dual-energy CT data (see 'Dual-Energy Data Processing' below), c) water density from a water/calcium material decomposition based on the dual-energy CT data (see 'Dual-Energy Data Processing' below), and d) material composition of the gel model (iron oxide-based hemorrhage model or hydroxyapatite-based calcification model).

Table 3.1: Imaging parameters for the single- and dual-energy CT protocols used in the study. For both protocols: Image thickness: 3.75 mm, Table Speed: 10.62 mm/rotation, Pitch: 0.531, Interval: 3 mm, Scan Field of View (SFOV): Head, Display Field of View (DFOV): 12 cm, Reconstruction Algorithm: Soft.

Protocol	Scan type	Rot time [s]	kVp	mA	$CTDI_{vol}$* [mGy]
Single-energy	Helical	0.8	140	440	66
Dual-energy	GSI-26	0.7	80/140	375	67

***Computed Tomography Dose Index Volumetric ($CTDI_{vol}$)**

3.2.3 Fabrication of Matched Hemorrhage and Calcification Gel Models

Iron oxide and hydroxyapatite gels were created at concentrations between 1 mg/mL and 100 mg/mL and scanned in the phantom using the single-energy CT protocol (Table 3.1). Images were viewed as described above. Each gel model's mean SECT attenuation (HU) was calculated and plotted against the gel model's concentration. The SECT attenuation (HU) was fitted to a linear function of the known concentration of each material and the concentration required to achieve a given SECT attenuation (HU) was then calculated from the fit.

Pairs of agar gels were fabricated with similar SECT attenuation (HU) levels and differed only in their composition (iron oxide-based hemorrhage model or hydroxyapatite-

based calcification model). These matched gel models were fabricated at SECT attenuation levels ranging from 0 to 100 HU, in roughly 10-HU intervals. Paired vials of similar attenuation (within 2 HU) were then scanned in the anthropomorphic head phantom and scanned using a) the single-energy in-house routine brain protocol, to verify the SECT attenuation (HU) level of each gel model, and b) the dual-energy protocol, to collect material density information.

3.2.4 Dual-Energy Data Processing

To extract the dual-energy signature of a material from the high- and low-kilovolt-peak data gathered in the dual-energy CT scan, GE Healthcare (Waukesha, WI) uses a process called material decomposition. This process is based on the concept that the energy-dependent attenuation of any material can be characterized as the linear combination of the energy-dependent attenuations of two basis materials (35,36). One of the unique capabilities of this approach is allowing the user to independently choose the basis materials. Theoretically, any two materials could be chosen, but biologically relevant pairs such as water and iodine give more meaningful results (26,40). Materials with k-edges within the relevant x-ray energy range of 40-140 keV should also be avoided as these discontinuities can give rise to erroneous material decomposition results. The materials chosen should also have sufficiently different atomic numbers and thus sufficiently different attenuation properties to produce meaningful material separation, thus generating clinically useful data (22,99). We chose calcium and water as our working pair because of their biological relevance and dissimilar attenuation properties. Iron-water and iodine –water material basis pairs were also investigated, however, preliminary data indicated the calcium-water material density pair as yielding separation plots that were more meaningful and convenient for our application. (Data not shown)

Data from the dual-energy images were collected using the GE Gemstone Spectral Imaging viewer in material density mode with a water/calcium material density pair. These images express the density of water and the density of calcium in each voxel needed to produce the observed linear attenuation coefficient.

3.2.5 Matched Model Pair Data Analysis

For each SECT attenuation (HU)-matched model pair, single-energy and dual-energy voxel data (6,032 voxels/gel model) for both the hemorrhage model and the calcification model were loaded into MATLAB software (R2012a; MathWorks, Natick, MA). The single-energy and dual-energy voxel data were registered based on the image number and voxel location data included in the region of interest data file.

A Gaussian mixture model (GMM) was performed to group the voxels into two populations: calcification and hemorrhage. Using the measured SECT attenuation (HU), water density and calcium density values for each voxel as input, a probability of belonging to either the calcification or the hemorrhage population was calculated for each voxel (see Chapter 8: Appendix), with a posterior probability of ≥0.5 as the criterion for population assignment (100,101).The analysis was performed using a 50% training set, 50% validation set approach to ensure that the data used to build the model (randomly assigned training set) was distinct from the data the model was used to evaluate (randomly assigned validation set) and was performed 1,000 times to ensure convergence in light of the non-stochastic nature of the GMM analysis.

The probabilistic assignments for the two populations (calcification and hemorrhage) were tested against the gold standard of actual gel composition, and an overall model accuracy was calculated as a function of the SECT attenuation (HU) of the matched model pair.

While Gaussian mixture model analysis can be quite powerful, its potential for application in a clinical setting is low due to the time and processing power needed to apply the technique. To provide a more clinically implementable test metric, a threshold plane was derived from the GMM data. For all matched model pairs included in the study, voxels receiving an assignment probability of 50 ± 1% (equal probabilities of being assigned to the hemorrhage or calcification cluster) were isolated, and a line of best fit was determined using regression analysis in three dimensions. Due to the correlated nature of the SECT attenuation (HU) and dual-energy material density data, gel model voxel data were found to be concentrated in a single plane in three-dimensional (3D) space (Figure 3.3). Using principle component analysis, the centroid and inertia axes of the plane were calculated and the equation for the plane of the data was determined. A second plane was then calculated which included the line fit of the equal-probability points and was orthogonal to the plane of the data, effectively bisected the voxel data into two groups. Based on the equation of this threshold plane, voxels were sorted into either a hemorrhage group or a calcification group according to their position relative to the threshold plane. For each matched model pair, the predicted material composition for each voxel was compared with actual composition, and the accuracy of the threshold plane's differentiation was calculated and plotted against the SECT attenuation (HU) of the matched model pair.

Statistical details describing the Gaussian mixture model formulation, fitting and analysis are included in the Appendix (Chapter 8).

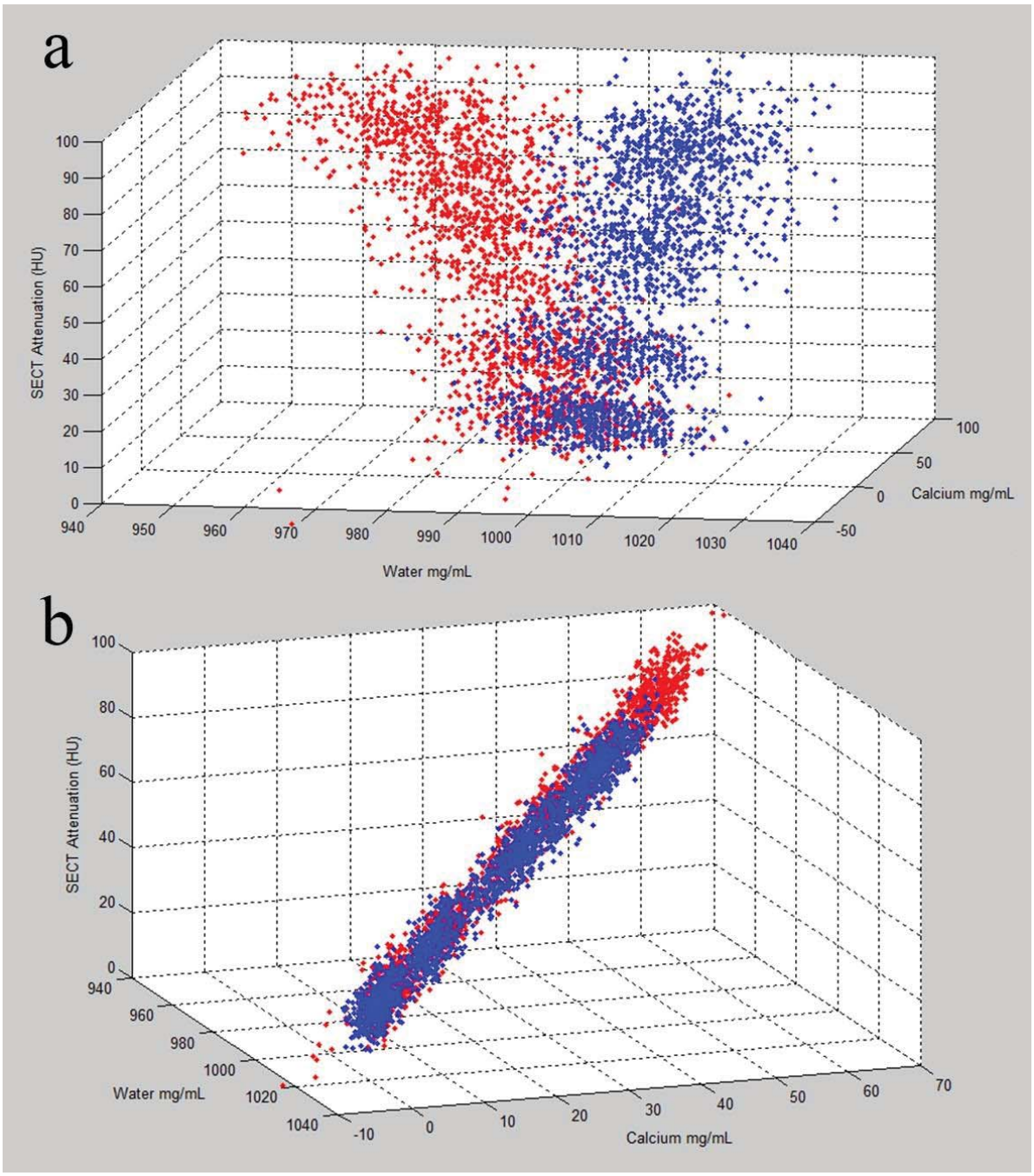

Figure 3.3: 3D plot of voxel data from all calcification and hemorrhage gel models used in this study, rotated to show the full distribution of the data (a) or the planar nature of these data in the 3D coordinate space (b). Hemorrhage gel model voxel data are shown in red; calcification gel model voxel data are shown in blue.

3.3 Results

3.3.1 Calcification and Hemorrhage Phantom Models

The results of the SECT attenuation (HU) calculation for all iron oxide and hydroxyapatite gels are shown in Figure 3.4, and indicate the concentration of the compounds in each of gel types needed to produce gel models of a specific SECT attenuation.

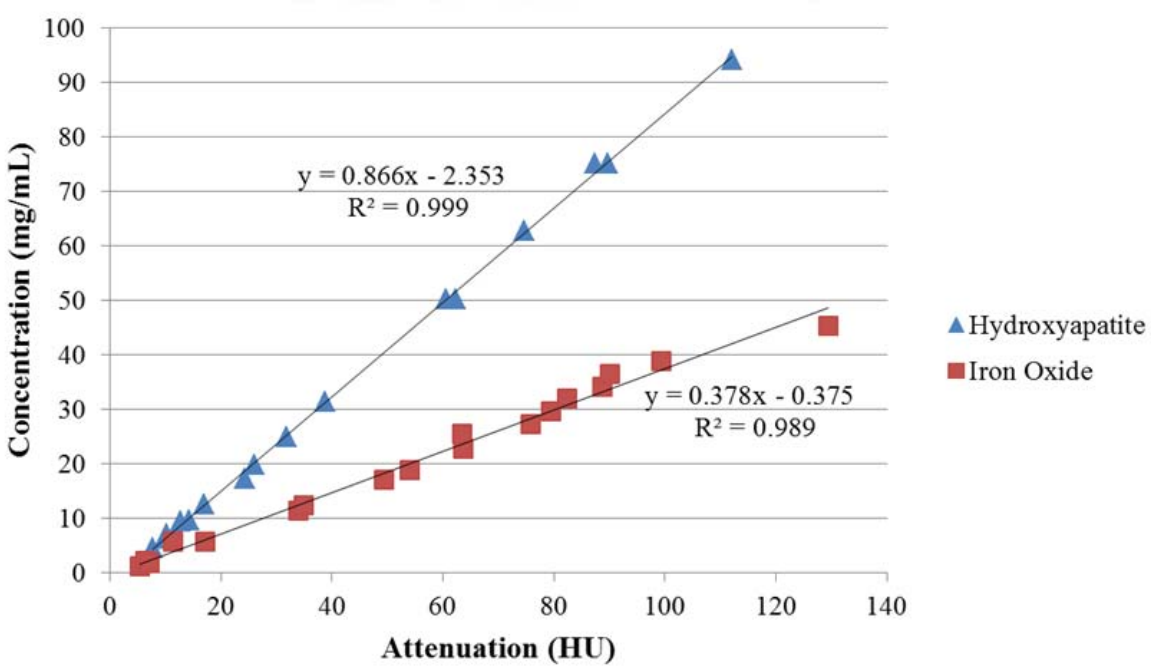

Figure 3.4: SECT attenuation (HU) for the concentration of iron oxide in the hemorrhage gel models and the hydroxyapatite in the calcification gel models. Linear regression equations and correlation coefficients are shown for each data set.

3.3.2 Fabrication of Matched Hemorrhage and Calcification Gel Models

The target concentration of iron oxide and of hydroxyapatite required to produce each desired SECT attenuation (HU) is presented in Table 3.2. The exact weight of each compound added to each gel vial is also presented and was calculated based on the concentration and the known volume of the gel vials used in the study.

Table 3.2: Concentrations and weights of iron oxide and hydroxyapatite needed to create hemorrhage and calcification models of specific SECT attenuation (HU).

Target attenuation [HU]	Concentration [mg/mL]*		Weight [mg]†	
	Hydroxyapatite	Iron Oxide	Hydroxyapatite	Iron oxide
10	6.32	3.41	16.11	8.69
20	14.98	7.19	38.20	18.34
30	23.64	10.97	60.29	27.98
40	32.31	14.76	82.38	37.63
50	40.97	18.54	104.47	47.28
60	49.63	22.32	126.55	56.92
70	58.29	26.11	148.64	66.57
80	66.95	29.89	170.73	76.22
90	75.62	33.67	192.82	85.86
100	84.28	37.46	214.91	95.51

*Derived from the linear-fit equation in Figure 4. †Weights required to achieve the concentrations listed were calculated based on the volume of specific gel vial used in the study.

3.3.3 Matched Model Pair Data Analysis

A total of 16 hemorrhage and calcification model pairs were matched. The average SECT attenuation (HU) of each pair, as well as the mean and standard deviation of the SECT attenuation (HU) for each gel model in the pair, is shown in Table 3.3.

Table 3.3: Average SECT attenuation (HU) of each matched pair and mean SECT attenuations (HU) for the hemorrhage gel model and the calcification gel model in each pair.

Average SECT attenuation of matched model pair [HU]*	Mean SE attenuation [HU] ± SD	
	Hemorrhage model (iron oxide)	Calcification model (hydroxyapatite)
12	11.4 ± 8.5	12.7 ± 3.4
14	13.9 ± 3.2	14.2 ± 3.4
17	17.1 ± 3.8	16.9 ± 3.3
20	20.8 ± 3.4	19.7 ± 3.2
30	30.4 ± 4.6	30.6 ± 3.5
32	31.3 ± 3.4	31.8 ± 3.3
39	39.2 ± 5.3	38.8 ± 3.5
50	49.4 ± 3.2	51.3 ± 3.9
60	59.7 ± 4.8	60.6 ± 3.6
62	62.3 ± 4.0	62.3 ± 4.4
71	70.7 ± 4.0	71.1 ± 5.0
75	75.7 ± 4.0	74.7 ± 9.5
82	82.4 ± 6.2	82.3 ± 4.4
88	88.7 ± 6.6	87.5 ± 4.2
89	88.7 ± 6.6	89.6 ± 7.6
90	90.1 ± 6.6	89.6 ± 7.6

*Hemorrhage and calcification gel models with attenuation levels within 2 HU of each other were organized into matched model pairs, and the average attenuation of each pair was the rounded average of the hemorrhage model attenuation and the calcification model attenuation.

As an example for the purposes of illustration, the voxel data for the 62-HU matched model pair along with the GMM predicted and actual gel model compositions are shown in Figure 3.5. For the GMM analysis (Figure 3.5), the accuracies for the calcification and hemorrhage models were 99.7% and 97.7%, respectively.

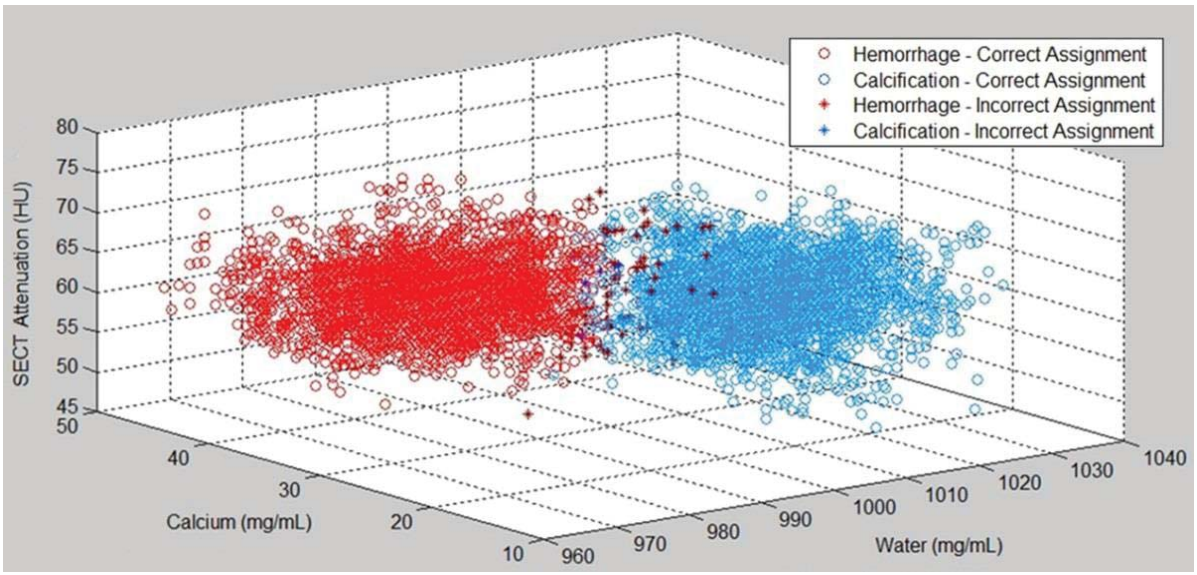

Figure 3.5: GMM assignment results for the 62-HU matched gel model pair (1 of 16 pairs). Each point represents a voxel within the 6,032-voxel volume of interest in one of the two gel models.

Matched calcification and hemorrhage gel model pairs were differentiated with >90% accuracy using GMM analysis starting at 50HU (Figure 3.6). A slight drop to just below the 90% threshold was seen at 60HU however, all subsequent matched model pairs exceeded 90% accuracy. All matched model pairs over 50HU, with the exception of the 60HU pair, possessed very narrow accuracy distributions, with standard deviations of <1%.

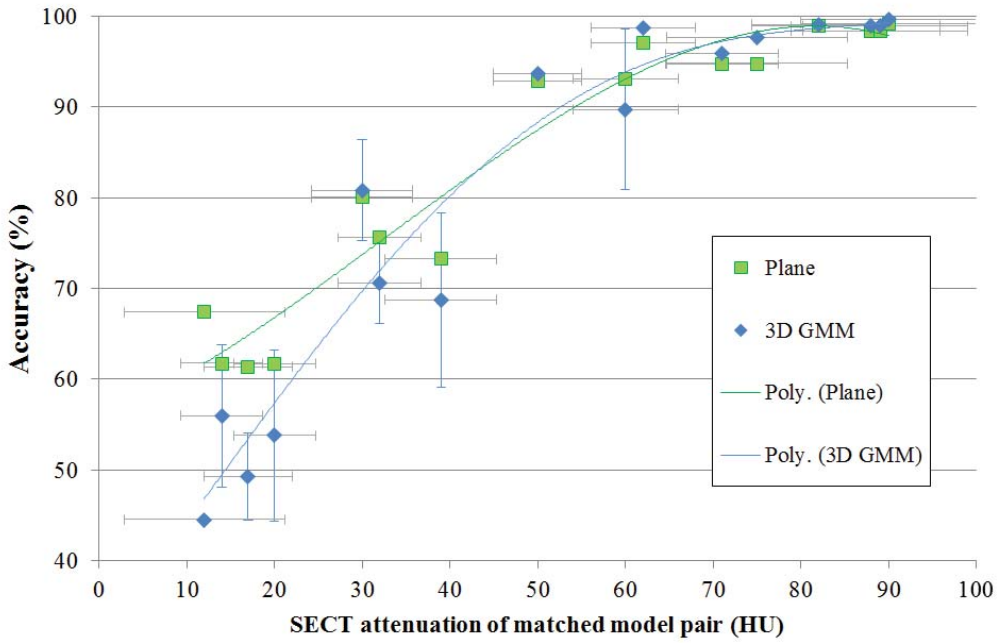

Figure 3.6: Accuracy of hemorrhage and calcification differentiation using the GMM and threshold plane analysis method for all attenuation-matched model pairs. For the GMM series, each point represents 1,000 iteratively filtered runs of the analysis. A third-order polynomial (Poly.) was fit to each series to facilitate visual interpretation of the data.

In order to derive the threshold plane, eight hundred thirty-six voxels with posterior probabilities of 50 ± 1% were isolated from the total 193,024 voxels on the basis of the 32 gel models included in this study. A coordinate system was established with the x-axis defined as the dual-energy CT water density, the y-axis defined as the dual-energy CT calcium density, and the z-axis defined as the SECT attenuation (HU). The line fit to the equal probability points had the vector equation <x,y,z> = <998.17, 11.88, 23.18> + t<0.06, -0.41, -0.91> where t is any real number. The 3D threshold plane had the equation -0.93x + 0.31y - 0.20z = -929.20 and clearly bisected the hemorrhage and calcification model voxel data (Figure 3.7). Matched model pairs with SECT attenuation levels ≥50 HU were differentiated with >90% accuracy for both the GMM analysis as well as its more clinically implementable threshold plane metric (Figure 3.6).

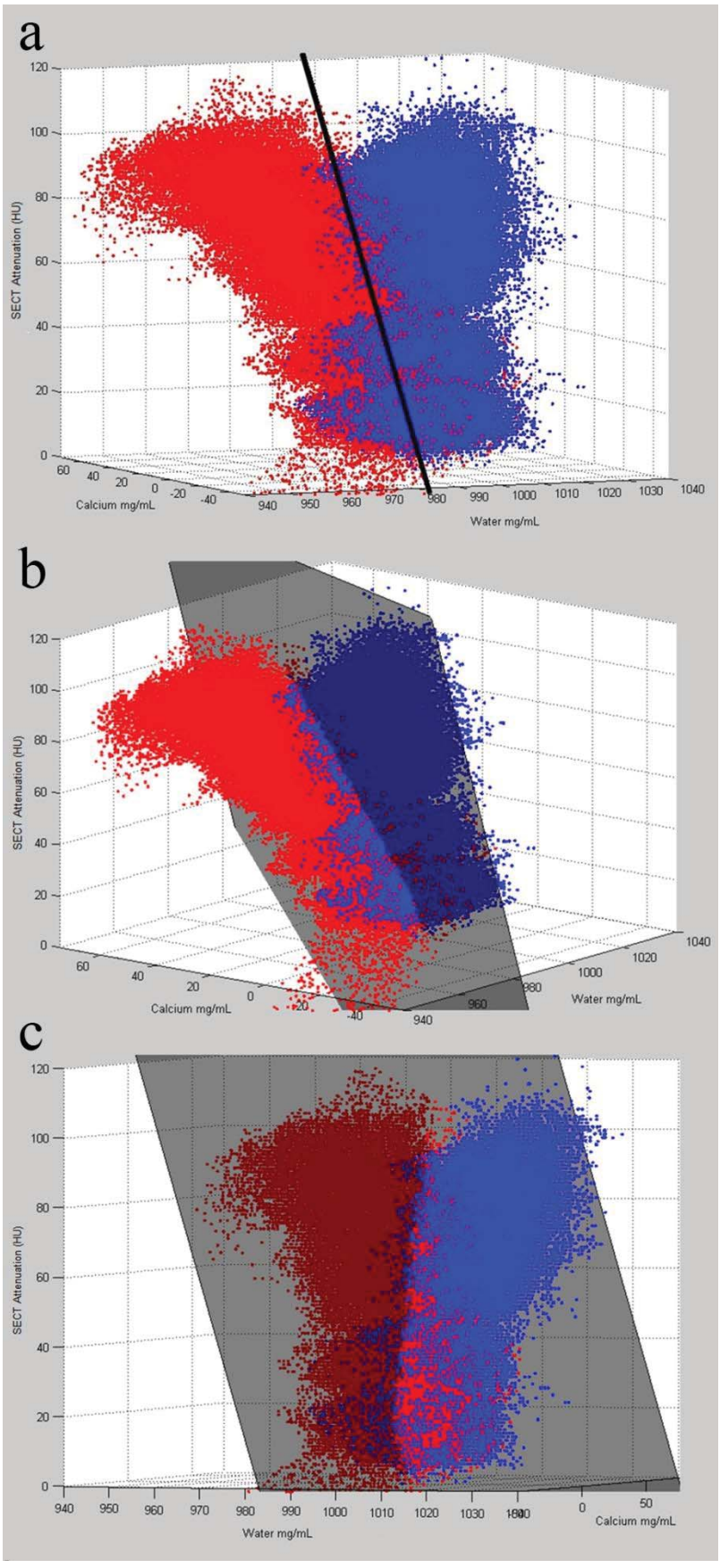
a
SECT Attenuation (HU)
Calcium mg/mL
Water mg/mL
b
SECT Attenuation (HU)
Calcium mg/mL
Water mg/mL
c
SECT Attenuation (HU)
Water mg/mL
Calcium mg/mL

Figure 3.7: 3D plot of all voxel data (n = 193,024) from all 16 hemorrhage/calcification matched model pairs. Hemorrhage gel model voxel data are shown in red; calcification gel model voxel data are shown in blue. (a) Threshold plane viewed edge on as black line [equation: -0.93x + 0.31y - 0.20z = -929.20]. (b) Voxel data viewed from an angle showing hemorrhage and calcification data falling on the hemorrhage side of the threshold plane. Bright blue calcification data would be incorrectly identified as belonging to the hemorrhage population, with greyed-out blue data being correctly classified. (c) Voxel data viewed from an angle showing hemorrhage and calcification data falling on the calcification side of the threshold plane. Bright red hemorrhage data would be incorrectly identified as belonging to the calcification population, with greyed-out red data being correctly classified.

3.4 Discussion

This study provides proof-of-concept in a phantom system that dual-energy CT can distinguish intracranial calcification from hemorrhage below the 100 HU limit imposed by currently available clinical modalities. Intracranial lesions over 100 HU are identifiable as calcification using SECT, however lesions under this attenuation are impossible to classify. Using conventional MR, both hemorrhage and calcification manifest as signal voids in Gradient Echo images. Without additional information, the cause of the signal voids, be it calcification or hemorrhage, cannot be determined.

The use of phase information in MR for the differentiation of diamagnetic materials, such as calcification, and paramagnetic materials, such as hemorrhage, has been under investigation for several years (79). Corrected gradient echo phase imaging (20), susceptibility-weighted imaging (21), and quantitative susceptibility mapping (78) have all been proposed to distinguish calcification from hemorrhage, however these methods have not yet found wide clinical acceptance. In each of these studies, SECT was used as the gold standard for presence of calcification, and thus the usefulness of these methods can

be reported only for hemorrhage and calcification above 100 HU. Preliminary work suggests that calcification and hemorrhage in glioma may be differentiable under the 100 HU limit using phase data derived from susceptibility-weighted imaging (77). However, the transition from research to clinical use of phase-dependent MR techniques has been difficult due to the sensitivity of the technique to magnetic field inhomogeneity, which is the rule, rather than the exception in clinical applications.

In this study, dual-energy CT in combination with Gaussian mixture model analysis was shown to be capable of differentiating intracranial calcification and hemorrhage models far below the level possible using currently available clinical modalities. Overall, the accuracy of the GMM differentiation of the hemorrhage and calcification model voxel data increased with the matched model pair's SECT attenuation (HU). Put simply, the denser the lesion model, the easier it was to differentiate hemorrhage from calcification. Strong differentiation with >90% accuracy can be seen starting at 50 HU. The dip in accuracy and associated increase in accuracy distribution at 60 HU in the GMM analysis (Figure 3.6) may be due to a higher heterogeneity in the SECT attenuation (HU) dimension from either the calcification or the hemorrhage gel model due to variability in gel model fabrication. Nevertheless, the overall trends in both the GMM and threshold plane accuracy results support the use of 50 HU as a threshold for highly accurate differentiation.

Gaussian mixture model analysis was chosen as the statistical analytic method for this study due to its ease of interpretation and to take advantage of the three dimensional and potentially overlapping nature of the data collected. The Gaussian assumption of the analysis was appropriate given the large amount of voxel data collected from each gel model. Traditional *t*-test analysis was contraindicated by both the vast amount of data and the differences in the manufacturing methods for the calcification and hemorrhage gel model. (Because of the large numbers of data points, slight differences in heterogeneity between the calcification and hemorrhage models resulted in statistically significant

differences when in fact the model's voxel data overlapped to a considerable extent. This observation indicated that *t*-test analysis was inappropriate.) Additionally, the ability to perform training/validation data set analysis using GMM allowed for a more robust test of differentiation as well as lending itself to the development of a model-based threshold for classification of unknown lesions.

For practical implementation of the GMM statistical separation procedure, we derived a simple threshold plane to divide the voxels into calcification and hemorrhage population. The discrimination performance of this plane was similar to the original GMM analysis (Figure 3.6) and actually outperformed the GMM analysis at low densities, likely by linearly extrapolating from higher densities to lower where the GMM itself became noise-limited.

To establish the use of dual-energy CT to discriminate calcification and hemorrhage clinically, an initial phantom study is necessary to allow essential variables to be interrogated and analysis tools and methods to be designed, trained, and optimized in a controlled fashion. However, due to the inherent constraints requisite to use of a phantom system there will always be limitations in the modeling. First, both hemorrhages and calcifications were modeled as relatively large cylindrical lesions positioned centrally in the brain. Second, both lesion types were modeled using an agar background and scanned in a water-filled insert, which does not accurately represent brain tissue. Third, both lesion types were modeled as uniform distributions, with no attempt made to model heterogeneous distribution or influences of local environment on the lesion. Lastly, hemorrhage models were created without any form of calcium contamination. It is likely that cross contamination will occur clinically, where biology is always more complex than phantoms. For example, it has been shown that cavernomas calcify in anywhere from 11-40% of cases (102,103), and in those cases we may expect to see both calcification and hemorrhage in the same lesion. Clearly there is potential for overlap and cross contamination between

blood and calcium in clinical applications. Our current study lays a groundwork for a “clean” uncontaminated case, leaving more complex mixture phantom models and more importantly, clinical applications, to future work.

Future studies are planned to extend our approach to encompass other dual-energy CT vendors, as well as to further test the limits of our method by varying the size and location of the lesions, more accurately modeling the brain tissue background and environment, and varying the imaging parameters of the dual-energy protocols to potentially optimize differentiation. The resulting data will be used to develop appropriate scan protocols based on the size and location of intracranial lesions for use in a prospective human trial.

In conclusion, this work has shown that hemorrhagic and calcific lesions with SECT attenuation levels between 50 and 100 HU can be reliably differentiated in a phantom system using dual-energy CT and material decomposition. The equation for a simple threshold plane of differentiation derived from the more complex GMM analysis provides a simplified metric for future clinical application. The ability to differentiate between low-attenuation hemorrhagic and calcific lesions has multiple clinical applications, both addressing current clinical needs, and also likely, future unforeseen applications. This data provides justification for future clinical studies in patients.

Chapter 4

Lesion Differentiation using a Biologically-Relevant Phantom

This chapter seeks to validate the results of the simplified physics model investigated in Chapter 3, using a more biologically relevant phantom system. Instead of agar, a spectrally-equivalent brain background material will be described that better mimics the spectral properties of brain tissue. Intracranial lesions will be modeled at a range of sizes and at varying locations within the cranial cavity. Acquisition parameters will be varied in an effort to elucidate the optimal imaging technique, patient population constraints and analysis methods for use in a future prospective clinical trial.

4.1 Materials and Methods

4.1.1 Phantom Preparation

For this project, an anthropomorphic nuclear medicine head phantom was acquired (Capintec, RS900T, Figure 4.1). The anthropomorphic nature of the interior of the phantom allowed for the design of a novel brain insert to hold lesion models of various compositions and sizes at multiple locations within the cranial cavity. Figure 4.2 shows the basic structure of the intracranial lesion phantom design. Spectrally equivalent brain slabs would be positioned to cover two regions at opposite ends of the imaging spectrum: the skull base surrounded by dense bone and the cerebrum with little bony anatomy. The cerebrum slab

Figure 4.1: Interior of anthropomorphic nuclear medicine phantom.

houses six cylindrical inserts (three hemorrhage inserts and three calcification inserts) at three diameters: 0.5 cm, 1 cm and 1.5 cm (Figure 4.2b). Due to its size as well as the difficult imaging environment, the skull base slab houses only two cylindrical inserts: a 1.5 cm hemorrhage and a 1.5 cm calcification insert (Figure 4.2c).

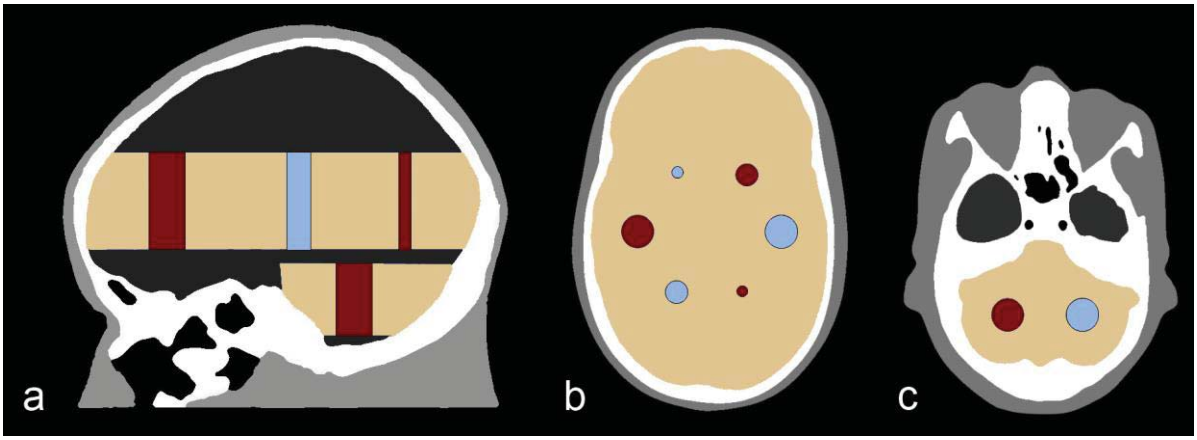

Figure 4.2: Intracranial lesion phantom plan showing brain slabs in tan, hemorrhage lesion models in red and calcification lesion models in blue. (a) sagittal view showing position of cerebrum and skull base brain slabs. (b) axial view of cerebrum brain slab showing position of hemorrhage and calcification lesion models. (c) axial view of skull base slab showing position calcification and hemorrhage model.

In order to maintain the position of the brain slabs and to ensure artifact-free helical imaging, a polyurethane rubber was used as a filler material between the slabs. The polyurethane product chosen (PMC-121/30-Dry) was a minimally shrinking, amber-colored rubber with a specific gravity of 1.04 and a mean CT number of 3 HU using a 120kVp scan technique (http://www.smooth-on.com/tb/files/PMC-121_SERIES.pdf). To ensure the easy release of the cured polyurethane rubber, the interior of the phantom was buffed with fine grain sand paper. Any occlusions or holes in the phantom interior were filled with an acrylic based epoxy and the final surface coated with several fine layers of aerosolized acrylic to obtain a smooth and sealed interior surface. Olive oil was used as a release agent for the

polyurethane due to its low effective Z composition in an attempt to avoid high Z contamination from the more common silicon based release agents.

4.1.2 Spectrally Equivalent Brain Material

Spectrally equivalent materials were created by Gammex, Inc. as part of a special custom order. Several samples of potential brain equivalent materials were supplied and imaged using both a single-energy CT routine brain protocol and a dual-energy CT protocol selected to match the imaging parameters and dose of the single energy protocol (Table 4.1). The monoenergetic dual-energy data was compared to existing data from a clinical brain study. Based on these results, the material with the closest spectral HU curve to human brain was selected. The final spectrally equivalent brain slab provided by Gammex was validated using the protocol in Table 4.1 and defect free regions were selected for use.

Table 4.1: Imaging Technique for basic single-energy and matched dual-energy data collection.

Name	Scan Type	Pitch	Rot	Beam Width	Img Thk	Interval	SFOV	DFOV	kVp	mA	Filter
Routine Brain	Helical	0.531	0.8s	20 mm	3.75 mm	3 mm	Head	25 cm	140	160	STND
GSI - 26 Brain	Helical	0.531	0.7s	20 mm	3.75 mm	3 mm	Head	25 cm	NA	NA	STND

In order to obtain a detailed model of the interior of the nuclear medicine phantom, a polyurethane cast was made of both the base and crown of the phantom. The polyurethane filled phantom was then imaged using the single-energy protocol detailed in Table 1 and the specific position and dimensions of the cerebrum and skull base slabs were determined. The polyurethane casts were then removed and models of the slabs were cut from the casts based on the measurements derived from the imaging. A projection view of the greatest diameter of the polyurethane slab model was made and the spectrally

equivalent brain material was cut to that shape. Orientation marks were added to the surfaces of both the polyurethane models and the brain slabs and rough contours were created using a belt sander. Fine details were later created using a combination of air powered die grinders and dremmel tools. Once construction on both brain slabs was complete, polyurethane filler slabs were created. The slabs were designed to be removable to allow easy access to all lesion models. The polyurethane filler slabs were created in sequence starting with the most inferior and working towards the most superior. To ensure a subsequent pour did not cure to a prior filler slab, heavily oiled plastic wrap was placed between the layers.

4.1.3 Lesion Models

Hemorrhage models were created by adding various concentrations of iron oxide to the spectrally equivalent brain material, while calcification models were created by adding various concentrations of calcium carbonate. Calcium carbonate was selected over our previously used hydroxyapatite due to its similar high calcium content but relatively higher ease of use. Lesion models ranging from 40 HU to 100 HU in 10 HU increments were created by Gammex and sent for validation in the form of 2.7 cm diameter, 25 cm long rods. These rods were validated using a Gammex Validation Phantom (Figure 4.3) consisting of a 15 cm thick, approximately 20 cm diameter solid water phantom with 8 insert positions. The two positions on either side of the target insert contained water balloons to provide an optimal imaging environment. All other inserts were relatively low density and did not affect imaging of the target insert in the 12 o'clock position. The validation phantom was imaged using a combined protocol covering single-energy acquisitions, dual-energy acquisitions and Gammex specific acquisitions (Table 4.2). The bold line denotes a break in the protocol when the insert was repositioned to scan the second half due to its length relative to the phantom (25 cm rod vs 15 cm thick phantom).

Figure 4.3: Gammex validation phantom. Water balloons are positioned in insert holes covered by tape. Target lesion was positioned at 12 o'clock.

Table 4.2: Imaging technique for validation of lesion model inserts. Bold line indicates break in protocol where insert was repositioned to allow imaging of second half of insert extent. Series 2 and 4 were not repeated since their relation to series 3 was already evaluated in the first imaging setting. For all series: SFOV: Head, DFOV: 25 cm, Filter: Standard.

Series	Name	Scan Type	Pitch	Rot (s)	Beam Width (mm)	Img Thk (mm)	Interval (mm)	kVp	mA
2	Routine Brain	Helical	0.531	0.8	20	3.75	3	140	160
3	New Routine Brain	Helical	0.531	0.8	20	3.75	3	120	220
4	GSI - 26	Helical	0.531	0.7	20	3.75	3	NA	NA
5	GMX Val 80kV	Axial	1	1	40	5	40	80	250
6	GMX Val 100kV	Axial	1		40	5	40	100	250
7	GMX Val 120kV	Axial	1	1	40	5	40	120	250
8	GMX Val 140kV	Axial	1	1	40	5	40	140	250
9	GMX Val 80kV	Axial	1	1	40	5	40	80	250
10	GMX Val 100kV	Axial	1	1	40	5	40	100	250
11	GMX Val 120kV	Axial	1	1	40	5	40	120	250
12	GMX Val 140kV	Axial	1	1	40	5	40	140	250
13	New Routine Brain	Helical	0.531	0.8	20	3.75	3	120	220

The single-energy images were downloaded and regions of interest (ROIs) were applied using MATLAB. ROIs were of diameter 0.5 cm, 1 cm and 1.5 cm and covered the entire length of the target lesion rod. The mean and standard deviation of each ROI for each image were exported to Excel where the average mean and average standard deviation of each ROI size were calculated for each rod. Outlier limits were set as ±2 HU from the average for the mean values and +1 HU from the average for the standard deviation. Using conditional formatting, outlier fields were highlighted in the rod data, allowing identification of segments of the lesion rod that were within tolerance based on both their mean value and their standard deviation. Based on the known thicknesses of the brain slabs and thus the desired lengths of the lesion models, running averages of set numbers of images were calculated. Those averages representing acceptable rod extents were tabulated and the two regions representing a calcification lesion and a hemorrhage lesion with equal ROI diameters that had the most similar mean CT number on the single-energy protocol were selected. This process was repeated until regions on the rods were identified for the creation of matched HU calcification and hemorrhage rods at all diameters and lengths. The desired region on each rod was marked and then sent back to Gammex for milling.

4.1.4 Selection of optimal keV level for simulated SECT scanning

The phantom was prepared with lesion models representing various SECT attenuation (HU) levels filling the cerebrum brain slab. The skull base slab was left empty for this experiment. Ultrasound gel was used to fill the space in the polyurethane at the back of the cerebrum slab where the pull ribbon exited the phantom. The brain and polyurethane filler slabs were positioned in the nuclear medicine phantom and the crown of the phantom affixed to its base using tape.

The phantom was then positioned in the CT head holder and aligned such that the plane of division between the crown and the base of the phantom was parallel to the imaging plane. The imaging protocol used is shown in Table 4.3. Data were collected from all lesion models using 11.25 mm diameter ROIs for the 15 mm diameter lesion models, 7.5 mm diameter ROIs for the 10 mm diameter lesion models and 3.75 mm diameter ROIs for the 5 mm diameter lesion models. ROIs were collected for each GSI-preset while in mega-mono mode to collect data from multiple monoenergetic keV levels simultaneously. The predicted attenuation (HU) data for keV reconstructions of 40 to 140 keV in 5 keV steps were then imported into excel where a second order polynomial was fit to the predicted attenuation (HU) curve for Monoenergetic reconstructions from 60 to 80 keV. Using this curve and the knowledge of the true SECT attenuation (HU) from series 2 of the protocol, the optimal keV for simulated SECT scanning was calculated. The average optimal keV across all GSI-presets and inserts was then calculated and the difference in attenuation from the optimal keV reconstruction and the SECT acquisition was determined.

Table 4.3: Imaging technique for intracranial lesion phantom scanning. For all series and groups (except series 1): SFOV: Head, DFOV: 25 cm, Scan Type: Helical, Beam Width: 20 mm.

Series	Name	Pitch	Img Thk (mm)	Interval (mm)	kVp	mA	Rot (s)	$CTDI_{vol}$ (mGy)	Filter	DE Recon
1	Scout				120	10				
2	Routine Brain	0.531	1.25	1.25	120	220	0.8	64.8	Standard	
3	GSI-26	0.969	1.25	1.25	80/140	375	0.7	36.7	Standard	Mega Mono
	GSI-20	0.969	1.25	1.25	80/140	630	0.5	44.6	Standard	Mega Mono
	GSI-19	0.969	1.25	1.25	80/140	640	0.6	54.7	Standard	Mega Mono
	GSI-30	0.969	1.25	1.25	80/140	550	0.8	57.9	Standard	Mega Mono
	GSI-14	0.969	1.25	1.25	80/140	600	0.8	64.2	Standard	Mega Mono
	GSI-9	0.969	1.25	1.25	80/140	600	0.9	72.7	Standard	Mega Mono
4	GSI-26	0.531	1.25	1.25	80/140	375	0.7	67	Standard	Mega Mono
	GSI-20	0.531	1.25	1.25	80/140	630	0.5	81.4	Standard	Mega Mono
	GSI-19	0.531	1.25	1.25	80/140	640	0.6	99.8	Standard	Mega Mono
	GSI-30	0.531	1.25	1.25	80/140	550	0.8	105.6	Standard	Mega Mono
	GSI-14	0.531	1.25	1.25	80/140	600	0.8	117.1	Standard	Mega Mono
	GSI-9	0.531	1.25	1.25	80/140	600	0.9	132.6	Standard	Mega Mono

4.1.5 Collection of Lesion Differentiation Data

Lesion models of a specific SECT attenuation (HU) level were loaded into the cerebrum brain slab of the intracranial lesion phantom and imaged using the protocol found in Table 4.3. This protocol allowed for the collection of lesion model data based on a variety of different GSI-presets and pitch values. This process was repeated for all SECT attenuation (HU) sets of lesion models. The data from all seven exams (representing the seven lesion SECT attenuation (HU) levels evaluated) were reconstructed to allow for collection of the optimal keV (determined in Chapter 4.1.4), Water(Calcium) and Calcium(Water) material density data, as well as for additional variations in image thickness and recon filter (Table 4.4).

Table 4.4: Dual-energy reconstructions for intracranial lesion phantom protocol (detailed in Table 4.3). Prospective recons are listed first and labeled with a P, followed by retrospective recons labeled with an R.

Recon	Image Thickness (mm)	DFOV (cm)	Filter	DE Recon
P2	1.25	25	Standard	Water/Ca
P3	2.5	25	Standard	Water/Ca
P4	3.75	25	Standard	Water/Ca
P5	5	25	Standard	Water/Ca
P6	1.25	25	Standard	Ca/Water
P7	2.5	25	Standard	Ca/Water
P8	3.75	25	Standard	Ca/Water
P9	5	25	Standard	Ca/Water
P10	1.25	25	Standard	Optimal keV
R1	2.5	25	Standard	Optimal keV
R2	3.75	25	Standard	Optimal keV
R3	5	25	Standard	Optimal keV
R4	1.25	25	Soft	Water/Ca
R5	2.5	25	Soft	Water/Ca
R6	3.75	25	Soft	Water/Ca
R7	5	25	Soft	Water/Ca
R8	1.25	25	Soft	Ca/Water
R9	2.5	25	Soft	Ca/Water
R10	3.75	25	Soft	Ca/Water
R11	5	25	Soft	Ca/Water
R12	1.25	25	Soft	Optimal keV
R13	2.5	25	Soft	Optimal keV
R14	3.75	25	Soft	Optimal keV
R15	5	25	Soft	Optimal keV
R16	1.25	25	Detail	Water/Ca
R17	2.5	25	Detail	Water/Ca
R18	3.75	25	Detail	Water/Ca
R19	5	25	Detail	Water/Ca
R20	1.25	25	Detail	Ca/Water
R21	2.5	25	Detail	Ca/Water
R22	3.75	25	Detail	Ca/Water
R23	5	25	Detail	Ca/Water
R24	1.25	25	Detail	Optimal keV
R25	2.5	25	Detail	Optimal keV
R26	3.75	25	Detail	Optimal keV
R27	5	25	Detail	Optimal keV

Data collection was repeated three times to form three separate studies. Studies 1 and 2 were performed on a single scanner, hereafter referred to as Scanner 1, while Study 3 was performed on a different scanner, hereafter referred to as Scanner 2. Repeat analysis was performed to allow for combined data with reduced noise, as well as to assess the inter-scanner and intra-scanner repeatability of this technique.

4.1.6 Data Organization and Structure

4.1.6.1 SQL Database

Because a large amount of image data were collected as part of this experiment, an SQL database was built in 3DSlicer (Version 4.3.1) to aid with data sorting and organization. The database contained one table with data about each series including the corresponding exam number and path name, and a second table with file names of individual images. This database was queried in Matlab (Version 2014a, MathWorks) using Mksqlite (www.sourceforge.net/projects/mksqlite), and the Patient ID, exam number, and the folder path name for each series were acquired and then stored in a Matlab structure.

4.1.6.2 Series Sorting

For each series, the folder path name was used to access the digital imaging and communications in medicine (DICOM) header of a representative image and the pitch, DFOV, image thickness, reconstruction filter, and GSI material/keV were acquired using the dicominfo function (Image Processing Toolbox 2014a; MathWorks, Natick, MA). These fields were then added to the existing Matlab structure for each series. In addition, any series not needed for analysis (i.e. scouts and dose reports) were filtered and discarded. The remaining series were then sorted first by exam number (which corresponded to the HU of the lesion model pair), then pitch, reconstruction filter, image thickness, and material/keV respectively.

4.1.6.3 Region of Interest Selection

Images were viewed on an Advantage Workstation (AW) using GSI viewer software (Version 2; GE Healthcare), and the image location extents corresponding to the top slab and bottom slab were recorded for each exam and each image thickness. Regions-of-interest (ROIs) corresponding to each of the six cerebral lesion models were placed on a single image within the cerebrum (Table 4.5). Similarly, ROIs corresponding to both of the skull base lesion models were placed on a single image in the skull base slab (Table 4.5). This procedure was repeated for each exam within the study. The ROIs were saved to a comma-separated-value (.csv) file on the AW, detailing the spatial location of each voxel. The .csv file for each ROI was then imported into Matlab (2014a; MathWorks, Natick, MA) and each voxel's position within the image was extracted from the ROI data file and converted to its corresponding image array position.

Table 4.5: ROI diameters and associated number of voxels based on lesion model size and location.

Lesion Model Location	Lesion Model Diameter (mm)	ROI Diameter (mm)	Number of Voxels
Cerebrum	15	12	465
	10	8	216
	5	4	60
Skull Base	15	12	465

In order to allow direct comparison of results from the cerebrum and skull base lesion models, the number of images analyzed would need to be identical. Since the cerebrum slab was designed 1 cm thicker than the skull base slab, the number of images analyzed from the cerebrum slab would need to be reduced to the maximum allowable in the skull base. The number of available images, and the associated image locations, for each acquired image thickness was determined using the AW and GSI-viewer software.

ROIs of 11.25 mm diameter were placed on the two lesion models in the skull base and all images where both models were within 5 HU of their mean model value were identified. This image number/location extent was then consolidated to ensure identical extents over all exams allowing inter-comparison. Due to the position the cerebrum slab within the cranial cavity of the phantom, a number of images were affected by artifact from the gap between the base and crown portions of the phantom (Figure 4.4). Images unaffected by this phantom discontinuity were identified on each acquired image thickness. The image number/location extents for the cerebrum were then consolidated to match the number of images determined in the skull base and to ensure identical extents over all exams. The final number of images and image extents for each acquired image thickness for both the cerebrum and skull base slab can be found in Table 4.6.

Figure 4.4: Artifact caused by phantom discontinuity.

Table 4.6: Number of images and extent analyzed for both the cerebrum and skull base brain slabs.

	Image Thickness (mm)			
	1.25	2.5	3.75	5
Number of Images	21	10	6	4
Extent (mm)	26.25	25	22.5	20

4.1.6.4 Voxel Data Extraction and Organization

Because the protocol included multiple scan groups within the same series (Table 4.3), multiple GSI presets were contained within the same series folder in the database. To resolve this issue, as well as to isolate images from the cerebrum and skull base regions of the phantom, a custom Matlab function was created. For each series folder in the structure, the function read in the image thickness and exam number fields and determined the appropriate image location extents for the cerebrum and skull base slabs based on Table 4.6. The function then accessed the DICOM header for each image and compared the image location to the previously determined extents. If the image location was within the extents for either the cerebrum or skull base brain slabs, this image information was appended as a new field within the structure. While the DICOM header was open, each image was also analyzed to determine the GSI preset used during acquisition. The structure was then reorganized to include GSI preset in its overall organization.

Images tagged as belonging to the cerebrum slab extent were opened in Matlab using the dicomread fuction (Image Processing Toolbox 2014a; MathWorks, Natick, MA). The ROIs determined above were then applied to the images and the voxel data concatenated into a single column vector and saved within the structure. This was repeated for the skull base slab and a separate single column vector saved within the structure. Table 4.7 shows the size of these column vectors based on the size of the lesion model and image thickness of the series in question.

Table 4.7: Total number of voxels included in analysis for both cerebrum and skull base brain slabs based on image thickness and lesion diameter. Note: This total includes multiple image locations as defined by Table 4.6.

		Lesion Diameter (mm)		
		15	10	5
Img Thk (mm)	1.25	9765	4536	1260
	2.5	4650	2160	600
	3.75	2790	1296	360
	5	1860	864	240

The Matlab structure was then collapsed by identifying matched series that had identical exam number, GSI preset, pitch, image thickness and reconstruction filter fields but different dual-energy reconstructions: optimal keV, Water(Calcium), or Calcium(Water). For a given lesion model size and location (i.e. 10 mm diameter and cerebrum brain slab) the ROI data in the column vectors for these three series were concatenated into an array where each column represented a different dual-energy reconstruction type. The structure then contained a list of series, each representing a unique acquisition type. For each series, three-dimensional dual-energy data was present for all eight lesion models in the intracranial lesion phantom: six lesion models in the cerebrum (1.5 cm hemorrhage model , 1.5 cm calcification model, 1.0 cm hemorrhage model, 1.0 cm calcification model, 0.5 cm hemorrhage model and 0.5 cm calcification model) and two lesion models in the skull base (1.5 cm hemorrhage model and 1.5 cm calcification model).

4.1.7 Determination of Differentiation Accuracy

4.1.7.1 Gaussian Mixture Model Analysis

For each series in the Matlab structure, the lesion models were paired based on matching diameter and brain slab location. For each matched model pair, the three-dimensional dual-energy voxel data for both the hemorrhage model and the calcification model were loaded into Matlab and a three dimensional Gaussian mixture model and plane analysis were performed as described in Chapter 3.2.5. The results of the GMM analysis, as well as the matched model pair and series acquisition specifics from all three studies conducted were printed to a text file and the Matlab workspace saved for future analysis. Data derived from all three studies were used to assess trends in differentiation accuracy based on all available lesion and acquisition parameters.

4.1.7.2 Support Vector Machine (SVM) Analysis

For each matched model pair and acquisition type ($CTDI_{vol}$, image thickness and recon filter) combination, the three-dimensional dual-energy voxel data for both the hemorrhage model and calcification model were loaded into Matlab (Version 2014a, MathWorks). This process was repeated for each exam, to build a distribution including all SECT attenuation (HU) matched model pairs of the given acquisition parameters. Each distribution was then analyzed using a Matlab supplied support vector machine (SVM) process employing a 50% trainer, 50% validation approach. The SVM process determined the equation of a plane that best separated the hemorrhage and calcification model data using the trainer data set (Figure 4.5). This plane was then applied to the validation data set and lesion type assignments were created for each voxel based on its position relative to the plane. The resulting lesion type assignments for each voxel in the distribution were then compared to the known voxel origin and the accuracy score was calculated. The results of the SVM analysis, as well as the matched model pair and series acquisition

specifics from all three studies conducted were printed to a text file and the Matlab workspace saved for future analysis. Data derived from all three studies were used to assess trends in differentiation accuracy based on all available lesion and acquisition parameters.

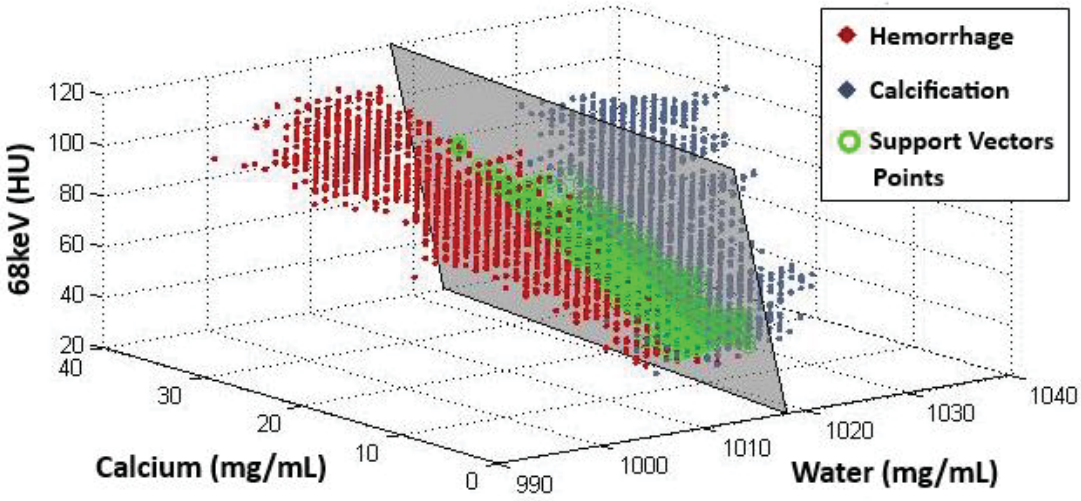

Figure 4.5: Support vector machine plane (gray) based on identified support vectors (green) for the hemorrhage (red) and calcification (blue) distributions.

4.1.7.3 Geometric Bisector (GB) Analysis

For each matched lesion pair and acquisition type distribution to be described in Section 4.2.6.7, a simplified bisector analysis was performed. Using Matlab, a three-dimensional linear regression was performed on both the hemorrhage and calcification data sets to derive a fit line for both distributions. These two lines of best fit were compared and the bisector was calculated. A bisector plane was then derived to include the bisector line in three-dimensional space and be perpendicular to the plane of the data (see section 3.2.5) (Figure 4.6). Each voxel was then assigned a lesion type based on its position relative to the geometric bisector plane. The resulting lesion type assignments for each voxel in the distribution were then compared to the known voxel origin and the accuracy

score was calculated. The results of the GB analysis, as well as the matched model pair and series acquisition specifics from all three studies conducted were printed to a text file and the Matlab workspace saved for future analysis. Data derived from all three studies were used to assess trends in differentiation accuracy based on all available lesion and acquisition parameters.

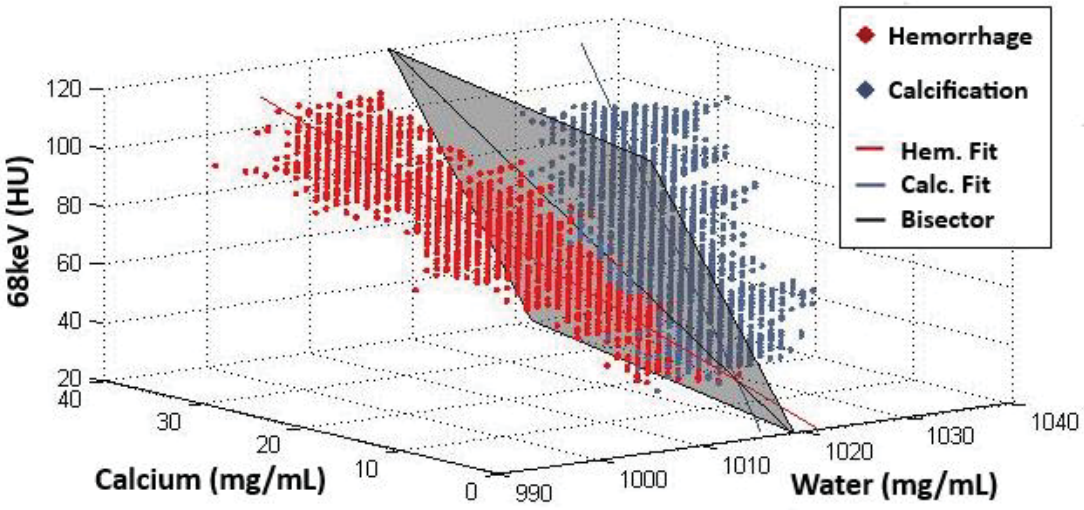

Figure 4.6: Geometric bisector plane (gray) shown separating the hemorrhage (red) and calcification (blue) distributions. Three dimensional linear regressions of the two distributions and the resulting bisector are shown in as color-matched lines.

4.1.7.4 Generalized Geometric Bisector (GGB) Solution

In order to pursue a generalized geometric bisector plane for optimum differentiation, a database containing all voxel data collected in Study 1 was constructed (see Chapter 4.1.6.1). These data were then randomly assigned to equal-sized trainer and validation datasets. A geometric bisector plane was calculated based on all voxel data within the trainer dataset. This plane represents the plane of optimal differentiation across all lesions and acquisition parameters. To determine the effect of lesion and acquisition parameters on this plane, this analysis was repeated for subsets of the data based on all

available values within each lesion and acquisition parameter. For example, the full trainer dataset was divided by image thickness of the protocol into 1.25 mm, 2.5 mm, 3.75 mm and 5 mm datasets. All data acquired using a given image thickness were used to create an image thickness-specific plane, including data from all lesions and other acquisition parameters. The general trainer dataset plane, and the parameter-specific planes, were each applied to the full validation dataset and the accuracy of differentiation was calculated. Each parameter-specific accuracy value was then compared to the general trainer dataset accuracy value to determine major sources of variability in the definition of the geometric bisector plane.

4.1.7.5 Inter-Method Correlation

To assess the correlation between the geometric bisector (GB) and support vector machine (SVM) analysis methods, Bland-Altman and correlation graphs were created. To assess sources of variability in this correlation, the analysis was repeated for subsets of the data based on all available parameters: $CTDI_{vol}$, rotation time, image thickness, study, and lesion size and location. Investigation of rotation time was included due to its impact on other concurrent projects (Chapter 6). Each parameter was investigated separately, while including all values for other variables. For example, investigation of variability by image thickness resulted in four graphs representing the investigated values (1.25, 2.5, 3.75 and 5 mm) with each graph containing all data from each of the other acquisition parameters ($CTDI_{vol}$, rotation time, study and lesion size and location). For all analyses, the coefficient of variation (CV) was tabulated as a measure of data correlation, while the square of the Pearson r-value (R^2) was tabulated as a measure of correlation linearity. The CV and R^2 from these parameter value specific Bland-Altman and correlation graphs were compared to the values derived from Bland-Altman and correlation graphs for the full data set. Based on visual assessment of minor and major sources of variability, static evaluation criteria

were determined to facilitate comparison of correlation data. Parameter-value specific R^2 values under 0.75 or CV values greater than 150% of the full data CV value were chosen as cutoff criteria for the identification of major sources of variability in the method correlation. Specific parameter values identified as major sources of variability were then removed from the full data set and the Bland-Altman analysis was repeated.

4.1.8 Inter-Scanner and Intra-Scanner Correlation

To assess inter-scanner and intra-scanner correlation, Bland-Altman and correlation graphs were created. Inter-scanner correlation was defined as the comparison of Study 1, performed on Scanner 1, to Study 3, performed on Scanner 2. Intra-scanner correlation was defined as the comparison of Study 1, performed on Scanner 1, to Study 2, performed on Scanner 1. To assess sources of variability in this correlation, the analysis was repeated for subsets of the data based on all available parameters: $CTDI_{vol}$, rotation time, image thickness, analysis method, and lesion size and location. Analysis was performed as described in Chapter 4.1.7.5.

4.1.9 Validation of Lesion Attenuation

4.1.9.1 SECT attenuation (HU) correlation with optimal keV HU

Verification of the selection of the optimum keV for dual-energy CT scanning of intracranial lesions was performed on Study 1.

The attenuation in HU derived from the optimal SECT corollary keV reconstructions (determined in Chapter 4.1.4) for all DECT protocol variations were compared to SECT attenuation in HU from reconstructions with matched image thickness and reconstruction filter for each lesion model used in the study. Given that the SECT protocol was acquired at a single dose level, comparisons were made between the single SECT protocol and each $CTDI_{vol}$ value within the DECT protocol set. For each lesion model

(Calcification/Hemorrhage, SECT attenuation (HU) level, lesion size and location) the mean and standard deviation of the error in HU between the SECT and optimal keV methods was calculated across all DECT protocol variations.

Bland-Altman analysis was performed to assess the correlation between the SECT attenuation (HU) and optimal keV HU values. To assess sources of variability, the analysis was repeated for subsets of the data based on all available parameters: $CTDI_{vol}$, rotation time, image thickness, lesion identity and lesion size and location (See Chapter 4.1.7.5). The CV and R^2 from the parameter-value specific Bland-Altman analyses were compared to the values derived from the analysis of the full data set. Parameter-value specific R^2 values under 0.75 or CV values greater than 150% of the full data CV value were identified as major sources of variability in the method correlation. Specific parameter values identified as major sources of variability were then removed from the full data set and the Bland-Altman analysis was repeated.

4.1.9.2 Lesion Matching using SECT and optimal keV

To ensure the matching of the calcification and hemorrhage models within the matched model pair, the difference in attenuation (HU) was calculated based on both SECT and optimal keV attenuation. This was repeated for each matched model pair (SECT attenuation (HU) level, lesion size and location) and the mean and standard deviation of the difference in attenuation (HU) between the calcification and hemorrhage was calculated for SECT and optimal keV image types across all DECT protocol variations.

4.2 Results

4.2.1 Spectrally Equivalent Brain Material

While all potential brain materials supplied by Gammex were equivalent to brain tissue using a single-energy acquisition (data not shown), the materials possessed very

different spectral characteristics using a dual-energy acquisition. The results of the spectral HU analysis can be seen in Figure 4.7. The stock Gammex brain material, shown in the figure as Gammex A, was similar to brain tissue on a single-energy acquisition using a 70 keV dual-energy reconstruction but differed greatly from brain tissue with respect to its spectral signature. Gammex B and C were more spectrally equivalent and ultimately, Gammex B was selected for our application based on this data.

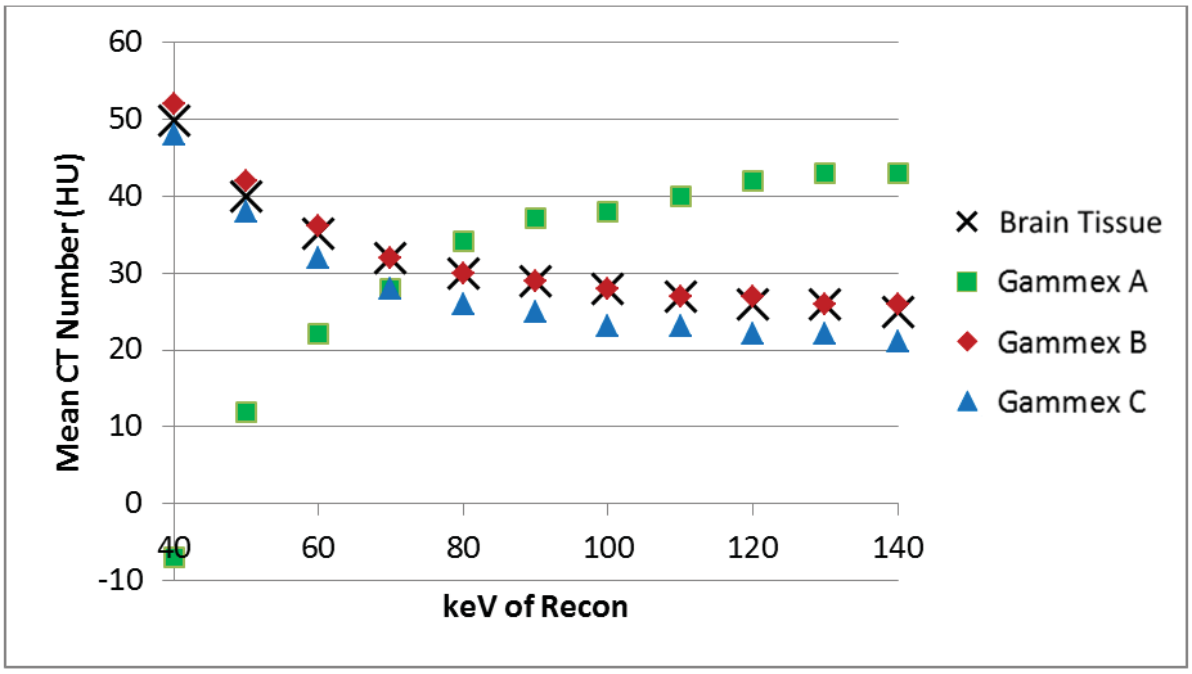

Figure 4.7: Results of dual-energy analysis for potential spectrally equivalent brain materials. Spectral data from a clinical brain study (GE, Waukesha, WI; personal contact) is shown in black.

A sagittal reformat of the polyurethane filled nuclear medicine phantom can be seen in Figure 4.8. This view indicated the optimal position and thickness for both the cerebrum and skull base slabs within the cranial cavity. Because the bony anatomy only extends upwards into the cranial cavity roughly 3 cm, the skull base slab was reduced from its

planned thickness of 4 cm to 3 cm. The cerebrum brain slab was then positioned in line with the phantom split so that equal portions of the slab thickness were in the base and crown portions of the phantom. This position also allowed for some intervening space between the end of the cerebrum slab and the start of the skull base slab. To simplify construction, the center of the 4 cm thick cerebrum slab was aligned with the division between the base and crown of the phantom.

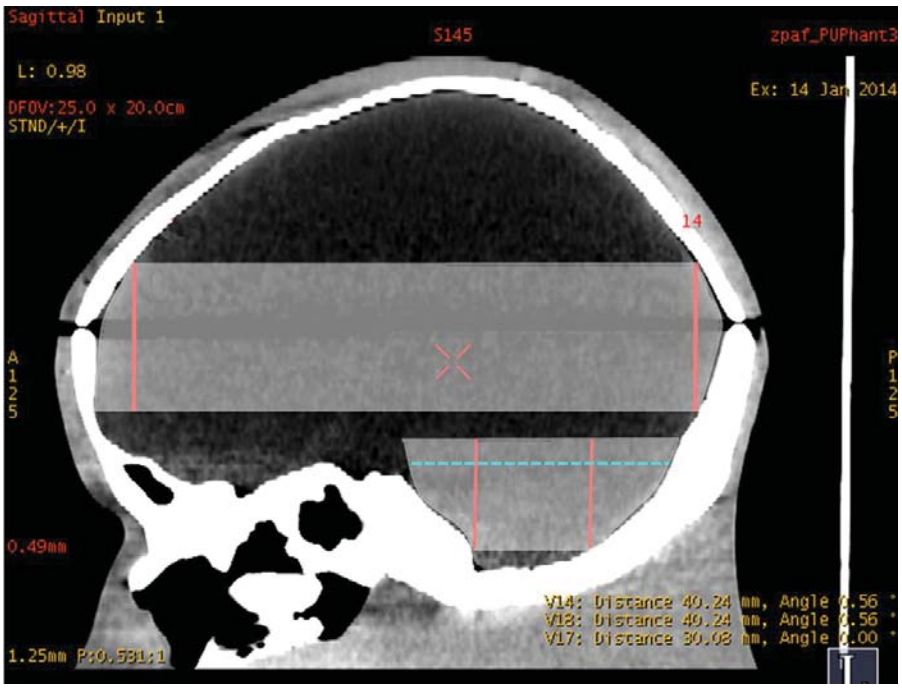

Figure 4.8: Sagittal reformat of intracranial lesion phantom showing potential positioning of cerebrum and skull base slabs. Red lines show the relative thickness of the cerebrum vs the skull base brain slabs while the blue dotted line represents the upper bound of the imaging area affected by the bony anatomy of the skull base.

Due to the organic shape of the phantom cranial cavity, the skull base brain slab was simplified into its major features and reduced in size slightly to allow for polyurethane to be poured around it in the final stage of phantom construction. Similarly, the shape of

the cerebrum brain slab had to be simplified due to the organic shape, as well as, the mismatch between the base and crown of the phantom. Because the edges of the skull component of the phantom did not meet perfectly, the outer contour of the slab was reduced to a simplified transition between the contours of the lower face of the slab to the contour of the upper face of the slab (Figure 4.9). Additional material was removed as needed for easy placement and removal of the brain slab. Polyurethane was then added to the outer contour of the cerebrum slab to fill air gaps left from this simplification and to ensure a tight fit in the phantom cranial cavity. Due to early experiences with the phantom, the decision was made to provide some tool to aid the removal of the cerebrum slab from the base of the phantom. A thin nylon ribbon was cured into the surrounding polyurethane and fed under the cerebrum slab. This ribbon would then distribute the user's force to the whole slab and break the vacuum commonly created between the brain and filler slabs.

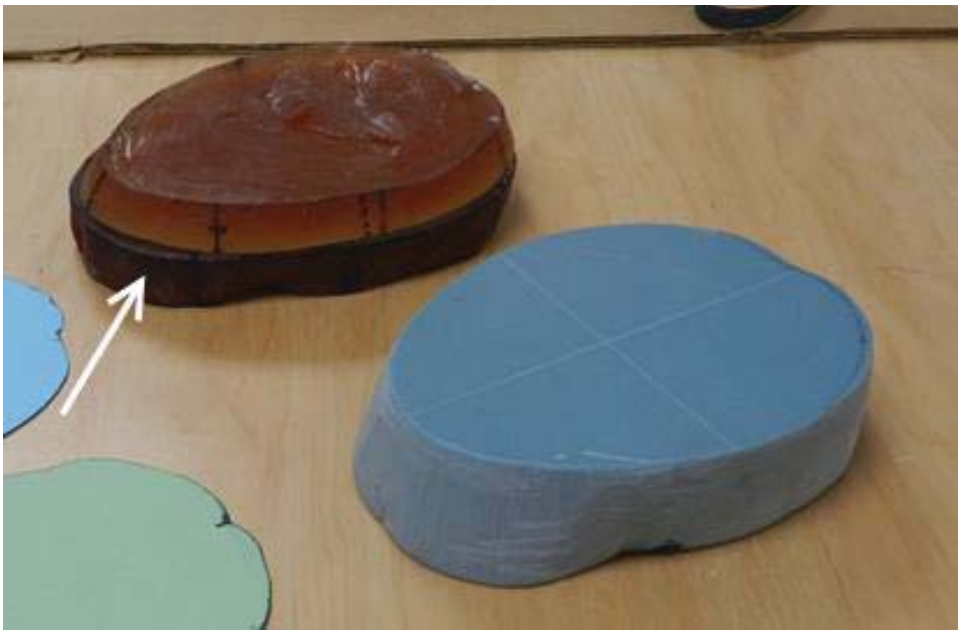

Figure 4.9: Simplified structure of cerebrum slab based on upper and lower curvatures with arrow showing mismatch between phantom base and crown interiors.

4.2.2 Lesion Models

Based on the results of the lesion rod imaging and ROI analysis (Chapter 4.1.3), calcification and hemorrhage lesion models free of any artifact or high variability were chosen at the required SECT attenuation (HU) levels. Of the 28 lesion model pairs isolated, only four had greater than 1 HU difference between the calcification and hemorrhage models based on their mean HU value on the single-energy images (Table 4.8). The image location ranges and series numbers for the chosen lesion model positions were translated into lengths in mm from the end of the rod and the lesion rods were marked appropriately for milling.

Table 4.8: Results of lesion rod imaging and ROI analysis using a SECT acquisition. Green fields represent a matched model pair with < 1 HU difference between the calcification and hemorrhage model while orange represents a difference > 1 HU but < 2 HU. Gray regions represent data that's not applicable given the skull base contained only 1.5 cm lesion models.

			0.5 cm Lesion	1.0 cm Lesion	1.5 cm Lesion
	SECT HU Level	Model	Mean SECT HU	Mean SECT HU	Mean SECT HU
Cerebrum	40	Calcification	40.14	40.06	40.10
		Hemorrhage	40.11	40.06	40.32
		Pair	0.03	0.00	0.22
	50	Calcification	50.87	50.81	50.44
		Hemorrhage	50.92	50.70	50.62
		Pair	0.05	0.11	0.18
	60	Calcification	60.20	59.86	60.10
		Hemorrhage	61.17	60.86	61.39
		Pair	0.97	1.01	1.29
	70	Calcification	70.70	70.46	70.37
		Hemorrhage	71.40	71.42	71.64
		Pair	0.70	0.96	1.26
	80	Calcification	79.99	80.09	79.92
		Hemorrhage	80.68	80.97	80.79
		Pair	0.69	0.88	0.87
	90	Calcification	89.83	89.71	89.97
		Hemorrhage	90.22	90.21	90.53
		Pair	0.39	0.50	0.56
	100	Calcification	100.20	100.41	100.08
		Hemorrhage	100.14	100.51	99.81
		Pair	0.06	0.10	0.27
Skull Base	40	Calcification			39.92
		Hemorrhage			40.28
		Pair			0.36
	50	Calcification			50.78
		Hemorrhage			50.65
		Pair			0.13
	60	Calcification			60.25
		Hemorrhage			61.37
		Pair			1.12
	70	Calcification			70.08
		Hemorrhage			71.00
		Pair			0.93
	80	Calcification			79.92
		Hemorrhage			80.51
		Pair			0.59
	90	Calcification			90.20
		Hemorrhage			90.79
		Pair			0.59
	100	Calcification			99.98
		Hemorrhage			99.61
		Pair			0.37

Initial validation of milled lesion models identified two matched model pairs with sub-optimal SECT attenuation (HU) matching (Table 4.9). Two matched attenuation lesion pairs were identified as exceeding 3 HU error in matching between the calcification and hemorrhage: 0.5 cm cerebrum lesions at 50 HU and 1.5 cm skull base lesions at 100 HU. New regions were identified from the reserved lesion model rods for these two SECT attenuation (HU) levels (50 and 100 HU) and marked for milling. These new lesion models were imaged using the single-energy protocol detailed in Table 4.3 and compared to the data from the old lesion models. New matched model pairs were identified which would have matched attenuation to within 3 HU SECT (Table 4.10).

Table 4.9: Initial SECT attenuation (HU) matching of milled lesion model pairs (calcification and hemorrhage). Green denotes matching < 2 HU, orange denotes matching < 3 HU and red denotes matching out of tolerance > 3 HU.

		Δ Mean SECT HU		
	SECT HU Level	0.5 cm	1.0 cm	1.5 cm
Cerebrum	40	0.24	0.21	0.08
	50	**3.99**	0.22	0.77
	60	1.14	0.51	1.48
	70	2.24	1.42	1.07
	80	1.67	1.01	1.61
	90	2.24	0.78	0.21
	100	2.29	0.80	1.21
Skull Base	40			1.42
	50			0.46
	60			0.17
	70			0.21
	80			0.15
	90			1.46
	100			**3.46**

Table 4.10: Final SECT attenuation (HU) matching of lesion model pairs (calcification and hemorrhage). Green denotes matching < 2 HU, orange denotes matching < 3 HU and red denotes matching out of tolerance > 3 HU. Note the improved lesion matching of the 50 HU, 0.5 cm cerebrum and 100 HU, 1.5 cm skull base lesion pairs.

		Δ SECT Mean		
	SECT HU Level	0.5 cm	1.0 cm	1.5 cm
Cerebrum	40	0.24	0.21	0.08
	50	0.51	0.22	0.77
	60	1.14	0.51	1.48
	70	2.24	1.42	1.07
	80	1.67	1.01	1.61
	90	2.24	0.78	0.21
	100	2.29	0.80	1.21
Skull Base	40			1.42
	50			0.46
	60			0.17
	70			0.21
	80			0.15
	90			1.46
	100			2.30

4.2.3 Selection of Optimal keV Level for Simulated SECT Scanning

In order to avoid the necessity of a separate single-energy acquisition that would increase patient dose and motion artifacts, we endeavored to determine the keV of a monoenergetic reconstruction that could be derived from the dual-energy acquisition but provide accurate SECT attenuation (HU) data. Using the monoenergetic keV and the resulting attenuation (HU), a second order polynomial was used to determine the monoenergetic kVp necessary to produce an attenuation (HU) equivalent to that from a SECT acquisition. This process was repeated for all inserts and dual-energy presets used in the study. This optimal keV level for simulated single-energy scanning was found to have a mean of 68 keV with a standard deviation of 1.75 keV. The minimum optimal keV

across all lesion models and dual-energy protocols was 65 keV while the maximum was 74 keV. The average error in the estimated HU using 68 keV and the SECT acquisition over all lesion models and dual-energy protocols was found to be 0.3 HU with a standard deviation of 1.4 HU. The minimum and maximum errors were -2.6 HU and 2.6 HU respectively.

4.2.4 Validation of Lesion Attenuation

4.2.4.1 SECT attenuation (HU) Correlation with 68 keV HU

Based on lesion data collected during Study 1, mean error was calculated between the attenuation (HU) estimation by the 68 keV reconstruction and the attenuation from the SECT acquisition performed as part of the overall protocol (Figure 4.10). Analysis was divided by lesion identity and includes all protocol variations including reconstruction filter, $CTDI_{vol}$ and image thickness. Mean errors based on protocol variation were within 3 HU for all cerebrum lesion models, and within 6 HU for skull base lesion models. Averaging over all lesion parameters and protocol variations, the average mean error was found to be 0.5 HU and 1 HU for calcification and hemorrhage respectively.

Bland-Altman analysis of the attenuation from 68 keV and SECT for all available protocol and acquisition parameters resulted in a CV of 2.8% and an R^2 of 0.990 (Figure 4.11). Repeated analysis for subsets of the data based on all available parameters yielded no major sources of variability based on the stated criteria (Table 4.11).

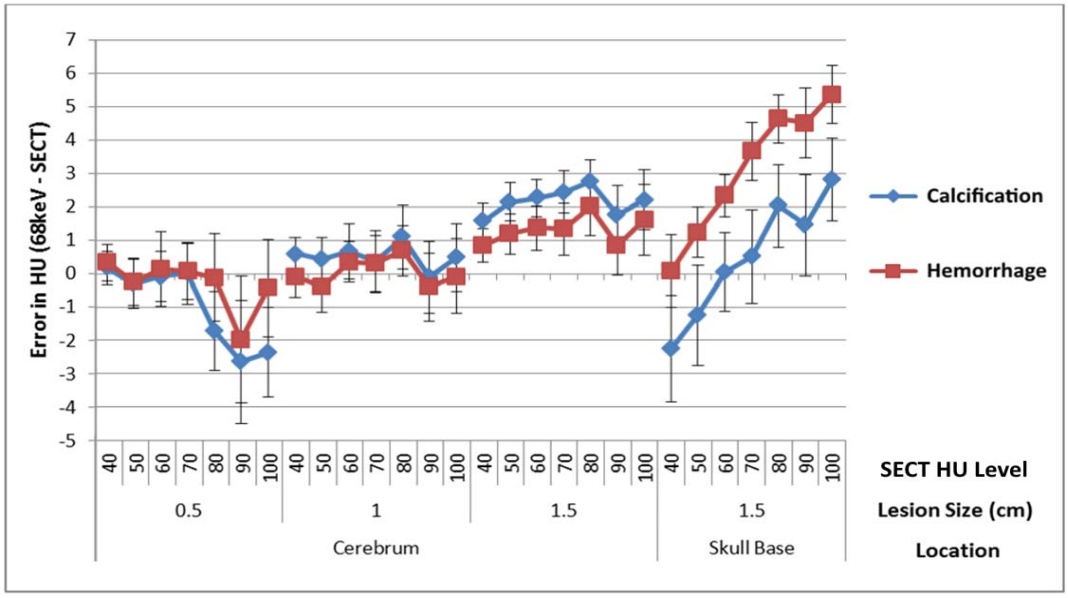

Figure 4.10: Error in attenuation (HU) measurement between SECT and 68 keV reconstructions for both calcification and hemorrhage models. Error bars represent one standard deviation (SD) of the distribution accounting for all image thickness, $CTDI_{vol}$ and reconstruction filter protocol variations.

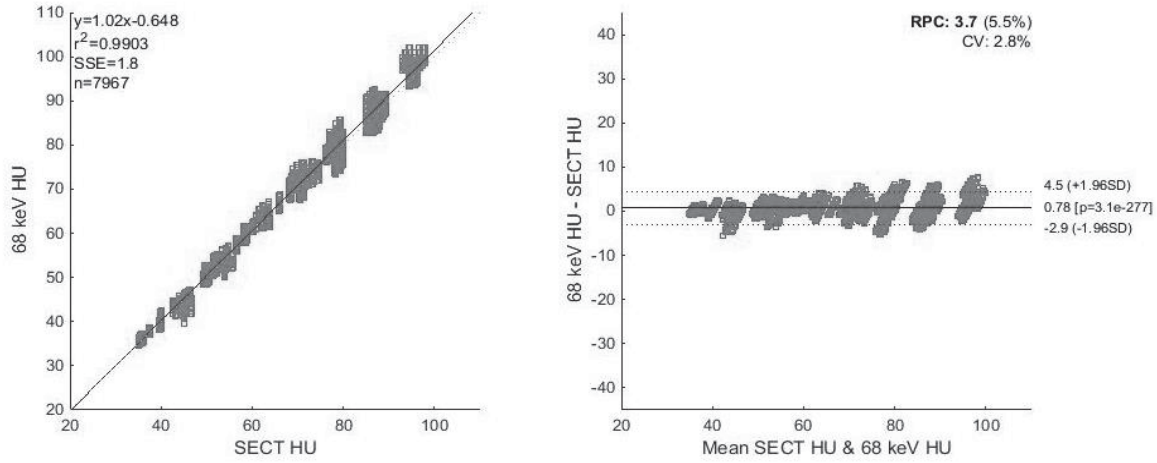

Figure 4.11: Bland-Altman and Correlation graphs for the correlation of SECT attenuation (HU) to 68 keV HU. Data includes all protocol variations and lesion models.

Table 4.11: Sorted results of Bland-Altman analysis of the correlation of attenuation (HU) from 68 keV and SECT acquisitions organized for subsets of the data based on available protocol and lesion parameters. Parameters and values above the double line indicate worse correlation or linearity than the analysis of the full data set while those below the double line indicate improved correlation or linearity.

CV - Correlation		
Full Data CV	**Criteria**	**Cutoff**
2.8	**150%**	**4.2**
Parameter	**Value**	**CV**
Lesion Model	1.5 cm Skull Base	3.5
$CTDI_{vol}$	132.6	3.1
Image Thickness	2.5	2.9
$CTDI_{vol}$	105.6	2.9
$CTDI_{vol}$	117.1	2.9
Image Thickness	1.25	2.8
$CTDI_{vol}$	81	2.8
$CTDI_{vol}$	99.8	2.8
Lesion Identity	Hemorrhage	2.8
Image Thickness	3.75	2.7
Image Thickness	5	2.7
Rotation Time	0.9	2.7
Lesion Identity	Calcification	2.7
$CTDI_{vol}$	67	2.6
Rotation Time	0.5	2.6
Rotation Time	0.6	2.6
Rotation Time	0.8	2.6
$CTDI_{vol}$	44.6	2.5
$CTDI_{vol}$	54.7	2.4
$CTDI_{vol}$	64.2	2.4
Lesion Model	0.5 cm Cerebrum	2.4
Rotation Time	0.7	2.4
$CTDI_{vol}$	57.9	2.3
$CTDI_{vol}$	72.7	2.3
$CTDI_{vol}$	36.7	2.2
Lesion Model	1.0 cm Cerebrum	1.4
Lesion Model	1.5 cm Cerebrum	1.3

Rsquared - Linearity		
Full Data R^2	**Criteria**	
0.9903	**< 0.75**	
Parameter	**Value**	**R^2**
$CTDI_{vol}$	132.6	0.988
$CTDI_{vol}$	99.8	0.989
$CTDI_{vol}$	105.6	0.989
$CTDI_{vol}$	117.1	0.989
Image Thickness	2.5	0.990
$CTDI_{vol}$	81	0.990
Lesion Model	1.5 cm Skull Base	0.990
Image Thickness	1.25	0.990
Lesion Identity	Hemorrhage	0.990
Image Thickness	3.75	0.991
Lesion Identity	Calcification	0.991
Image Thickness	5	0.991
Rotation Time	0.5	0.991
Rotation Time	0.9	0.991
Rotation Time	0.6	0.991
Rotation Time	0.8	0.992
$CTDI_{vol}$	44.6	0.992
$CTDI_{vol}$	67	0.992
$CTDI_{vol}$	54.7	0.993
$CTDI_{vol}$	64.2	0.993
$CTDI_{vol}$	57.9	0.994
$CTDI_{vol}$	72.7	0.994
Lesion Model	0.5 cm Cerebrum	0.994
Rotation Time	0.7	0.994
$CTDI_{vol}$	36.7	0.995
Lesion Model	1.0 cm Cerebrum	0.998
Lesion Model	1.5 cm Cerebrum	0.998

4.2.4.2 Lesion Matching using SECT and 68 keV

Average differences between the calcification and hemorrhage models within each matched model pair are shown in Figure 4.12 for both 68 keV and SECT acquisitions. Error bars represent one standard deviation (SD) based on the combined data across all protocol variations. Based on evaluation using SECT, all matched model pairs had differences in attenuation of less than 3 HU. Evaluation using 68 keV reconstruction closely followed the SECT results, however the two methods agreed to a lesser extent in the skull base. This result is not unexpected given the greater errors between SECT and 68 keV attenuation measurements in the skull base, shown in Chapter 4.2.4.1.

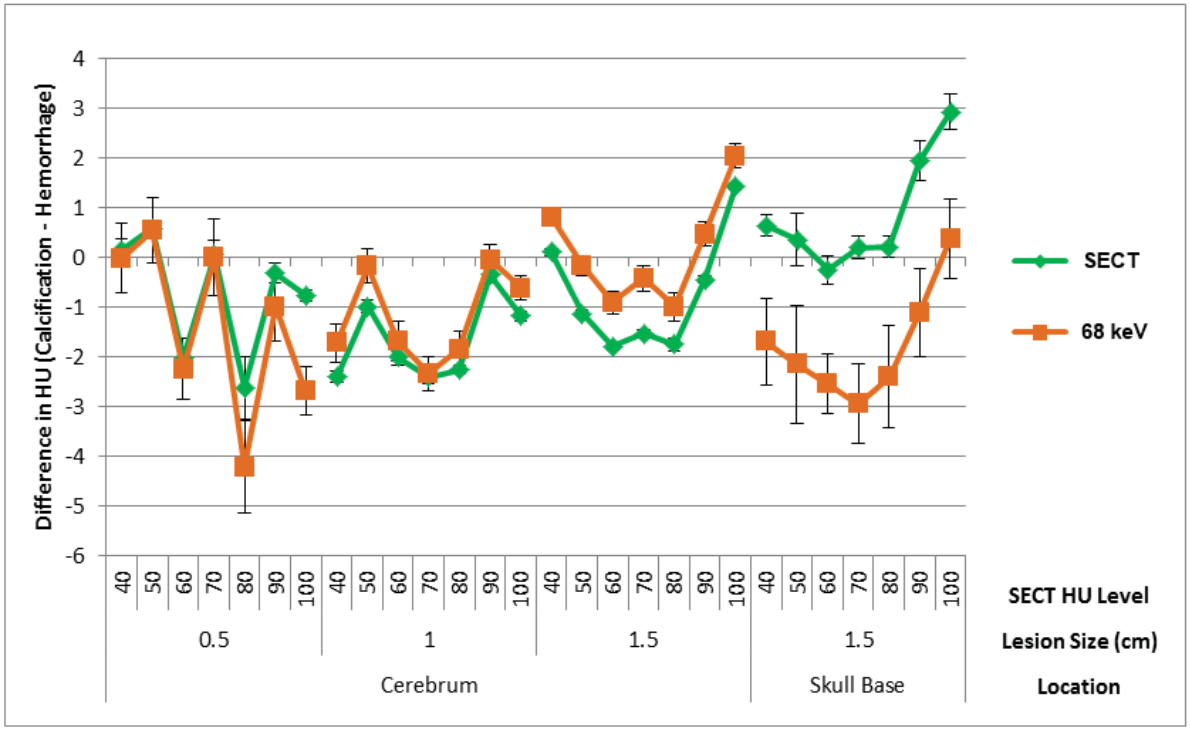

Figure 4.12: Lesion matching results based on SECT and 68 keV attenuation evaluation. Values represent mean difference in calcification and hemorrhage models across all available protocol variations. Error bars represent one SD of this distribution.

4.2.5 Determination of Differentiation Accuracy

Using the methods described in Chapter 4.1.5 and the scan protocol outlined in Table 4.3 and Table 4.4, a total of 407,925 images were collected for analysis across the three studies. Of those images collected, 95,571 images were used to collect a total of 230,517,252 unique voxels used in the analysis of lesion differentiation.

4.2.5.1 Gaussian Mixture Model Analysis

By averaging over all three studies and all imaging techniques investigated, the effect of lesion size and location on GMM differentiation accuracy can be easily seen (Figure 4.13). Error bars represent one standard deviation within each distribution. Differentiation accuracy under 80% is shaded in dark gray while differentiation accuracy between 80% and 90% is shaded in light gray. Averaged over all imaging protocols investigated, the maximum average accuracy at 100 HU was 58%, 73% and 97% for the 0.5 cm cerebrum, 1.0 cm cerebrum and 1.5 cm cerebrum matched model pairs respectively. The maximum average accuracy at 100 HU was 81% for the 1.5 cm skull base matched model pair, reflecting the more challenging imaging environment of the skull base.

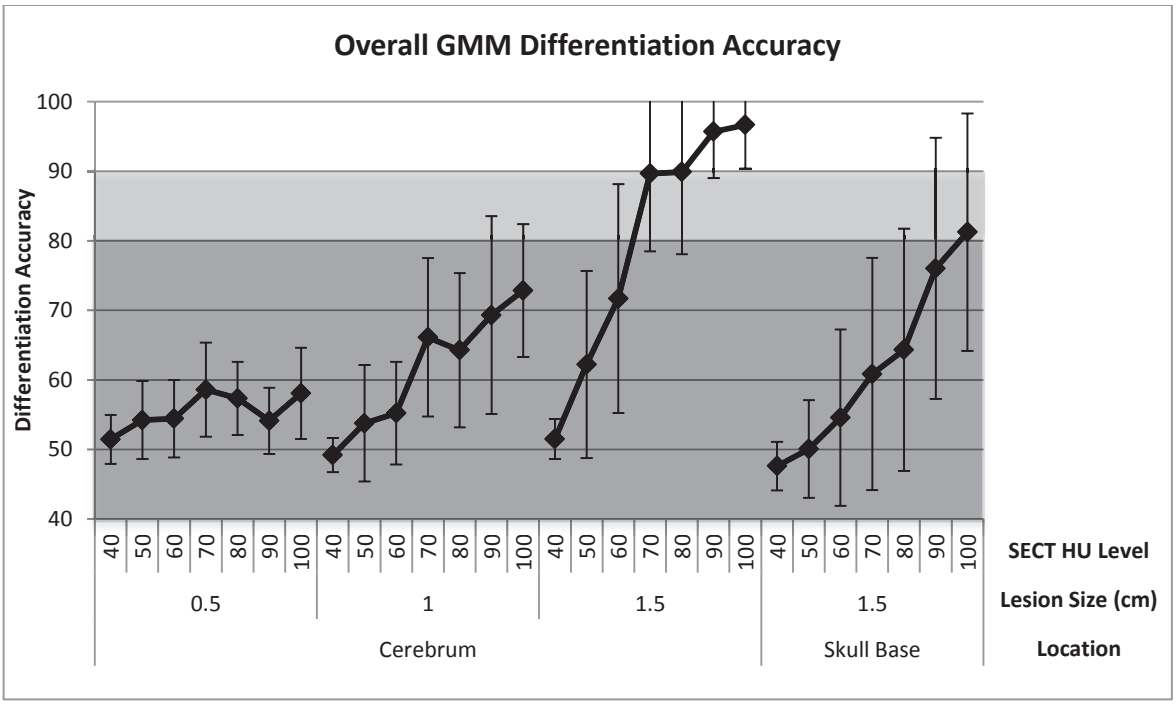

Figure 4.13: Accuracy of 3D GMM differentiation for intracranial lesion pairs based on lesion model size and location. Displayed values represent mean of accuracy across the three studies and all protocol variations: $CTDI_{vol}$, image thickness and reconstruction filter. Error bars represent one SD of the distribution.

Accuracy results were then graphed by relevant protocol factors including $CTDI_{vol}$, image thickness and reconstruction filter. In all graphs, darker colored lines were used to indicate an increase in protocol value; be it an increase in dose level, image thickness, or perceived noise. Accuracy results graphed by $CTDI_{vol}$ (mGy), revealed increasing GMM differentiation accuracy with increasing dose level for 1.5 cm lesion models in the cerebrum and skull base (Figure 4.14). No dose effect was observed in 0.5 cm or 1.0 cm cerebrum lesion models. The effect of dose on differentiation accuracy was more pronounced at higher matched model pair SECT attenuation (HU) levels.

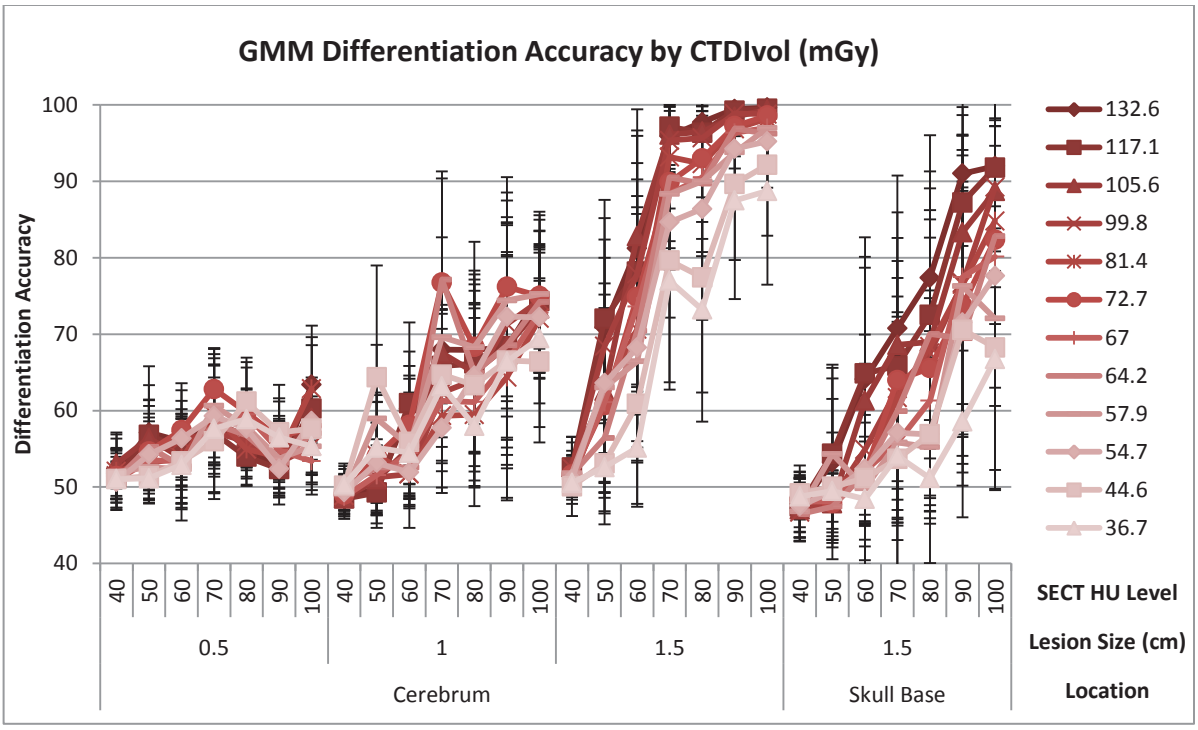

Figure 4.14: Differentiation Accuracy using Gaussian Mixture Model (GMM) method analyzed by $CTDI_{vol}$. Displayed values represent mean of accuracy across the three studies and additional protocol variations: image thickness and reconstruction filter. Error bars represent one SD for each distribution.

Accuracy results graphed by image thickness (mm), revealed increasing GMM differentiation accuracy with increasing image thickness (Figure 4.15) for all lesion models except the 0.5 cm cerebrum. Again, the effect of increased image thickness on differentiation accuracy was more pronounced at higher matched model pair SECT attenuation (HU) levels.

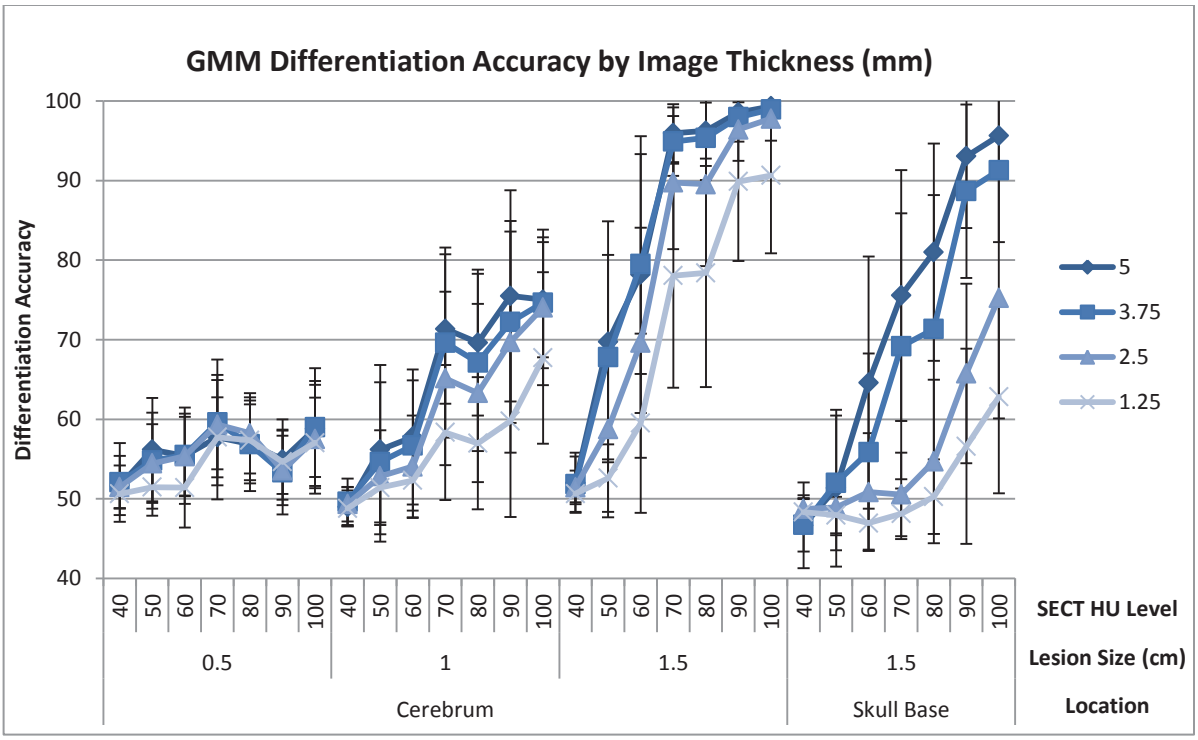

Figure 4.15: Differentiation Accuracy using Gaussian Mixture Model (GMM) method analyzed by image thickness. Displayed values represent mean of accuracy across the three studies and additional protocol variations: $CTDI_{vol}$ and reconstruction filter. Error bars represent one SD for each distribution.

Accuracy results graphed by reconstruction filter showed that decreasing smoothing increased GMM differentiation accuracy in the 1.0 cm cerebrum lesions (Figure 4.16). All other lesions showed no effect of filter selection on GMM differentiation accuracy. Error bars represent variation across $CTDI_{vol}$, image thickness and study and show considerable overlap between the reconstruction filter types.

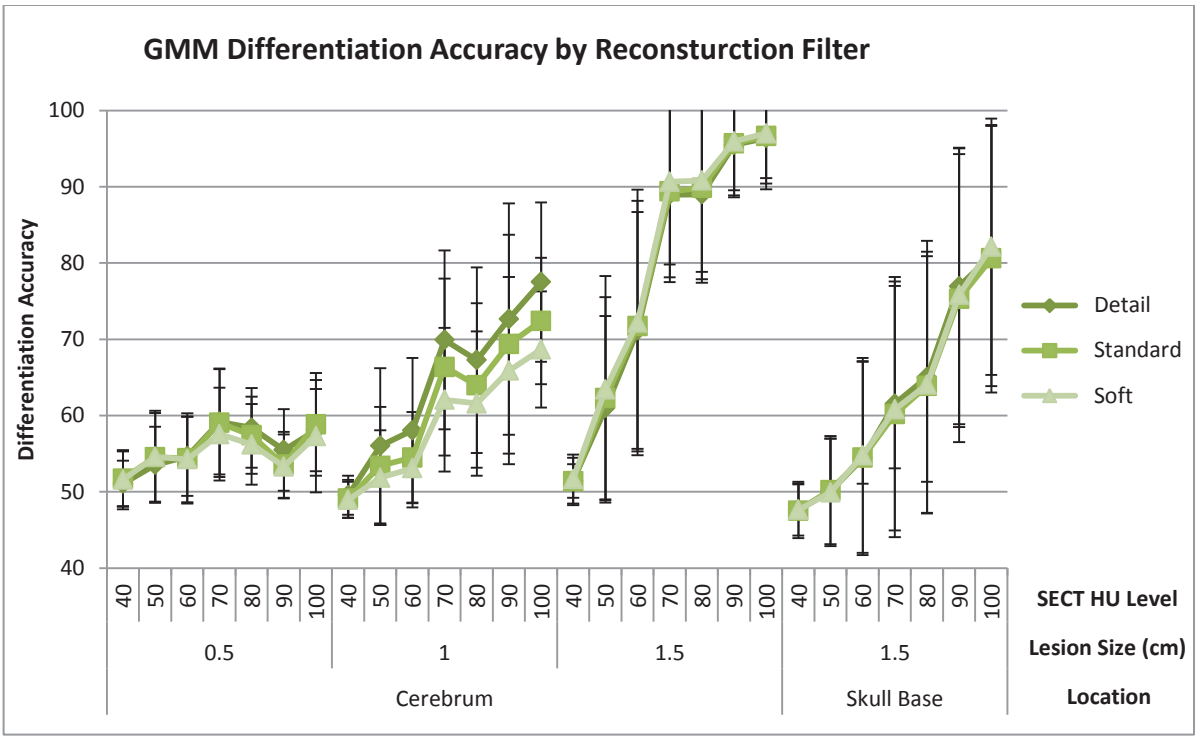

Figure 4.16: Differentiation Accuracy using Gaussian Mixture Model (GMM) method analyzed by reconstruction filter. Displayed values represent mean of accuracy across the three studies and additional protocol variations: $CTDI_{vol}$ and image thickness. Error bars represent one SD for each distribution

4.2.5.2 Gaussian Mixture Model Instability

Particularly of note from the GMM results was the unexpected plateau in differentiation accuracy at 80 HU and above for the 1 cm cerebrum matched lesion pair. Given the similarity in size between these lesion models and the gel vials used in the physics model (Chapter 3), these results were unexpected. Investigation into the results of the 1,000 GMMs for all lesion model attenuations for a given acquisition showed that the distribution of the differentiation accuracies was, in fact, bimodal (Figure 4.17)

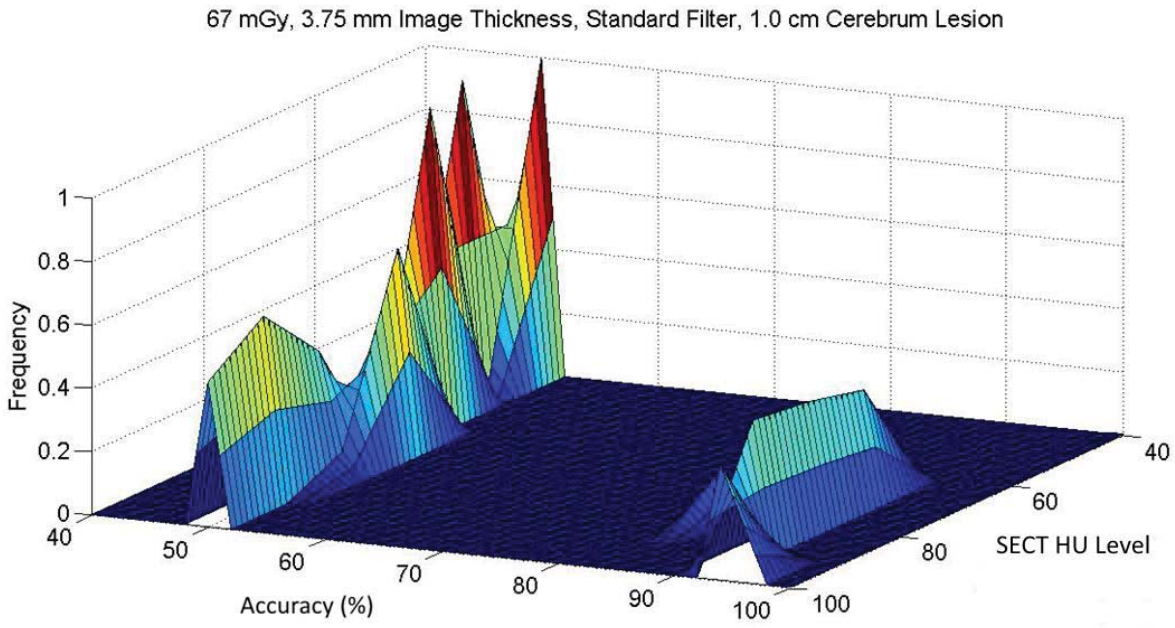

Figure 4.17: Distribution of differentiation accuracy results from 7,000 GMMs (1,000 per lesion pair) graphed versus the attenuation of lesion pair. Data represents 67 mGy $CTDI_{vol}$, 3.75 mm image thickness, standard filter acquisition of 1 cm cerebrum matched lesion pairs.

Further analysis pursued by plotting the component accuracies, calcification model accuracy and hemorrhage model accuracy, with the general matched model pair result (Figure 4.18). The general matched model pair accuracy was in all cases primarily affected by the calcification model component accuracy, while the hemorrhage model component accuracy was always greater than 80%.

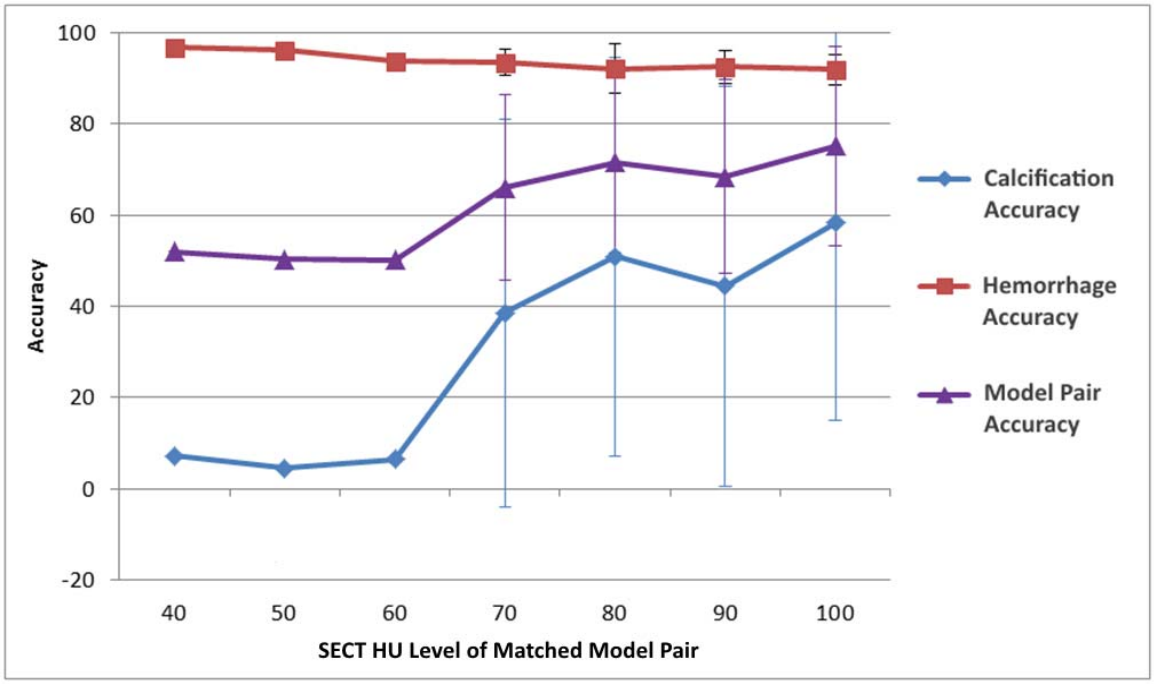

Figure 4.18: Differentiation accuracy results for calcification model, hemorrhage model and combined matched model pair. Error bars represent standard deviation in accuracy value over the 1,000 GMM repetitions. Data represents 67 mGy $CTDI_{vol}$, 3.75 mm image thickness, standard filter acquisition of 1 cm cerebrum matched lesion pairs.

The 80 HU matched lesion pair data for this acquisition method was visualized and seen to be non-Gaussian in nature (Figure 4.19). Outliers are assumed to be a result of inadequate mixing of the compound additives, calcium carbonate or iron oxide, into the background material leaving areas of reduced attenuation. Given that the prime assumption of a Gaussian data distribution was invalidated, the GMM iterative fit of the two potentially overlapping Gaussian distributions was unstable resulting in two general solutions. The first solution yielded hemorrhage and calcification distributions that included their respective outliers resulting in high calcification model accuracy and high overall matched model pair accuracy. The second solution yielded a hemorrhage distribution covering both the calcification and hemorrhage main distributions and a calcification

distribution covering all outliers. This resulted in a low calcification model accuracy and thus high overall matched model pair accuracy.

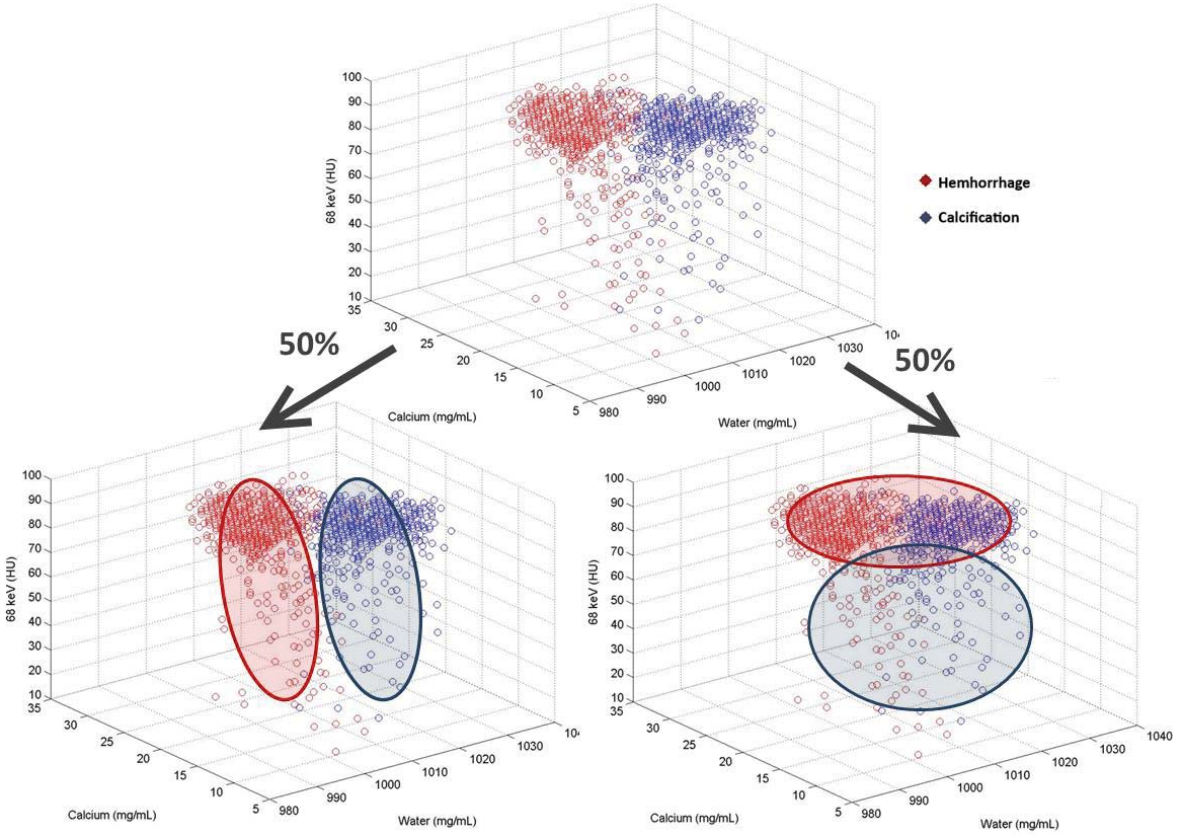

Figure 4.19: Top: Raw voxel data from a $CTDI_{vol}$, 3.75 mm image thickness, standard filter acquisition of 1 cm cerebrum matched lesion pairs at 80 HU. Lower Left: GMM solution resulting in high calcification model and overall matched model pair accuracies. Lower Right: GMM solution resulting in low calcification model and overall matched model pair accuracies.

Based on these results revealing the instability of the GMM analysis, this method was dropped from all further analysis, including Studies 2 and 3. Only the geometric bisector and support vector machine methods were retained.

4.2.5.3 Support Vector Machine (SVM) Analysis

By averaging over all three studies and all imaging techniques investigated, the effect of lesion size and location on SVM differentiation accuracy can be easily seen (Figure 4.20). Error bars represent one standard deviation within each distribution. Differentiation accuracy under 80% is shaded in dark gray while differentiation accuracy between 80% and 90% is shaded in light gray. Averaged over all imaging protocols investigated, the maximum average accuracy at 100 HU was 78%, 92% and 96% for the 0.5 cm cerebrum, 1.0 cm cerebrum and 1.5 cm cerebrum matched model pairs respectively. The maximum average accuracy at 100 HU was 90% for the 1.5 cm skull base matched model pair, reflecting the more challenging imaging environment of the skull base.

Compared to GMM analysis (Figure 4.13), SVM analysis increased the average maximum differentiation accuracy by 20% for 0.5 cm cerebrum lesions, 29% for 1.0 cm cerebrum lesions and 8% for 1.5 cm skull base lesions. No improvement was seen in 1.5 cm cerebrum lesions.

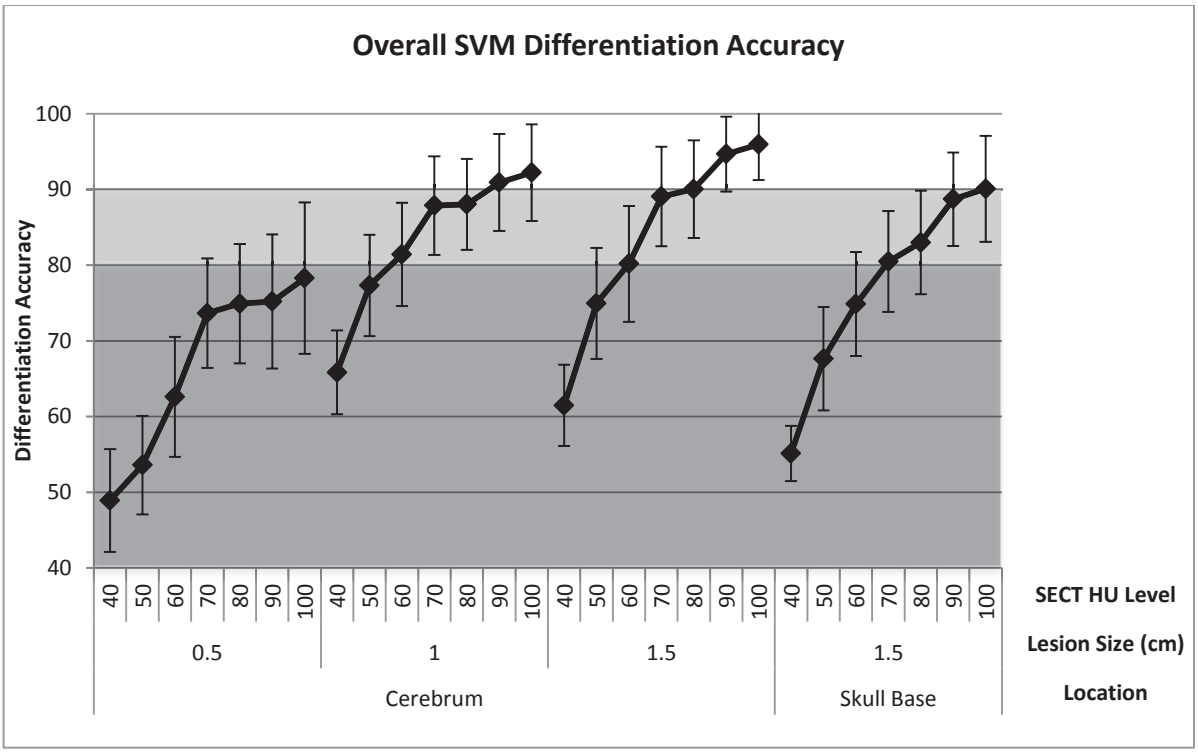

Figure 4.20: Differentiation accuracy using support vector machine method. Displayed values represent mean of accuracy across the three studies and all protocol variations: $CTDI_{vol}$, image thickness and reconstruction filter. Error bars represent one SD of the distribution.

Accuracy results were then graphed by relevant protocol factors including $CTDI_{vol}$, image thickness and reconstruction filter. In all graphs, darker colored lines were used to indicate an increase in protocol value; be it an increase in dose level, image thickness, or perceived noise. Accuracy results graphed by $CTDI_{vol}$ (mGy), revealed increasing SVM differentiation accuracy with increasing dose level (Figure 4.21). Note that error bars represent variation across image thickness, reconstruction filter and study. The effect of dose on differentiation accuracy was more pronounced at higher matched model pair SECT attenuation (HU) levels.

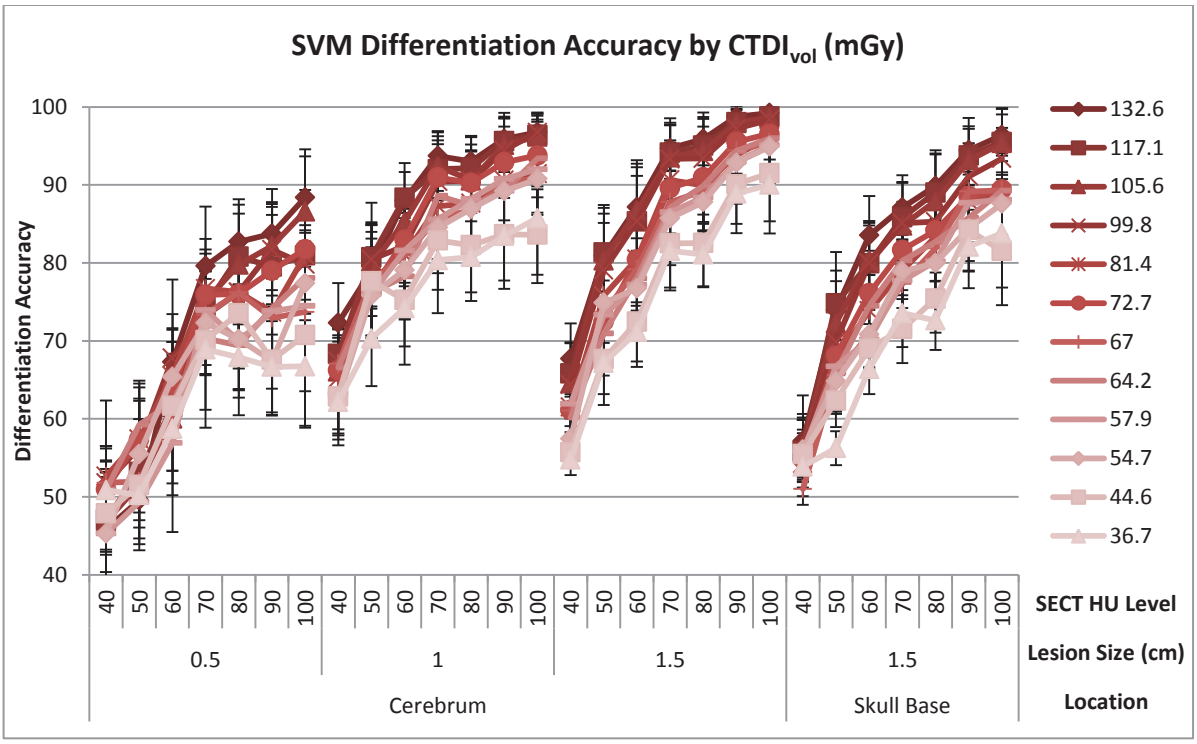

Figure 4.21: Differentiation accuracy using support vector machine method analyzed by $CTDI_{vol}$. Displayed values represent mean of accuracy across the three studies and additional protocol variations: image thickness and reconstruction filter. Error bars represent one SD for each distribution.

Accuracy results graphed by image thickness (mm), revealed increasing SVM differentiation accuracy with increasing image thickness (Figure 4.22). In this case, error bars represent variation across $CTDI_{vol}$, reconstruction filter and study. Again, the effect of increased image thickness on differentiation accuracy was more pronounced at higher matched model pair SECT attenuation (HU) levels.

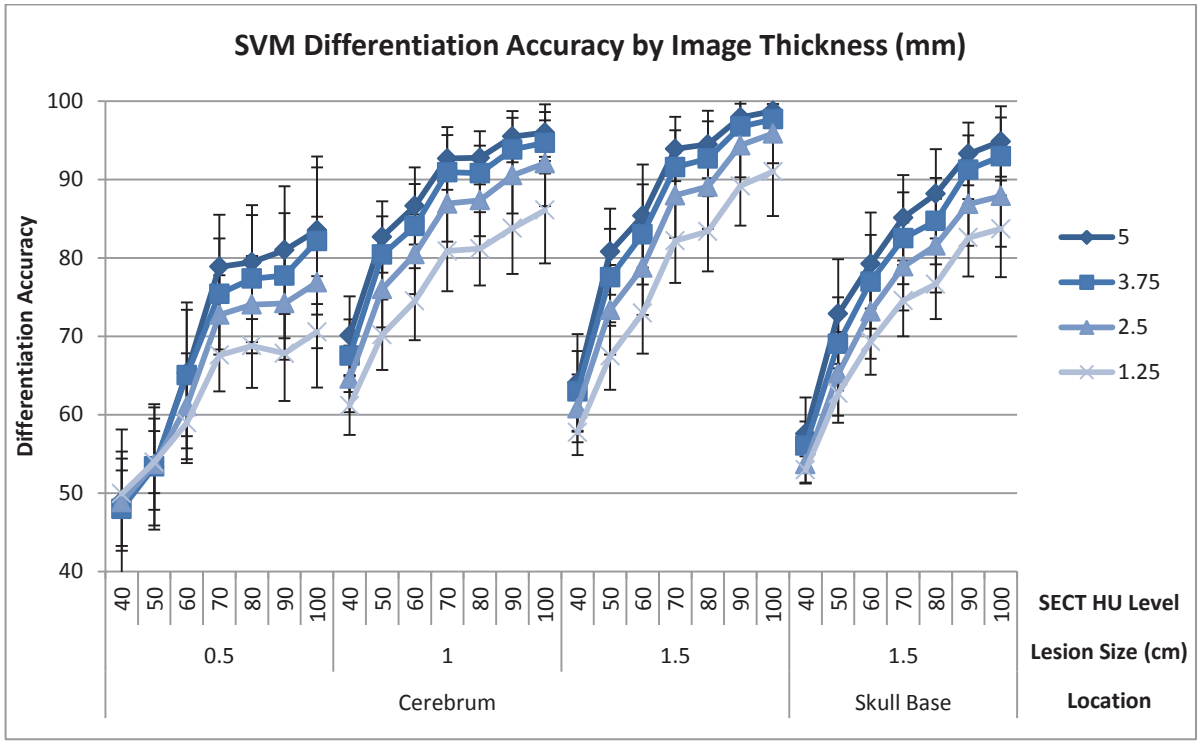

Figure 4.22: Differentiation accuracy using support vector machine method analyzed by image thickness. Displayed values represent mean of accuracy across the three studies and additional protocol variations: $CTDI_{vol}$ and reconstruction filter. Error bars represent one SD for each distribution.

Accuracy results graphed by reconstruction filter showed no effect of filter selection on SVM differentiation accuracy (Figure 4.23). Error bars represent variation across $CTDI_{vol}$, image thickness and study and show considerable overlap between the reconstruction filter types. Based on these results, further analysis and visualization of support vector machine data was limited to Standard filter to facilitate viewing of the multi-dimensional data gathered in this study.

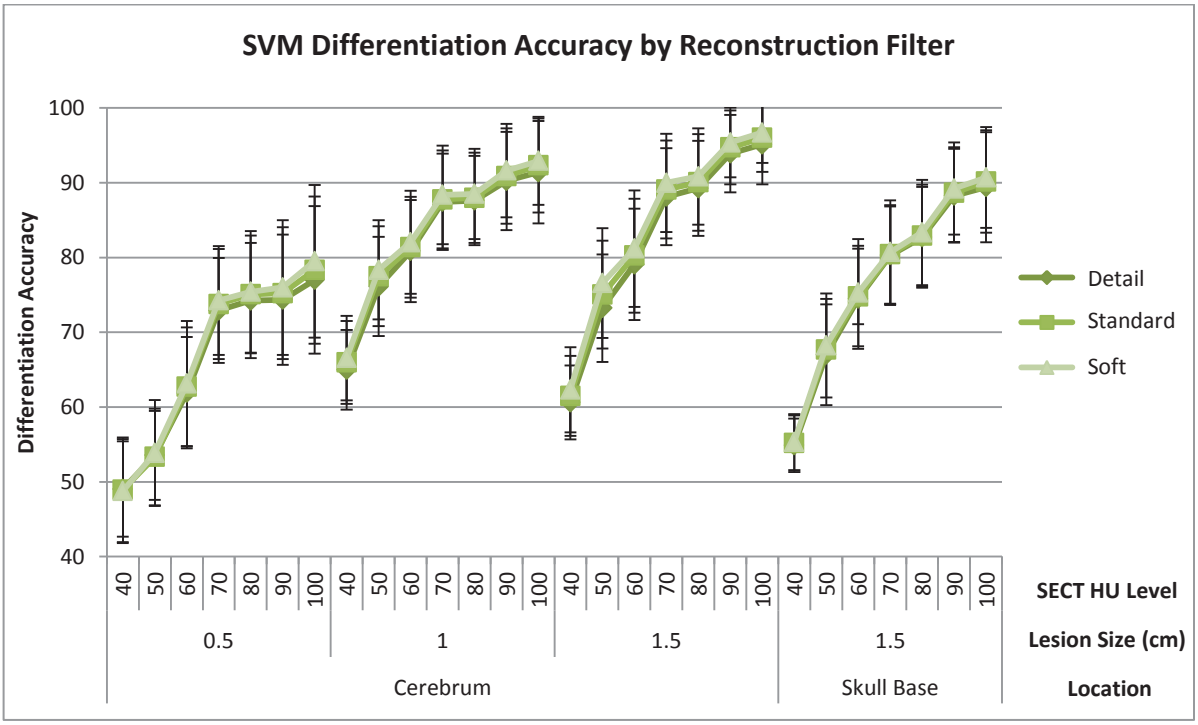

Figure 4.23: Differentiation accuracy using support vector machine method analyzed by reconstruction filter. Displayed values represent mean of accuracy across the three studies and additional protocol variations: $CTDI_{vol}$ and image thickness. Error bars represent one SD for each distribution.

Surface plots for the SVM differentiation accuracy based on attenuation (HU) level of the matched model pair and the $CTDI_{vol}$ of the acquisition were created for all lesion sizes and locations (Figure 4.24, Figure 4.25). Data for all image thickness values investigated are shown; all data shown are based on a Standard reconstruction filter. A transparent gray plane was included to show 90% differentiation accuracy. The array of plots shows the effect of these lesion (size and location) and acquisition parameters on the final SVM differentiation accuracy. Increasing $CTDI_{vol}$, attenuation (HU) level of the matched model pair, image thickness and lesion size all resulted in increased SVM differentiation accuracy.

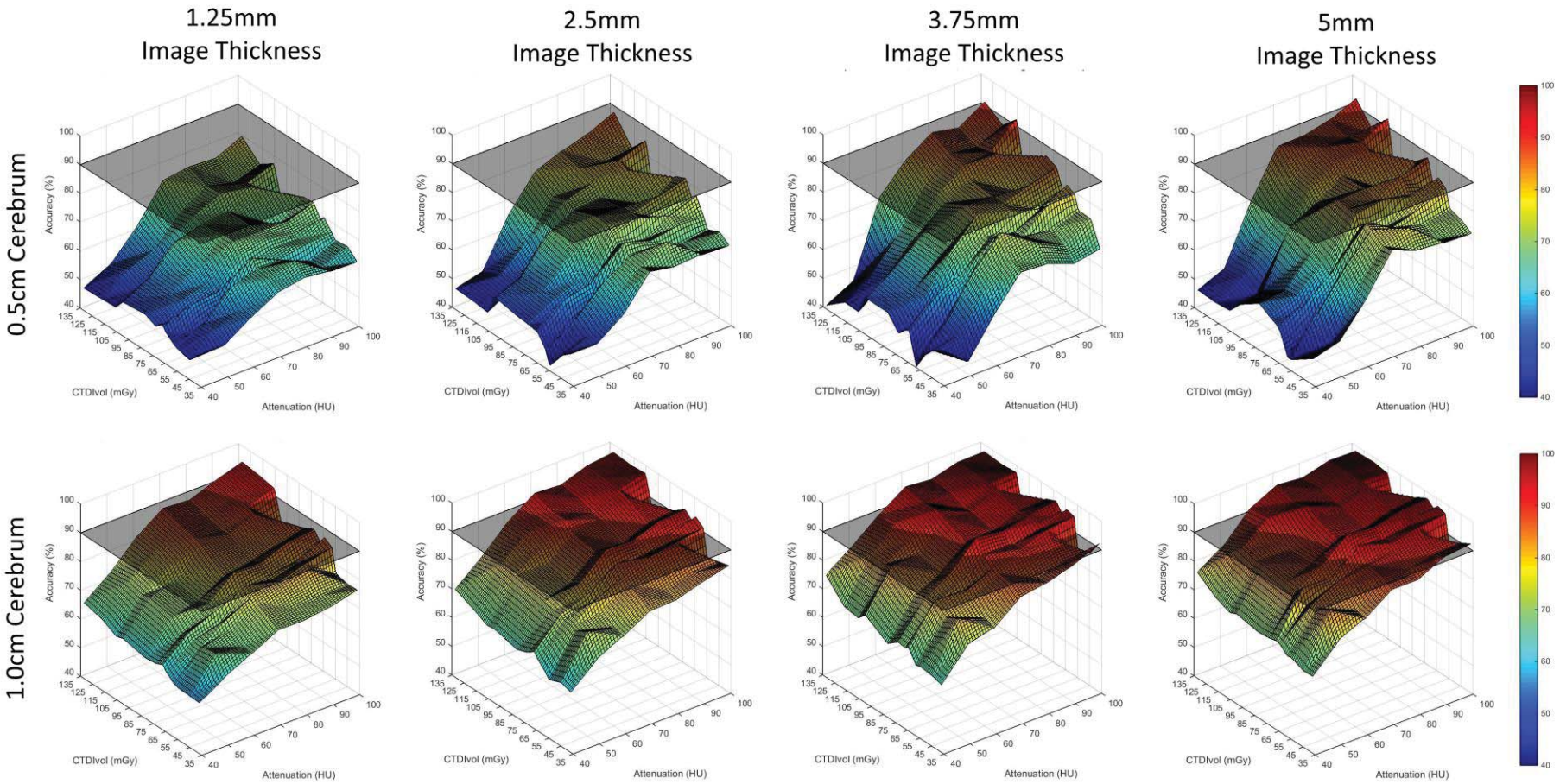

Figure 4.24: Surface plots for SVM differentiation accuracy (z-axis) for 0.5 cm and 1.0 cm cerebrum matched model pairs based on the attenuation (HU) of the lesion pair (x-axis, right) and the $CTDI_{vol}$ of the acquisition (y-axis, left) for all image thicknesses. Standard filter used for all visualizations. Color bar provided to assist in visualization of higher accuracy results (warmer colors correspond with higher accuracies). The gray plane is fixed at 90% differentiation accuracy.

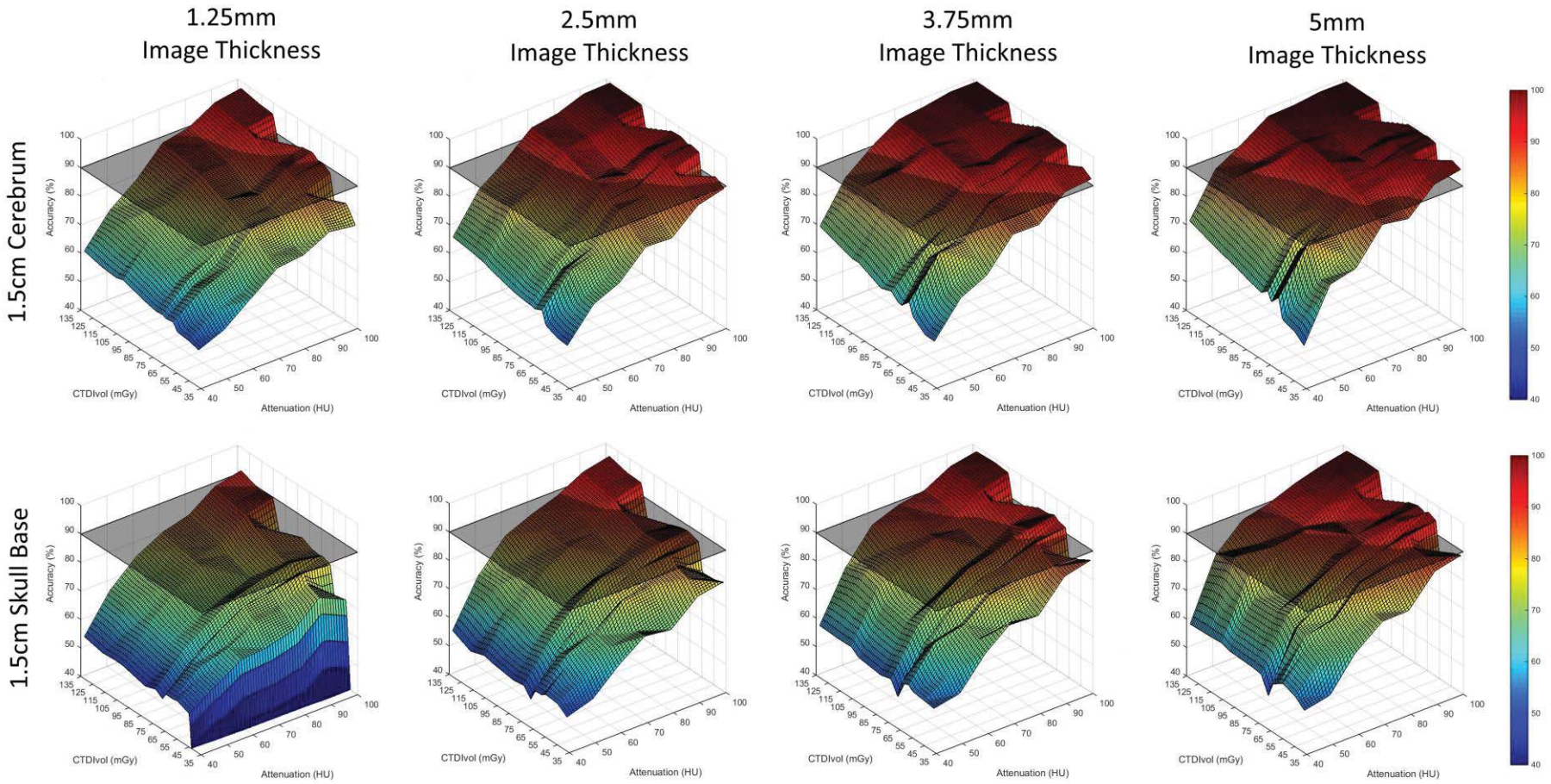

Figure 4.25: Surface plots for SVM differentiation accuracy (z-axis) for 1.5 cm cerebrum and 1.5 cm skull base matched model pairs based on the attenuation (HU) of the lesion pair (x-axis, right) and the $CTDI_{vol}$ of the acquisition (y-axis, left) for all image thicknesses. Standard filter used for all visualizations. Color bar provided to assist in visualization of higher accuracy results (warmer colors correspond with higher accuracies). The gray plane is fixed at 90% differentiation accuracy.

Based on a second order power fit of available data from studies 1-3, the $CTDI_{vol}$ (mGy) to ensure 90% SVM differentiation accuracy for a given matched model pair attenuation (HU) was calculated. The results of this calculation for all available SECT attenuation (HU) levels and image thicknesses are shown in Table 4.12. Given that reconstruction filter was found to have no effect on differentiation accuracy, the results were limited to the standard filter to facilitate visualization of the data.

Curve fits of 90-100 HU 1 cm lesions in the cerebrum estimating dose necessary for 90% SVM differentiation accuracy resulted in $CTDI_{vol}$ values below the minimum investigated level using 3.75 or 5 mm thick images. This implies that all dose levels investigated would result in 90% differentiation accuracy using SVM method and 3.75-5 mm thick images. This was also the case for 1.5 cm cerebrum lesions of 90-100 HU acquired with 3.75 or 5 mm thick images. With the exception of 100 HU lesions acquired with 3.75-5 mm thick images, none of the 0.5 cm cerebrum lesions were differentiated with greater than 90% accuracy for any of the $CTDI_{vol}$ levels currently available for use on the DECT scanner.

In addition, a second order power fit of available data from studies 1-3 was used to calculate the attenuation (HU) to ensure 90% SVM differentiation accuracy assuming a specific $CTDI_{vol}$ (mGy) value. The results of this calculation for all available $CTDI_{vol}$ values and image thicknesses are shown in Table 4.13. Given that reconstruction filter was found to have no effect on differentiation accuracy, the results were limited to the standard filter to facilitate visualization of the data. In general, the curve fit for 0.5 cm cerebrum lesions resulted in attenuation values above 100 HU for most $CTDI_{vol}$ and image thickness combinations. This implies that investigation of 0.5 cm cerebrum lesions using these methods would not provide additional information beyond that already available using SECT. Curve fits for 1.5 cm cerebrum lesions resulted in attenuation values under 100 HU using all $CTDI_{vol}$ values investigated using either 3.75 or 5 mm image thickness. In general, the HU value to ensure 90% differentiation accuracy decreased with both increasing image

thickness and $CTDI_{vol}$, as expected. A graphical representation of these data is shown in Figure 4.26 with the shaded region representing lesion attenuations already differentiable using conventional SECT. The un-shaded region, therefore, represents previously un-differentiable lesion attenuations now differentiable with high accuracy using various DECT imaging techniques.

Table 4.12: $CTDI_{vol}$ (mGy) necessary for 90% SVM differentiation accuracy by HU of matched model pair based on a second order power fit of available data from studies 1-3. Areas in gray indicate 90% SVM differentiation accuracy was not possible at any dose level investigated. Areas in green indicate 90% SVM differentiation accuracy was achieved at all dose levels investigated (minimum dose investigated shown). Remaining areas in white indicate 90% SVM differentiation accuracy was reached within the investigated dose range and show the minimum $CTDI_{vol}$ required for this level of accuracy. Values in red indicate a fit with an R^2 value of less than 0.8.

	Recon Filter	STANDARD															
	Lesion	0.5 cm Cerebrum				1.0 cm Cerebrum				1.5 cm Cerebrum				1.5 cm Skull Base			
	Img Thk (mm)	1.25	2.5	3.75	5	1.25	2.5	3.75	5	1.25	2.5	3.75	5	1.25	2.5	3.75	5
SECT HU Level of Matched Model Pair	40																
	50																
	60								107.6			118.2	99.9				
	70						95.1	64.5	51.2		81.3	60.8	47.9			129.2	112.8
	80						92.2	60.4	47.4	125	72.9	53.9	46.2			112.5	75.9
	90					115.3	65.7	46.6	36.7	78.4	46.6	36.7	36.7		92.9	64.3	48.7
	100			123.9	125.3	91.4	56.8	38.4	36.7	66.5	40.1	36.7	36.7		83.0	54.5	44.1

**Note: Values represent $CTDI_{vol}$ in units of mGy.

Table 4.13: Lesion attenuation (HU) necessary for 90% SVM differentiation accuracy by acquisition parameters based on a second order power fit of available data from studies 1-3. Areas in gray indicate 90% SVM differentiation accuracy was not possible under 100 HU. Attenuation (HU) values in red indicate a fit with an R^2 values less than 0.8.

	Recon Filter	STANDARD															
	Lesion	0.5 cm Cerebrum				1.0 cm Cerebrum				1.5 cm Cerebrum				1.5 cm Skull Base			
	Img Thk (mm)	1.25	2.5	3.75	5	1.25	2.5	3.75	5	1.25	2.5	3.75	5	1.25	2.5	3.75	5
$CTDI_{vol}$ (mGy)	36.7							96	89			93	84				
	44.6										97	86	80				
	54.7								83			82	69				
	57.9						90	73	65		83	76	67			93	86
	64.2						90	74	68	98	81	72	68			93	82
	67						95	78	66	99	80	71	66			90	82
	72.7						77	66	60	94	77	69	64			87	76
	81.4						94	73	65	96	77	67	62			92	81
	99.8						91	69	61		73	60	55				90
	105.6			96	92	91	70	61	59	81	65	58	54		85	74	66
	117.1					87	67	59	55	79	65	59	54		83	72	65
	132.6			92	89	81	67	61	58	76	64	57	54	93	77	69	64

**Note: Values represent SECT attenuation in units of HU.

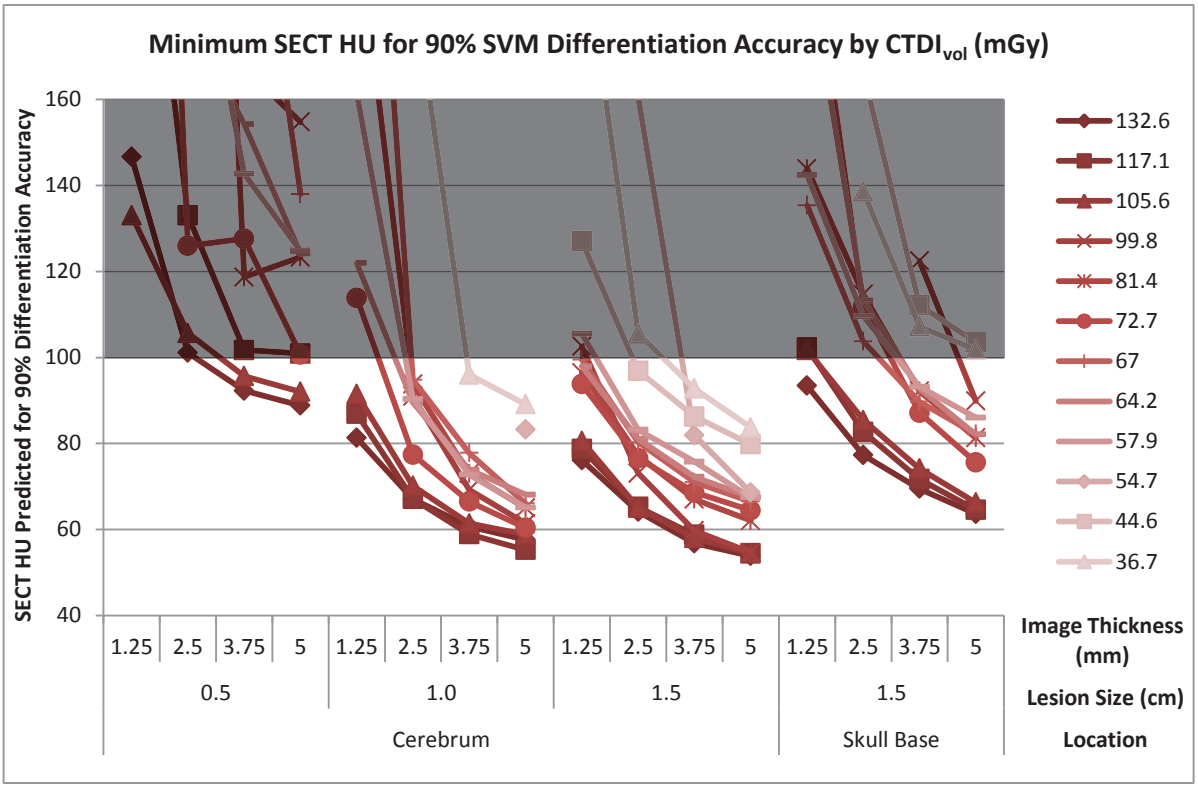

Figure 4.26: Graphical representation of lesion attenuation (HU) necessary for 90% SVM differentiation accuracy by acquisition parameters (Table 4.13). The un-shaded region represents $CTDI_{vol}$ and image thickness values allow 90% differentiation accuracy under the current clinical limit of 100 HU imposed by SECT.

4.2.5.4 Geometric Bisector (GB) Analysis

By averaging over all three studies and all imaging techniques investigated, the effect of lesion size and location on GB differentiation accuracy can be easily seen (Figure 4.27). Error bars represent one standard deviation within each distribution. Differentiation accuracy under 80% is shaded in dark gray while differentiation accuracy between 80% and 90% is shaded in light gray. Averaged over all imaging protocols investigated, the maximum average accuracy at 100 HU was 77%, 92% and 95% for the 0.5 cm cerebrum, 1.0 cm cerebrum and 1.5 cm cerebrum matched model pairs respectively. The maximum average accuracy at 100 HU was 91% for the 1.5 cm skull base matched model pair,

reflecting the more challenging imaging environment of the skull base. The average differentiation accuracies predicted for 100 HU lesions for SVM (Figure 4.20) and GB analyses were within 1%, potentially indicating a high degree of correlation between the methods.

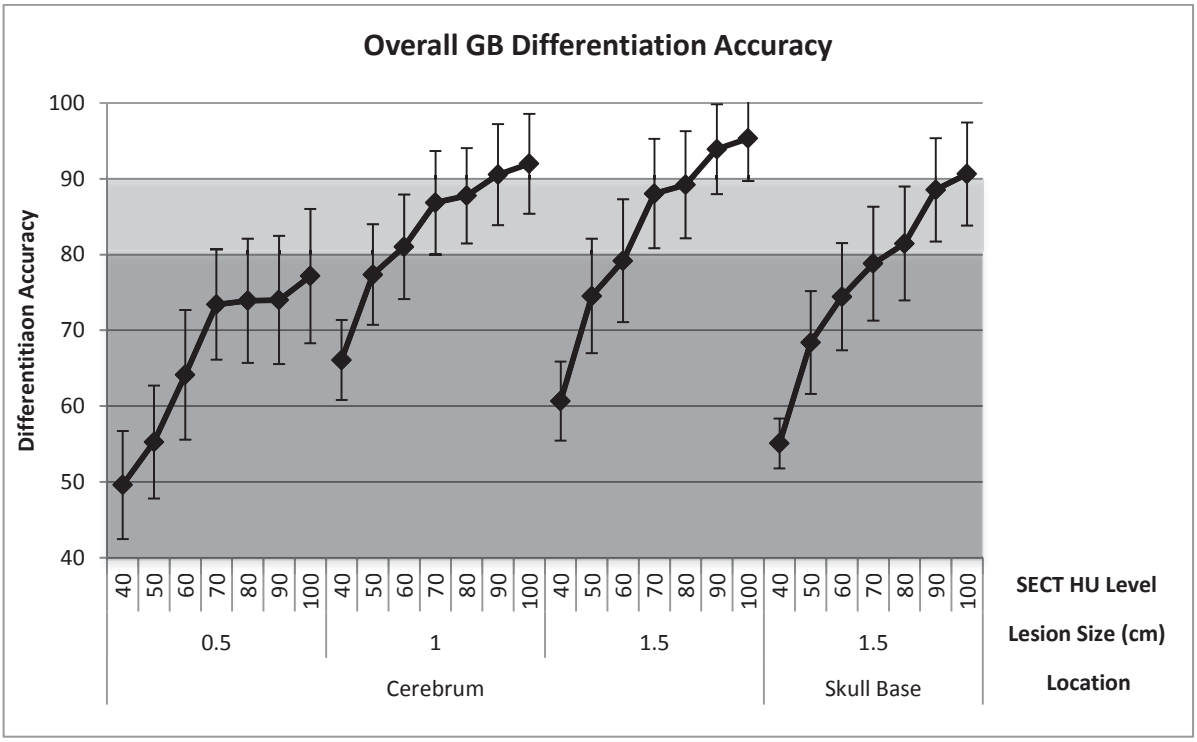

Figure 4.27: Differentiation accuracy using geometric bisector method. Displayed values represent mean of accuracy across the three studies and all protocol variations: $CTDI_{vol}$, image thickness and reconstruction filter. Error bars represent one SD of the distribution.

Accuracy results were then graphed by relevant protocol factors including $CTDI_{vol}$, image thickness and reconstruction filter. In all graphs, darker colored lines were used to indicate an increase in protocol value; be it an increase in dose level, image thickness, or perceived noise. Accuracy results graphed by $CTDI_{vol}$ (mGy), revealed increasing GB differentiation accuracy with increasing dose level (Figure 4.28). Note that error bars represent variation across image thickness, reconstruction filter and study. The effect of

dose on differentiation accuracy was more pronounced at higher matched model pair SECT attenuation (HU) levels.

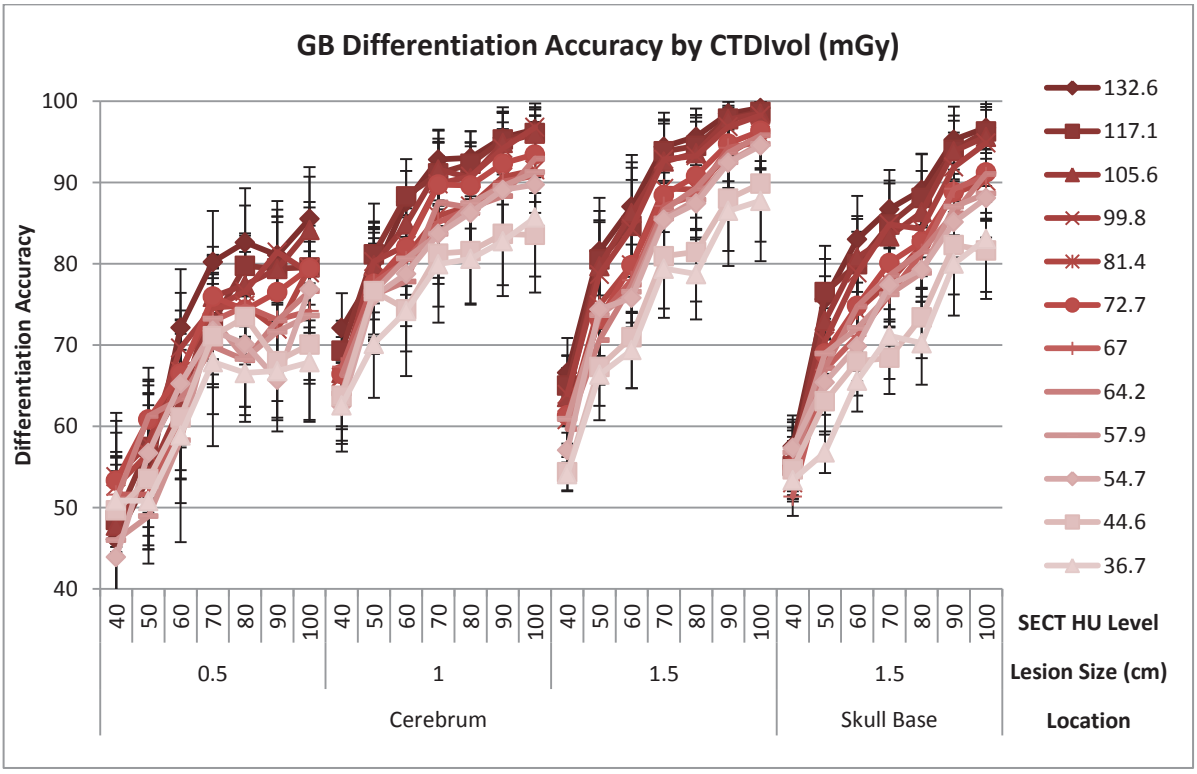

Figure 4.28: Differentiation accuracy using geometric bisector method analyzed by $CTDI_{vol}$. Displayed values represent mean of accuracy across the three studies and additional protocol variations: image thickness and reconstruction filter. Error bars represent one SD for each distribution.

Accuracy results graphed by image thickness (mm), revealed increasing GB differentiation accuracy with increasing image thickness (Figure 4.29). In this case, error bars represent variation across $CTDI_{vol}$, reconstruction filter and study. Again, the effect of increased image thickness on differentiation accuracy was more pronounced at higher matched model pair SECT attenuation (HU) levels.

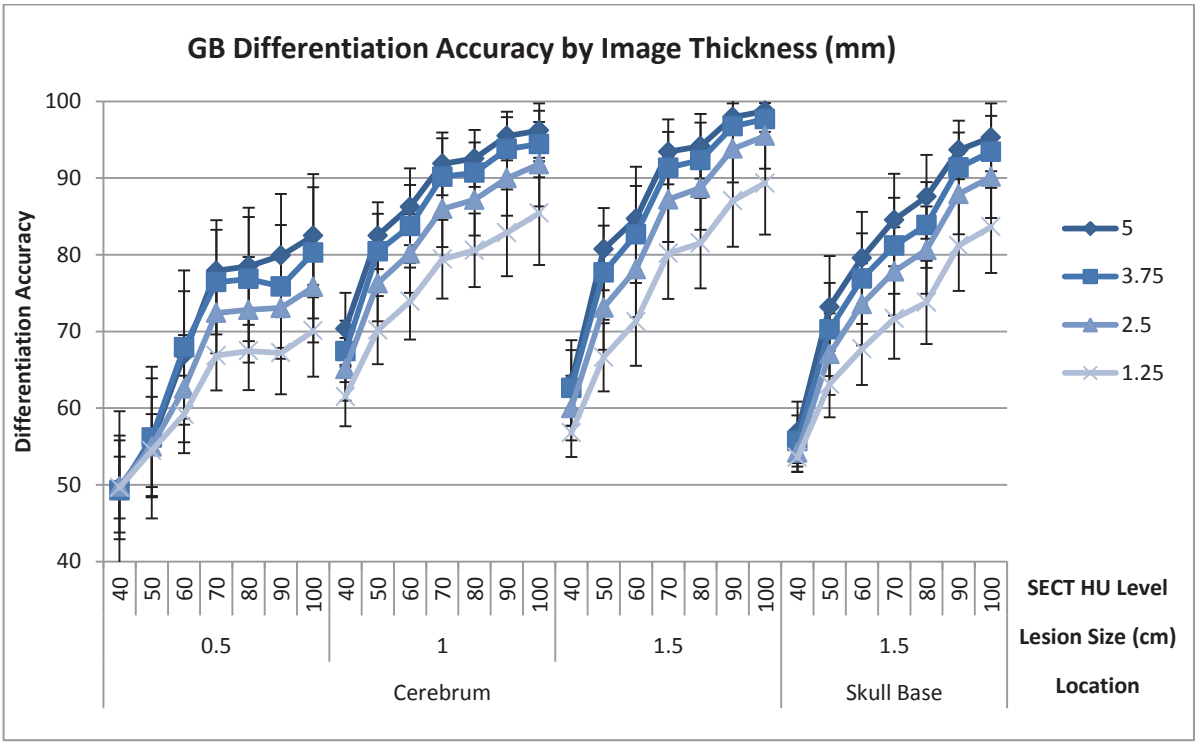

Figure 4.29: Differentiation accuracy using geometric bisector method analyzed by image thickness. Displayed values represent mean of accuracy across the three studies and additional protocol variations: $CTDI_{vol}$ and reconstruction filter. Error bars represent one SD for each distribution.

Accuracy results graphed by reconstruction filter showed no effect of filter selection on GB differentiation accuracy (Figure 4.30). Error bars represent variation across $CTDI_{vol}$, image thickness and study and show considerable overlap between the reconstruction filter types. Based on these results, further analysis and visualization of geometric bisector data was limited to Standard filter to facilitate viewing of the multi-dimensional data gathered in this study.

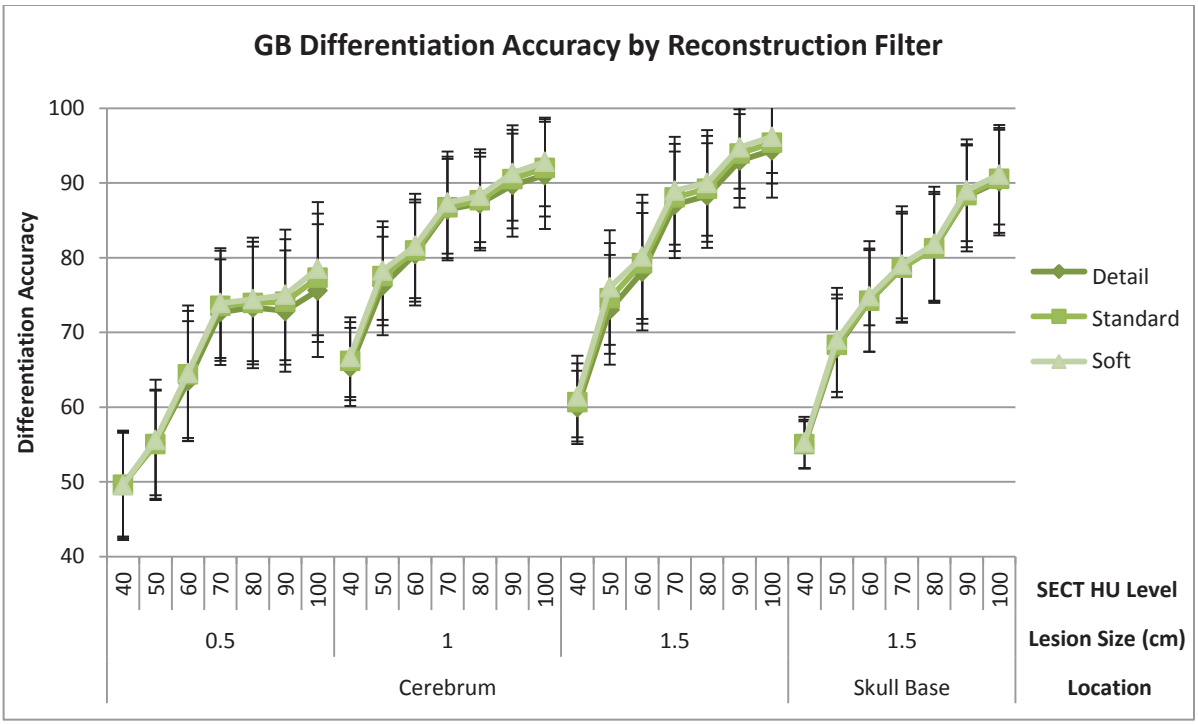

Figure 4.30: Differentiation accuracy using geometric bisector method analyzed by reconstruction filter. Displayed values represent mean of accuracy across the three studies and additional protocol variations: $CTDI_{vol}$ and image thickness. Error bars represent one SD for each distribution.

Surface plots for the GB differentiation accuracy based on attenuation (HU) level of the matched model pair and the $CTDI_{vol}$ of the acquisition were created for all lesion sizes and locations (Figure 4.31, Figure 4.32). Data for all image thickness values investigated are shown; all data shown are based on a Standard reconstruction filter. A transparent gray plane was included to show 90% differentiation accuracy. The array of plots shows the effect of these lesion (size and location) and acquisition parameters on the final GB differentiation accuracy. Increasing $CTDI_{vol}$, attenuation (HU) level of the matched model pair, image thickness and lesion size all result in increased GB differentiation accuracy.

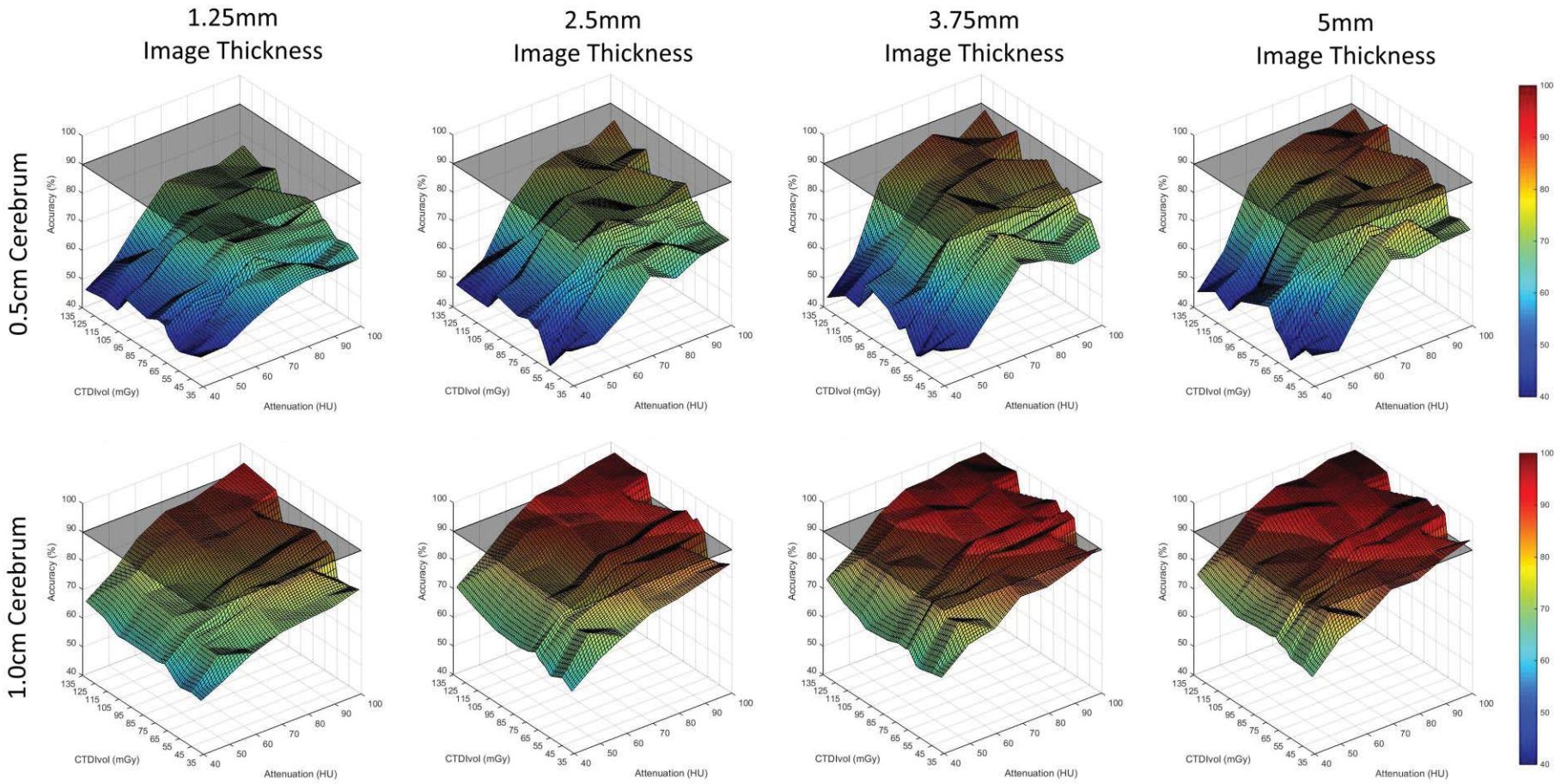

Figure 4.31: Surface plots for GB differentiation accuracy (z-axis) for 0.5 cm and 1.0 cm cerebrum matched model pairs based on the attenuation (HU) of the lesion pair (x-axis, right) and the $CTDI_{vol}$ of the acquisition (y-axis, left) for all image thicknesses. Standard filter used for all visualizations. Color bar provided to assist in visualization of higher accuracy results (warmer colors correspond with higher accuracies). The gray plane is fixed at 90% differentiation accuracy.

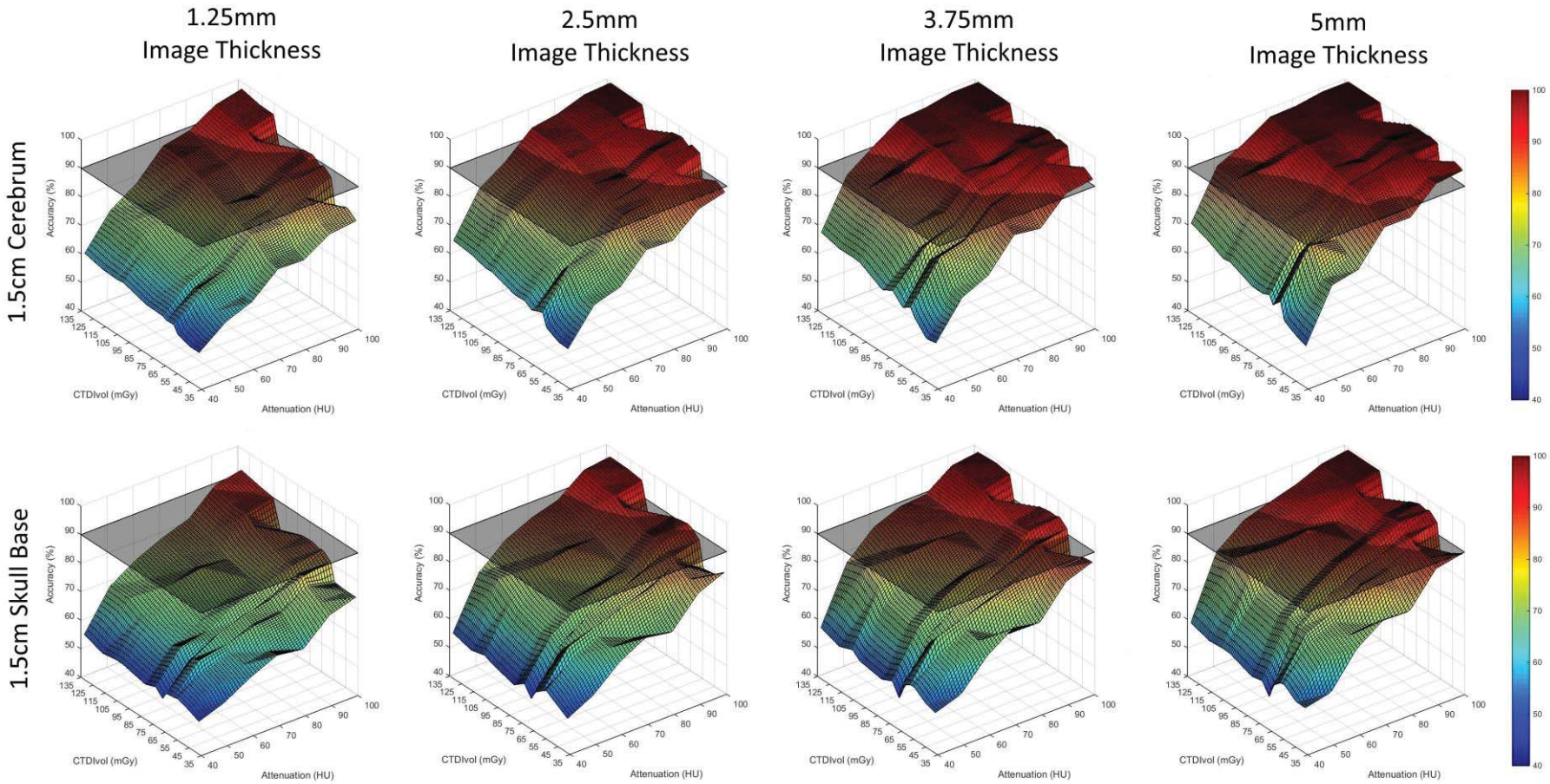

Figure 4.32: Surface plots for GB differentiation accuracy (z-axis) for 1.5 cm cerebrum and 1.5 cm skull base matched model pairs based on the attenuation (HU) of the lesion pair (x-axis, right) and the $CTDI_{vol}$ of the acquisition (y-axis, left) for all image thicknesses. Standard filter used for all visualizations. Color bar provided to assist in visualization of higher accuracy results (warmer colors correspond with higher accuracies). The gray plane is fixed at 90% differentiation accuracy.

Based on a second order power fit of available data from studies 1-3, the $CTDI_{vol}$ (mGy) to ensure 90% GB differentiation accuracy for a given matched model pair attenuation (HU) was calculated. The results of this calculation for all available SECT attenuation (HU) levels and image thicknesses are shown in Table 4.14. Given that reconstruction filter was found to have no effect on differentiation accuracy, the results were limited to the standard filter to facilitate visualization of the data.

Curve fits for 100 HU 1 cm lesions in the cerebrum estimating dose necessary for 90% GB differentiation accuracy resulted in $CTDI_{vol}$ values below the minimum investigated level when using 5 mm image thickness. This implies that all dose levels investigated would result in 90% differentiation accuracy using the GB method and 5 mm-thick images. This was also the case for 1.5 cm cerebrum lesions of 90 to 100 HU acquired with 3.75 or 5 mm-thick images. None of the 0.5 cm cerebrum lesions were differentiated with greater than 90% accuracy for any of the $CTDI_{vol}$ levels currently available for use on the DECT scanner.

In addition, a second order power fit of available data from studies 1-3 was used to calculate the attenuation (HU) to ensure 90% GB differentiation accuracy assuming a specific $CTDI_{vol}$ (mGy) value. The results of this calculation for all available $CTDI_{vol}$ values and image thicknesses are shown in Table 4.15. Given that reconstruction filter was found to have no effect on differentiation accuracy, the results were limited to the standard filter to facilitate visualization of the data.

With the possible exception of 105.6 and 132.6 mGy acquisitions reconstructed at 5 mm image thickness, curve fits for 0.5 cm cerebrum lesions resulted in attenuation values above 100 HU for all $CTDI_{vol}$ and image thickness combinations. This implies that investigation of 0.5 cm cerebrum lesions using these methods would not provide additional information beyond that already available using SECT. Curve fits for 1.5 cm cerebrum lesions resulted in attenuation values under 100 HU using all $CTDI_{vol}$ values investigated

using either 3.75 or 5 mm image thickness. In general, the HU value to ensure 90% differentiation accuracy decreased with both increasing image thickness and $CTDI_{vol}$, as expected. A graphical representation of these data is shown in Figure 4.33 with the shaded region representing lesion attenuations already differentiable using conventional SECT. The un-shaded region, therefore, represents previously un-differentiable lesion attenuations now differentiable with high accuracy using various DECT imaging techniques.

Table 4.14: $CTDI_{vol}$ (mGy) necessary for 90% GB differentiation accuracy by HU of matched model pair based on a second order power fit of available data from studies 1-3. Areas in gray indicate 90% GB differentiation accuracy was not possible at any dose level investigated. Areas in green indicate 90% GB differentiation accuracy was achieved at all dose levels investigated (minimum dose investigated shown). Remaining areas in white indicate 90% GB differentiation accuracy was reached within the investigated dose range and show the minimum $CTDI_{vol}$ required for this level of accuracy. Values in red indicate a fit with an R^2 value of less than 0.8.

	Recon Filter	STANDARD															
	Lesion	0.5 cm Cerebrum				1.0 cm Cerebrum				1.5 cm Cerebrum				1.5 cm Skull Base			
	Img Thk (mm)	1.25	2.5	3.75	5	1.25	2.5	3.75	5	1.25	2.5	3.75	5	1.25	2.5	3.75	5
SECT HU Level of Matched Model Pair	40																
	50																
	60								111.8			121.7	104.2				
	70						104.2	71.5	57.1		87.6	63.1	49.7				111.9
	80						93.6	62.1	49.9		74.5	54.6	46.2			129.4	82.1
	90					123.4	70.8	48.0	37.8	86.9	49.5	36.7	36.7	128.2	85.5	62.9	47.5
	100					96.5	58.9	41.9	36.7	71.3	42.5	36.7	36.7	111.1	70.6	51.7	43

**Note: Values represent $CTDI_{vol}$ in units of mGy.

Table 4.15: Lesion attenuation (HU) necessary for 90% GB differentiation accuracy by acquisition parameters based on a second order power fit of available data from studies 1-3. Areas in gray indicate 90% GB differentiation accuracy was not possible under 100 HU. Attenuation (HU) values in red indicate a fit with an R^2 values less than 0.8.

	Recon Filter	STANDARD															
	Lesion	0.5 cm Cerebrum				1.0 cm Cerebrum				1.5 cm Cerebrum				1.5 cm Skull Base			
	Img Thk (mm)	1.25	2.5	3.75	5	1.25	2.5	3.75	5	1.25	2.5	3.75	5	1.25	2.5	3.75	5
$CTDI_{vol}$ (mGy)	36.7								88			93	84				
	44.6											86	80				
	54.7											83	73				
	57.9							75	68		85	76	68			95	87
	64.2						93	75	70		83	72	68			91	83
	67						96	79	67		82	71	67		99	90	81
	72.7						80	67	61	97	79	69	64		99	88	76
	81.4						97	73	67	100	79	68	64			91	81
	99.8							68	63		75	60	57				87
	105.6				95	96	71	62	61	82	66	58	56		84	75	67
	117.1					91	67	59	56	80	66	60	56		81	71	64
	132.6				97	84	68	62	58	78	64	56	53	94	77	69	63

**Note: Values represent SECT attenuation in units of HU.

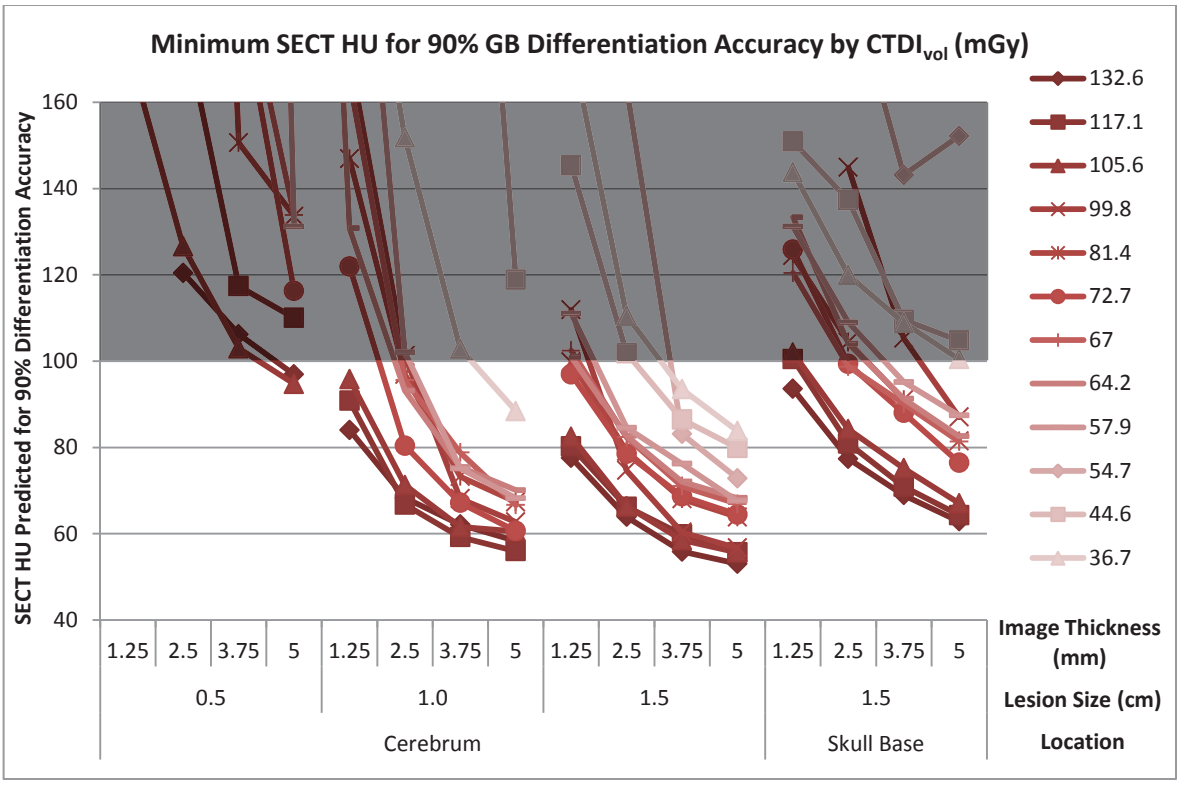

Figure 4.33: Graphical representation of lesion attenuation (HU) necessary for 90% GB differentiation accuracy by acquisition parameters (Table 4.15). The un-shaded region represents $CTDI_{vol}$ and image thickness values allow 90% differentiation accuracy under the current clinical limit of 100 HU imposed by SECT.

4.2.5.5 Generalized Geometric Bisector (GGB) Solution

The results of the parameter-specific geometric bisector planes can be seen in Table 4.16. The major sources of variability identified were the 0.5 cm cerebrum lesions and 1.5 cm skull base lesions. All other accuracy differences were less than 2%. Plane coefficients were remarkably stable across parameter-specific solutions. The equations for the three generalized geometric bisector plane solutions can be found in Table 4.17.

Table 4.16: Results of parameter-specific geometric bisector plane calculations. Both raw accuracy and accuracy difference (relative to all data solution) are shown. Plane coefficients follow the equation form Ax+By+Cz+D = 0, where x is water density, y is calcium density and z is measured attenuation (HU) at 68 keV. Those parameters identified as major sources of variability based on their accuracy difference are shown in red. Note: Location (Skull Base) and Lesion Model (1.5 cm Skull Base) represent identical analysis because only 1.5 cm lesions were evaluated in the skull base.

		Plane Equation Coefficients					
Parameter	**Value**	**A**	**B**	**C**	**D**	**Accuracy**	**Accuracy Difference**
Lesion Model	**0.5 cm Cerebrum**	-0.93	0.37	0.03	939.94	69.82	-5.74
Location	**Skull Base**	-0.94	0.33	-0.07	950.47	73.31	-2.26
Lesion Model	**1.5 cm Skull Base**	-0.94	0.33	-0.07	950.47	73.31	-2.26
$CTDI_{vol}$	**44.6**	-0.94	0.34	-0.06	949.74	74.04	-1.53
Rotation	**0.5**	-0.94	0.33	-0.08	952.76	74.24	-1.32
$CTDI_{vol}$	**81.4**	-0.94	0.32	-0.10	955.18	74.43	-1.14
Location	**Cerebrum**	-0.94	0.33	-0.07	955.73	75.07	-0.50
Lesion Model	**1.0 cm Cerebrum**	-0.94	0.34	-0.05	952.84	75.11	-0.46
Lesion Model	**1.5 cm Cerebrum**	-0.94	0.33	-0.08	957.56	75.24	-0.33
$CTDI_{vol}$	**36.7**	-0.94	0.34	-0.05	951.76	75.38	-0.19
$CTDI_{vol}$	**57.9**	-0.94	0.33	-0.06	954.30	75.42	-0.15
$CTDI_{vol}$	**54.7**	-0.94	0.34	-0.06	952.51	75.48	-0.09
Filter	**Detail**	-0.94	0.34	-0.06	953.13	75.49	-0.07
Image Thickness	**1.25**	-0.94	0.33	-0.06	953.41	75.52	-0.05
$CTDI_{vol}$	**117.1**	-0.94	0.32	-0.09	956.48	75.52	-0.05
$CTDI_{vol}$	**64.2**	-0.94	0.33	-0.08	954.84	75.52	-0.05
Rotation	**0.7**	-0.94	0.33	-0.07	954.83	75.53	-0.04
Rotation	**0.6**	-0.94	0.33	-0.07	953.87	75.54	-0.03
$CTDI_{vol}$	**105.6**	-0.94	0.32	-0.10	958.35	75.56	-0.01
Image Thickness	**2.5**	-0.94	0.33	-0.08	955.71	75.56	-0.01
$CTDI_{vol}$	**99.8**	-0.94	0.33	-0.08	955.09	75.57	0.00
All Data	**All Data**	**-0.94**	**0.33**	**-0.08**	**955.18**	**75.57**	**0.00**
Filter	**Soft**	-0.94	0.32	-0.09	956.78	75.57	0.00
Filter	**Standard**	-0.94	0.33	-0.08	955.43	75.57	0.00
$CTDI_{vol}$	**67**	-0.94	0.33	-0.09	957.28	75.59	0.02
Image Thickness	**5**	-0.94	0.32	-0.11	957.92	75.60	0.03
Image Thickness	**3.75**	-0.94	0.32	-0.10	957.52	75.60	0.03
Rotation	**0.8**	-0.94	0.33	-0.08	956.11	75.64	0.08
Rotation	**0.9**	-0.94	0.32	-0.10	957.71	75.66	0.09
$CTDI_{vol}$	**72.7**	-0.94	0.33	-0.09	956.81	75.66	0.09
$CTDI_{vol}$	**132.6**	-0.94	0.32	-0.11	958.48	75.67	0.10

Table 4.17: Generalized geometric bisector plane results assuming prior knowledge of lesion location and size. Plane coefficients follow the equation form Ax+By+Cz+D = 0, where x is water density, y is calcium density and z is measured attenuation (HU) at 68 keV.

	Plane Equation Coefficients			
Lesion Population	**A**	**B**	**C**	**D**
Cerebrum Lesions ≤ 0.5 cm diameter	-0.93	0.37	0.03	939.94
Cerebrum Lesions > 0.5 cm diameter	-0.94	0.33	-0.07	956.15
Skull Base Lesions	-0.94	0.33	-0.07	950.47

4.2.5.6 Inter-Method Correlation

Inter-method correlation of geometric bisector and support vector machine resulted in a CV correlation of 2.6% and R^2 linearity of 0.980. Repeated analysis for subsets of the data based on all available parameters yielded one major source of variability based on CV and R^2 cutoff criteria: 0.5 cm Cerebrum matched model pairs (Table 4.18). Bland-Altman and correlation graphs for the full data as well as the 0.5 cm Cerebrum matched model pair data can be seen in Figure 4.34. Removing these data from analysis reduced the overall CV correlation to 1.7% and increased the R^2 linearity to 0.988.

Table 4.18: Sorted results of Bland-Altman analysis for inter-method correlation between SVM and GB methods for subsets of data based on available protocol and lesion parameters. Parameters and values above the double line indicate worse correlation or linearity than the full data set while those below the double line indicate improved correlation or linearity. Text in red indicates a major source of variability based on CV or R^2 cutoff criteria.

CV – Correlation		
Full Data CV	**Criteria**	**Cutoff**
2.61	**150%**	**3.92**
Parameter	**Value**	**CV**
Lesion Model	0.5 cm Cerebrum	4.9
ImageThickness	3.75	2.8
$CTDI_{vol}$	36.7	2.8
Study	3	2.8
$CTDI_{vol}$	54.7	2.8
ImageThickness	5	2.8
$CTDI_{vol}$	105.6	2.8
$CTDI_{vol}$	132.6	2.8
RotationTime	0.9	2.8
$CTDI_{vol}$	72.7	2.67
RotationTime	0.6	2.7
$CTDI_{vol}$	57.9	2.6
RotationTime	0.7	2.6
RotationTime	0.8	2.6
$CTDI_{vol}$	44.6	2.5
$CTDI_{vol}$	99.8	2.5
Study	1	2.5
RotationTime	0.5	2.5
Study	2	2.45
$CTDI_{vol}$	117.1	2.5
$CTDI_{vol}$	81.4	2.5
ImageThickness	2.5	2.4
$CTDI_{vol}$	67	2.3
$CTDI_{vol}$	64.2	2.3
Lesion Model	1.5 cm Skull Base	2.1
ImageThickness	1.25	2.1
Lesion Model	1.0 cm Cerebrum	1.6
Lesion Model	1.5 cm Cerebrum	1.2

Rsquared - Linearity		
Full Data R^2	**Criteria**	
0.9803	**< 0.75**	
Parameter	**Value**	**R^2**
Lesion Model	0.5 cm Cerebrum	0.942
$CTDI_{vol}$	36.7	0.974
ImageThickness	5	0.976
$CTDI_{vol}$	54.7	0.976
$CTDI_{vol}$	132.6	0.977
ImageThickness	3.75	0.977
$CTDI_{vol}$	72.7	0.977
RotationTime	0.9	0.977
$CTDI_{vol}$	105.6	0.978
RotationTime	0.6	0.978
$CTDI_{vol}$	99.8	0.979
Study	3	0.979
$CTDI_{vol}$	81.4	0.980
RotationTime	0.7	0.981
RotationTime	0.5	0.981
Study	1	0.981
$CTDI_{vol}$	44.6	0.981
$CTDI_{vol}$	57.9	0.981
RotationTime	0.8	0.981
Study	2	0.981
ImageThickness	2.5	0.982
$CTDI_{vol}$	117.1	0.982
$CTDI_{vol}$	64.2	0.983
$CTDI_{vol}$	67	0.983
Lesion Model	1.5 cm Skull Base	0.984
ImageThickness	1.25	0.985
Lesion Model	1.0 cm Cerebrum	0.985
Lesion Model	1.5 cm Cerebrum	0.994

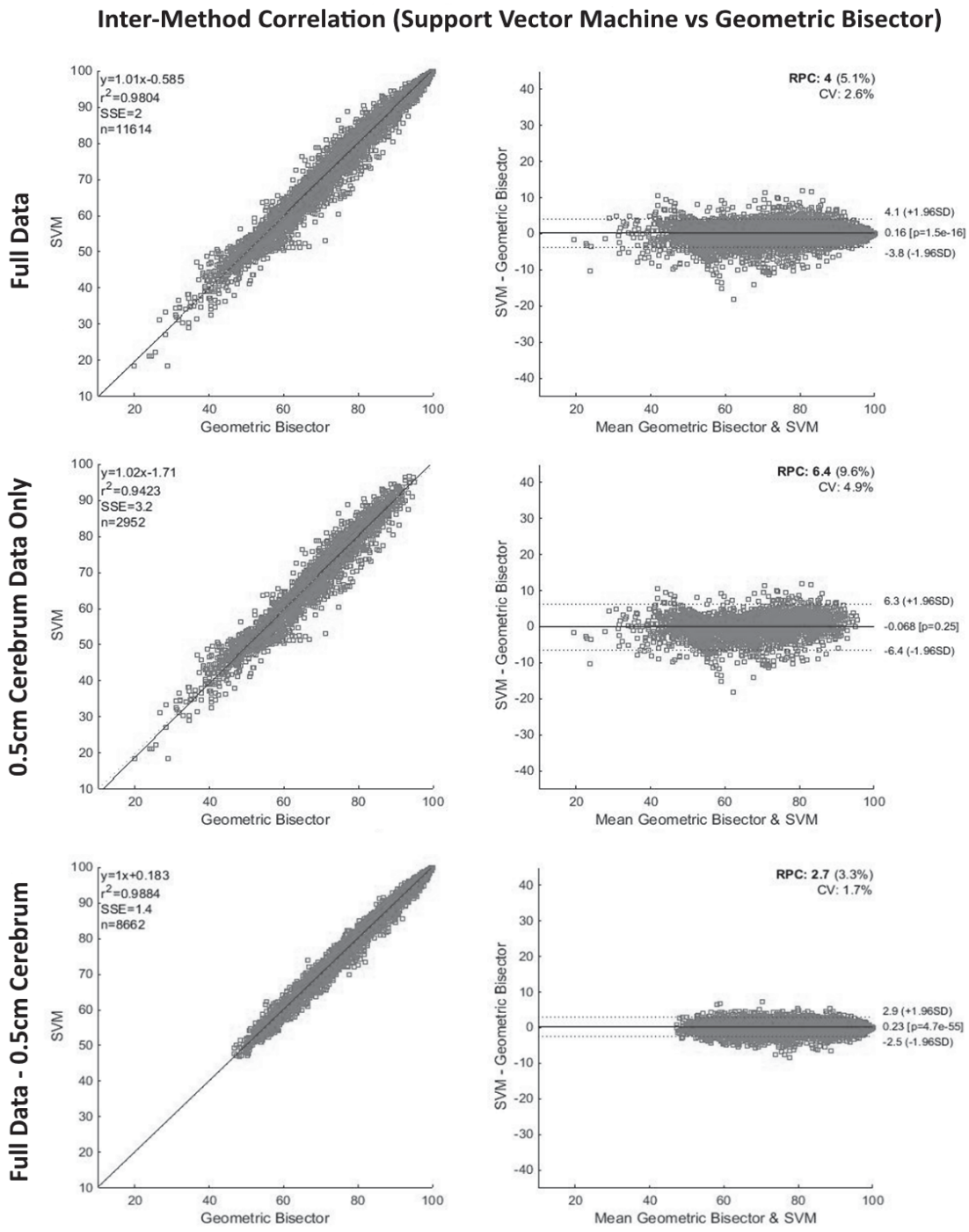

Figure 4.34: Bland-Altman and Correlation graphs for inter-method correlation between SVM and GB methods. Top: Full data results including all protocol variations and lesion models. Middle: Results for 0.5 cm cerebrum matched model pair, identified as a major source of variability in Table 4.18. Bottom: Results for full data excluding 0.5 cm cerebrum matched model pair values.

4.2.6 Inter-Scanner and Intra-Scanner Correlation

4.2.6.1 Inter-Scanner Correlation

Support Vector Machine Inter-Scanner Correlation

Inter-scanner correlation of Study 1 and Study 3 based on support vector machine differentiation accuracy data resulted in a CV correlation of 8.1% and R^2 linearity of 0.824. Repeated analysis for subsets of the data based on all available protocol and lesion parameters yielded three major sources of variability based on CV and R^2 cutoff criteria: 44.6 mGy $CTDI_{vol}$, 0.5 cm Cerebrum matched model pairs and 0.5sec rotation time (Table 4.19). Bland-Altman and correlation graphs for the full data as well as the parameters and values identified as major sources of variability can be seen in Figure 4.35. Removing the data for these major sources of variability from analysis reduced the overall CV correlation to 4.8% and increased the R^2 linearity to 0.908. Note that extreme outliers in the correlation were influenced by all three major sources of variability: 0.5 cm lesion models scanned using 44.6 mGy $CTDI_{vol}$ and a 0.5sec rotation time.

Table 4.19: Sorted results of Bland-Altman analysis of SVM inter-scanner correlation for subsets of data based on available protocol and lesion parameters. Parameters and values above the double line indicate worse correlation or linearity than the full data set while those below the double line indicate improved correlation or linearity. Text in red indicates a major source of variability based on CV or R^2 cutoff criteria.

CV - Correlation		
Full Data CV	Criteria	Cutoff
8.1	150%	12.2

Parameter	Value	CV
$CTDI_{vol}$	44.6	15.2
Lesion Model	0.5 cm Cerebrum	14.9
RotationTime	0.5	12.5
$CTDI_{vol}$	81.4	9.7
ImageThickness	3.75	9.6
$CTDI_{vol}$	54.7	8.5
$CTDI_{vol}$	36.7	8.5
ImageThickness	5	8.4
RotationTime	0.7	7.8
RotationTime	0.6	7.7
$CTDI_{vol}$	57.9	7.6
$CTDI_{vol}$	67	7.3
ImageThickness	2.5	7.3
RotationTime	0.9	7.1
$CTDI_{vol}$	72.7	7.1
$CTDI_{vol}$	99.8	7.0
$CTDI_{vol}$	132.6	7.0
$CTDI_{vol}$	64.2	6.6
ImageThickness	1.25	6.3
RotationTime	0.8	6.3
$CTDI_{vol}$	105.6	5.5
Lesion Model	1.0 cm Cerebrum	5.5
Lesion Model	1.5 cm Skull Base	5.4
$CTDI_{vol}$	117.1	5.1
Lesion Model	1.5 cm Cerebrum	4.1

Rsquared - Linearity	
Full Data R^2	Criteria
0.824	< 0.75

Parameter	Value	R^2
$CTDI_{vol}$	44.6	0.467
Lesion Model	0.5 cm Cerebrum	0.561
RotationTime	0.5	0.596
$CTDI_{vol}$	81.4	0.756
ImageThickness	3.75	0.764
$CTDI_{vol}$	36.7	0.795
ImageThickness	5	0.802
Lesion Model	1.0 cm Cerebrum	0.817
RotationTime	0.7	0.827
$CTDI_{vol}$	54.7	0.833
$CTDI_{vol}$	67	0.840
RotationTime	0.6	0.843
$CTDI_{vol}$	57.9	0.844
$CTDI_{vol}$	99.8	0.850
ImageThickness	2.5	0.852
$CTDI_{vol}$	64.2	0.864
$CTDI_{vol}$	72.7	0.864
RotationTime	0.9	0.865
ImageThickness	1.25	0.867
$CTDI_{vol}$	132.6	0.870
RotationTime	0.8	0.892
Lesion Model	1.5 cm Skull Base	0.902
$CTDI_{vol}$	105.6	0.916
Lesion Model	1.5 cm Cerebrum	0.929
$CTDI_{vol}$	117.1	0.933

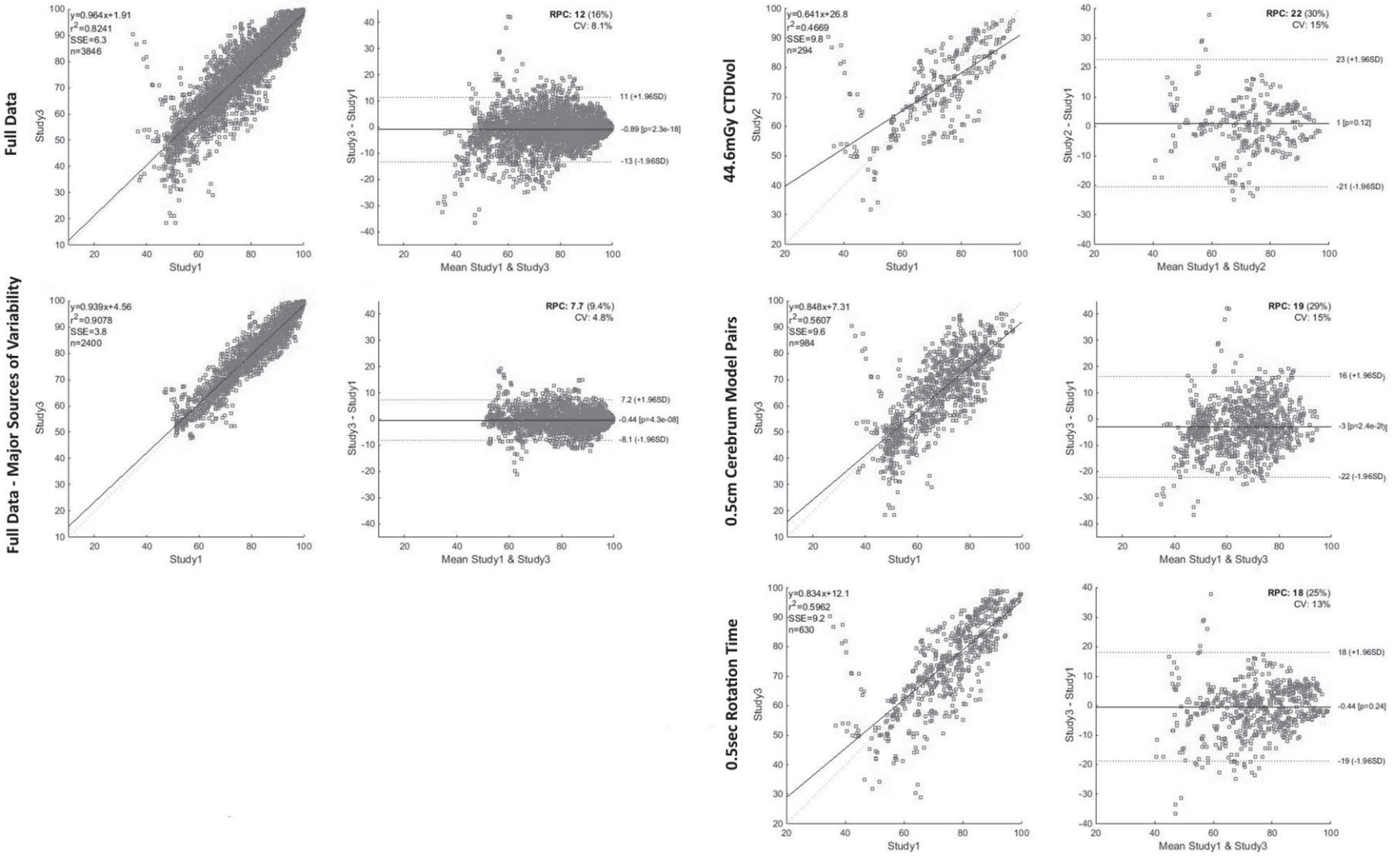

Figure 4.35: Bland-Altman and correlation graphs for SVM inter-scanner correlation. Upper Left: Analysis of full data. Right: Analysis of major sources of variability based on results in Table 4.19. Lower Left: Analysis of full data with the data associated with these major sources of variability removed.

Geometric Bisector Inter-Scanner Correlation

Inter-scanner correlation of Study 1 and Study 3 based on geometric bisector differentiation accuracy data resulted in a CV correlation of 8.3% and R^2 linearity of 0.814. Repeated analysis for subsets of the data based on all available protocol and lesion parameters yielded three major sources of variability based on CV and R^2 cutoff criteria: 44.6 mGy $CTDI_{vol}$, 0.5 cm Cerebrum matched model pairs and 0.5sec rotation time (Table 4.20). Based solely on R^2 criteria, an additional two parameters were identified as major sources of variability: 81.4 mGy $CTDI_{vol}$ and 3.75 mm image thickness. Bland-Altman and correlation graphs for the full data as well as the parameters and values identified as major sources of variability by both CV and R^2 cutoffs can be seen in Figure 4.36. Removing the data for these major sources of variability from analysis reduced the overall CV correlation to 4.6% and increased the R^2 linearity to 0.915. Note that extreme outliers in the correlation were influenced by all three major sources of variability: 0.5 cm lesion models scanned using 44.6 mGy $CTDI_{vol}$ and a 0.5sec rotation time.

Table 4.20: Sorted results of Bland-Altman analysis of GB inter-scanner correlation for subsets of data based on available protocol and lesion parameters. Parameters and values above the double line indicate worse correlation or linearity than the full data set while those below the double line indicate improved correlation or linearity. Text in red indicates a major source of variability based on CV or R^2 cutoff criteria.

CV - Correlation		
Full Data CV	Criteria	Cutoff
8.3	150%	12.4
Parameter	Value	CV
Lesion Model	0.5 cm Cerebrum	15.2
$CTDI_{vol}$	44.6	15.0
RotationTime	0.5	12.6
$CTDI_{vol}$	81.4	10.3
ImageThickness	3.75	9.9
$CTDI_{vol}$	36.7	8.8
ImageThickness	5	8.4
$CTDI_{vol}$	54.7	8.0
RotationTime	0.7	7.9
$CTDI_{vol}$	57.9	7.6
RotationTime	0.6	7.6
ImageThickness	2.5	7.4
$CTDI_{vol}$	72.7	7.2
$CTDI_{vol}$	67	7.2
$CTDI_{vol}$	99.8	7.1
RotationTime	0.9	7.0
$CTDI_{vol}$	132.6	6.7
RotationTime	0.8	6.7
$CTDI_{vol}$	64.2	6.6
$CTDI_{vol}$	105.6	6.3
ImageThickness	1.25	6.2
$CTDI_{vol}$	117.1	6.1
Lesion Model	1.0 cm Cerebrum	5.7
Lesion Model	1.5 cm Skull Base	4.7
Lesion Model	1.5 cm Cerebrum	4.3

Rsquared - Linearity		
Full Data R^2	Criteria	
0.814	< 0.75	
Parameter	Value	R^2
$CTDI_{vol}$	44.6	0.453
Lesion Model	0.5 cm Cerebrum	0.515
RotationTime	0.5	0.581
$CTDI_{vol}$	81.4	0.717
ImageThickness	3.75	0.738
$CTDI_{vol}$	36.7	0.772
ImageThickness	5	0.796
Lesion Model	1.0 cm Cerebrum	0.812
RotationTime	0.7	0.822
ImageThickness	2.5	0.841
$CTDI_{vol}$	54.7	0.842
$CTDI_{vol}$	57.9	0.843
$CTDI_{vol}$	72.7	0.843
$CTDI_{vol}$	99.8	0.844
RotationTime	0.6	0.846
$CTDI_{vol}$	67	0.848
$CTDI_{vol}$	64.2	0.860
RotationTime	0.9	0.865
ImageThickness	1.25	0.868
RotationTime	0.8	0.874
$CTDI_{vol}$	132.6	0.881
$CTDI_{vol}$	105.6	0.890
$CTDI_{vol}$	117.1	0.895
Lesion Model	1.5 cm Cerebrum	0.926
Lesion Model	1.5 cm Skull Base	0.927

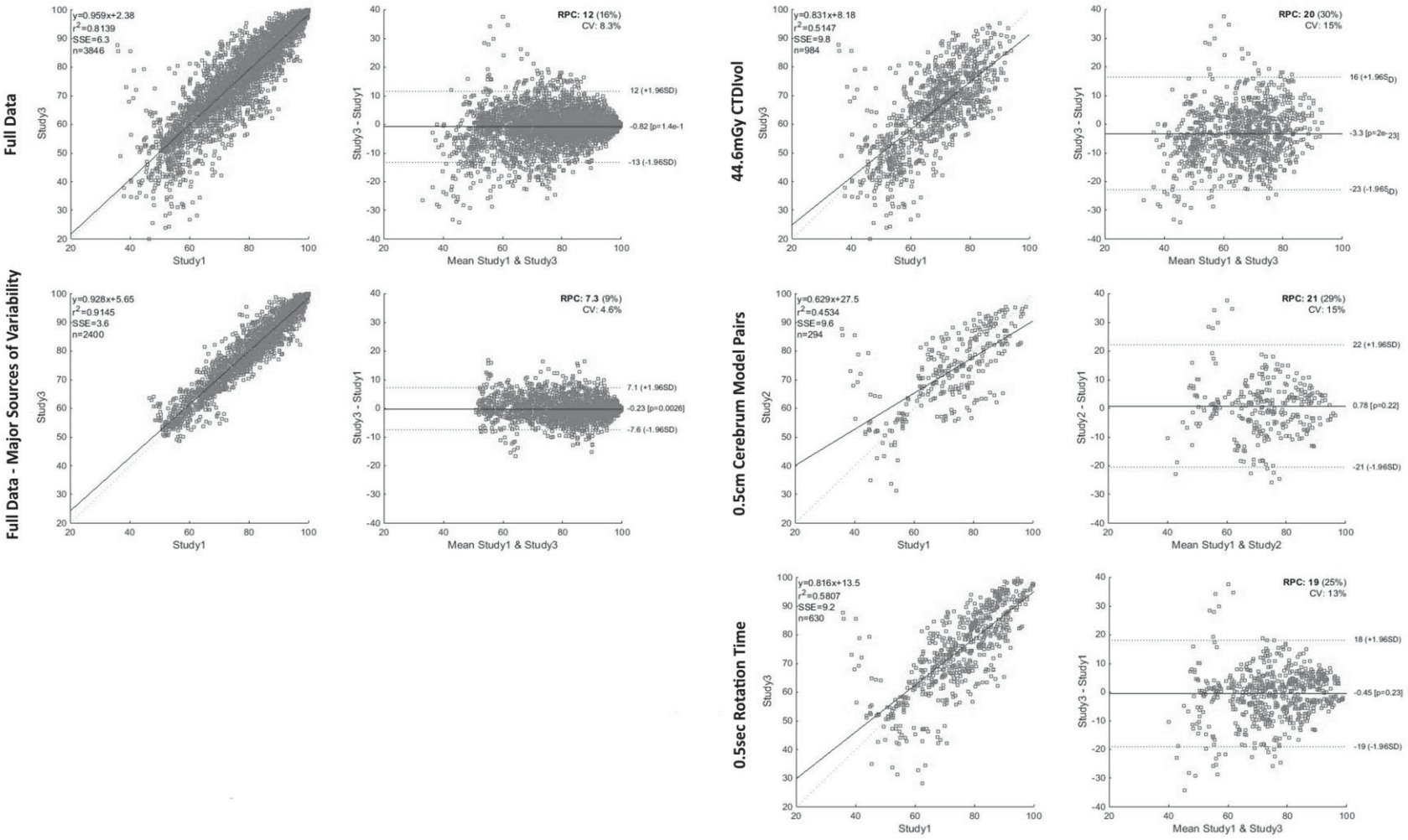

Figure 4.36: Bland-Altman and correlation graphs for GB inter-scanner correlation. Upper Left: Analysis of full data. Right: Analysis of major sources of variability based on both CV and R^2 cutoff criteria (Table 4.20). Sources of variability identified solely by R^2 criteria were excluded for simplicity of visualization. Lower Left: Analysis of full data with the data associated with these major sources of variability removed

4.2.6.2 Intra-Scanner Correlation

Support Vector Machine Intra-Scanner Correlation

Intra-scanner correlation of Study 1 and Study 2 based on support vector machine differentiation accuracy data resulted in a CV correlation of 6.2% and R^2 linearity of 0.886. Repeated analysis for subsets of the data based on all available protocol and lesion parameters yielded two major sources of variability based on CV and R^2 cutoff criteria: 44.6 mGy $CTDI_{vol}$ and 0.5 cm Cerebrum matched model pairs (Table 4.21). Bland-Altman and correlation graphs for the full data as well as the parameters and values identified as major sources of variability can be seen in Figure 4.37. Removing the data for these major sources of variability from analysis reduced the overall CV correlation to 3.7% and increased the R^2 linearity to 0.945. Note that extreme outliers in the correlation were influenced by both major sources of variability: 0.5 cm lesion models scanned using a 44.6 mGy $CTDI_{vol}$ protocol.

Table 4.21: Sorted results of Bland-Altman analysis of SVM intra-scanner correlation for subsets of data based on available protocol and lesion parameters. Parameters and values above the double line indicate worse correlation or linearity than the full data set while those below the double line indicate improved correlation or linearity. Text in red indicates a major source of variability based on CV or R^2 cutoff criteria.

CV - Correlation		
Full Data CV	**Criteria**	**Cutoff**
6.2	**150%**	**9.3**
Parameter	**Value**	**CV**
Lesion Model	0.5 cm Cerebrum	11.6
$CTDI_{vol}$	44.6	10.7
RotationTime	0.5	9.0
$CTDI_{vol}$	54.7	8.9
$CTDI_{vol}$	36.7	8.3
RotationTime	0.6	7.7
$CTDI_{vol}$	81.4	7.2
ImageThickness	5	7.1
RotationTime	0.7	6.9
$CTDI_{vol}$	99.8	6.4
ImageThickness	3.75	6.3
ImageThickness	2.5	5.9
$CTDI_{vol}$	67	5.5
ImageThickness	1.25	5.0
$CTDI_{vol}$	105.6	4.7
Lesion Model	1.0 cm Cerebrum	4.7
$CTDI_{vol}$	57.9	4.6
$CTDI_{vol}$	64.2	4.5
RotationTime	0.8	4.4
$CTDI_{vol}$	72.7	4.2
RotationTime	0.9	4.0
Lesion Model	1.5 cm Skull Base	3.8
$CTDI_{vol}$	132.6	3.6
$CTDI_{vol}$	117.1	3.6
Lesion Model	1.5 cm Cerebrum	3.0

Rsquared - Linearity		
Full Data R^2	**Criteria**	
0.886	**< 0.75**	
Parameter	**Value**	**R^2**
Lesion Model	0.5 cm Cerebrum	0.657
$CTDI_{vol}$	44.6	0.701
RotationTime	0.5	0.750
$CTDI_{vol}$	54.7	0.757
$CTDI_{vol}$	36.7	0.791
RotationTime	0.6	0.818
$CTDI_{vol}$	81.4	0.822
ImageThickness	5	0.845
RotationTime	0.7	0.863
$CTDI_{vol}$	99.8	0.865
ImageThickness	3.75	0.878
Lesion Model	1.0 cm Cerebrum	0.879
ImageThickness	2.5	0.890
$CTDI_{vol}$	67	0.912
ImageThickness	1.25	0.915
$CTDI_{vol}$	64.2	0.932
$CTDI_{vol}$	105.6	0.935
$CTDI_{vol}$	57.9	0.942
$CTDI_{vol}$	72.7	0.943
RotationTime	0.8	0.943
RotationTime	0.9	0.946
Lesion Model	1.5 cm Skull Base	0.952
$CTDI_{vol}$	117.1	0.959
Lesion Model	1.5 cm Cerebrum	0.963
$CTDI_{vol}$	132.6	0.964

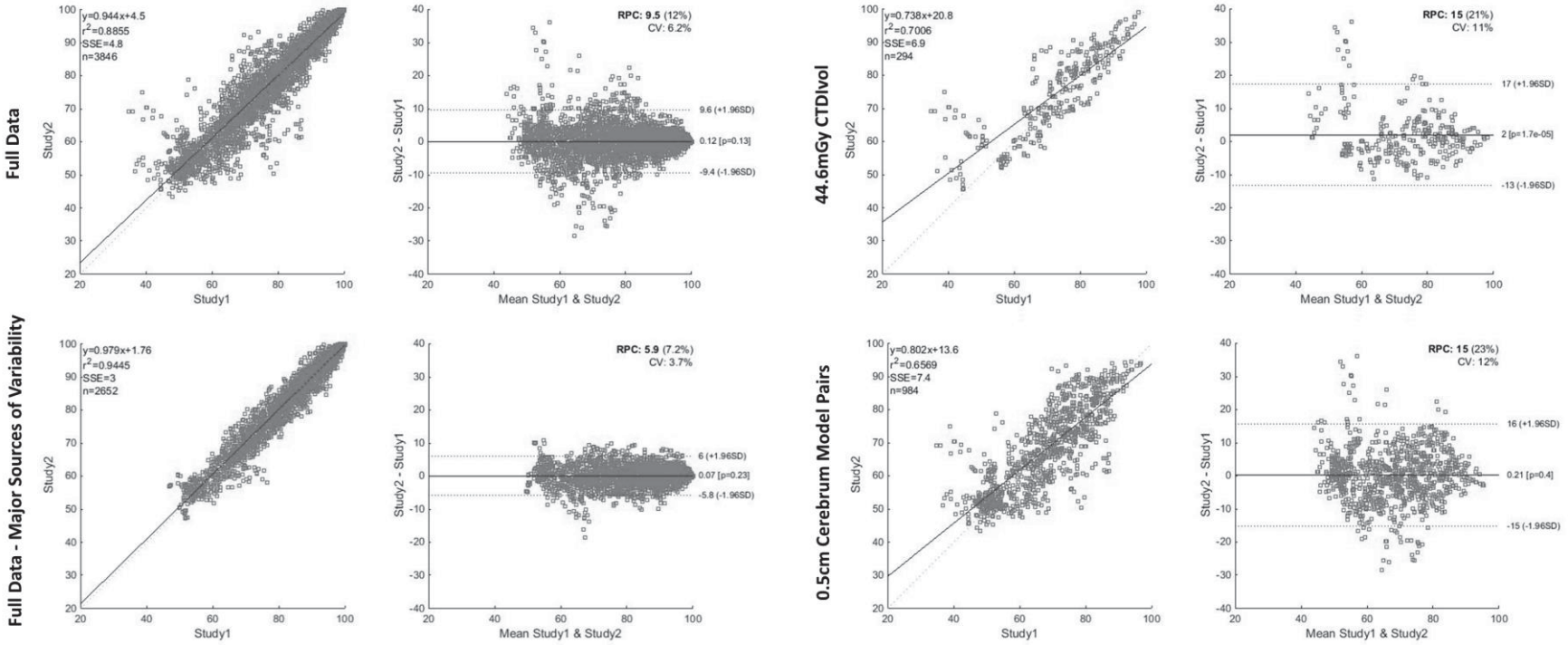

Figure 4.37: Bland-Altman and correlation graphs for SVM intra-scanner correlation. Upper Left: Analysis of full data. Right: Analysis of major sources of variability based on results in Table 4.21. Lower Left: Analysis of full data with the data associated with these major sources of variability removed.

Geometric Bisector Intra-Scanner Correlation

Intra-scanner correlation of Study 1 and Study 2 based on geometric bisector differentiation accuracy data resulted in a CV correlation of 6.1% and R^2 linearity of 0.885. Repeated analysis for subsets of the data based on all available protocol and lesion parameters yielded three major sources of variability based on CV and R^2 cutoff criteria: 44.6 mGy $CTDI_{vol}$, 0.5 cm Cerebrum matched model pairs and 0.5sec rotation time (Table 4.22). Bland-Altman and correlation graphs for the full data as well as the parameters and values identified as major sources of variability can be seen in Figure 4.38. Removing the data for these major sources of variability from analysis reduced the overall CV correlation to 3.3% and increased the R^2 linearity to 0.946. Note that extreme outliers in the correlation were influenced by all three major sources of variability: 0.5 cm lesion models scanned using 44.6 mGy $CTDI_{vol}$ and a 0.5sec rotation time.

Table 4.22: Sorted results of Bland-Altman analysis of GB intra-scanner correlation for subsets of data based on available protocol and lesion parameters. Parameters and values above the double line indicate worse correlation or linearity than the full data set while those below the double line indicate improved correlation or linearity. Text in red indicates a major source of variability based on CV or R^2 cutoff criteria.

CV - Correlation			Rsquared - Linearity		
Full Data CV	Criteria	Cutoff	Full Data R^2	Criteria	
6.1	150%	9.2	0.885	< 0.75	
Parameter	Value	CV	Parameter	Value	R^2
Lesion Model	0.5 cm Cerebrum	11.7	Lesion Model	0.5 cm Cerebrum	0.610
$CTDI_{vol}$	44.6	11.2	$CTDI_{vol}$	44.6	0.659
RotationTime	0.5	9.2	RotationTime	0.5	0.739
$CTDI_{vol}$	36.7	8.5	$CTDI_{vol}$	36.7	0.778
$CTDI_{vol}$	54.7	7.5	$CTDI_{vol}$	54.7	0.824
$CTDI_{vol}$	81.4	7.1	$CTDI_{vol}$	81.4	0.825
RotationTime	0.6	7.0	RotationTime	0.6	0.846
ImageThickness	5	7.0	ImageThickness	5	0.847
RotationTime	0.7	6.8	$CTDI_{vol}$	99.8	0.861
$CTDI_{vol}$	99.8	6.3	RotationTime	0.7	0.865
ImageThickness	3.75	6.3	ImageThickness	3.75	0.872
ImageThickness	2.5	5.9	ImageThickness	2.5	0.888
$CTDI_{vol}$	67	5.2	Lesion Model	1.0 cm Cerebrum	0.895
ImageThickness	1.25	4.8	ImageThickness	1.25	0.915
$CTDI_{vol}$	72.7	4.6	$CTDI_{vol}$	67	0.922
$CTDI_{vol}$	57.9	4.6	$CTDI_{vol}$	72.7	0.923
$CTDI_{vol}$	64.2	4.6	RotationTime	0.9	0.929
RotationTime	0.9	4.5	$CTDI_{vol}$	64.2	0.930
Lesion Model	1.0 cm Cerebrum	4.3	$CTDI_{vol}$	57.9	0.940
RotationTime	0.8	4.2	RotationTime	0.8	0.945
$CTDI_{vol}$	132.6	4.0	$CTDI_{vol}$	117.1	0.946
$CTDI_{vol}$	117.1	4.0	Lesion Model	1.5 cm Cerebrum	0.954
Lesion Model	1.5 cm Skull Base	3.7	$CTDI_{vol}$	132.6	0.954
$CTDI_{vol}$	105.6	3.6	$CTDI_{vol}$	105.6	0.959
Lesion Model	1.5 cm Cerebrum	3.0	Lesion Model	1.5 cm Skull Base	0.964

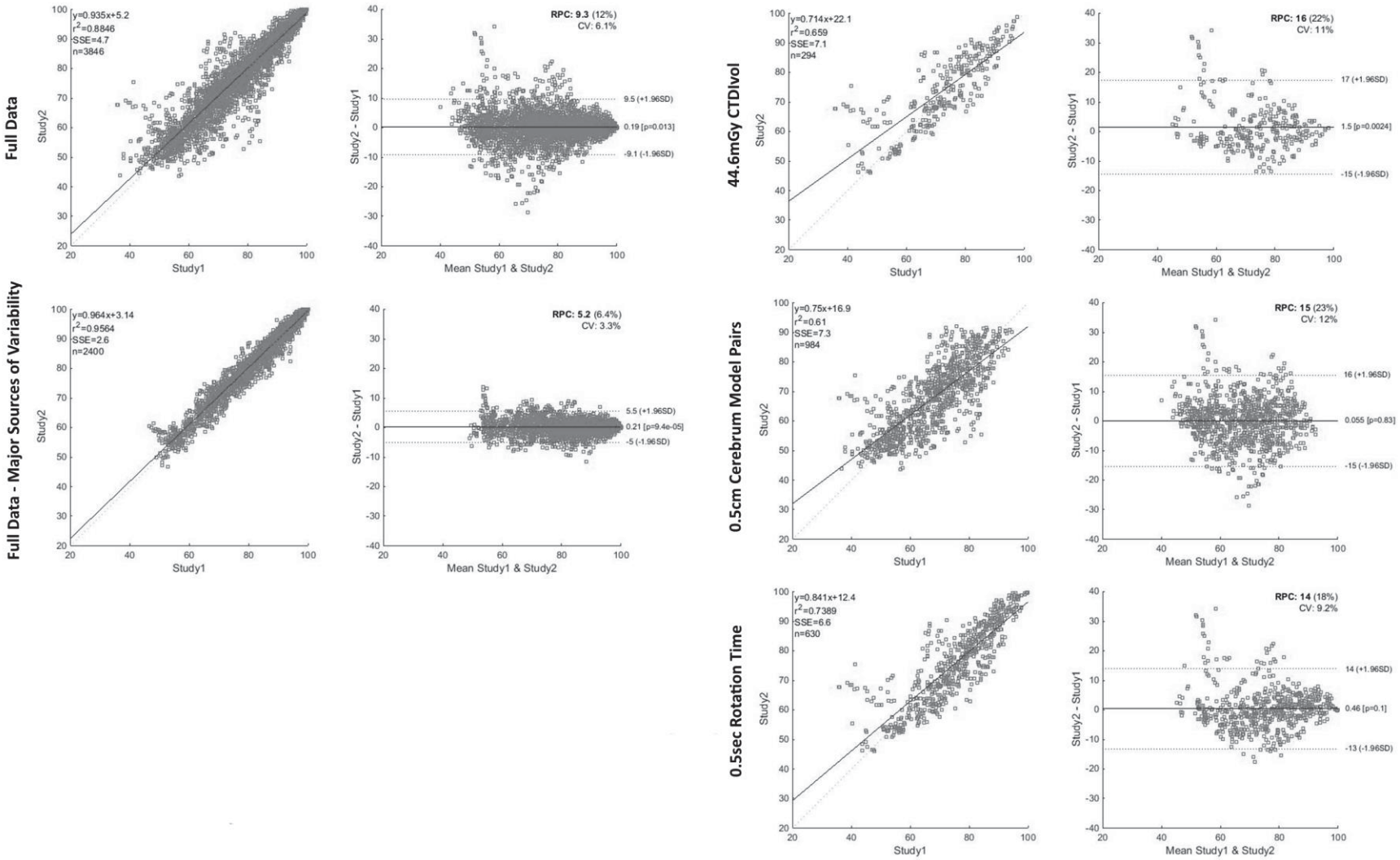

Figure 4.38: Bland-Altman and correlation graphs for GB intra-scanner correlation. Upper Left: Analysis of full data. Right: Analysis of major sources of variability based on results in Table 4.22. Lower Left: Analysis of full data with the data associated with these major sources of variability removed

4.3 Discussion

4.3.1 Gaussian Mixture Model (GMM) Analysis

Prior work (Chapter 3) investigating the differentiation of calcification and hemorrhage using 1.0 cm diameter agar gel lesion models and GMM analysis resulted in 90% differentiation accuracy starting at 50 HU. Repeat analysis of the same lesion size using an equivalent protocol in the current project, resulted in a maximum differentiation accuracy of 81% at 100 HU. In fact, the only lesion type differentiable using GMM analysis was the 1.5 cm cerebrum lesion. Investigation of the reduced accuracy results from the current project led to the identification of higher order heterogeneity in the epoxy resin lesion models relative to the agar gel models used in the prior work. Although the compound used in the calcification lesion type for this project was changed from hydroxyapatite to calcium carbonate, the increase in heterogeneity was similar for both hemorrhage and calcification model types, indicating the mixing method, rather than the compound change, was likely responsible. The epoxy resin materials used in this project were created by an outside vendor (Gammex, Middleton, WI) using an automated mixing method. All lesion models were validated to ensure general homogeneity, however, estimation of low frequency heterogeneity due to material fabrication would have required more advanced analysis considered beyond the scope of this work.

4.3.2 Support Vector Machine and Geometric Bisector Analyses

While this heterogeneity had a negative impact on the GMM analysis by invalidating the base assumption of a Gaussian distribution, the support vector and geometric bisector analyses were unaffected. First, neither SVM nor GB analyses assume a specific distribution type. Second, since the “tails” in the distribution (Figure 4.19) were simply due to areas with less compound additive, they were in line with the full distribution of multiple attenuation (HU) level lesion models. As a consequence, methods based on analysis of the full multiple- SECT attenuation (HU) level distributions were less affected by the more

heterogeneous models. Support vector analysis was found to increase the accuracy of differentiation relative to GMM analysis for all lesions except the 1.5 cm cerebrum lesions, where the limited overlap of the two distributions likely outweighed the effect of the tails for the GMM method. The increase in accuracy of SVM relative to GMM analysis was less for the 0.5 cm cerebrum and 1.5 cm skull base lesions, most likely due to the increased noise found in these data sets. The 0.5 cm cerebrum lesions have a much smaller sample size and are more likely to be affected by partial volume and sub-optimal ROI placement than all other lesion types. The 1.5 cm skull base lesions, while large, are more heavily affected by the surrounding bony anatomy than those lesions in the cerebrum, increasing both overlap and spread of the distributions.

Several differentiation accuracy trends were identified based on acquisition parameters using both the SVM and GB analysis methods. In general, increased accuracy was associated with increased $CTDI_{vol}$ (Figure 4.21, Figure 4.28). As the number of photons incident on the phantom (or patient) increases, the number of photons incident on the detector increases. While the percentage of photons attenuated is constant, the number of photons un-attenuated and thus reaching the detector is increased. More photons at the detector means improved counting statistics and thus a richer data set to pull from to characterize the attenuations of the materials within the phantom (or patient). In the case of dual-energy CT, the increased dose benefits the lower 80kVp projections preferentially, where a larger percentage of the beam is attenuated by the patient. If too few of the 80kVp photons make it to the detector, the material decomposition process will be poorly characterized, resulting in errors in both the material density and monoenergetic images. Increased image thickness led to increased differentiation accuracy for both SVM and GB methods (Figure 4.22, Figure 4.29). This is likely due to the reduction in low frequency noise (mottled appearance on a level greater than the voxel scale) by data averaging resulting in reduced lesion inhomogeneity. Reconstruction filter was found to have no effect on differentiation accuracy using either SVM or GB method (Figure 4.23,

Figure 4.30). It seems that reduction in high frequency noise (white noise on the level of the voxel scale) does not have as pronounced an effect as the reduction in low frequency noise by data averaging.

Based on these trends, a generalized protocol can be recommended: high dose with thick images using any of the investigated filters. Dose ($CTDI_{vol}$) should be as high as possible while balancing risk with clinical need. Image thickness should be as thick as possible without exceeding the dimensions of the lesion and including partial volume effect of the surrounding tissues. One recommendation would be the acquisition of data at 1.25 mm images followed by reconstruction at increasingly higher image thicknesses until the maximum image thickness to avoid partial volume effect is determined. Since it has no effect on differentiation accuracy, the reconstruction filter may be selected based on clinical use at the institution and visual preference of the radiologists.

Results of the generalized geometric bisector solution indicate that a combination of three plane definitions should provide equally accurate results to the un-generalized geometric bisector method: cerebrum lesions less than 0.5 cm in diameter, cerebrum lesions greater than 0.5 cm in diameter, and skull base lesions (Table 4.16). While this would necessitate some prior knowledge of the lesion's size and location, all protocol variations were included in the creation of the plane, allowing physicians to determine $CTDI_{vol}$ and image thickness on a case by case basis.

4.3.3 Inter- and Intra-Scanner Correlation

In addition to the similar trends discussed above, the SVM and GB methods were found to have a high degree of correlation (CV of 1.7%) and linearity (R^2 of 0.988) once the effect of the 0.5 cm cerebrum lesions were removed from analysis. Neither method was preferred for these lesions, instead the noise due to their small size, partial volume effects and ROI placement variability simply obscured the correlation between the two analysis methods (Figure 4.34). Given the high degree of correlation between the two methods, it is

reasonable to recommend the GB over the SVM due to the former's simplicity and ease of use. While the support vector machine method requires iterative analysis and heavy computational power, the geometric bisector method requires only linear regression and simple geometric calculations. The simplicity of this method would also lead to easier implementation and would allow for interim updates to the plane of optimal differentiation as patient data is collected.

Table 4.23: Summary of inter-scanner (Study 1 versus Study 3) and intra-scanner (Study 1 versus Study 2) correlations based on both SVM and GB methods. Parameters identified as major sources of variability are listed along with the initial CV and R^2 for the full data, as well as, the final CV and R^2 with the sources of variability removed from analysis.

	Method	CV (Initial)	R^2 (Initial)	Sources of Variability			CV (Final)	R^2 (Final)
Inter-Scanner	SVM	8.1%	0.824	44.6 mGy $CTDI_{vol}$	0.5 cm Cerebrum Lesions	0.5sec Rotation Time	4.8%	0.908
	GB	8.3%	0.814	44.6 mGy $CTDI_{vol}$	0.5 cm Cerebrum Lesions	0.5sec Rotation Time	4.6%	0.915
Intra-Scanner	SVM	6.2%	0.886	44.6 mGy $CTDI_{vol}$	0.5 cm Cerebrum Lesions		3.7%	0.945
	GB	6.1%	0.885	44.6 mGy $CTDI_{vol}$	0.5 cm Cerebrum Lesions	0.5sec Rotation Time	3.3%	0.946

In general, intra-scanner correlations were better than inter-scanner correlations, indicating that repeatability of the differentiation accuracy result would be greater if the same scanner were used (Table 4.23). These differences were quite small however, and as such, the clinical impact of scanner selection would be minimal, assuming the behavior of the scanners investigated is representative of overall scanner behavior. In general, correlations for the GB method were better than those of the SVM method, supporting limiting future use to the simpler GB method. All evaluations of inter- and intra-scanner correlation identified the same major sources of variability: 44.6 mGy $CTDI_{vol}$, 0.5 cm

cerebrum lesions and 0.5 cm rotation time. Intra-scanner correlation using SVM method did not identify 0.5sec rotation time as a major source of variability; however, it was the parameter with the next highest CV and next lowest R^2 value (Table 4.21). The issues associated with 0.5 cm cerebrum lesions have already been discussed and these issues' effect on inter- and intra- scanner correlations is expected. Low dose ($CTDI_{vol}$) has also been discussed, however the $CTDI_{vol}$ level identified as a major source of variability was not the lowest dose level investigated. By investigating the GSI-presets associated with the two lowest $CTDI_{vol}$ values (36.7 mGy and 44.6 mGy), it was found that the preset associated with the 36.7 mGy $CTDI_{vol}$ used a 0.7sec rotation time, while the preset associated with the 44.6 mGy $CTDI_{vol}$ used a 0.5sec rotation time. Thus it is reasonable to conclude that the 44.6 mGy $CTDI_{vol}$ level was identified due to a combination of its low dose and a rotation time identified separately as a major source of variability. Concurrent work has suggested that reduced rotation times have a detrimental effect on the fast-kVp switching x-ray tube, specifically resulting in reduced uniformity (see Chapter 6.3.2.2). Given the speed of the fast-kVp switching waveform, and the time required to transition from one kVp to the other, it is reasonable to suggest that a faster rotation time may result in reduced spectral separation between the high and low kVp projections. This reduced separation may lead to reduced accuracy of the material decomposition process, errors in material density and monoenergetic images and thus reduced differentiation accuracy between calcification and hemorrhage.

4.3.4 Validation of Optimal keV Level for Simulated SECT Scanning

Calculation of the difference between 68 keV attenuation (HU) and the gold standard SECT attenuation (HU) yielded errors within 3 HU for lesion models in the cerebrum (Figure 4.10). This is in line with error estimates of -2.6 HU to 2.6 HU from the initial selection of 68 keV as the optimal keV level for simulated SECT scanning (Chapter 4.2.3). The mean error across all acquisition parameters for cerebrum lesions was found to be 0.5 HU, again

supporting the estimated mean error of 0.3 HU during keV selection. Mean error in the skull base was found to be 1.0 HU with a maximum error of approximately 6 HU, surpassing the estimated error during the selection process. Since the keV selection process was performed using only cerebrum lesions, it is not surprising that the keV was not optimized for equivalent attention between 68 keV and SECT in the skull base. Due to the increased bony anatomy in the skull base relative to the cerebrum, it is likely that the 80kVp beam was more highly attenuated, affecting the results of the material decomposition. However, given the high degree of correlation (CV 2.8%) and linearity (R^2 0.99) between the 68 keV and SECT attenuation (HU) across all lesion and acquisition parameters (Table 4.11), 68 keV dual-energy reconstruction seems to be a reasonable substitute for SECT acquisition for intracranial lesions in this attenuation range. An added SECT acquisition does not appear warranted for in-vivo scanning at this time.

4.3.5 Power Fits for 90% Differentiation Accuracy

Second order power fits of available data yielded results in the form of $CTDI_{vol}$ necessary for 90% differentiation accuracy based on a given lesion attenuation (HU) and lesion attenuation (HU) necessary for 90% differentiation accuracy based on a given protocol $CTDI_{vol}$ (mGy). In both cases, the relationship of the resulting values to the given parameter was not linear. In other words, linearly increasing lesion attenuation (HU) did not always result in a linear decrease in $CTDI_{vol}$ necessary for 90% differentiation accuracy. This is likely an effect of the $CTDI_{vol}$ values being associated with specific GSI-presets. These presets are a fixed combination of a dose ($CTDI_{vol}$), beam width, mA, bowtie filter and rotation time. In order to obtain data on a wide range of dose values, the scan protocol used was generated with a wide range of GSI-presets with varying mA values and rotation times. The effects of these other components of the GSI-preset cannot be controlled at this time, and may have a substantial effect on the differentiation accuracy results. Given this

constraint, the use of these tables showing the relationship of lesion attention (HU) and dose ($CTDI_{vol}$) for protocol development is limited.

4.3.6 Limitations

As with any phantom study, there are limitations stemming from the inexact modeling of the biological system. Calcification and hemorrhage lesion models were created using a cylindrical shape, and assessed at three sizes (0.5, 1.0 and 1.5 cm) and two locations within the cranium (cerebrum and skull base). Given the large differences in differentiation accuracy between the 0.5 cm and 1.0 cm cerebrum lesions, further investigation into intermediate sizes is warranted. Lesion models were also created to be homogeneous and without contamination, thus the usefulness of this technique for heterogeneous or mixed lesions cannot be confirmed. Protocol recommendations are based on fixed GSI-presets, limiting the ability to evaluate protocol parameters such as mA, rotation time and $CTDI_{vol}$ directly. In addition, a range of $CTDI_{vol}$ values was created through manipulating the pitch, which might have different effects on differentiation than increasing the mA. The DFOV was limited to 25 cm to allow for visualization of the full cranium. Reduced DFOV may aid the differentiation accuracy of the 0.5 cm cerebrum lesions through an increase in sample size, reduction in partial volume effect and increased ease of ROI placement. Finally, inter- and intra-scanner correlations were based on single study comparisons which may affect the results.

Chapter 5

Lesion Classification using Unknown Lesion Models

This chapter applies the methods and protocols developed in Chapter 4 to the classification of unknown intracranial lesions of either hemorrhagic or calcific composition. Unknown lesion models were created at varying attenuation, size and location within the cranial cavity. The lesions were blinded for data acquisition (scanning) and analysis, and the ability of DECT to correctly classify these lesions with 90% confidence was determined.

5.1 Materials and Methods

5.1.1 Fabrication and Evaluation of Unknown Lesion Models

To validate the results from Chapter 4, and move beyond differentiation and towards identification, a new set of "validation" hemorrhage and calcification lesion models were fabricated by the third party vendor (Gammex Inc., Middleton, WI) used for the previous biologically relevant phantom (Chapter 4). Five calcification and five hemorrhage lesion models were commissioned at varying SECT attenuation (HU) between 50 and 100 HU. Given that the previous differentiation work was performed on calcification and hemorrhage models within 3 HU of each decade between 40 and 100 HU, unknown lesions were requested at varying SECT attenuation (HU) from 50 to 100 HU while avoiding ± 2 HU of each decade. For example, in order to avoid a repeat measure of a 70 HU calcification model, unknown lesions were ordered to be between 62 and 68 HU and between 72 and 78 HU. Each lesion type and attenuation level resulted in the fabrication of a 15 cm long, 2.8 cm diameter rod. In order to minimize the handling of the unknown lesion models by the evaluation group, these rods were immediately machined to create each lesion size and location specific model: 0.5 cm cerebrum, 1.0 cm cerebrum, 1.5 cm cerebrum and 1.5 cm skull base. The lesion models were then grouped by the vendor into lesion composition

and attenuation specific bags, each labeled with a letter to allow blinded material verification, data collection and analysis. These lesion models (n=40) will be referred to throughout this document as “unknown lesions”.

These pre-milled, unknown lesions were then simply evaluated for defects and uniformity by a third party. The lesion models were imaged on the table top using a basic protocol (Table 5.1). Single-energy, 60 keV and Iodine(Water) images were evaluated visually for defects and overall homogeneity. This lesion model fabrication and verification process differed from that used in the earlier differentiation work (Chapter 4). The original lesion models used for evaluation of lesion differentiation were milled after extensive verification of the bulk material (Chapter 4.1.3). This was necessary due to validate the untested methods used by the lesion material manufacturer as well as to ensure the attenuation matching of the calcification and hemorrhage matched model pairs. Given that the lesion models needed for the lesion classification work did not require attenuation matched model pairs and that the methods used by the manufacturer had been previously validated, the validation methods were streamlined to allow for the pre-milling of the lesion models by the manufacturer.

Table 5.1: Unknown lesion material verification and evaluation protocol. Both series were acquired in helical mode, using a 20 mm beam width, 25 cm DFOV and Head SFOV. Images were evaluated visually to confirm the lesion models were homogeneous and free of defects.

Series	Name	Pitch	Image Thickness (mm)	Interval (mm)	kVp	mA	Rot (s)	$CTDI_{vol}$ (mGy)	Filter
1	SE	0.531	3.75	3.75	120	220	0.8	64	Standard
2	GSI-26	0.531	3.75	3.75	NA	375	0.7	67	Standard

5.1.2 Unknown Lesion Data Acquisition

Unknown lesion models were scanned using the same phantom used for lesion differentiation (Chapter 4). Each of the 10 lesion groups defined by a composition (hemorrhage or calcification) and an attenuation (roughly 50-100 HU in decades) were imaged individually. For each of the 10 exams, the four lesion sizes and locations (0.5 cm cerebrum, 1.0 cm cerebrum, 1.5 cm cerebrum and 1.5 cm skull base) corresponding to that lesion type and attenuation were inserted into the phantom. Low attenuation (40 HU) lesion models from the prior differentiation work (Chapter 4) were used to fill the remaining four available spaces (Figure 4.2).

5.1.2.1 Determination of Scan Protocol

Based on the results of the prior differentiation work (Chapter 4), a more limited scan protocol was designed for validation of unknown lesion classification (Table 5.2). Specifically, higher dose protocols reconstructed with thicker images were targeted for investigation and the use of GSI-presets with 0.5sec rotation time was avoided. To this aim, three $CTDI_{vol}$ levels were selected: 132.6 mGy to evaluate the highest dose available on the system, 67 mGy to represent a dose level similar to the institution's routine brain protocol (Table 4.3, series 2), and 105.6 mGy as a midpoint between the two. All three dose levels were evaluated using an image thickness of 3.75 and a standard filter to mimic routine clinical practice. A single-energy 64 mGy acquisition was added to provide verification of 68 keV attenuation values. All dual-energy acquisitions were reconstructed at 68 keV, Water(Calcium) and Calcium(Water) to allow for the collection of the three-dimensional (3D) DECT signature data.

Table 5.2: Unknown lesion validation protocol. For all acquisitions: helical, 20 mm beam width, 25 cm DFOV, Head SFOV.

Series	Name	Pitch	Image Thickness (mm)	Interval (mm)	kVp	mA	Rot (s)	$CTDI_{vol}$ (mGy)	Filter
1	SE	0.531	3.75	3.75	120	220	0.8	64	Standard
2	GSI-26	0.531	3.75	3.75	NA	375	0.7	67	Standard
	GSI-30	0.531	3.75	3.75	NA	550	0.8	105.6	Standard
	GSI-9	0.531	3.75	3.75	NA	600	0.9	132.6	Standard

5.1.2.2 Data Collection and Organization

Data were collected and organized following the same method used for the prior differentiation work (Chapter 4.1.6.1-4). Series sorting was limited to relevant parameters including, but not limited to, image number, GSI-preset, and dual-energy reconstruction type. Matlab (Version 2014a, MathWorks) was used to query the database to combine the dual-energy reconstructions to create 3D-DECT data for each lesion model based on acquisition type. Given two lesion types (calcification and hemorrhage), five attenuation levels (roughly 50 to 100 HU in decades), 4 lesion sizes/location combinations (0.5 cm cerebrum, 1.0 cm cerebrum, 1.5 cm cerebrum and 1.5 cm skull base), and 3 DECT acquisitions (67, 105.6 and 132.6 mGy), a total of 120 unique unknown lesion data sets were collected.

5.1.3 Unknown Lesion Classification Methods

5.1.3.1 Geometric Bisector (GB) Method

Due to the equivalence of the support vector machine and geometric bisector methods found in the prior differentiation work (Chapter 4), Geometric bisector was selected due to its ease of use and overall simplicity. A lookup table was created in Matlab based on the geometric bisector plane results from the prior differentiation work (Chapter 4.1.7.3) for all acquisitions and lesion size and locations investigated in this validation study. 12 planes were compiled: 3 $CTDI_{vol}$ levels (67 mGy, 105.6 mGy and 132.6 mGy) for

each lesion size and location (0.5 cm cerebrum, 1.0 cm cerebrum, 1.5 cm cerebrum and 1.5 cm skull base). Then 3D-DECT unknown lesion data was opened in Matlab and the database queried for the matched-acquisition, matched-lesion parameter geometric bisector plane (Figure 5.1). The mean of the 3D-DECT data for the unknown lesion model (black diamond) was applied to the plane and lesion classification derived from the position of the mean location relative to the plane (gray). . Mean values that shared the side of the plane as the original hemorrhage differentiation data (red) were classified as hemorrhage while mean values that shared the side of the plane as the original calcification differentiation data (blue) were classified as calcification. The confidence in this classification was defined as the percentage of voxels within the unknown lesion distribution that were on the same side of the plane as the mean value (here, 90%).

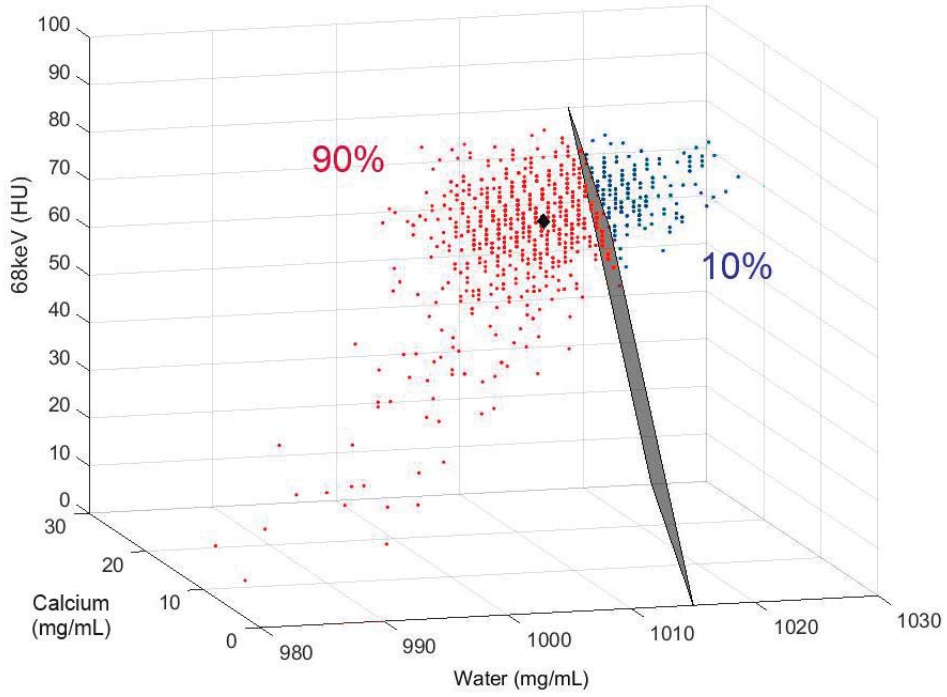

Figure 5.1: Application of lesion and acquisition specific geometric bisector plane (gray) to an example unknown lesion model. The lesion model mean is shown as a black diamond to the left of the plane. The voxel data also on the left of the plane (and thus contributing to the classification confidence) is shown in red, while the voxel data on the right side of the plane (and thus counting against the classification confidence) is shown in blue.

The final classification of each lesion was compared to the lesion composition and the number of lesions with correct classification was calculated. Next, the number of lesions correctly classified with greater than 80% and greater than 90% confidence was calculated. To assess trends in classification confidence with $CTDI_{vol}$, second order power fits were employed to determine the lowest lesion attenuation (HU) necessary for 90% and 80% confidence given a particular $CTDI_{vol}$. While this process was repeated in the past to obtain the $CTDI_{vol}$ necessary given a certain lesion attenuation (HU), the limited number of data points for $CTDI_{vol}$ made this curve fit highly unstable and thus was not pursued.

5.1.3.2 Generalized Geometric Bisector (GGB) Method

Based on the results of prior work comparing lesion and acquisition parameter-specific geometric bisector planes (Chapter 4.2.5.5), three parameters were identified as major sources of variability in the geometric bisector plane solution (Table 4.16): cerebrum lesions of 0.5 cm in diameter, cerebrum lesions of greater than 0.5 cm in diameter and skull base lesions. In order to assess whether a more generalized geometric bisector plane might provide similar results to lesion and acquisition parameter-specific planes, these three generalized planes were evaluated for their ability to classify the validation unknown lesions. Unknown lesion data were analyzed using lesion parameter-specific plane (cerebrum lesions of 0.5 cm diameter, cerebrum lesions of greater than 0.5 cm diameter, and skull base lesions) and the classification, and the confidence in that classification, was calculated as described above (Chapter 5.1.3.1).

5.1.3.3 Probability Distribution (PD) Method

Using the raw 3D-DECT data collected as part of the prior differentiation work, a distribution of calcification probability was derived. For each acquisition (n=3 based on series 2 of Table 5.2) and lesion size and location (n=4) combination investigated as part of the validation study, a distribution of the raw 3D-DECT data was created based on data

from Study1 of the prior differentiation project described in Chapter 4. Using this prior differentiation data collected in Study 1, each lesion (size and location) specific and acquisition ($CTDI_{vol}$, image thickness, reconstruction filter) specific matched model pair (n=12) was analyzed using a multivariate logistic regression model (104). This model correlated the 3D-DECT measurements (68 keV attenuation, water material density and calcium material density) with the probability of being calcification. Odds ratios were then derived based on the increased probability of being calcification given a unit increase in a measurement (68 keV, Water(Calcium) or Calcium(Water)). In addition, the coefficients of the multivariate logistic regression model were used to create a formula for the probability the lesion is a calcification and probability the lesion is a hemorrhage based on input of the mean lesion value in the 3D-DECT signature space (Equation 12,Equation 13,Equation 14).

Equation 12
$$Lesion\ Probability\ Coefficient\ (LPC) = b_0 + b_1(Water\ density) + b_2(Calcium\ density) + b_3(68keV\ HU)$$

Equation 13
$$Probability(Calcification) = \frac{e^{LPC}}{(1 + e^{LPC})}$$

Equation 14
$$Probability(Hemorrhage) = 1 - Probability(Calcification)$$

Lookup tables were created in Matlab for these acquisition and lesion specific probability formulas. Then 3D-DECT unknown lesion data was opened in Matlab and the database then queried for the acquisition and lesion specific probability formula. The mean unknown lesion value based on the 3D-DECT data was then input into the formula and the probability the lesion is calcification was derived (Equation 12, Equation 13). The probability the lesion is hemorrhage was then calculated using Equation 14. Unknown lesions were classified as either calcification or hemorrhage based on a greater than 50% probability. The probability was then used a measure of confidence in that classification.

The final classification of each lesion was compared to the actual lesion composition and the number of lesions with correct classification was calculated. Next, the number of lesions correctly classified with greater than 80% and greater than 90% confidence was calculated. To assess trends in classification confidence with $CTDI_{vol}$, second order power fits were employed to determine the lowest lesion attenuation (HU) necessary for 90% and 80% confidence given a particular $CTDI_{vol}$.

5.1.4 Inter-Method correlation

To assess the correlation between the geometric bisector (GB) and probability distribution (PD) analysis methods, Bland-Altman and correlation graphs were created. To assess sources of variability in this correlation, the analysis was repeated for subsets of the data based on all available parameters: lesion model composition, $CTDI_{vol}$, rotation time and lesion size and location. Investigation of rotation time was included due to its impact in other concurrent analyses (Chapter 6). Each parameter was investigated separately, while including all values for other variables. For all analyses, the coefficient of variation (CV) was tabulated as a measure of data correlation, while the square of the Pearson r-value (R^2) was tabulated as a measure of correlation linearity. The CV and R^2 from these parameter value specific Bland-Altman and correlation graphs were compared to the values derived from Bland-Altman and correlation graphs for the full data set. Parameter-value specific R^2 values under 0.75 or CV values greater than 150% of the full data CV value were identified as major sources of variability in the method correlation (see Chapter 4.1.7.5 for description of criteria development). Specific parameter values identified as major sources of variability were then removed from the full data set and the Bland-Altman analysis was repeated.

This method was repeated to assess the correlation between the geometric bisector and generalized geometric bisector analysis methods. Given that the correlation was already assessed between the geometric bisector and probability distribution methods, and

that the generalized geometric bisector was an extension of the geometric bisector method, the correlation between the generalized geometric bisector and probability distribution methods was not assessed.

5.2 Results

5.2.1 Fabrication and Evaluation of Unknown Lesion Models

All unknown lesion models were free of defects and homogeneous. None of the lesion models required replacement or modification.

5.2.2 Probability Distribution Definition

Odds ratios correlating the 3D-DECT measurements with probability of being calcification based on multivariate logistic regression model of differentiation data collected as part of Study 1 in Chapter 4 can be seen in Table 5.3. The odds ratio represents the increase in probability of calcification based on a unit increase on one of the 3D-DECT image types. For example, an odds ratio of 1.59 means that the probability of being a calcification is increased 59% by a unit increase in the voxel measurement on that image type. Increased water and calcium density image measurements were significantly associated with increased probability of calcification for all acquisitions and lesion parameters save one: calcium density image for a 132.6 mGy acquisition of a 1.0 cm cerebrum lesion. Decreased 68 keV monoenergetic image measurements were significantly associated with increased probability of being calcification. This is most likely due to hemorrhage lesion models having slightly higher attenuations than calcification models but still within our 2 HU matching constraint for the differentiation study (Chapter 4.2.4.2).

Coefficients of the multivariate logistic regression model can be found in Table 5.4. For a specific lesion and acquisition, the coefficients form a formula describing the point estimate of a lesions probability of being calcification (Equation 11, Equation 12). While the

coefficients themselves have 95% upper confidence levels (UCL) and 95% lower confidence levels (LCL), no estimate can be made on the confidence interval of the lesion probability.

Table 5.3: Summary of multivariate logistic regression model results correlating water, calcium, and 68 keV measurements with probability of the unknown lesion being calcification. Odds ratio is for each unit increase in the measurement. Odds ratio greater than 1 means an increased probability of being calcification. LCL and UCL refer to the lower and upper confidence limits, respectively.

Lesion Location	$CTDI_{vol}$ (mGy)	Lesion Size (cm)	DECT Image Type	Odds Ratio	95% LCL	95% UCL	P-value
Cerebrum	67	0.5	Water	1.59	1.51	1.68	<.0001
			Calcium	2.10	1.85	2.38	<.0001
			68 keV	0.72	0.69	0.76	<.0001
		1	Water	1.65	1.60	1.71	<.0001
			Calcium	1.54	1.42	1.67	<.0001
			68 keV	0.83	0.80	0.86	<.0001
		1.5	Water	1.98	1.92	2.04	<.0001
			Calcium	1.84	1.71	1.97	<.0001
			68 keV	0.78	0.76	0.80	<.0001
	105	0.5	Water	1.39	1.32	1.46	<.0001
			Calcium	1.27	1.11	1.46	0.0004
			68 keV	0.88	0.84	0.93	<.0001
		1	Water	1.68	1.62	1.75	<.0001
			Calcium	1.14	1.03	1.26	0.01
			68 keV	0.92	0.89	0.96	<.0001
		1.5	Water	2.54	2.44	2.64	<.0001
			Calcium	1.85	1.69	2.03	<.0001
			68 keV	0.76	0.74	0.79	<.0001
	132	0.5	Water	1.46	1.38	1.54	<.0001
			Calcium	1.37	1.19	1.58	<.0001
			68 keV	0.86	0.81	0.91	<.0001
		1	Water	1.66	1.59	1.73	<.0001
			Calcium	1.10	0.99	1.22	0.06
			68 keV	0.94	0.90	0.98	0.002
		1.5	Water	2.57	2.46	2.68	<.0001
			Calcium	1.49	1.35	1.65	<.0001
			68 keV	0.84	0.81	0.87	<.0001
Skull Base	67	1.5	Water	1.63	1.60	1.67	<.0001
			Calcium	1.87	1.78	1.97	<.0001
			68 keV	0.77	0.76	0.79	<.0001
	105	1.5	Water	1.96	1.91	2.02	<.0001
			Calcium	1.98	1.85	2.11	<.0001
			68 keV	0.75	0.73	0.77	<.0001
	132	1.5	Water	2.06	2.00	2.12	<.0001
			Calcium	1.98	1.85	2.12	<.0001
			68 keV	0.75	0.73	0.77	<.0001

Table 5.4: Summary of logistic regression model coefficients based on analysis of Study 1 differentiation data (Chapter 4). These coefficients work with Equations 12-14 to calculate the probability of being calcification based on an unknown lesion's mean 3D-DECT measurement.

Lesion Location	$CTDI_{vol}$ (mGy)	Lesion Size (cm)	Coefficient	Estimate	95% LCL	95% UCL
Cerebrum	67	0.5	b_0 (Intercept)	-467.408	-517.763	-417.052
			b_1 (Water)	0.4656	0.4153	0.5159
			b_2 (Calcium)	0.7407	0.6145	0.8669
			b_3 (68 keV)	-0.3233	-0.3737	-0.273
		1	b_0 (Intercept)	-507.724	-541.804	-473.644
			b_1 (Water)	0.5025	0.4685	0.5365
			b_2 (Calcium)	0.4331	0.3506	0.5155
			b_3 (68 keV)	-0.188	-0.22	-0.1561
		1.5	b_0 (Intercept)	-690.804	-720.042	-661.566
			b_1 (Water)	0.6829	0.6538	0.7121
			b_2 (Calcium)	0.6082	0.5386	0.6778
			b_3 (68 keV)	-0.2475	-0.2744	-0.2206
	105	0.5	b_0 (Intercept)	-330.154	-382.396	-277.912
			b_1 (Water)	0.3271	0.2749	0.3793
			b_2 (Calcium)	0.2423	0.107	0.3776
			b_3 (68 keV)	-0.1244	-0.1781	-0.0707
		1	b_0 (Intercept)	-528.486	-569.166	-487.806
			b_1 (Water)	0.5215	0.4809	0.5621
			b_2 (Calcium)	0.1315	0.0317	0.2314
			b_3 (68 keV)	-0.0782	-0.1168	-0.0397
		1.5	b_0 (Intercept)	-943.308	-983.62	-902.997
			b_1 (Water)	0.9316	0.8914	0.9718
			b_2 (Calcium)	0.6177	0.5252	0.7102
			b_3 (68 keV)	-0.2682	-0.304	-0.2323
	132	0.5	b_0 (Intercept)	-381.112	-434.797	-327.426
			b_1 (Water)	0.3777	0.324	0.4314
			b_2 (Calcium)	0.3165	0.1761	0.4569
			b_3 (68 keV)	-0.1521	-0.2079	-0.0963
		1	b_0 (Intercept)	-512.821	-553.609	-472.033
			b_1 (Water)	0.506	0.4653	0.5467
			b_2 (Calcium)	0.0953	-0.0057	0.1963
			b_3 (68 keV)	-0.0612	-0.1003	-0.0222
		1.5	b_0 (Intercept)	-956.451	-1000.16	-912.743
			b_1 (Water)	0.943	0.8994	0.9866
			b_2 (Calcium)	0.3992	0.299	0.4994
			b_3 (68 keV)	-0.175	-0.2139	-0.1362
Skull Base	67	1.5	b_0 (Intercept)	-493.734	-514.718	-472.75
			b_1 (Water)	0.4915	0.4706	0.5125
			b_2 (Calcium)	0.6266	0.5759	0.6772
			b_3 (68 keV)	-0.2599	-0.2797	-0.2402
	105	1.5	b_0 (Intercept)	-678.958	-706.174	-651.742
			b_1 (Water)	0.6745	0.6474	0.7017
			b_2 (Calcium)	0.681	0.617	0.745
			b_3 (68 keV)	-0.2863	-0.3111	-0.2614
	132	1.5	b_0 (Intercept)	-725.187	-754.321	-696.053
			b_1 (Water)	0.7204	0.6913	0.7495
			b_2 (Calcium)	0.6854	0.6172	0.7535
			b_3 (68 keV)	-0.2858	-0.3122	-0.2593

5.2.3 Classification of Unknown Lesions

5.2.3.1 Binary Classification

Geometric Bisector Method

Given binary classification (hemorrhage or calcification), 98% of unknown lesions/acquisition combinations investigated (n=120) were classified correctly using the GB method. Two lesions/acquisition combinations were misclassified: 49.9 HU, 0.5 cm hemorrhage in the cerebrum imaged with 67 mGy and the same lesion model imaged with 132.6 mGy. 60% (73/120) of those were classified with greater than 90% confidence, while 74% (90/120) were classified with greater than 80% confidence. GB confidence for all unknown lesions based on composition, location, size and attenuation can be seen in Figure 5.2.

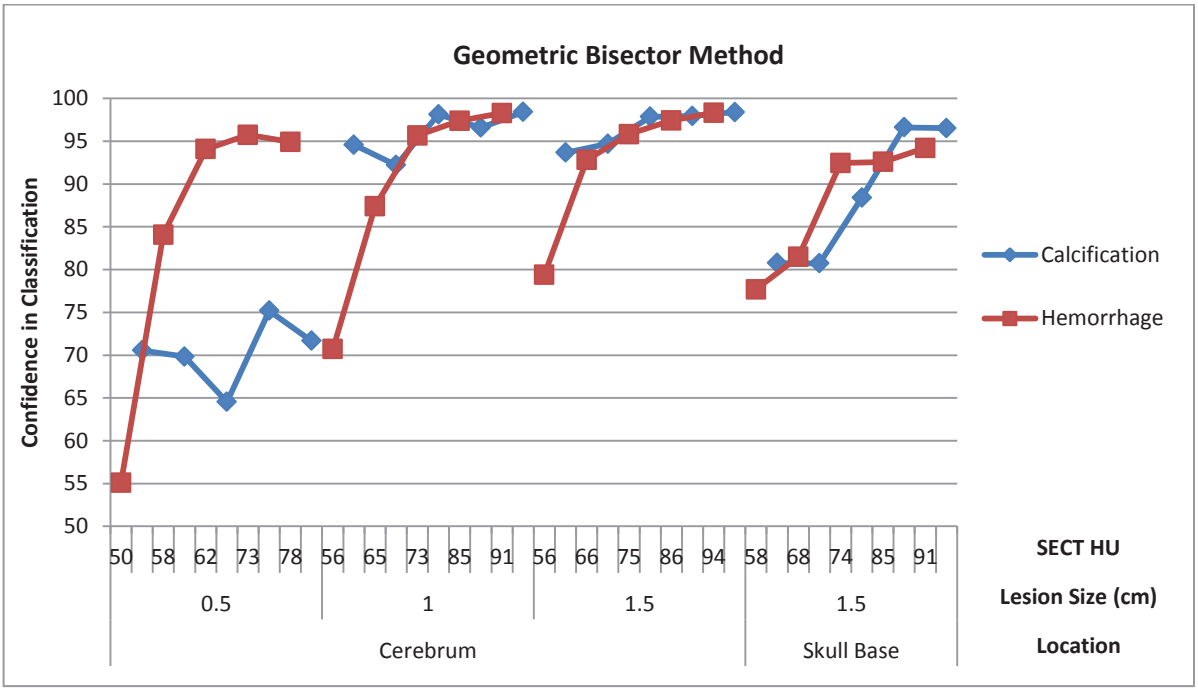

Figure 5.2: Classification confidence results for all unknown lesion models using the geometric bisector method. Calcification lesion models are shown in blue while hemorrhage models are shown in red.

Generalized Geometric Bisector Method

96% of unknown lesions/acquisition combinations investigated (n=120) were classified correctly using the GGB method. Three lesions/acquisition combinations were misclassified: 49.9 HU, 0.5 cm hemorrhage in the cerebrum imaged with 67 mGy, 105.6 mGy and 132.6 mGy. 61% (75/120) of those were classified with greater than 90% confidence, while 75% (92/120) were classified with greater than 80% confidence. GGB confidence for all unknown lesions based on composition, location, size and attenuation can be seen in Figure 5.3.

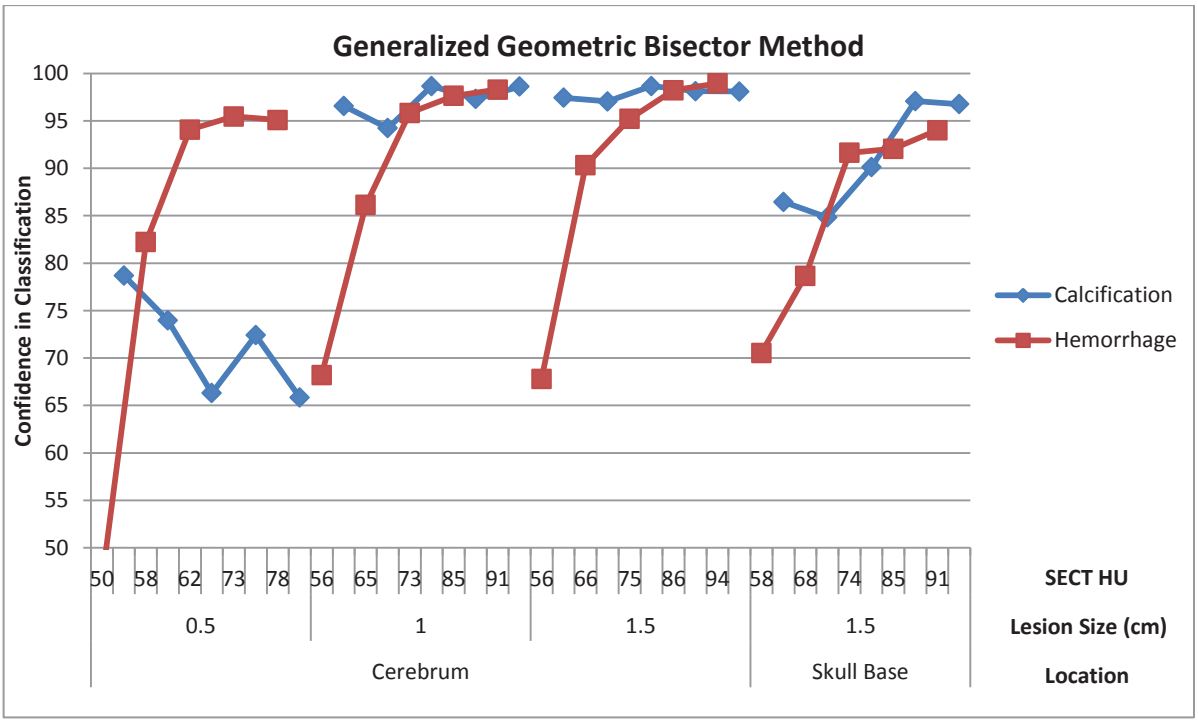

Figure 5.3: Classification confidence results for all unknown lesion models using the generalized geometric bisector method. Calcification lesion models are shown in blue while hemorrhage models are shown in red.

Probability Distribution Method

98% of unknown lesions/acquisition combinations investigated (n=120) were classified correctly using the probability distribution (PD) method. The two misclassified lesion/acquisition combinations were the same as those misclassified by the GB method above. Again, similarly to the GB and GGB methods, 59% (71/120) of lesion/acquisition combinations were classified with greater than 90% confidence, and 74% (90/120) were classified with greater than 80% confidence. Of the lesion/acquisition combinations classified with greater than 90% confidence, 62 were so classified using all three methods (84%, 83% and 87% agreement for GB, GGB and PD methods respectively). Of the lesion/acquisition combinations classified with greater than 80% confidence, 84 were so classified using all three methods (93%, 91% and 93% for GB, GGB, and PD methods respectively). PD confidence for all unknown lesions based on composition, location, size and attenuation can be seen in Figure 5.4.

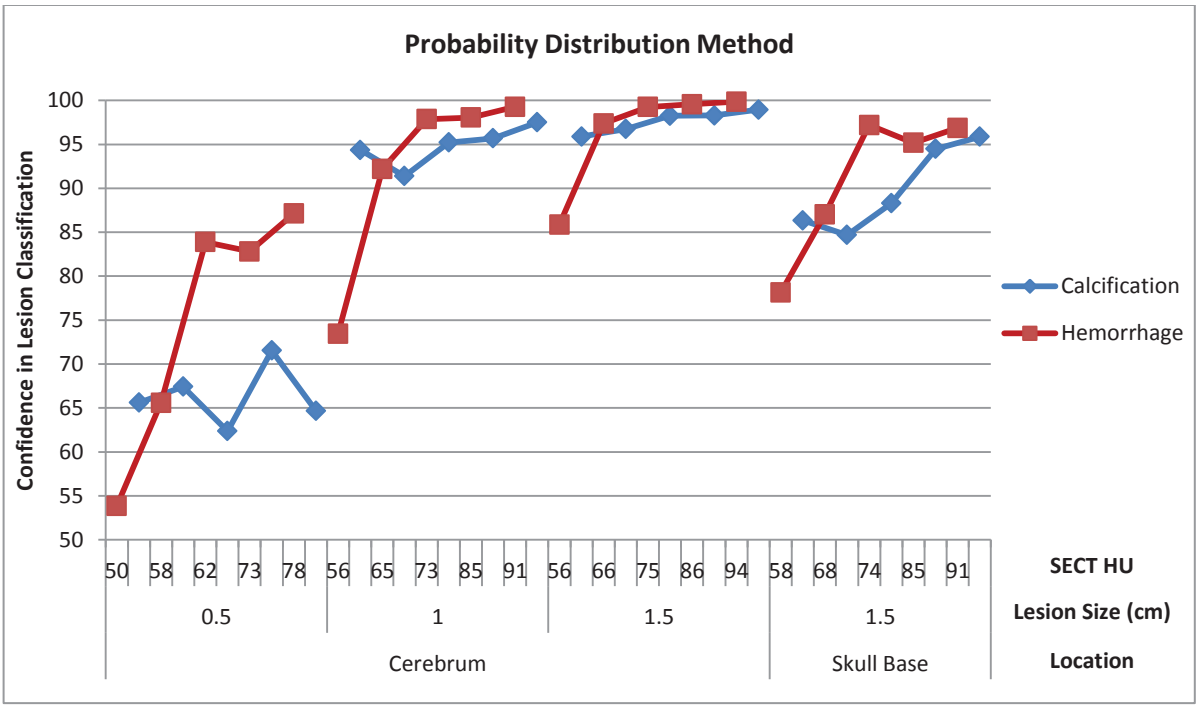

Figure 5.4: Classification confidence results for all unknown lesion models using the probability distribution method. Calcification lesion models are shown in blue while hemorrhage models are shown in red.

5.2.3.2 Classification Trends with $CTDI_{vol}$

Geometric Bisector Method

GB confidence trends with acquisition $CTDI_{vol}$ for all hemorrhage lesion models (based on lesion composition not method classification) can be seen in Figure 5.5. GB confidence trends with acquisition $CTDI_{vol}$ for all calcification lesion models can be seen in Figure 5.6.

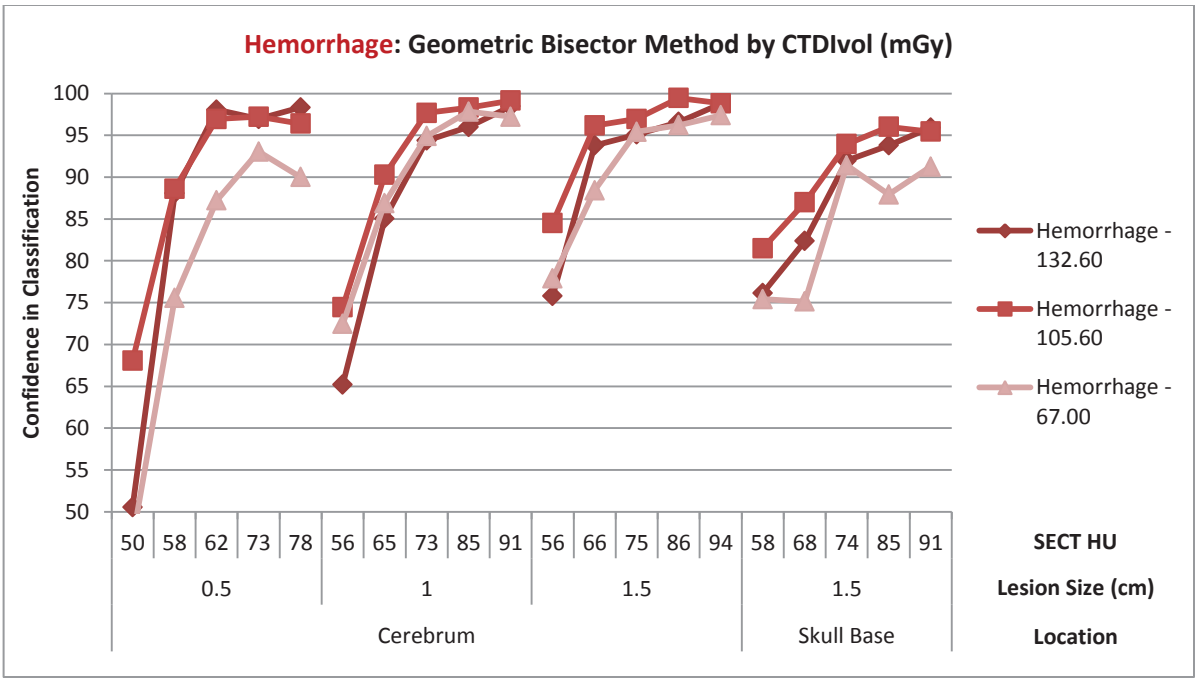

Figure 5.5: Geometric bisector confidence in classification of hemorrhage unknown lesions. Darker shades of red indicate higher $CTDI_{vol}$ levels.

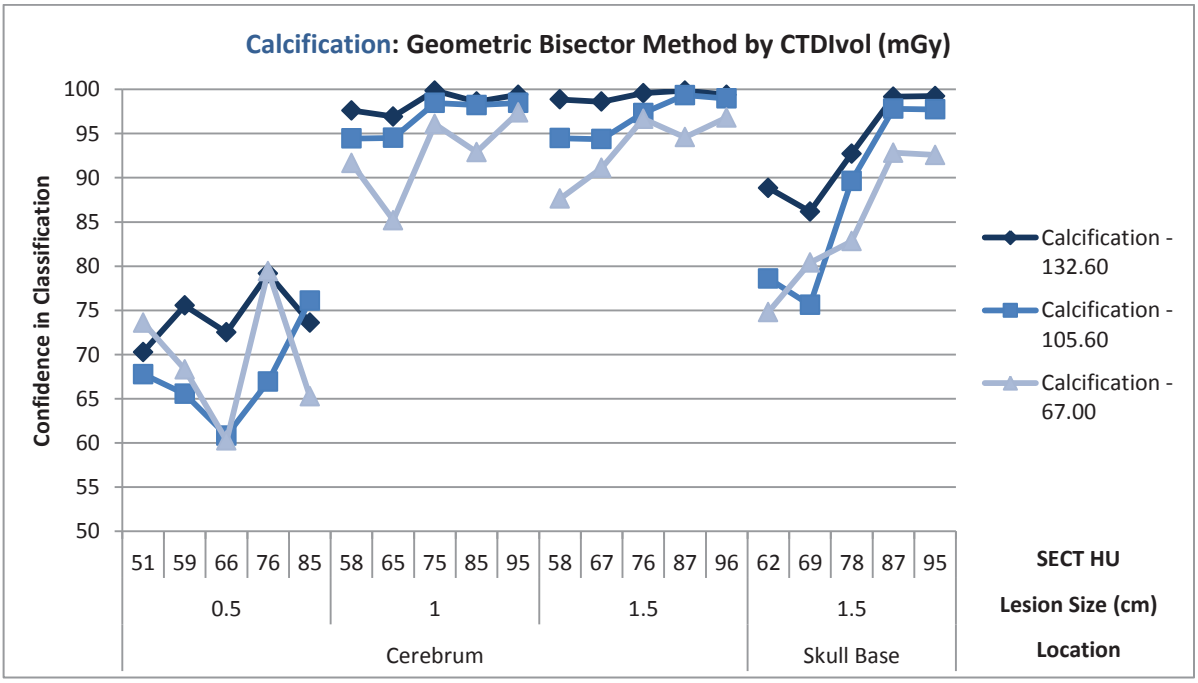

Figure 5.6: Geometric bisector confidence in classification of calcification unknown lesions. Darker shades of blue indicate higher $CTDI_{vol}$ levels.

Second order power fits of GB confidence data for all available lesion/acquisition combinations resulted in the SECT attenuation (HU) necessary for 90% classification confidence (Table 5.5). 0.5 cm calcification lesions in the cerebrum could not be classified with greater than 90% confidence using any of the available $CTDI_{vol}$ levels. 1.0 and 1.5 cm calcifications in the cerebrum could be classified with 90% confidence down to the minimum investigated SECT attenuation (HU) using either 105.6 or 132.6 mGy $CTDI_{vol}$.

Table 5.5: SECT attenuation (HU) necessary for 90% classification confidence using the GB method. Gray regions represent lesion/acquisition combinations that would only be classified with 90% confidence above the 100 HU limit imposed by SECT. Green regions represent lesion/acquisition combinations that would be classified with 90% confidence below the minimum SECT investigated. White regions represent lesion/acquisition combinations that would be classified with 90% confidence within the investigated lesion attenuation range. Text in red indicates a curve fit R^2 with less than 0.8.

	Lesion Composition	Calcification				Hemorrhage			
	Lesion Location	Cerebrum			Skull Base	Cerebrum			Skull Base
	Lesion Size (cm)	0.5	1.0	1.5	1.5	0.5	1.0	1.5	1.5
CTDIvol (mGy)	67.0	>100 HU	63 HU	62 HU	87 HU	70 HU	68 HU	67 HU	87 HU
	105.6	>100 HU	58 HU	58 HU	81 HU	58 HU	64 HU	59 HU	70 HU
	132.6	>100 HU	58 HU	58 HU	71 HU	59 HU	69 HU	63 HU	76 HU

Second order power fits of GB confidence data for all available lesion/acquisition combinations resulted in the SECT attenuation (HU) necessary for 80% classification confidence (Table 5.6). 1.0 and 1.5 cm calcification lesions in the cerebrum could be classified with 80% confidence down the minimum investigated SECT attenuation (HU) using any of the available $CTDI_{vol}$ levels. 1.5 cm hemorrhage lesions in either the cerebrum or skull base could be classified with 80% confidence down to the minimum investigated SECT attenuation (HU) using either 105.6 or 132.6 mGy $CTDI_{vol}$.

Table 5.6: SECT attenuation (HU) necessary for 80% classification confidence using the GB method. Gray regions represent lesion/acquisition combinations that would only be classified with 80% confidence above the 100 HU limit imposed by SECT. Green regions represent lesion/acquisition combinations that would be classified with 80% confidence below the minimum SECT investigated. White regions represent lesion/acquisition combinations that would be classified with 80% confidence within the investigated lesion attenuation range. Text in red indicates a curve fit R^2 with less than 0.8.

	Lesion Composition	Calcification				Hemorrhage			
	Lesion Location	Cerebrum			Skull Base	Cerebrum			Skull Base
	Lesion Size (cm)	0.5	1.0	1.5	1.5	0.5	1.0	1.5	1.5
CTDIvol (mGy)	67.0	>100 HU	58 HU	58 HU	70 HU	68 HU	59 HU	57 HU	65 HU
	105.6	>100 HU	58 HU	58 HU	67 HU	60 HU	57 HU	56 HU	58 HU
	132.6	>100 HU	58 HU	58 HU	62 HU	72 HU	61 HU	56 HU	58 HU

Generalized Geometric Bisector Method

GGB confidence trends with acquisition $CTDI_{vol}$ for all hemorrhage lesion models (based on lesion composition not method classification) can be seen in Figure 5.7. GB confidence trends with acquisition $CTDI_{vol}$ for all calcification lesion models can be seen in Figure 5.8.

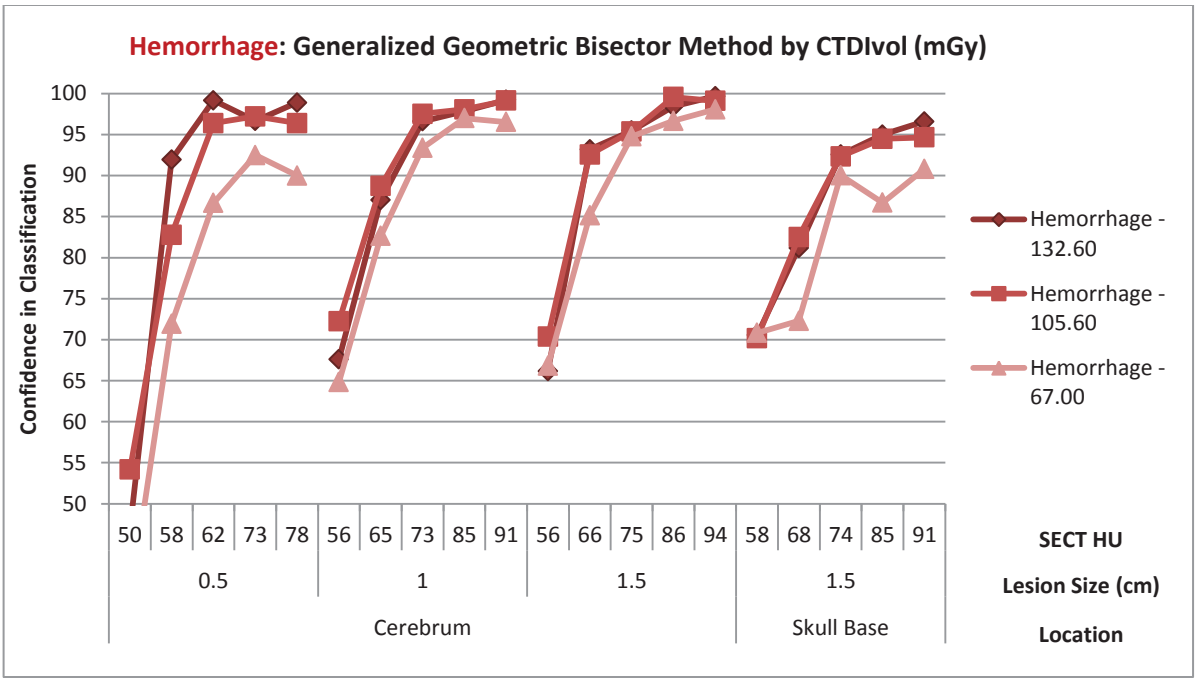

Figure 5.7: Generalized geometric bisector confidence in classification of hemorrhage unknown lesions. Darker shades of red indicate higher $CTDI_{vol}$ levels.

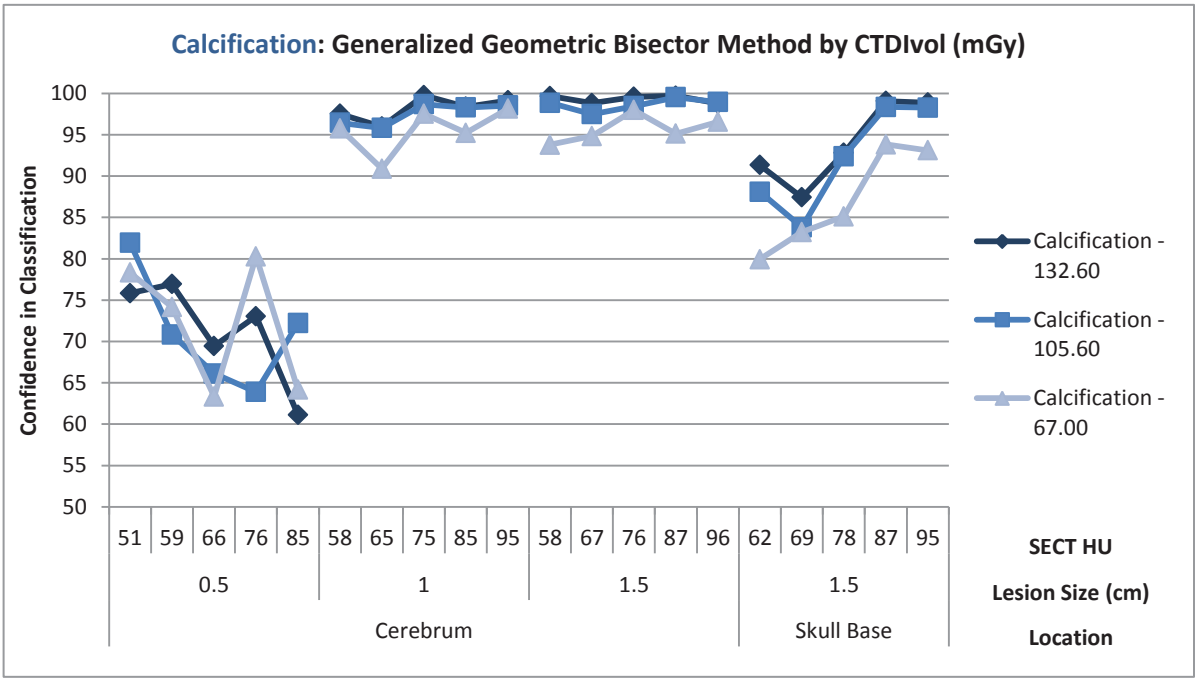

Figure 5.8: Generalized geometric bisector confidence in classification of calcification unknown lesions. Darker shades of red indicate higher $CTDI_{vol}$ levels.

Second order power fits of GGB confidence data for all available lesion/acquisition combinations resulted in the SECT attenuation (HU) necessary for 90% classification confidence (Table 5.7). 0.5 cm calcification lesions in the cerebrum could not be classified with greater than 90% confidence using any of the available $CTDI_{vol}$ levels. 1.0 and 1.5 cm calcifications in the cerebrum could be classified with 90% confidence down to the minimum investigated SECT attenuation (HU) using any of the investigated $CTDI_{vol}$ levels.

Table 5.7: SECT attenuation (HU) necessary for 90% classification confidence using the GGB method. Gray regions represent lesion/acquisition combinations that would only be classified with 90% confidence above the 100 HU limit imposed by SECT. Green regions represent lesion/acquisition combinations that would be classified with 90% confidence below the minimum SECT investigated. White regions represent lesion/acquisition combinations that would be classified with 90% confidence within the investigated lesion attenuation range. Text in red indicates a curve fit R^2 with less than 0.8.

	Lesion Composition	Calcification				Hemorrhage			
	Lesion Location	Cerebrum			Skull Base	Cerebrum			Skull Base
	Lesion Size (cm)	0.5	1	1.5	1.5	0.5	1	1.5	1.5
CTDIvol (mGy)	67.0	>100 HU	58 HU	58 HU	85 HU	70 HU	71 HU	70 HU	89 HU
	105.6	>100 HU	58 HU	58 HU	74 HU	60 HU	65 HU	64 HU	75 HU
	132.6	>100 HU	58 HU	58 HU	66 HU	59 HU	67 HU	65 HU	75 HU

Second order power fits of GGB confidence data for all available lesion/acquisition combinations resulted in the SECT attenuation (HU) necessary for 80% classification confidence (Table 5.8). All calcification lesions greater than 0.5 cm in diameter could be classified with 80% confidence down the minimum investigated SECT attenuation (HU) using any of the available $CTDI_{vol}$ levels. Hemorrhage lesions of any size in the cerebrum could be classified with 80% confidence down to approximately 60 HU using any of the

$CTDI_{vol}$ levels investigated. Hemorrhage lesions in the skull base could be classified with 80% confidence down to approximately 70 HU using any of the $CTDI_{vol}$ values investigated.

Table 5.8: SECT attenuation (HU) necessary for 80% classification confidence using the GGB method. Gray regions represent lesion/acquisition combinations that would only be classified with 90% confidence above the 100 HU limit imposed by SECT. Green regions represent lesion/acquisition combinations that would be classified with 90% confidence below the minimum SECT investigated. White regions represent lesion/acquisition combinations that would be classified with 90% confidence within the investigated lesion attenuation range. Text in red indicates a curve fit R^2 with less than 0.8.

	Lesion Composition	Calcification				Hemorrhage			
	Lesion Location	Cerebrum			Skull Base	Cerebrum			Skull Base
	Lesion Size (cm)	0.5	1	1.5	1.5	0.5	1	1.5	1.5
CTDIvol (mGy)	67	>100 HU	58 HU	58 HU	62 HU	60 HU	62 HU	62 HU	70 HU
	105.6	>100 HU	58 HU	58 HU	62 HU	55 HU	59 HU	59 HU	64 HU
	132.6	>100 HU	58 HU	58 HU	62 HU	55 HU	60 HU	59 HU	65 HU

Probability Distribution Method

PD confidence trends with acquisition $CTDI_{vol}$ for all hemorrhage lesion models (based on lesion composition not method classification) can be seen in Figure 5.9. PD confidence trends with acquisition $CTDI_{vol}$ for all calcification lesion models can be seen in Figure 5.10.

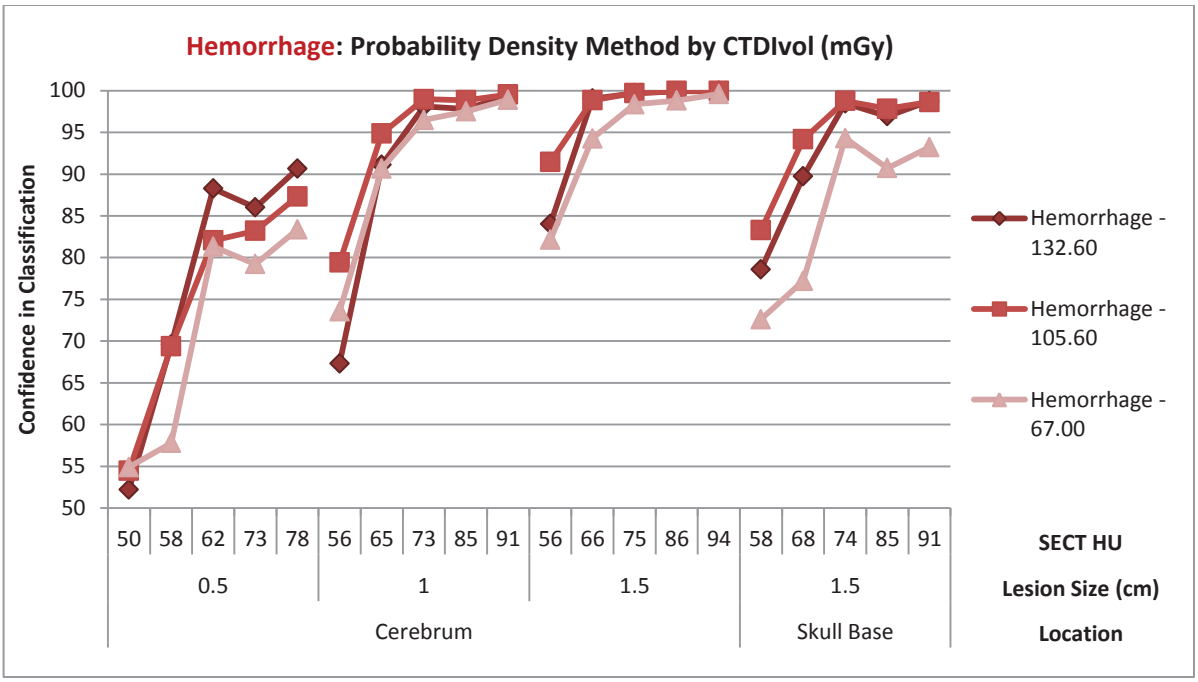

Figure 5.9: Probability distribution confidence in classification of hemorrhage unknown lesions. Darker shades of red indicate higher $CTDI_{vol}$ levels.

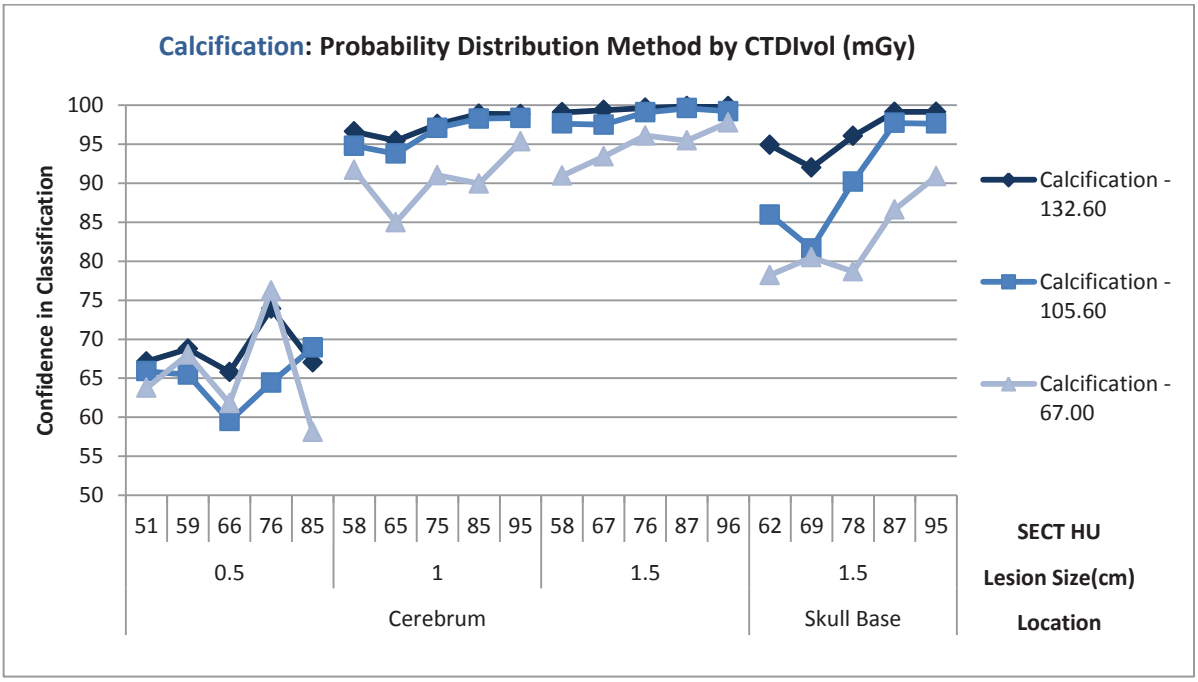

Figure 5.10: Probability distribution confidence in classification of calcification unknown lesions. Darker shades of blue indicate higher $CTDI_{vol}$ levels.

Second order power fits of PD confidence data for all available lesion/acquisition combinations resulted in the SECT attenuation (HU) necessary for 90% classification confidence (Table 5.9). With the exception of hemorrhage lesions imaged using 132.6 mGy, 0.5 cm cerebrum lesions could not be classified with greater than 90% confidence using any of the available $CTDI_{vol}$ levels. 1.5 cm calcifications in the cerebrum could be classified with 90% confidence down to the minimum investigated SECT attenuation (HU) using all $CTDI_{vol}$ levels investigated. 1.5 cm cerebrum lesions of either calcification or hemorrhage composition could be classified with greater than 90% confidence down to the minimum investigated SECT attenuation (HU) using 132.6 mGy $CTDI_{vol}$.

Table 5.9: SECT attenuation (HU) necessary for 90% classification confidence using the PD method. Gray regions represent lesion/acquisition combinations that would only be classified with 90% confidence above the 100 HU limit imposed by SECT. Green regions represent lesion/acquisition combinations that would be classified with 90% confidence below the minimum SECT investigated. White regions represent lesion/acquisition combinations that would be classified with 90% confidence within the investigated lesion attenuation range. Text in red indicates a curve fit R^2 with less than 0.8.

	Lesion Composition	Calcification				Hemorrhage			
	Lesion Location	Cerebrum			Skull Base	Cerebrum			Skull Base
	Lesion Size (cm)	0.5	1.0	1.5	1.5	0.5	1.0	1.5	1.5
CTDIvol (mGY)	67.0	>100 HU	79 HU	58 HU	94 HU	>100 HU	64 HU	61 HU	79 HU
	105.6	>100 HU	58 HU	58 HU	78 HU	>100 HU	61 HU	55 HU	62 HU
	132.6	>100 HU	58 HU	58 HU	62 HU	77 HU	64 HU	56 HU	66 HU

Second order power fits of PD confidence data for all available lesion/acquisition combinations resulted in the SECT attenuation (HU) necessary for 80% classification confidence (Table 5.10). 1.5 cm lesions in the cerebrum could be classified with greater than 80% confidence down to the minimum investigated SECT attenuation (HU) for both

lesion compositions and all $CTDI_{vol}$ levels investigated. 1.0 cm calcification lesions in the cerebrum were classifiable with greater than 80% confidence down to the minimum SECT attenuation (HU) investigated. 1.0 cm hemorrhage lesions in the cerebrum resulted in SECT attenuation (HU) necessary for 80% confidence within 2 HU of the minimum investigated value. Both lesion compositions in the skull base were classified with greater than 80% confidence down to the minimum investigated SECT attenuation (HU) for both 105.6 and 132.6 mGy $CTDI_{vol}$ acquisitions.

Table 5.10: SECT attenuation (HU) necessary for 80% classification confidence using the PD method. Gray regions represent lesion/acquisition combinations that would only be classified with 80% confidence above the 100 HU limit imposed by SECT. Green regions represent lesion/acquisition combinations that would be classified with 80% confidence below the minimum SECT investigated. White regions represent lesion/acquisition combinations that would be classified with 80% confidence within the investigated lesion attenuation range. Text in red indicates a curve fit R^2 with less than 0.8.

	Lesion Composition	Calcification				Hemorrhage			
	Lesion Location	Cerebrum			Skull Base	Cerebrum			Skull Base
	Lesion Size (cm)	0.5	1.0	1.5	1.5	0.5	1.0	1.5	1.5
CTDIvol (mGY)	67.0	>100 HU	58 HU	58 HU	74 HU	85 HU	58 HU	56 HU	65 HU
	105.6	>100 HU	58 HU	58 HU	62 HU	76 HU	57 HU	56 HU	58 HU
	132.6	>100 HU	58 HU	58 HU	62 HU	72 HU	59 HU	56 HU	58 HU

5.2.4 Inter-Method Correlations

Inter-method correlation of geometric bisector and probability distribution methods resulted in a CV correlation of 6.2% and R^2 linearity of 0.824. Repeated analysis for subsets of the data based on all available parameters yielded one major source of variability based on R^2 cutoff criteria: hemorrhage lesion models (Table 5.11). Bland-Altman and correlation graphs for the full data as well as the hemorrhage lesion model data

can be seen in Figure 5.11. Removing these data from analysis reduced the overall CV correlation to 3.9% and increased the R^2 linearity to 0.938. While the estimation of inter-method correlation for only a single lesion model type is not particularly informative, it was assessed in an effort to provide uniform analysis of correlation with and without major sources of variability across both the differentiation (Chapter 4) and unknown lesion studies.

Table 5.11: Sorted results of GB vs PD inter-method Bland-Altman analysis for subsets of data based on available protocol and lesion parameters. Parameters and values above the double line indicate worse correlation or linearity than the full data set while those below the double line indicate improved correlation or linearity. Text in red indicates a major source of variability based on CV or R^2 cutoff criteria.

CV - Correlation		
Full Data CV	**Criteria**	**Cutoff**
6.25	**150%**	**9.37**

Parameter	Value	CV
Lesion Model	0.5 cm Cerebrum	8.2
Model Composition	Hemorrhage	7.9
$CTDI_{vol}$	105.6	6.8
RotationTime	0.8	6.8
$CTDI_{vol}$	132.6	6.2
RotationTime	0.9	6.2
$CTDI_{vol}$	67	5.8
RotationTime	0.7	5.8
Model Composition	Calcification	3.9
Lesion Model	1.5 cm Skull Base	3.8
Lesion Model	1.0 cm Cerebrum	2.6
Lesion Model	1.5 cm Cerebrum	2.3

Rsquared - Linearity	
Full Data R^2	**Criteria**
0.8242	**< 0.75**

Parameter	Value	R^2
Model Composition	Hemorrhage	0.705
$CTDI_{vol}$	105.6	0.791
RotationTime	0.8	0.791
$CTDI_{vol}$	132.6	0.820
RotationTime	0.9	0.820
Lesion Model	1.5 cm Skull Base	0.831
Lesion Model	0.5 cm Cerebrum	0.834
$CTDI_{vol}$	67	0.850
RotationTime	0.7	0.850
Lesion Model	1.5 cm Cerebrum	0.918
Lesion Model	1.0 cm Cerebrum	0.925
Model Composition	Calcification	0.938

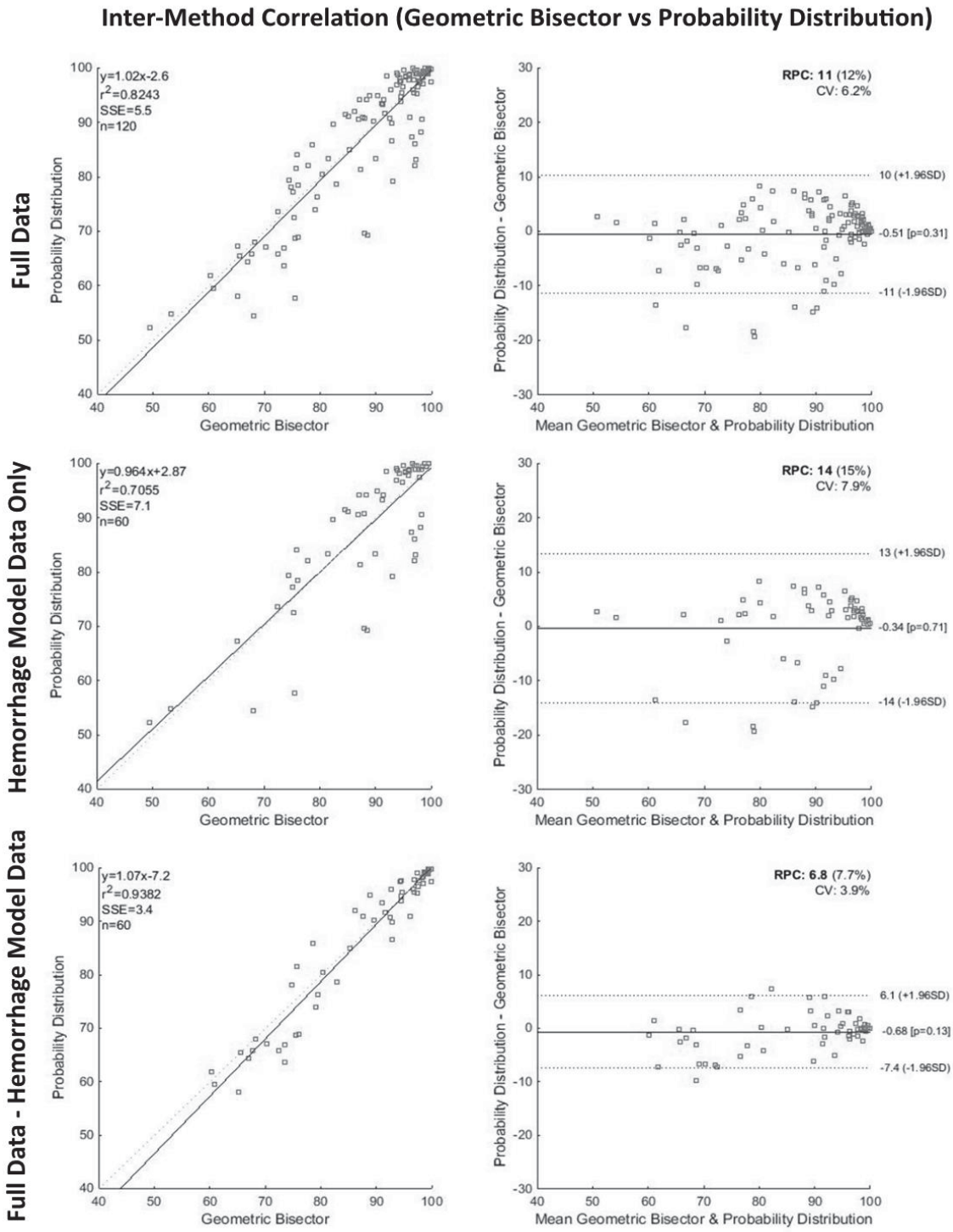

Figure 5.11: Bland-Altman and Correlation graphs for inter-method correlation between GB and PD methods. Top: Full data results including all lesion/acquisition combinations. Middle: Results for hemorrhage lesion models, identified as a major source of variability in Table 5.11. Bottom: Results for full data excluding hemorrhage lesion model values.

Inter-method correlation of geometric bisector and generalized geometric bisector methods resulted in a CV correlation of 4.7% and R^2 linearity of 0.899. Repeated analysis for subsets of the data based on all available parameters yielded one major source of variability based on CV cutoff criteria: 0.5 cm cerebrum lesion models (Table 5.12). Bland-Altman and correlation graphs for the full data as well as the hemorrhage lesion model data can be seen in Figure 5.12. Removing these data from analysis reduced the overall CV correlation to 3.9% and decreased the R^2 linearity to 0.8608. Given the 0.5 cm cerebrum data was not identified as a major source of variability by the linearity criteria and in fact had greater linearity than the general data set, it is not surprising the linearity decreased in this way. It is likely this decrease has minimal clinical significance.

Table 5.12: Sorted results of GB vs GGB inter-method Bland-Altman analysis for subsets of data based on available protocol and lesion parameters. Parameters and values above the double line indicate worse correlation or linearity than the full data set while those below the double line indicate improved correlation or linearity. Text in red indicates a major source of variability based on CV or R^2 cutoff criteria.

CV - Correlation		
Full Data CV	**Criteria**	**Cutoff**
4.72	**150%**	**7.08**
Parameter	**Value**	**CV**
Lesion Model	0.5 cm Cerebrum	7.3
$CTDI_{vol}$	105.6	5.9
RotationTime	0.8	5.9
Lesion Model	1.5 cm Cerebrum	4.5
Model Composition	Hemorrhage	4.4
$CTDI_{vol}$	67	4.4
RotationTime	0.7	4.4
Lesion Model	1.5 cm Skull Base	4.4
Model Composition	Calcification	4.2
$CTDI_{vol}$	132.6	3.7
RotationTime	0.9	3.7
Lesion Model	1.0 cm Cerebrum	2.6

Rsquared - Linearity		
Full Data R^2	**Criteria**	
0.8990	**< 0.75**	
Parameter	**Value**	**R^2**
Lesion Model	1.5 cm Skull Base	0.802
$CTDI_{vol}$	105.6	0.818
RotationTime	0.8	0.818
Lesion Model	0.5 cm Cerebrum	0.875
Lesion Model	1.5 cm Cerebrum	0.881
Model Composition	Calcification	0.906
$CTDI_{vol}$	67	0.923
RotationTime	0.7	0.923
Lesion Model	1.0 cm Cerebrum	0.935
$CTDI_{vol}$	132.6	0.947
RotationTime	0.9	0.947
Model Composition	Hemorrhage	0.948

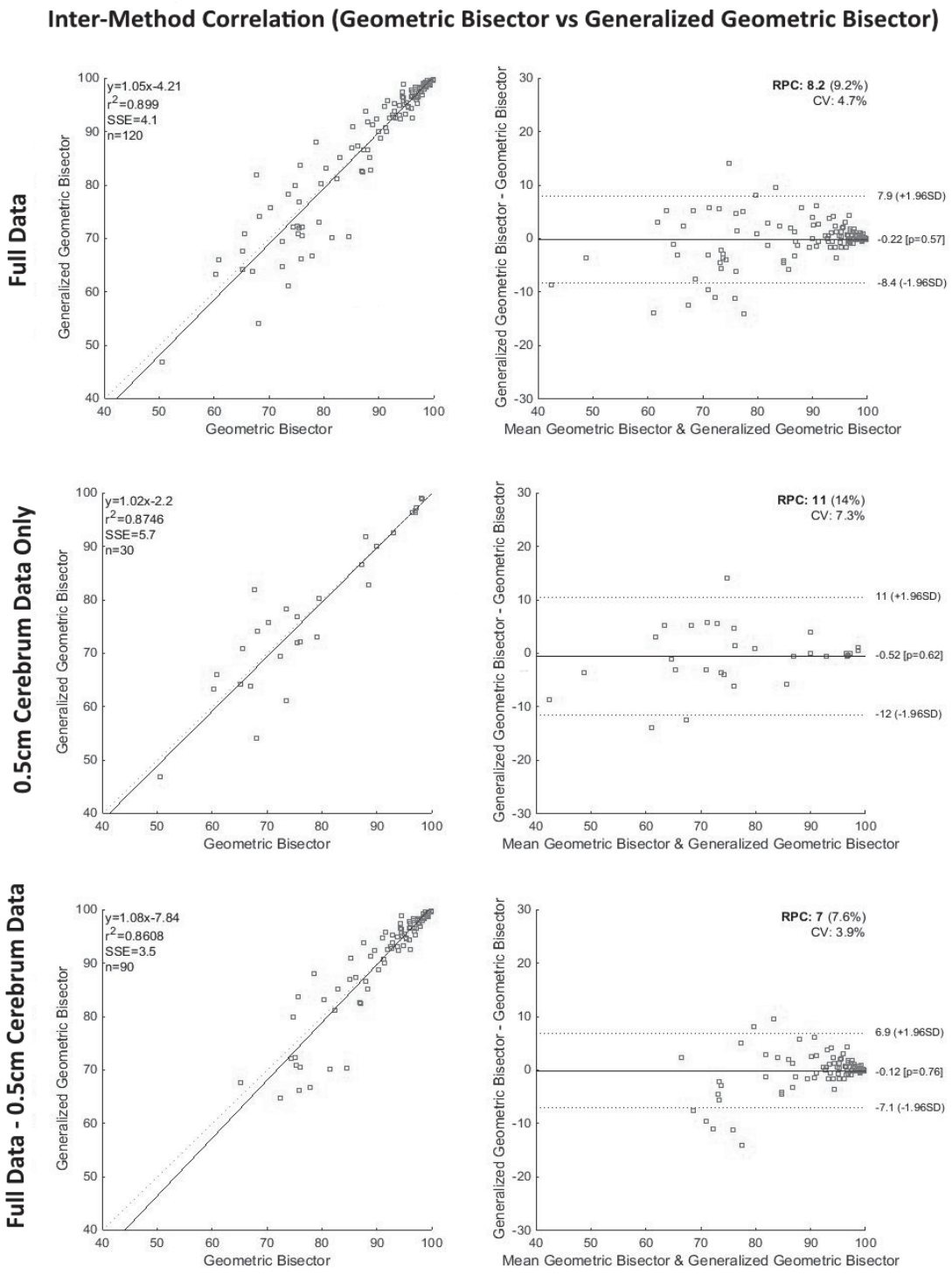

Figure 5.12: Bland-Altman and Correlation graphs for inter-method correlation between GB and GGB methods. Top: Full data results including all lesion/acquisition combinations. Middle: Results for 0.5 cm cerebrum lesion models, identified as a major source of variability in Table 5.12. Bottom: Results for full data excluding 0.5 cm cerebrum lesion model values.

5.3 Discussion

5.3.1 Effect of Lesion Parameters on Classification Confidence

Intracranial unknown lesion models 1.0 cm and larger, were correctly classified to a SECT attenuation (HU) level beyond that currently possible using SECT using DECT and either GB or PD methods. This improvement was present regardless of lesion location or $CTDI_{vol}$ used. In general, 1.0 and 1.5 cm cerebrum lesion models were correctly classified with 80% confidence down to approximately 60 HU using either GB or PD method and using any of the $CTDI_{vol}$ levels investigated. 1.5 cm skull base lesion models were correctly classified with 80% confidence down to approximately 70 HU using either GB or PD method and using any of the $CTDI_{vol}$ levels investigated.

Classification results for 0.5 cm cerebrum lesion were less encouraging, especially in the case of the calcification models. For both GB and PD methods, the classification confidence for 0.5 cm calcification models was substantially less than that of the hemorrhage models (Figure 5.13). In order to determine the cause of this difference in classification confidence, the distance of the lesion mean value to the matched-acquisition GB plane was plotted (Figure 5.14). Calcification models show reduced relative Euclidian distance to the plane within the 3D-DECT environment relative to hemorrhage models for the 0.5 cm cerebrum lesions, consistent with lower confidence in classification as defined by our methods. In addition, the 1.0 cm cerebrum, 1.5 cm cerebrum and 1.5 cm skull base results showed a decrease in distance to the plane for the low attenuation hemorrhage lesions, similar to the reduced confidence in the classification of these lesions shown in Figure 5.13. Since the pattern in distance to the plane and classification confidence is so similar, it is reasonable to assume the reduced confidence for the calcifications occurred due to their proximity to the differentiating GB plane.

It is worth noting however that the correct classification of small intracranial hemorrhage is of greater clinical importance than the correct classification of small

intracranial classification. The incorrect classification of intracranial hemorrhage as calcification would prompt physicians to administer potentially harmful anticoagulant therapies to patients with high risk of repeat brain hemorrhage. The incorrect classification of intracranial calcification as hemorrhage, on the other hand, may keep physicians from administering anticoagulant therapies however would not lead to a life threatening outcome.

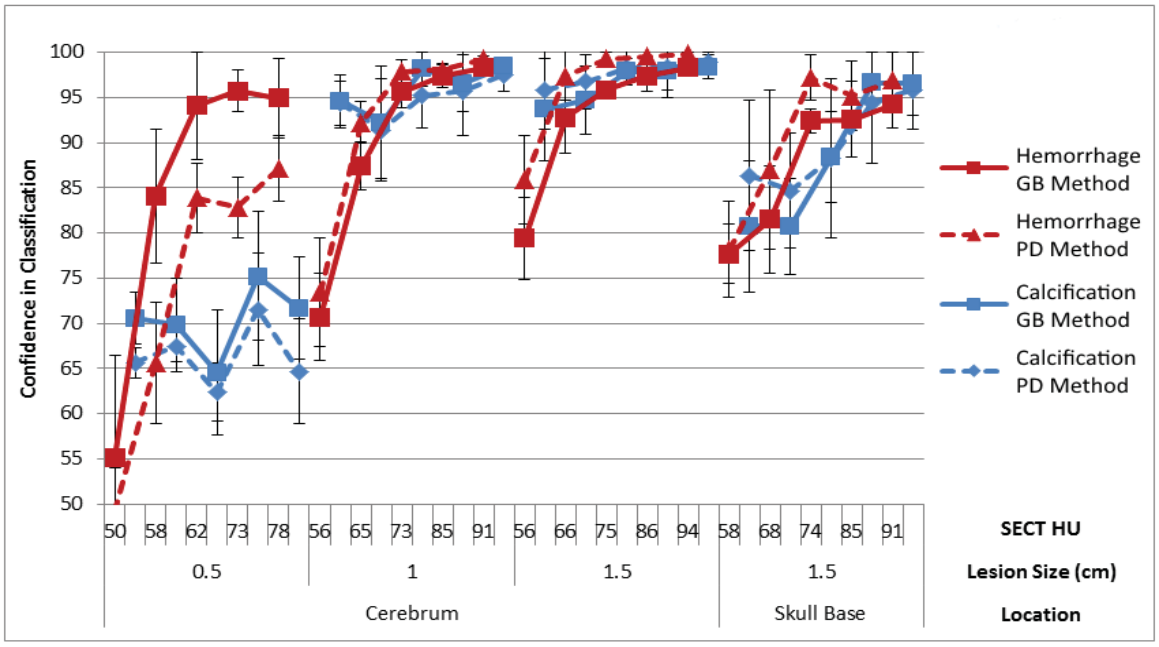

Figure 5.13: Summary of GB (solid lines) and PD (dashed lines) classification confidence based on lesion size and location. Error bars represent one SD of the $CTDI_{vol}$ levels investigated. Hemorrhage data is shown in red while calcification data is shown in blue.

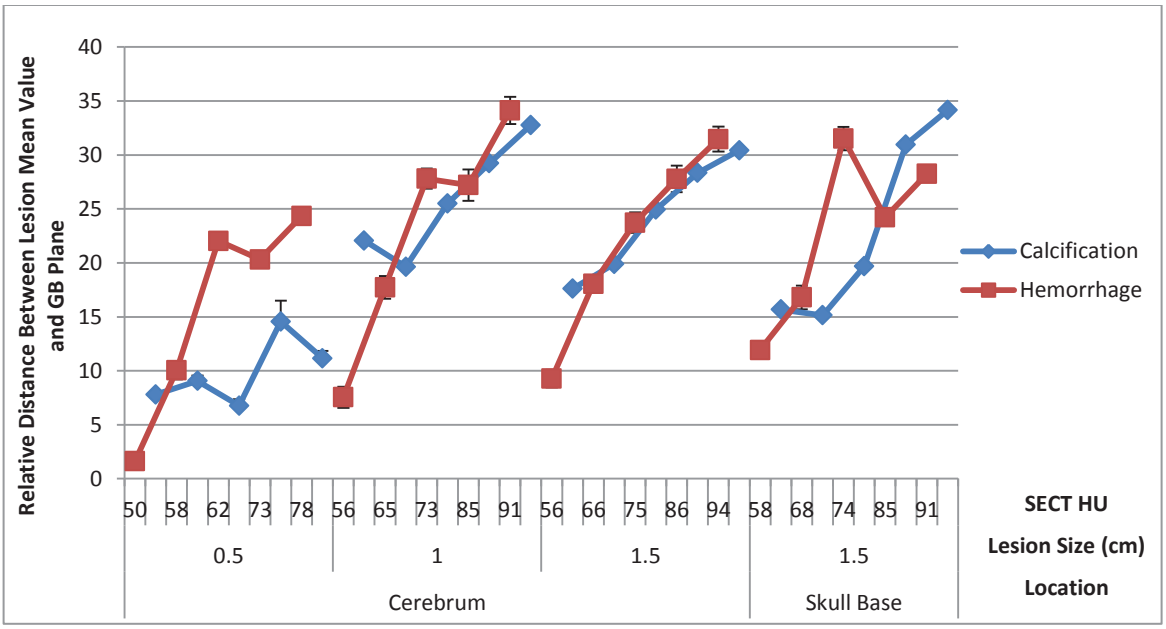

Figure 5.14: Distance between unknown lesion mean value and parameter-specific GB plane. Error bars represent one SD of the $CTDI_{vol}$ levels investigated. Hemorrhage model data is shown in red while calcification model data is shown in blue.

To assess if the unknown lesion models are in some way distinct from the differentiation lesion models used in the prior work to determine the GB plane, the mean lesion values for both populations were plotted together on a single figure. Figure 5.15 and Figure 5.16 show the relative position of the unknown lesion mean values (shown as circles) to the differentiation lesion mean values (shown as Xs) for a 0.5 cm and 1.0 cm cerebrum lesion. GB plane and fit lines for both calcification and hemorrhage derived from data collected as part of the prior differentiation work (Chapter 4) are shown as reference.

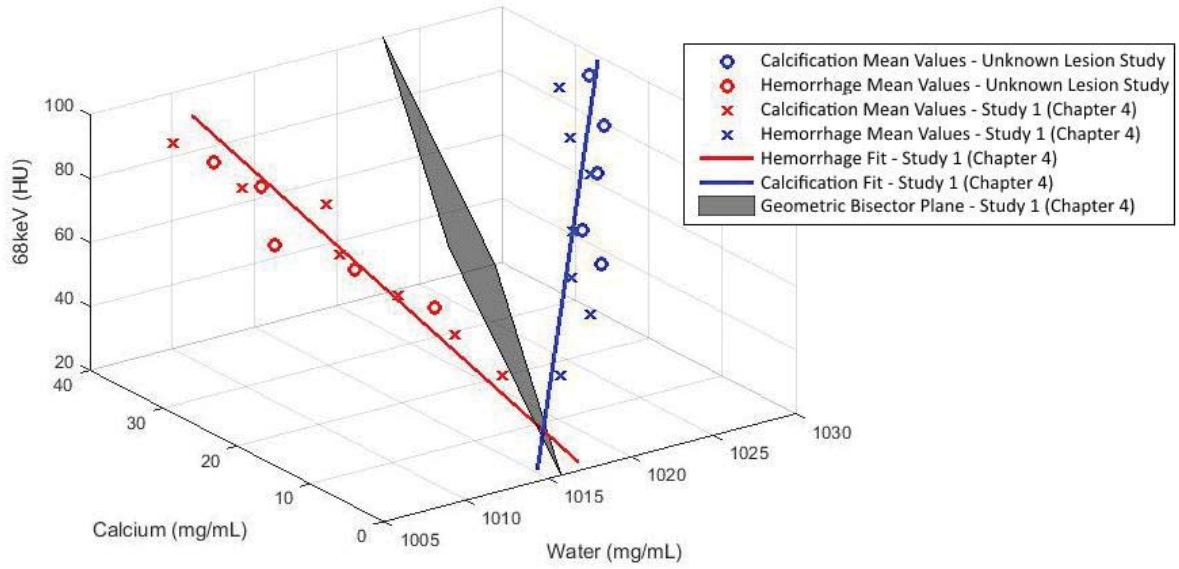

Figure 5.15: Visualization of unknown lesion and prior differentiation lesion mean values for a 1.0 cm cerebrum lesion imaged using 105.6 mGy, 3.75 mm image thickness, and Standard reconstruction filter. Acquisition matched GB plane and hemorrhage and calcification line fits shown.

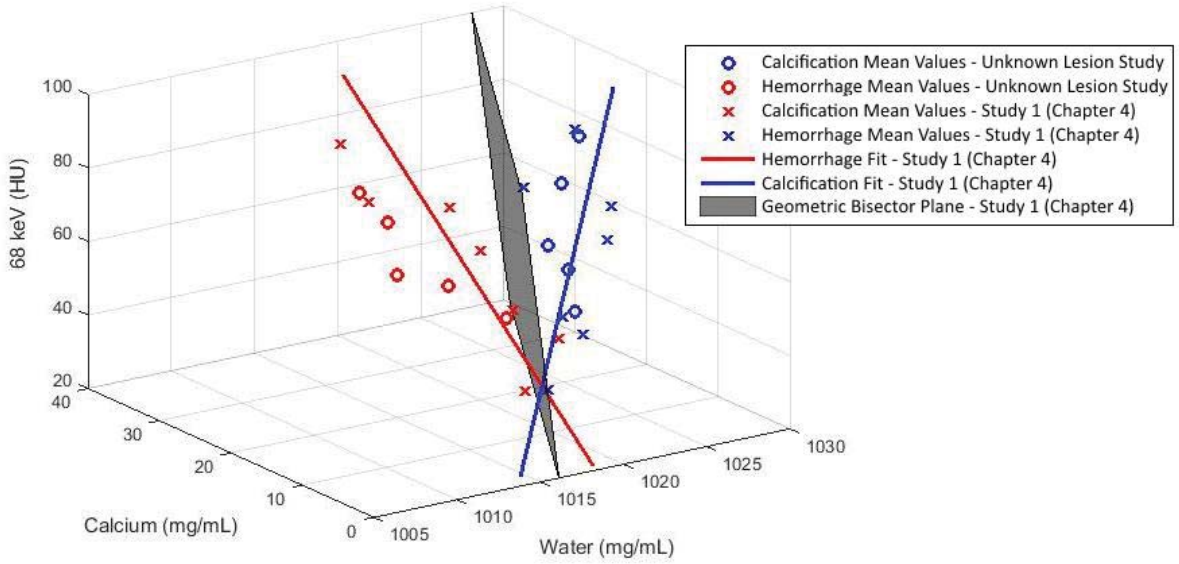

Figure 5.16: Visualization of unknown lesion and prior differentiation lesion mean values for a 0.5 cm cerebrum lesion imaged using 105.6 mGy, 3.75 mm image thickness, and Standard reconstruction filter. Acquisition matched GB plane and hemorrhage and calcification line fits shown.

Visual comparison of the unknown lesion and differentiation lesion mean values for the 1.0 cm cerebrum lesion (Figure 5.15) seems to support that both data sets occupy the same general region of space.

For both lesion types (calcification and hemorrhage) and both model populations (differentiation lesions and unknown lesions), the lesion means seemed to trend at lower 68 keV attenuation towards higher water density values than the linear fit would have predicted. This trend led to lower attenuation lesion models having skewed classification confidence due to the deviation from the linear fits used to calculate the geometric bisector plane. For example, low attenuation hemorrhage which trended towards higher water density brought the lesion mean artificially closer to the geometric bisector line and leaded to an artificially low classification confidence. On the other side, low attenuation calcification which trended towards higher water density pushed the lesion mean artificially farther from the geometric bisector line and leaded to an artificially high classification confidence. This discrepancy between the predicted line fit and the lesion means at the lower 68 keV attenuations is likely due to increased distributions overlap and variability in this lower attenuation range. This led to the geometric bisector solution being ill characterized at the lower attenuations and eventually led to the difference in the classification confidence between the hemorrhage and calcification unknown lesion models.

Visual comparison of the unknown lesion and differentiation lesion mean values for the 0.5 cm cerebrum lesion (Figure 5.16) showed a much smaller angle between the hemorrhage and calcification distributions, resulting in lesion means much closer to the GB plane. Visual comparison also showed higher variability in the distributions for both the unknown lesion models and differentiation lesion models. The hemorrhage mean values from the unknown lesion study (red circles) do appear to be farther from the geometric bisector plane than the calcification mean values (blue circles). As discussed above, high

variability and overlap directly lead to the definition of the GB plane being ill characterized. Without strong separation between the calcification and hemorrhage distributions to form the plane, the definition of the plane will be suboptimal. It is likely that the small angle between the distributions is directly responsible for the larger discrepancy between the classification confidences derived for the hemorrhage and calcification unknown lesion models.

While both GB and PD methods showed a discrepancy between hemorrhage and calcification classification confidence for 0.5 cm cerebrum lesions, the effect was greater for the GB method than for the PD method. In addition to the position of the mean lesion value relative to the plane, the GB method uses raw voxel data to determine the confidence in the classification. This allows the GB method to account for the variance within the lesion distribution. The PD method however, is limited to a point measurement of probability at the mean lesion value and does not take into account the variance in the lesion distribution. The effect of lesion variance on final classification confidence is likely the reason the two methods were less correlated for hemorrhage lesions (Table 5.11).

5.3.2 Effect of $CTDI_{vol}$ on Classification Confidence

The effect of $CTDI_{vol}$ on calcification classification was minimal for 0.5 cm cerebrum lesions using either GB or PD methods. Increased $CTDI_{vol}$ led to increased classification accuracy for all other lesion sizes and locations using either method. The effect of $CTDI_{vol}$ on hemorrhage classification was minimal for 1.0 and 1.5 cm cerebrum lesion models using either the GB or PD method. 0.5 cm cerebrum and 1.5 cm skull base lesion models showed increased confidence using either the 105.6 or 132.6 mGy $CTDI_{vol}$ levels relative to the 67 mGy $CTDI_{vol}$ level. Increased $CTDI_{vol}$ from 105.6 mGy to 132.6 mGy did not universally lead to an increase in hemorrhage classification confidence (Figure 5.5, Figure 5.9). While statistical significance cannot be assessed without repeat measures, the

difference in classification confidence between the 105.6 mGy and 132.6 mGy acquisition is likely below clinical significance.

5.3.3 Generalizability of the Geometric Bisector Plane Solution

Based on the results of prior differentiation work, the geometric bisector plane was found to be generalizable across acquisition protocol (see Chapter 4.2.5.5). Lesion size and location was found to have a major effect on the plane and thus three generalized geometric bisector solutions were identified: cerebrum lesions of 0.5 cm diameter, cerebrum lesions of greater than 0.5 cm diameter and skull base lesions. Assuming prior knowledge of the lesion size and location, a generalized solution could be applied, allowing physicians to select the acquisition protocol on a case by case basis. This added flexibility did not highly influence the confidence in lesion classification, as shown by the high degree of correlation between the two methods (Figure 5.12). Without prior knowledge of the lesion size and location, a plane derived from all available data, or super generalized geometric bisector (SGGB) plane could be employed, however the classification confidence tends to suffer (Figure 5.17 and Figure 5.18). In some cases, the application of the SGGB plane to the unknown lesion data seems to improve the confidence in classification. This is however a simple bias in the results due to misregistration between the SGGB plane and the unknown lesion data, and the overall confidence across the paired calcification and hemorrhage lesion results is not improved. Because of this, the SGGB method should be avoided.

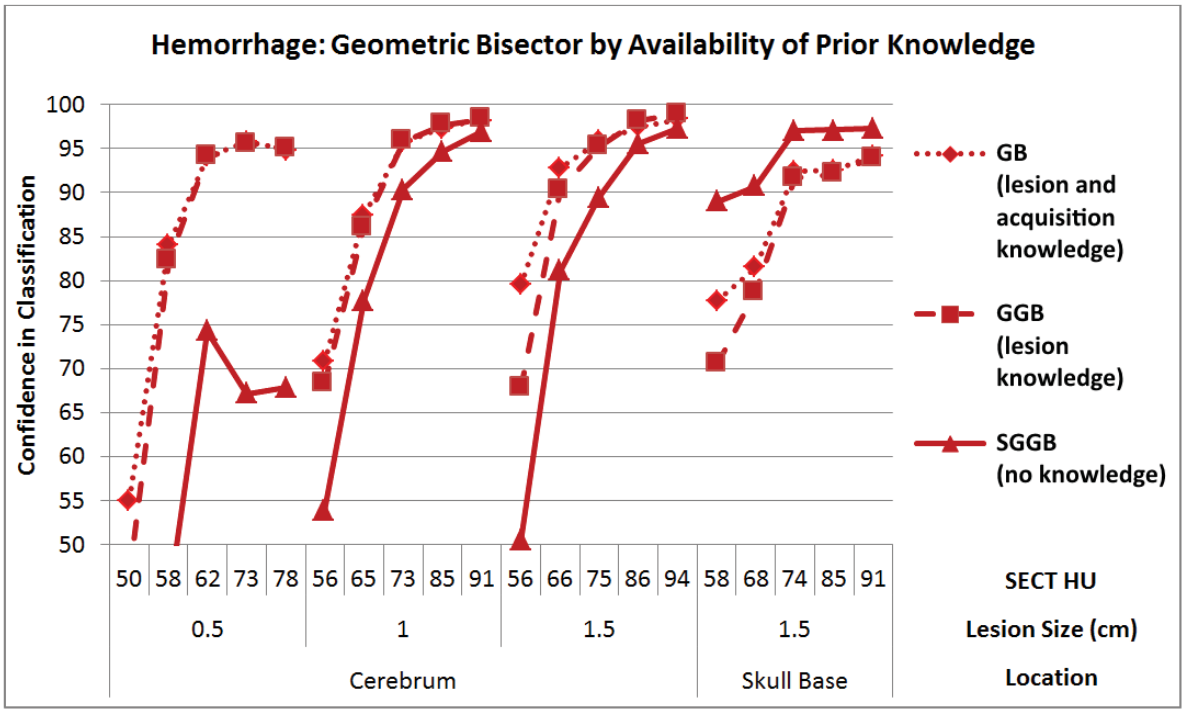

Figure 5.17: Summary of geometric bisector results for hemorrhage lesions by availability of prior knowledge. GB (dotted line) is lesion and acquisition parameter-specific and thus requires prior knowledge of the lesion size and location and acquisition to be used. GGB (dashed line) requires knowledge of only the lesion size and location. SGGB (solid line) assumes no prior knowledge of either the lesion or acquisition.

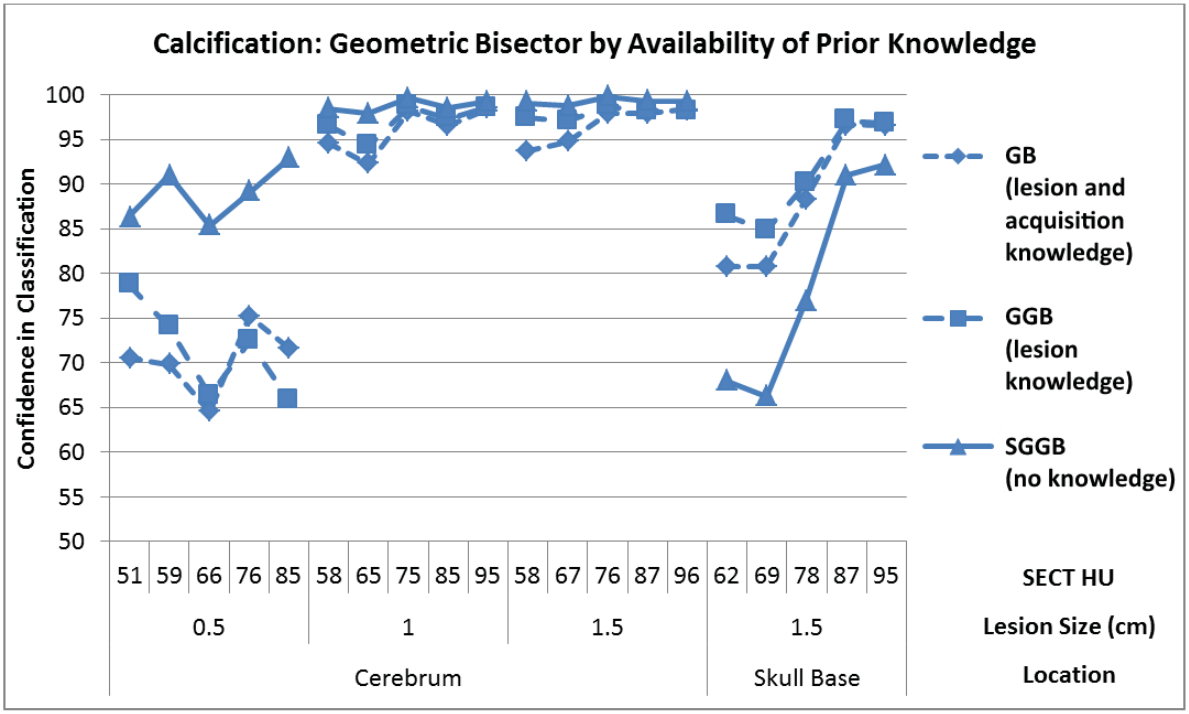

Figure 5.18: Summary of geometric bisector results for calcification lesions by availability of prior knowledge. GB (dotted line) is lesion and acquisition parameter-specific and thus requires prior knowledge of the lesion size and location and acquisition to be used. GGB (dashed line) requires knowledge of only the lesion size and location. SGGB (solid line) assumes no prior knowledge of either the lesion or acquisition.

5.3.4 Protocol Recommendations for Optimal Classification Confidence

Based on the above discussed effect of lesion and acquisition parameters on classification confidence, several recommendations can be formed. 105.6 and 132.6 mGy $CTDI_{vol}$ acquisitions generally yielded similar results, with the exception of low-attenuation calcification lesion models in the skull base where increased dose led to substantially higher classification confidence. For both the calcification and hemorrhage lesion model analysis, 67 mGy $CTDI_{vol}$ acquisitions led to substantially reduced classification confidence in all lesion sizes and locations. Thus it is recommended that without prior knowledge of lesion size, location or attenuation, $CTDI_{vol}$ values less than or equal to 67 mGy be avoided.

Lesions known to be in the skull base would benefit from the added classification confidence associated with the 132.6 mGy $CTDI_{vol}$ level.

Given that the GB and PD methods resulted in highly correlated data (Figure 5.11), the GB method is recommended due to its increased simplicity and ease of use. The PD method, while effective, requires additional statistical analysis and does not take into account the distribution of voxels within the unknown lesion. While the lesion and acquisition parameter-specific GB method is supported when both lesion and acquisition specifics are known, the GGB method can be employed for more flexibility in protocol selection.

5.3.5 Limitations

In addition to the limitations associated with phantom materials discussed in Chapter 4.3.6, the results of this work are limited by the methods employed for unknown lesion classification. Both the GB and PD methods assumed additive binary classification and therefore did not allow for identification of materials other than hemorrhage and calcification. Applying this method to intracranial lesions other than hemorrhage or calcification would result in incorrect classification of the intracranial lesion as either hemorrhage or calcification. In addition, the probability distribution method was employed assuming voxel data was independent due to computational limits. Assuming some structure or dependence within the voxel data might strengthen the model. Future work includes pursuing this structured model as well as employing cross validation and independent validation through a trainer-validation approach. Finally, a Bayesian logistic model could be pursued to allow for the derivation of upper and lower confidence intervals on the confidence in lesion classification.

While this project represents our best approximation of intracranial lesion classification in patients, there are still several limitations on clinical implementation using

these data. Calcification and hemorrhage lesion models were created using a cylindrical shape, and assessed at three sizes (0.5, 1.0 and 1.5 cm) and two locations within the cranium (cerebrum and skull base). Given the large differences in both differentiation accuracy and classification confidence between the 0.5 cm and 1.0 cm cerebrum lesions, further investigation into intermediate sizes is warranted. Calcification and hemorrhage lesion models were created to be homogeneous and free of contamination and as such, the effect of heterogeneity and contamination on classification confidence cannot be assessed. Finally, the applicability of the geometric bisector plane equations to patient data cannot be established without further investigation beyond that possible in a phantom study.

Chapter 6

Dual-Energy CT Quality Control Program Development

This chapter investigates the accuracy and stability of dual-energy data derived from DECT scanning based on a phantom and protocol variations. Given that the data collection for Chapters 3-5 spanned several years, verification that the data and results collected throughout the dissertation research are comparable is necessary. A dual-energy quality control phantom system was developed to evaluate a number of test metrics including uniformity, noise, iodine accuracy and monoenergetic attenuation (HU) stability. In order to evaluate the effect of acquisition parameters on the results of these test metrics, quality control protocols were developed to cover a wide range of protocol variation. In addition, inter- and intra-scanner variances were assessed to inform the design of a future prospective clinical trial.

6.1 Introduction

Recently, the ACR has released its recommendations for routine quality control of computed tomography scanners, including daily monitoring of the mean and standard deviation of the CT number of water and artifact analysis (105). While this document represents an excellent standard for use with single-energy CT imaging, little attention has been paid to quality control of clinical dual-energy CT systems. These scanners often incorporate more advanced hardware such as the fast-kVp switching system used by GE (29) or the dual-source system used by Siemens (27,28). In addition, dual-energy CT scanners produce distinct image types such as virtual monoenergetic, virtual non-contrast and material density images that are unique to dual-energy imaging (37,106). Neither the

capabilities of this hardware nor the consistency of these unique image types can be monitored using a single-energy quality control program.

Since the release of the first clinical dual-energy CT scanner in 2005 (27), many studies have been performed in an attempt to characterize the system response. Of particular interest was the use of the virtual monoenergetic reconstructions, which allow for variable contrast by modulating the keV of the reconstruction and thus the relative influence of photoelectric and Compton processes (22,35,99). Several studies have shown that monoenergetic reconstructions of 65 to 72 keV provide improved iodine contrast-to-noise ratio (CNR) compared to standard single-energy acquisitions of 100kVp or greater (41,62,107). Evaluation of noise for the monoenergetic reconstructions has shown a similar range of 65 to 77 keV to have equivalent or improved noise measurements relative to traditional single-energy CT (41,42,48,63,107). Zhang et al. investigated the noise properties of the monoenergetic reconstructions based on the fast-kVp switching technique. They concluded that while the shape of the noise power spectrum (NPS) curve was similar regardless of reconstruction keV, noise was optimal at 65 keV but lower energy reconstructions resulted in higher noise (42). In addition to noise and CNR, dual-energy images have also been evaluated for spatial resolution (42) and low contrast detectability (43). Due to the theoretical reduction in beam hardening possible with dual-energy techniques (22,35,99,106), monoenergetic images have been investigated for their reduction in beam hardening from bone (48,108), as well as reduction in metal artifact (109–113).

Since dual-energy CT is used in an increasingly quantitative fashion, it is vital to validate the attenuations derived from monoenergetic reconstructions as well as the material concentrations derived from material density images. Of particular interest has been the accuracy of iodine, either using calculated concentration (56,114,115) or enhancement (106,116,117) based on iodine overlay images provided by Siemens systems

or concentration values from a material density image provided by GE systems (42,118). In general, measurements of iodine concentration and enhancement were found to be highly correlated with true iodine concentration (56,115,118). Iodine accuracy was shown to vary with position within a phantom by Zhang et al. (42), however the opposite was found by Matsuda et al. (118). It is worth noting, however, that Matsuda et al. evaluated iodine accuracy solely based on a 65 keV monoenergetic reconstruction and not with material density images. Iodine accuracy was also shown to decrease with increasing phantom size (115), however, this effect has been disputed by other studies (56,106,118). Evaluation of the attenuation accuracy for monoenergetic reconstructions has shown dependence on phantom size, as well as greater inaccuracies for dense materials for low keV reconstructions (61). This effect may be due to lesser correction of beam hardening effects for these energies. The presence of tin filtration has also been shown to effect the attenuation from monoenergetic reconstructions created using the Siemens systems (116,117).

While these studies have shed light on the characterization of these dual-energy CT systems, evaluation has yet to be performed on multiple scanners over time in order to lay the framework for a dual-energy quality control (DEQC) process. In this paper, we develop a phantom system and protocol for collection of these data. Protocol development will cover a wide range of acquisition parameters and dual-energy reconstructions. Metrics evaluated will include iodine accuracy and stability of the attenuations derived from monoenergetic reconstructions, as well as, single-energy QC analogs such as noise and uniformity. Longitudinal data will be acquired in order to develop a clinically implementable quality control program for long-term validation of dual-energy CT data.

6.2 Materials and Methods

6.2.1 Phantom Design

In order to validate both body specific and neuro specific GSI-presets as part of our DEQC program, a two-part phantom was designed (Figure 6.1). The outer shape of the phantom was elliptical in design to better approximate the shape of the human torso. The phantom dimensions were 30 cm in height by 40 cm in width to mimic the challenges of imaging a somewhat larger patient with a waist circumference of 109 cm. This elliptical body phantom contained an insert 22 cm in diameter which could be removed for separate scanning of the neuro specific GSI-presets. When separate from the body phantom, this insert will be referred to as the "head phantom". Both phantoms were designed to be 15 cm in length (z-direction) to allow for continuous helical acquisition.

Unfortunately a 15 cm thick piece of solid water could not be obtained for fabrication of the phantom, therefore three separate 5 cm thick slabs were used. To ensure the slabs would not drift apart with use, fixation bolts were added to keep the slabs tightly pressed together. Two bolts were included in the head phantom, while four were included in the body phantom. The bolts in the head phantom were constructed to allow for the inclusion of a polyvinyl chloride (PVC) bar, 14 cm by 3.8 cm and 2.5 cm deep to provide a surface for use of a bubble level on both phantoms (see Figure 6.1). The bolts were fabricated using high density polyethylene (HDPE) and threaded on one side to allow for manual tightening. The body and head phantom were both machined from the same pieces of solid water, so a 1 cm wide, HDPE slip-ring was needed between the head and body phantom portions to replace material lost during milling. This ring was permanently affixed to the inside of the body phantom and remained attached to the body phantom shell when the head phantom was removed for separate scanning.

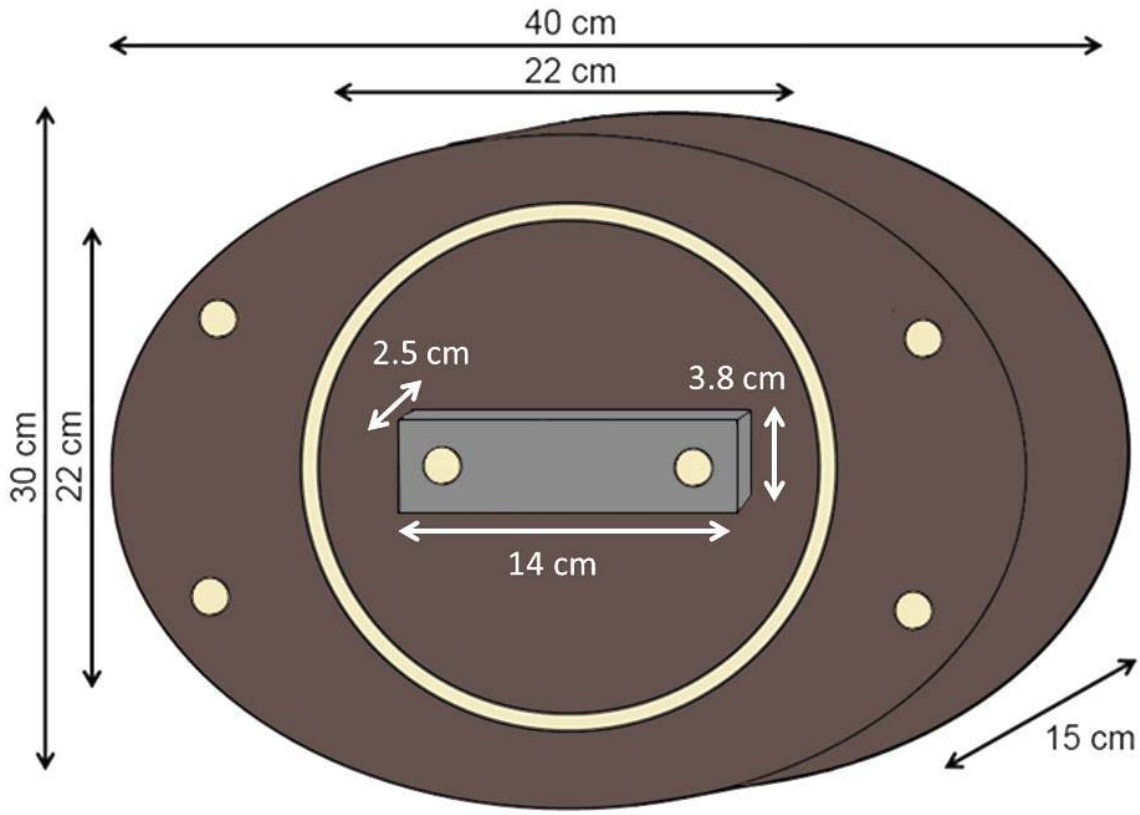

Figure 6.1: Basic structure and measurements of DEQC phantom. Solid water components are shown in dark brown, HDPE components in tan and PVC in light gray.

6.2.1.1 Tissue and Material Inserts

Due to DECT's focus on tissue characterization and material separation, a variety of tissue and material inserts were included in the DEQC phantom (Table 6.1). Insert compositions were chosen based on current clinical applications of DECT, as well as the prevalence of materials or tissue types in research studies and emerging applications. The concentrations of various materials selected were then referenced to either clinically used values, as in the case of the iodine enhancement rods, or relevant concentration in the human body, as in the case of the calcium rods. For the calcium and iodine material inserts, three concentrations were selected so that the linearity of the DECT response to the material could be assessed over a range of concentrations in both the head and body

phantom. The arrangement of the inserts within the phantom is shown in Figure 6.2 and was determined based on the reduction of beam hardening and test metric considerations (see Chapter 6.2.2). The insert rods measure 2.8 cm in diameter and extend the entire 15 cm length of the phantom.

Table 6.1: List of DEQC phantom insert types.

Insert	Background	Additive	HU at 120 kVp	Biology Modeled
Blood	Solid Water	Fe_2O_3	40	Blood
Blood	Solid Water	Fe_2O_3	70	Clot (Normal)
Blood	Solid Water	Fe_2O_3	100	Clot (Extreme)
Calcium	Solid Water	$CaCo_3$	198	Calcification
Calcium	Solid Water	$CaCo_3$	334	Bone
Calcium	Solid Water	$CaCo_3$	838	Bone (dense)
Iodine	Solid Water	C6H5I	51	NA
Iodine	Solid Water	C6H5I	128	NA
Iodine	Solid Water	C6H5I	356	NA
Iodine Enhancement	Solid Water	Fe_2O_3 + C6H5I	40+50	Typical enhancement threshold for neuro studies
Iodine Enhancement	Solid Water	Fe_2O_3 + C6H5I	40+100	Typical enhancement threshold for thoracic studies
Soft Tissue	NA	NA	35	Soft Tissue
Adipose	NA	NA	-100	Adipose
Brain	NA	NA	15	Brain

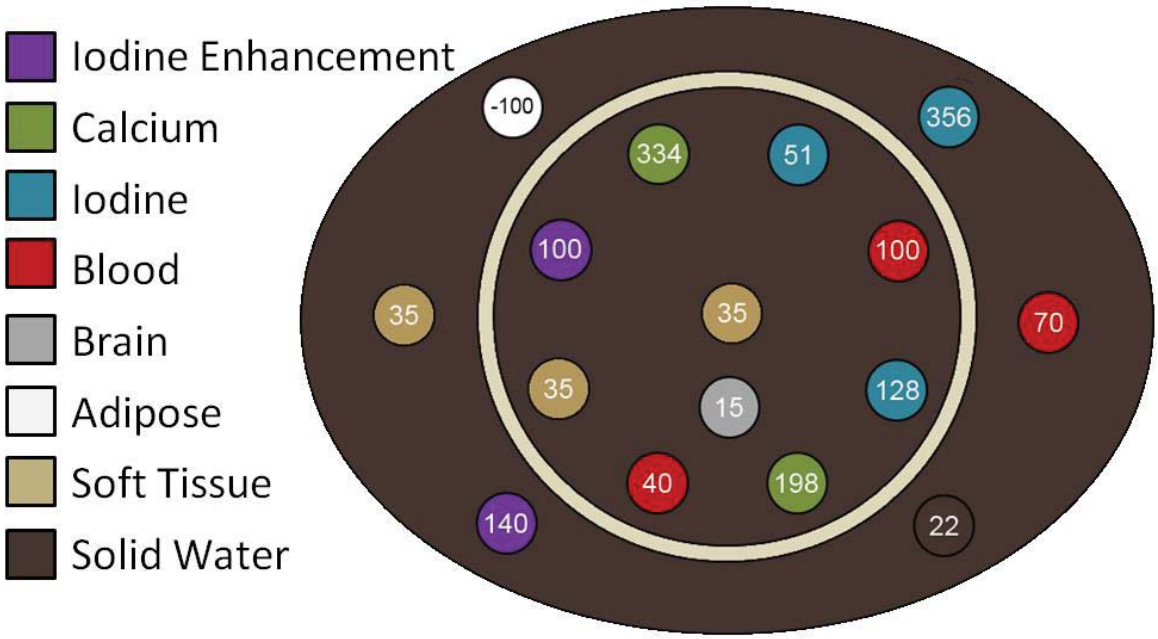

Figure 6.2: DEQC insert layout with average 120kVp HU level of inserts labeled.

To ensure repeatable positioning of the rod inserts within the DEQC phantom, a thin, transparent polycarbonate plate was added to the back surface of the phantom (Figure 6.3a). This would allow the rods to be positioned flush with this fixed surface, allowing repeatable positioning. In addition, the plate was designed with several 2 cm diameter holes, matching the positions of the rod inserts so that a thin tool through the hole in the plate and the inserts could be easily removed. The plate was affixed to the posterior slab of the body phantom by three solid water bolts extending 2 cm into the body phantom. To ensure the proper alignment of the head insert within the body phantom, an orientation peg was added to the posterior surface of the head phantom, and a matching hole was drilled through the acrylic plate (Figure 6.3b). The surface of the peg was rounded, allowing the peg to naturally seek its corresponding hole in the acrylic alignment plate without significant effort on the part of the user.

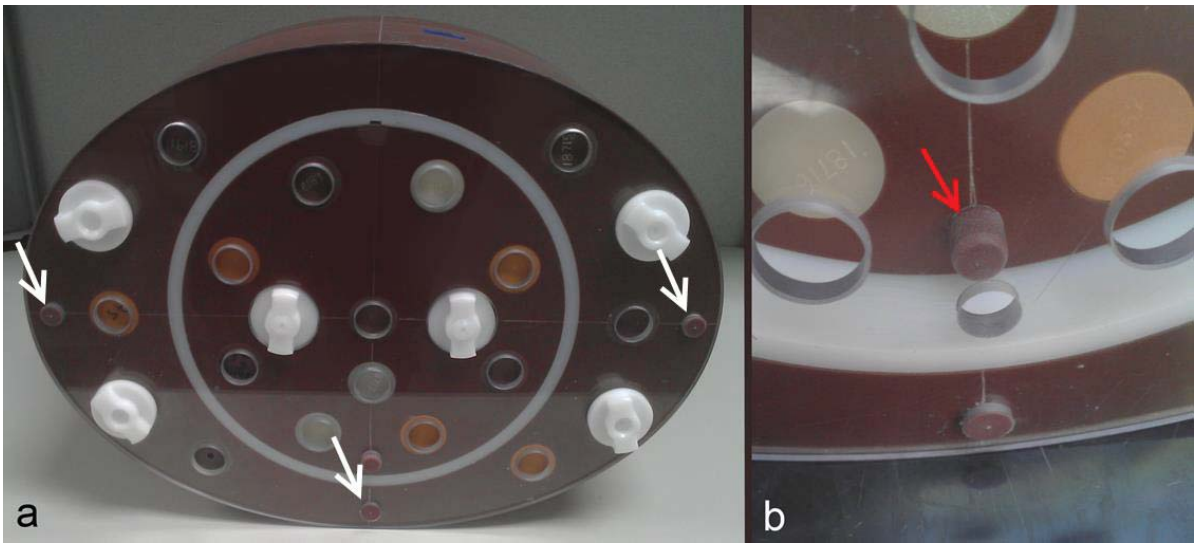

Figure 6.3: a) Polycarbonate plate attached to back of phantom with solid water bolts visible at the bottom and side periphery of the phantom (white arrows). b) Detail of lower solid water bolt as well as the orientation plug (red arrow) used to ensure proper alignment of the head phantom within the body phantom.

6.2.1.2 Insert Validation

Material and tissue equivalent inserts detailed in Table 6.1 were acquired from Gammex, Inc. All inserts underwent both quantitative and qualitative testing to ensure uniformity, accuracy and if needed, inter-comparability. Inserts were scanned using a vendor-provided 20 cm diameter, 15 cm long solid water phantom with eight insert positions. Two water balloons were inserted in the positions on either side of the DEQC insert under evaluation to minimize artifacts or beam hardening. The phantom was then imaged using the scan protocol in Table 6.2 which included several vendor-specified protocols (series 3-6). Images were viewed with GSI viewer software (Version 2; GE Healthcare). Using 20 mm x 20 mm ROIs, quantitative data (Table 6.3) was collected at several points along the insert, and all images were viewed for any signs of defects. Any inserts not uniform to within 2 HU along their length or showing any visible defects were returned to the vendor for replacement. The three soft tissue inserts included in the phantom were further validated to verify they were interchangeable based on both their single-energy attenuation data and dual-energy spectral curves.

Table 6.2: DEQC insert validation protocol. For all series: SFOV: Head, DFOV: 25 cm, Filter: Standard.

Series	Mode	Name	Scan Type	Pitch	Rot (s)	Beam Width (mm)	Image Thickness (mm)	Interval (mm)	kVp	mA
1	SE	Routine Brain	Helical	0.531	0.8	20	3.75	3	140	160
2	DE	GSI - 26 Brain	Helical	0.531	0.7	20	3.75	3	80/140	375
3	SE	Gammex Val 80kV	Axial	1	1	40	5	40	80	250
4	SE	Gammex Val 100kV	Axial	1	1	40	5	40	100	250
5	SE	Gammex Val 120kV	Axial	1	1	40	5	40	120	250
6	SE	Gammex Val 140kV	Axial	1	1	40	5	40	140	250

Table 6.3: Reconstructions created from DEQC validation data and quantitative data acquired.

Series	Mode	Description/Reconstruction	Quantitative Data Acquired	
1	SE	Routine Brain	Mean	SD
102	DE	50 keV	Mean	SD
102	DE	70 keV	Mean	SD
102	DE	100 keV	Mean	SD
102	DE	140 keV	Mean	SD
102	DE	Water (Iodine)	Mean	SD
102	DE	Iodine (Water)	Mean	SD
102	DE	Water (Calcium)	Mean	SD
102	DE	Calcium (Water)	Mean	SD
3	SE	Gammex Val 80kV	Mean	SD
4	SE	Gammex Val 100kV	Mean	SD
5	SE	Gammex Val 120kV	Mean	SD
6	SE	Gammex Val 140kV	Mean	SD

6.2.2 Test Metrics

SECT QC has converged on a number of routine tests reflecting important imaging parameters: standard deviation of water (noise), mean CT# of water (absolute CT number accuracy), artifact analysis (detector uniformity), Uniformity (field homogeneity) and Linearity (relative CT number accuracy). Due to the unique capabilities and imaging concerns revolving around DECT, as well as the structure of our DEQC phantom, modifications were made to these standard SEQC tests.

Noise is usually assessed over a large ROI in a uniform phantom, however due to the constraints of our phantom model, noise was assessed as the standard deviation within the brain insert in the head phantom portion of the DEQC phantom system. This insert is present during both body phantom and separate head phantom scanning and is the insert with the SECT attenuation (HU) closest to water (15 HU vs 0 HU). This noise test metric was applied to both monoenergetic and material density image types.

Due to the ability of DECT to create virtual monoenergetic data visualizations at a variety of different keV levels, the concept of absolute CT number accuracy takes on an additional dimension. An effective DEQC program must not only test that the CT number is consistent using a single protocol, but that it is also spectrally consistent over a range of monoenergetic visualizations. This new test metric, Monoenergetic HU Stability, was defined as the average CT number over all voxels within the three soft tissue rods in the DEQC phantom. This definition provides positional independence due to the spacing of the soft tissue rods within the phantom as well as basing the metric in a clinical CT number range (approximately 35 HU). To allow for the verification of Monoenergetic HU Stability at various points along the dual-energy spectral curve, four keV energy levels were chosen: 50 keV, 70 keV, 110 keV and 140 keV. These specific keV energy levels were selected due to their common clinical use for iodine conspicuity – 50 keV (62), 120kVp corollary and low noise – 70 keV (41,107), and metal artifact reduction – 140 keV (110,111,113), respectively.

In SECT, linearity is assessed by documenting the mean CT number of several substances, most commonly, water, air and acrylic. While the mean CT number of water is meant to be an absolute measure of CT number accuracy, linearity, is more a relative measure of CT number accuracy, because the Hounsfield unit is a material's linear attenuation relative to that of water. In DECT, the process of material decomposition is used to create paired material density images which display the densities of two different materials that together would mimic the attenuation properties of the target material or tissue (29,37). These material density images are expressed in mg/mL and, unlike Hounsfield numbers, are absolute measures of a physical quantity associated with the material or tissue. These values can be quantitative if the material is made solely of the two materials present in the material basis pair. For example, a water/iodine material decomposition of a solution of iodine and water should yield accurate material densities on

both images. To test the accuracy and linearity of this response, three inserts consisting solely of solid water and iodine were included in the DEQC phantom, each with a different known density of iodine. The accuracy of the material density on the iodine material density image from a water/iodine material decomposition was then compared to the known iodine density for each rod. This value was investigated as both absolute error and percent error relative to the known iodine material density for each of the three rods.

While uniformity is commonly defined in a water phantom, the heterogeneity of our DEQC phantom required modification from this classical definition. Soft tissue rods were positioned at the center of the DEQC phantom, periphery of the DEQC head phantom and periphery of the DEQC body phantom (Figure 6.2). To minimize the potential of beam hardening from linearly positioned inserts, the head phantom peripheral inserts were offset from body phantom peripheral inserts. Uniformity was then defined as the mean ROI value of the most peripheral soft tissue rod minus the mean ROI value of the central soft tissue rod. Uniformity was assessed on both monoenergetic and material density image types. Both water and iodine material density images were assessed due to the differing influence of the 80 and 140kV acquisitions on these image types. Water density images have a higher percent contribution from the higher 140kV beam, while iodine density images have a higher percent contribution from the lower 80kV beam. Given that the two energies would likely be effected by phantom (or patient) size and beam hardening to different extents, the collection of uniformity data using both water and iodine density images was pursued.

A full list of test metrics included in the DEQC program as well as applicable image types can be found in Table 6.4.

Table 6.4: List of test metrics included in DEQC program and their application to various image reconstruction types, as well as the composition and position of the rods used to evaluate the metric.

	Test Metric	Noise	Monoenergetic HU Stability	Iodine Accuracy	Uniformity
	Rod Composition	Brain	Soft Tissue	Iodine	Soft Tissue
	Rod Position	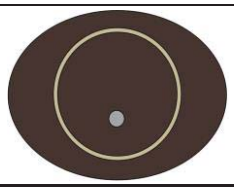	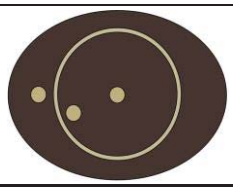	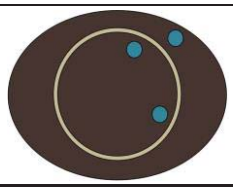	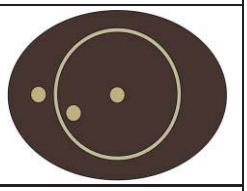
Image Type	50 keV	X	X		X
	70 keV	X	X		X
	110 keV	X	X		X
	140 keV	X	X		X
	Iodine (Water)	X		X	X
	Water (Iodine)	X			X

6.2.3 Protocol Development

6.2.3.1 DEQC Protocol Version 1: Initial Data Collection

In order to determine which acquisition parameters may play a role in the overall performance of the DECT system and would warrant further investigation, highly variable scan protocols were designed for both the head and body phantoms. Both protocols contained variations in $CTDI_{vol}$, rotation time, image thickness and pitch. For the head phantom, three GSI-presets were chosen covering a $CTDI_{vol}$ range of 36.7 to 132.6 mGy, rotation times from 0.5 to 1s, pitch values of 0.531 and 0.969 and two image thicknesses, 1.25 and 3.75, selected for their clinical applicability (Table 6.5). For the body phantom, four GSI-presets were chosen covering a $CTDI_{vol}$ range of 10.3 to 62 mGy, rotation times from 0.5 to 1s, pitch values of 0.516 and 0.984 and two image thicknesses, 2.5 and 3.75,

selected for their clinical applicability (Table 6.6). Both protocols included a single energy acquisition selected to mimic a current routine SECT protocol.

Table 6.5: Head Phantom DEQC Protocol Version 1. All acquisitions used helical acquisition mode, beam width of 20 mm, Head SFOV, DFOV of 25 cm, and Standard reconstruction algorithm. A total of 5 images were acquired per group.

Series	Name	GSI-Preset	Pitch	Rot (s)	mA	$CTDI_{vol}$ (mGy)	Img Thk (mm)
2	**Single Energy**	**(120kVp)**	0.531	1	300	54.65	3.75
3	**GSI-26**	**GSI-26**	0.531	0.7	375	67	1.25
		GSI-26	0.531	0.7	375	67	3.75
		GSI-26	0.969	0.7	375	36.7	1.25
		GSI-26	0.969	0.7	375	36.7	3.75
4	**GSI-20**	**GSI-20**	0.531	0.5	630	81.4	1.25
		GSI-20	0.531	0.5	630	81.4	3.75
		GSI-20	0.969	0.5	630	44.6	1.25
		GSI-20	0.969	0.5	630	44.6	3.75
5	**GSI-9**	**GSI-9**	0.531	0.9	600	132.6	1.25
		GSI-9	0.531	0.9	600	132.6	3.75
		GSI-9	0.969	0.9	600	72.7	1.25
		GSI-9	0.969	0.9	600	72.7	3.75

Table 6.6: Body Phantom DEQC Protocol Version 1. All acquisitions used helical acquisition mode, beam width of 40 mm, Large Body SFOV, 42 cm DFOV, and Standard reconstruction algorithm. A total of 5 images were acquired per group.

Series	Name	GSI-Preset	Pitch	Rot (s)	mA	$CTDI_{vol}$ (mGy)	Img Thk (mm)
2	Single Energy	(120kVp)	0.984	0.5	400	12.46	2.5
3	GSI-36	GSI-36	0.516	0.8	260	19.6	2.5
		GSI-36	0.516	0.8	260	19.6	5
		GSI-36	0.984	0.8	260	10.3	2.5
		GSI-36	0.984	0.8	260	10.3	5
4	GSI-1	GSI-1	0.516	0.5	630	33.9	2.5
		GSI-1	0.516	0.5	630	33.9	5
		GSI-1	0.984	0.5	630	17.8	2.5
		GSI-1	0.984	0.5	630	17.8	5
5	GSI-10	GSI-10	0.516	0.8	600	48.6	2.5
		GSI-10	0.516	0.8	600	48.6	5
		GSI-10	0.984	0.8	600	25.5	2.5
		GSI-10	0.984	0.8	600	25.5	5
6	GSI-5	GSI-5	0.516	1	600	62	2.5
		GSI-5	0.516	1	600	62	5
		GSI-5	0.984	1	600	32.5	2.5
		GSI-5	0.984	1	600	32.5	5

Both the DEQC head and body protocols included several dual-energy reconstructions. These reconstructions were selected based on the test metrics listed in Chapter 6.2.2 and are shown in Table 6.7. They include monoenergetic reconstructions at 50 keV, 70 keV, 110 keV and 140 keV, used in tests of monoenergetic HU stability, uniformity and noise. Also included were material density images from a water/iodine material decomposition, used in tests of iodine accuracy, uniformity and noise. For all reconstructions, the minimum number of images allowable were created to facilitate data transmission and storage. The minimum number of images allowed using a material density reconstruction was one, while monoenergetic reconstructions required the full image set to be reconstructed.

Table 6.7: Dual-energy reconstructions applied to all dual-energy acquisitions in both the version 1 DEQC Body and Head protocols. The number of images reconstructed was based on the minimum setting for each reconstruction type: five for monoenergetic and one for material density.

Recon	Recon Name	Dual-energy Recon Details	No. of Images
R1	Mega Mono	70 keV + GSI Data File	5
R2	Water (Iodine)	Water(Iodine)	1
R3	Iodine (Water)	Iodine(Water)	1
R4	70 keV	70 keV	5
R5	110 keV	110 keV	5
R6	140 keV	140 keV	5
Manual	50 keV	50 keV	5

These protocols were used to scan the DEQC head and DEQC body phantoms ten times over the course of two weeks on a single GE 750HD CT scanner to assess intra-scanner repeatability, and twice on nine other scanners to assess inter-scanner repeatability. The results of this trial were used to inform the development of the DEQC protocol version 2 for extended data collection.

6.2.3.2 DEQC Protocol Version 2: Extended Data Collection

After the initial data collection based on DEQC Protocol Version 1, a second protocol version was developed to target those factors found influential while removing those found unnecessary for further investigation (see Chapter 6.3.1). Additional GSI presets were included in both the head and the body protocols to better separate the dose and rotation time effects. In each protocol, GSI presets were chosen that had similar $CTDI_{vol}$ values but with different rotation times. Three such groups were found among the body GSI presets, while only one dose matched pair was found among the head GSI presets. Pitch was varied solely to provide additional variation in $CTDI_{vol}$ across the limited GSI-preset options. Image thickness was reduced to a single value across both head and

body phantom protocols to allow for more direct comparison of DEQC results. A 5 mm thickness was selected due to its clinical applicability and reduced noise. Prep group delays were added between all acquisitions to minimize tube cooling delays. The updated DEQC head and body phantom protocols are shown in Table 6.8 and Table 6.9 for the head and body phantoms, respectively.

Table 6.8: DEQC Head Phantom Protocol Version 2. All acquisitions used helical scan mode, 20 mm beam width, Head SFOV, 25 cm DFOV, and Standard reconstruction algorithm.

Series	GSI-Preset	Pitch	Rot (s)	mA	$CTDI_{vol}$ (mGy)	Img Thk (mm)	Prep (s)
1	GSI-30	0.531	0.8	550	105.6	5	0
	GSI-20	0.531	0.5	630	81.4	5	15
	GSI-26	0.531	0.7	375	67	5	15
	GSI-19	0.969	0.6	640	54.7	5	15
	GSI-39	0.531	0.8	208	47.8	5	15
	GSI-20	0.969	0.5	630	44.6	5	15
	GSI-26	0.969	0.7	375	36.7	5	15
	GSI-39	0.969	0.8	208	26.2	5	15

Table 6.9: DEQC Body Phantom Protocol Version 2. All acquisitions used helical scan mode, 40 mm beam width, Large Body SFOV, 42 cm DFOV, and Standard reconstruction algorithm.

Series	GSI-Preset	Pitch	Rot (s)	mA	$CTDI_{vol}$ (mGy)	Img Thk (mm)	Prep (s)
1	GSI-5	0.516	1	600	62	5	0
	GSI-10	0.516	0.8	600	48.6	5	15
	GSI-1	0.516	0.5	630	33.9	5	15
	GSI-5	0.984	1	600	32.5	5	15
	GSI-10	0.984	0.8	600	25.5	5	15
	GSI-1	0.984	0.5	630	17.8	5	15
	GSI-54	0.516	0.6	275	17.4	5	15
	GSI-48	0.516	0.7	260	17.2	5	15
	GSI-51	0.984	0.5	360	10.3	5	15
	GSI-36	0.984	0.8	260	10.3	5	15

Table 6.10: Dual-energy reconstructions applied to all dual-energy acquisitions in both the version 2 DEQC body and head protocols. The number of images reconstructed was based on the minimum setting for each reconstruction type: five for monoenergetic and one for material density.

Recon	Recon Name	Dual-Energy Recon Details	No. of Images
R1	Mega Mono	70 keV + GSI Data File	5
R2	Water(Iodine)	MD: Water(Iodine)	1
R3	Iodine(Water)	MD: Iodine(Water)	1
R4	70 keV	70 keV	5
R5	110 keV	110 keV	5
R6	140 keV	140 keV	5
Manual	50 keV	50 keV	5

Weekly DEQC scans were performed on ten GE 750HD CT scanners over a 12 week period in order to characterize the test metric dependence on acquisition parameters, assess inter-scanner and intra-scanner variance and to inform the creation of a streamlined DEQC protocol appropriate for clinical implementation.

6.2.4 Data Collection

6.2.4.1 DEQC Protocol Version 1

Due to inherent limitations on the GE 750HD CT scanners, 50 keV reconstructions could not be made automatically and necessitated manual intervention. The GSI data file for each acquisition was opened using the GSI viewer (version 2, Wakausha, WI) available on the scanner at time of scan. A 50 keV reformat was then created and saved as a separate series. This series, along with all other images acquired or reconstructed as part of the DEQC Protocol Version1 were transferred to a local workstation where the data were downloaded for further analysis. A representative image from the DEQC body phantom data with an S0 image location was then opened using the GSI viewer (version 2, Waukesha, WI) and 20 mm diameter ROIs were placed on all inserts. Each ROI was saved

as a comma delimited file to retain the spatial coordinates of each voxel contained within the ROI. This procedure was then repeated for a representative image from the DEQC head phantom.

All images were loaded into Matlab (Version 2014a, MathWorks) and filtered to retain only those images with an S0 image location. Comma delimited ROI files from both the representative DEQC body and head phantoms were loaded into Matlab and the spatial coordinates of each voxel were transformed into voxel locations using the known DFOV and image matrix dimensions. The voxel locations for each ROI were then applied to the appropriate phantom images and the mean and standard deviation calculated. Test metrics were calculated for appropriate image types for both the DEQC body and head phantom. The ROI summary statistics, as well as the results of the test metrics were then written out to a text file for all images and exams.

Test metric results were plotted against a range of acquisition parameters to isolate parameters with the greatest impact on dual-energy QC. Those with limited or well established effects on test metrics were excluded, while acquisition parameters with marked and uncharacterized effects on test metrics were retained for further study.

6.2.4.2 DEQC Protocol Version 2: Creation of an In-House AutoQC Program

Due to the large amount of data collected as part of this protocol as well as the long duration of data collection, a more automated and robust analysis method was needed. Weekly DEQC exams were sent to a DICOM server which archived all relevant images in a MySQL database (Oracle, Redwood City, CA). A custom analysis program was written in Python which processed the images allowing for collection of DEQC results and test metrics. The analysis program, or AutoQC, queried unprocessed images from the MySQL database with image location equal to S0. The AutoQC then segmented the phantom from the surrounding air by means of k-means segmentation (119) followed by post-processing

using a morphological closing operator to remove small air gaps and outliers (120). This mask was then processed to identify the two centrally-located fixation bolts and the mask was transformed using a Radon transform to produce a sinogram (121). In sinogram space, the center of the phantom is identified by minimizing the sum of the squares of the distance between the center of the phantom and its periphery, while any rotation in the phantom was identified by the average of the angles between the phantom center and the left and right fixation bolts. After the phantom image was centered and corrected for rotation, 12 mm diameter ROIs were applied to all rods based on a lookup table which contains distances from the center of the phantom as well as angles from the center of the right fixation bolt. Mean and standard deviation values were calculated for each ROI and saved to a separate MySQL database for archival.

A web interface was developed in Python (Python Software Foundation), to allow for download of the DEQC ROI statistics as well as visualization of DEQC results. The interface allowed both scanner-specific and date range searches of the database. For each exam, a single representative image was shown as well as representative test metrics calculated from the ROI statistics. Test metrics falling outside established constraints can be displayed in red for increased ease of identification.

6.2.4.3 DEQC Protocol Version 2: Statistical Analysis

In order to assess whether changes in acquisition parameters resulted in statistically significant changes in the test metric results, linear mixed models were used (122). This method was able to take into account any correlation between the multiple measurements from a given scanner. In the case where the overall likelihood ratio test was significant implying differences between groups, pairwise comparisons with Tukey-Kramer adjustment were performed between the values for a given acquisition parameter (122). In the case of noise, values were logarithmically transformed before statistical modeling due to right

skewness. Statistical significance was set at a two-sided p-value of 0.05. Variance component analysis was performed on uniformity, iodine accuracy and monoenergetic HU stability to estimate both inter-scanner and intra-scanner variation (122). All statistical analysis was performed using SAS version 9 (SAS Institute, Cary, NC).

6.3 Results

6.3.1 Determination of Relevant Acquisition Parameters

Results of DEQC protocol version 1 (Chapter 6.2.4.1) are shown in Table 6.11 and Table 6.12 for the DEQC body phantom and DEQC head phantom respectively. $CTDI_{vol}$ was found to influence iodine accuracy, monoenergetic HU stability and noise for the DEQC body phantom, and only iodine accuracy and noise for the DEQC head phantom. While the relationship between $CTDI_{vol}$ and noise is known, the effect on the other two metrics warranted further investigation. Rotation time was found to influence iodine accuracy, uniformity and noise using both the DEQC body and DEQC head phantoms. Effects due to $CTDI_{vol}$ and effects due to rotation time were compounded due to the fixed nature of the GSI-presets. Future investigation would require the two parameters to be separated through the selection of GSI presets where one parameter (e.g. $CTDI_{vol}$) could be varied independently of the other (e.g. rotation time). Other than the obvious association with dose, pitch was found to have no effect on any of the test metrics for either the DEQC body or DEQC head phantoms and was therefore excluded from further analysis. Image thickness was only found to affect noise using either the DEQC body or DEQC head phantom. Given that this effect is known and straightforward, image thickness was also excluded from further analysis.

Table 6.11: Results of DEQC protocol 1 for the DEQC Body phantom showing which factors were found to influence the test metrics investigated. Marked cells indicate that the acquisition parameter was found to have an effect on the test metric. Empty cells indicate no effect was identified.

		Acquisition Parameter			
		$CTDI_{vol}$	Rotation Time	Pitch	Image Thickness
Test Metric	Iodine Accuracy	X	X		
	Monoenergetic HU Stability	X			
	Uniformity		X		
	Noise	X	X		X

Table 6.12: Results of DEQC protocol 1 for the DEQC head phantom showing which factors were found to influence the test metrics investigated. Marked cells indicate that the acquisition parameter was found to have an effect on the test metric. Empty cells indicate no effect was identified.

		Acquisition Parameter			
		$CTDI_{vol}$	Rotation Time	Pitch	Image Thickness
Test Metric	Iodine Accuracy	X	X		
	Monoenergetic HU Stability				
	Uniformity		X		
	Noise	X	X		X

6.3.2 DECT Response by Test Metric

For each test metric under evaluation, results were plotted against all acquisition parameters investigated to determine the parameter(s) responsible for trends in the test metric results. In some cases, the effect was complex, requiring the visualization of primary and secondary effects on the test metric. In the figures that follow, primary effects are

shown on the lower portion of the x-axis while secondary effects are shown directly above the primary. Results are shown by scanner to allow for a visual interpretation of the inter-scanner variance. Results for the inter- and intra-scanner variance (based on statistical analysis described in Chapter 6.2.4.3) were also investigated graphically and primary and secondary effects determined.

6.3.2.1 Iodine Accuracy

DEQC Body Phantom:

Iodine accuracy using the DEQC body phantom was found to be affected primarily by effective milliampere-second (mAs) and secondarily by $CTDI_{vol}$ for all three iodine rods investigated (Figure 6.4). Images obtained using low mAs protocols tended to over-estimate the iodine concentration in the case of the 2 mg/mL rod, however the iodine concentration for the 5 mg/mL rod was under-estimated. Effects of both mAs and $CTDI_{vol}$ were fairly limited for the 15 mg/mL rod. The variation in the effect of these parameters could potentially be due to their position within the phantom and their surrounding environment (e.g. the effect of surrounding material rods). Both inter- and intra- scanner variance were primarily affected by $CTDI_{vol}$ and secondarily affected by mAs likely indicating the effect of image noise on the repeatability of these results.

Results of the linear mixed model analysis for the effect of the primary acquisition parameter, mAs, on iodine accuracy in the DEQC body phantom can be seen in Table 6.13. The over-estimation of the 2 mg/mL iodine rod and the under-estimation of the 5 mg/mL iodine rod at low mAs values can been seen in the reversed ranking order.

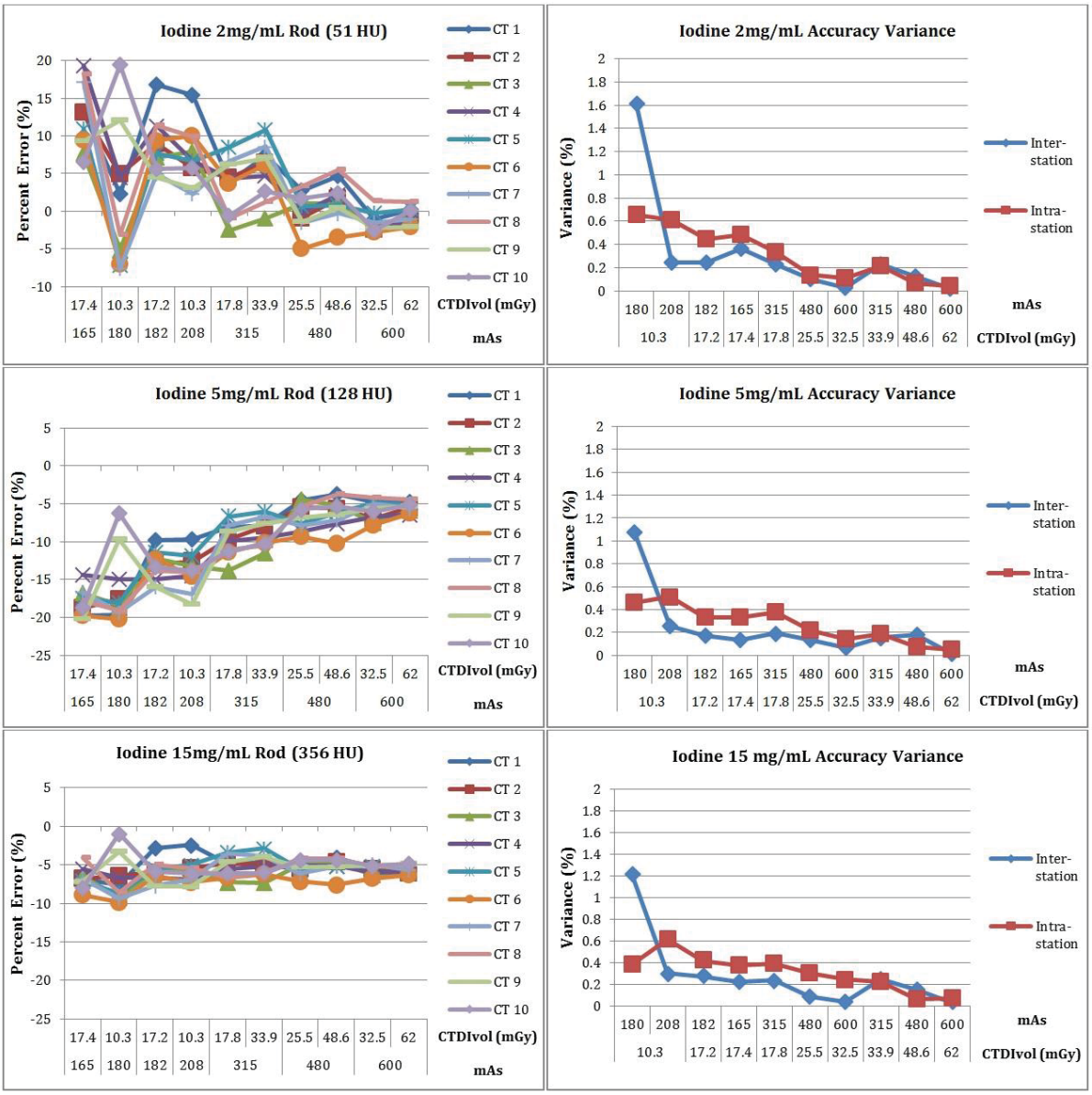

Figure 6.4: DEQC body phantom results for iodine accuracy. Left: Iodine accuracy trends sorted primarily by mAs and secondarily by $CTDI_{vol}$ for 2 mg/mL, 5 mg/mL, and 15 mg/mL iodine rods displayed by scanner. Right: Iodine accuracy inter- and intra-scanner variance trends sorted primarily by $CTDI_{vol}$ and secondarily by mAs for 2 mg/mL, 5 mg/mL, and 15 mg/mL iodine rods.

Table 6.13:DEQC body phantom results for the effect of mAs on iodine accuracy based on linear mixed model analysis.

Iodine Rod	mAs effect on Iodine Accuracy
2 mg/mL	165 >> 182 > 208 >> 315 >> 180 = 480 >> 600
5 mg/mL	600 > 480 >> 315 >> 182 > 208 >> 180 >> 165
15 mg/mL	480 = 315 >> 600 > 182 = 208 >> 165 > 180

Legend		
>>	Significantly Different	P < 0.05
>	Not Significantly Different	0.05 < P < 0.9
=	Statistically Equivalent	P > 0.9

DEQC Head Phantom:

Iodine accuracy using the DEQC head phantom was found to be affected primarily by mAs and secondarily by $CTDI_{vol}$, similar to that determined using the DEQC body phantom (Figure 6.5). In contrast to the DEQC body phantom, lower mAs protocols provided higher iodine accuracy, while higher mAs protocols provided lower iodine accuracy, underestimating the concentration. It is worth noting however that the variance between scanners is somewhat higher using these lower mAs protocols. This trend is supported by the inter- and intra-scanner variance results showing increasing mAs has a beneficial result on inter-scanner variance. However due to the matched scaling between the DEQC body and DEQC head phantom results, this cannot easily be visualized. Intra-scanner variance did not seem to be directly affected by any of the acquisition parameters investigated. Compared to the results from the DEQC body phantom, the iodine accuracy using the DEQC head phantom was much improved. The maximum error in the iodine concentration measurement was approximately 20% using the DEQC body phantom, but only 8% using the DEQC head phantom. Inter- and intra- scanner variances were also reduced from a maximum value of 1.61% and 0.66%, respectively, to 0.009% and 0.012%. This represents a dramatic improvement in result repeatability for the DEQC head phantom, relative to that of the DEQC body phantom.

Results of the linear mixed model analysis for the effect of the primary acquisition parameter, mAs, on iodine accuracy in the DEQC body phantom can be seen in Table 6.14.

Figure 6.5: DEQC head phantom results for iodine accuracy. Left: Iodine accuracy trends sorted primarily by mAs and secondarily by $CTDI_{vol}$ for 2 mg/mL and 5 mg/mL iodine rods displayed by scanner. Right: Iodine accuracy inter- and intra-scanner variance trends sorted primarily by mAs and secondarily by $CTDI_{vol}$ for 2 mg/mL and 5 mg/mL iodine rods.

Table 6.14: DEQC head phantom results for the effect of mAs on iodine accuracy based on linear mixed model analysis.

Iodine Rod	mAs effect on Iodine Accuracy
2 mg/mL	315 >> 208 >> 262.5 > 440 > 384
5 mg/mL	208 >> 315 = 262.5 >> 440 >> 384

Legend		
>>	Significantly Different	P < 0.05
>	Not Significantly Different	0.05 < P < 0.9
=	Statistically Equivalent	P > 0.9

6.3.2.2 Uniformity

DEQC Body Phantom:

Uniformity using the DEQC body phantom was affected primarily by rotation time and secondarily by $CTDI_{vol}$ for all dual-energy reconstructions investigated (Figure 6.6, Figure 6.7). For 50 keV and Iodine(Water) reconstructions, low mAs protocols resulted in high uniformity values (peripheral results greater than central), which was improved by increasing the mAs. For 110 keV, 140 keV and Water(Iodine) reconstructions, low mAs protocols resulted in slightly low (-2 HU on average) uniformity values (central results greater than peripheral). Increasing the mAs resulted in initial improvement followed by increasingly high (5-6 HU on average) uniformity values (peripheral results greater than central). Uniformity response for 70 keV was flat across all rotation times investigated; however, the uniformity result was routinely high with an average of approximately 4 HU. Maximum absolute uniformity was found in 50 keV (17.8 HU) followed by Water(Iodine) (-6.6 mg/mL), 70 keV (6.2 HU), Iodine(Water) (4.6 mg/mL), 140 keV (-4.2 HU), and finally 110 keV (-2.7 HU). Both inter- and intra-scanner variance was primarily affected by $CTDI_{vol}$ and secondarily by mAs. With the exception of the inter-scanner variance for 50 keV reconstruction, increasing $CTDI_{vol}$ and mAs were associated with reduced variance. In

general, intra-scanner variance was greater than inter-scanner variance, with increased intra-scanner variance corresponding with increased absolute uniformity.

Results of the linear mixed model analysis for the effect of the primary acquisition parameter, rotation time, on uniformity in the DEQC body phantom can be seen in Table 6.15. The opposite effects of increased rotation time on the 50 keV and Iodine(Water) versus the 110 keV, 140 keV and Water(Iodine) can be seen in the reversed ranking order.

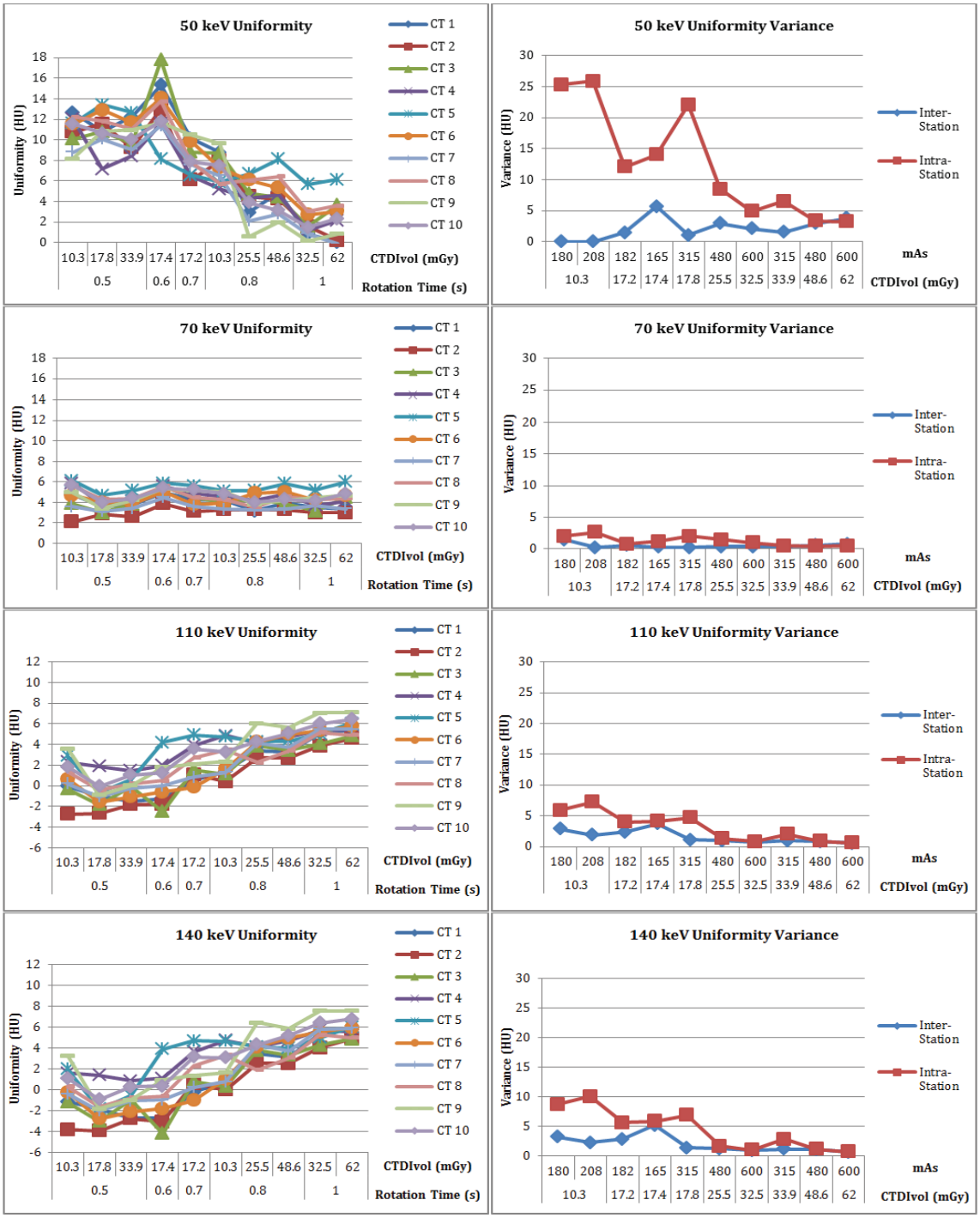

Figure 6.6: DEQC body phantom results for uniformity. Left: Uniformity trends sorted primarily by rotation time and secondarily by $CTDI_{vol}$ for 50, 70, 110 and 140 keV monoenergetic reconstructions and displayed by scanner. Right: Uniformity inter- and intra-scanner variance trends sorted primarily by $CTDI_{vol}$ and secondarily by mAs for 50, 70, 110, and 140 keV monoenergetic reconstructions.

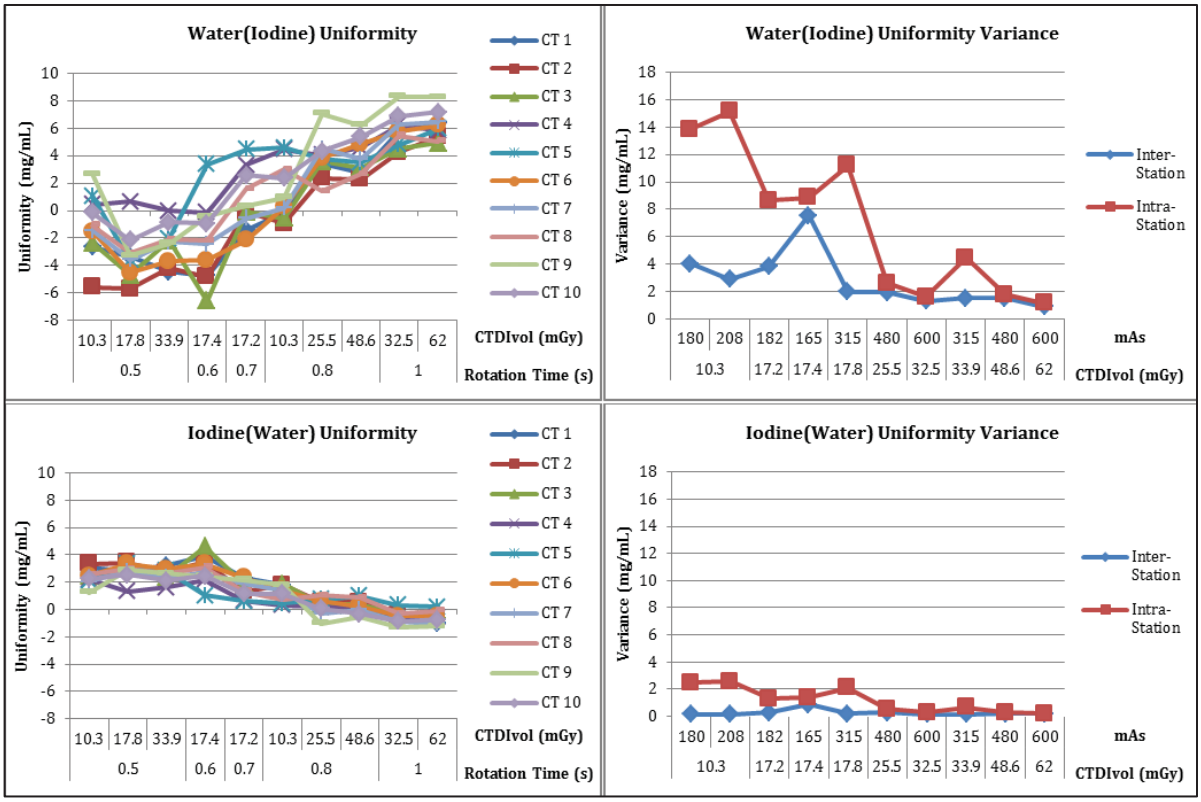

Figure 6.7: DEQC body phantom results for uniformity. Left: Uniformity trends sorted primarily by rotation time and secondarily by $CTDI_{vol}$ for Water(Iodine) and Iodine(Water) material density reconstructions and displayed by scanner. Right: Uniformity inter- and intra-scanner variance trends sorted primarily by $CTDI_{vol}$ and secondarily by mAs for Water(Iodine) and Iodine(Water) material density reconstructions.

Table 6.15: DEQC body phantom results for the effect of rotation time on uniformity based on linear mixed model analysis.

Dual-Energy Reconstruction	Rotation Time effect on Uniformity
50 keV	0.6 >> 0.5 >> 0.7 >> 0.8 >> 1
70 keV	0.6 >> 0.7 >> 1 = 0.5 = 0.8
110 keV	1 >> 0.8 >> 0.7 >> 0.6 > 0.5
140 keV	1 >> 0.8 >> 0.7 >> 0.5 = 0.6
Water (Iodine)	1 >> 0.8 >> 0.7 >> 0.5 = 0.6
Iodine (Water)	0.6 >> 0.5 >> 0.7 >> 0.8 >> 1

Legend		
>>	Significantly Different	P < 0.05
>	Not Significantly Different	0.05 < P < 0.9
=	Statistically Equivalent	P > 0.9

The effect of rotation time, mAs and the keV of the monoenergetic reconstruction can be seen in Figure 6.8. Uniformity is independent of reconstructed keV only using only one of the protocols investigated: GSI-10 (0.8sec rotation time, 480mAs). Low rotation time protocols resulted in wide variation in uniformity based on keV of the monoenergetic reconstruction.

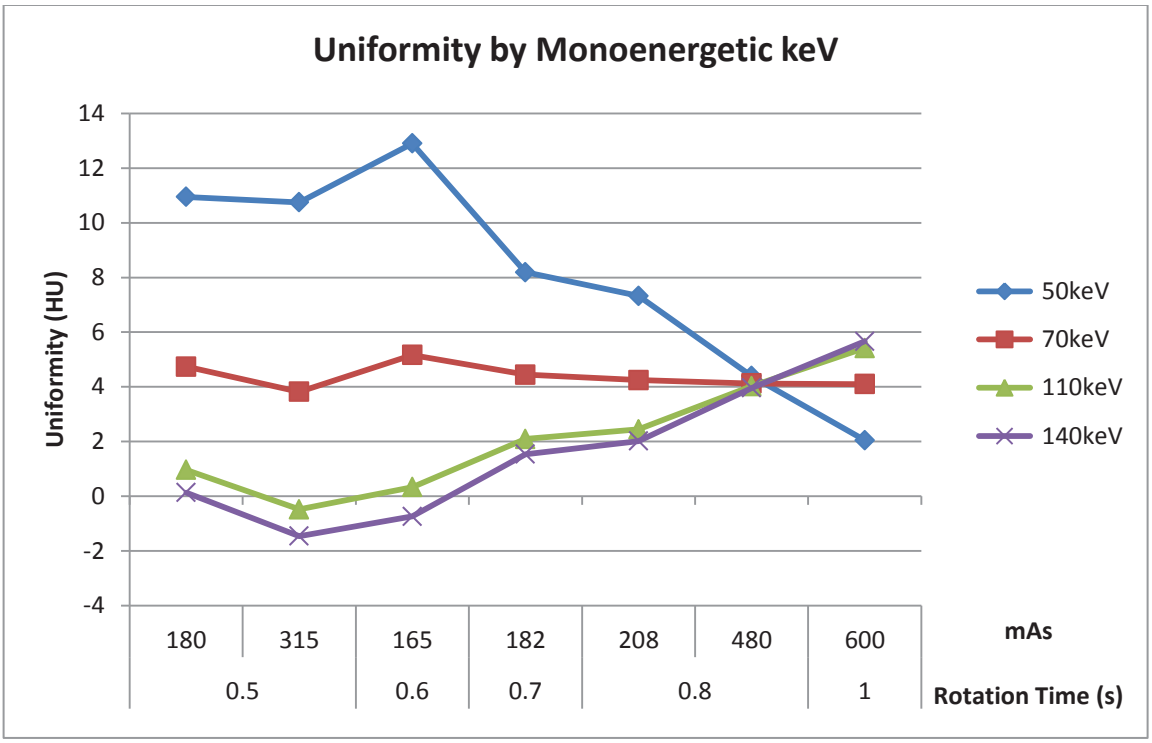

Figure 6.8: DEQC body phantom results for uniformity sorted primarily by rotation time and secondarily by mAs for 50, 70, 110 and 140 keV monoenergetic reconstructions.

DEQC Head Phantom:

Uniformity using the DEQC head phantom was found to be affected primarily by mAs and secondarily by $CTDI_{vol}$ for all dual-energy reconstructions investigated (Figure 6.9, Figure 6.10). Unlike the DEQC body phantom, uniformity was not noticeably affected by rotation time. In addition, uniformity using the DEQC head phantom was universally improved by increases in the primary acquisition parameter (mAs). Similarly to the DEQC body phantom results, uniformity for 70 keV monoenergetic reconstruction was fairly invariant to changes in acquisition parameter; however, the DEQC head phantom uniformity result was much closer to 0 HU than that of the DEQC body phantom. Uniformity was vastly improved for 50 keV monoenergetic reconstruction from a maximum absolute value of 17.8 HU in the DEQC body phantom to 4.9 HU in the DEQC head phantom. Maximum

absolute uniformity, representing the greatest deviation from the ideal value of zero, was found in Water(Iodine) (5.2 mg/mL) followed by 50 keV (-4.9 HU), 140 keV (4.2 HU), 110 keV (3.5 HU), Iodine(Water) (-1.9 mg/mL), and finally 70 keV (-1.8 HU). Intra-scanner variance was primarily affected by $CTDI_{vol}$ and secondarily by mAs and corresponded with increased absolute uniformity. Inter-scanner variance was generally on the same order as intra-scanner variance, however, none of the acquisition parameters investigated were found to correlate with reduced inter-scanner variance.

Of note in Figure 6.9 are the abnormal uniformity results for CT 6 using 50 keV monoenergetic reconstruction. For all protocols investigated, acquisitions on CT 6 resulted in substantially higher uniformity values than the rest of the scanner population. This might indicate a service issue present on this scanner, however, since the metric value is improved relative to the other scanners, the appropriate course of action is uncertain at this point.

Results of the linear mixed model analysis for the effect of the primary acquisition parameter, mAs, on uniformity in the DEQC head phantom can be seen in Table 6.16. Although increased mAs did seem to lead to improved uniformity, statistical analysis indicated that the 315 and 384 mAs protocols resulted in the best uniformity for the DEQC head phantom. These results are supported by the simplified visualization of uniformity results by mAs and reconstructed keV (Figure 6.11). The lowest mAs value investigated, 208mAs, results in wider uniformity variation with changes in the keV of the monoenergetic reconstruction.

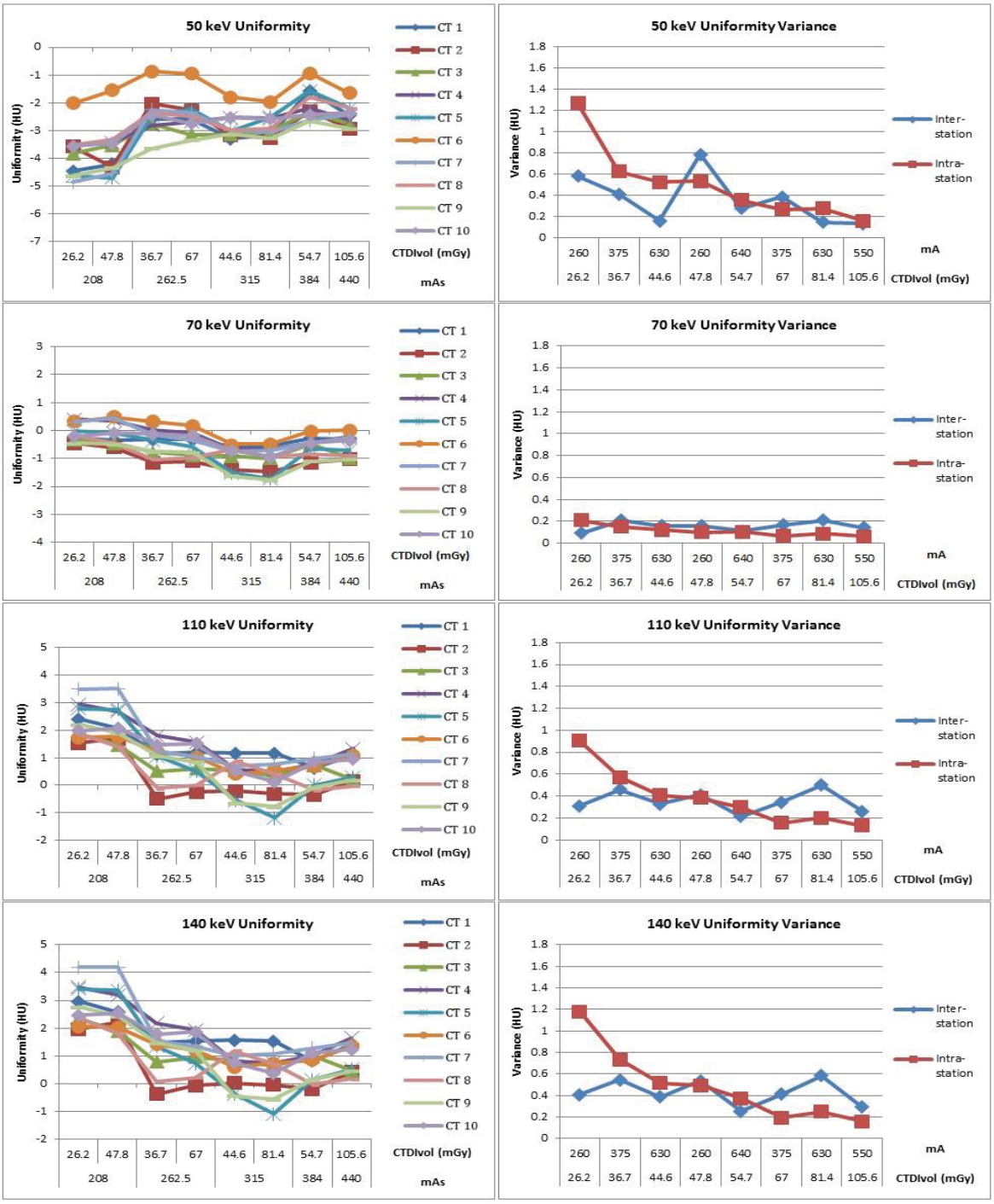

Figure 6.9: DEQC head phantom results for uniformity. Left: Uniformity trends sorted primarily by mAs and secondarily by $CTDI_{vol}$ for 50, 70, 110 and 140 keV monoenergetic reconstructions and displayed by scanner. Right: Uniformity inter- and intra-scanner variance trends sorted primarily by CTDIvol and secondarily by mA for 50, 70, 110, and 140 keV monoenergetic reconstructions.

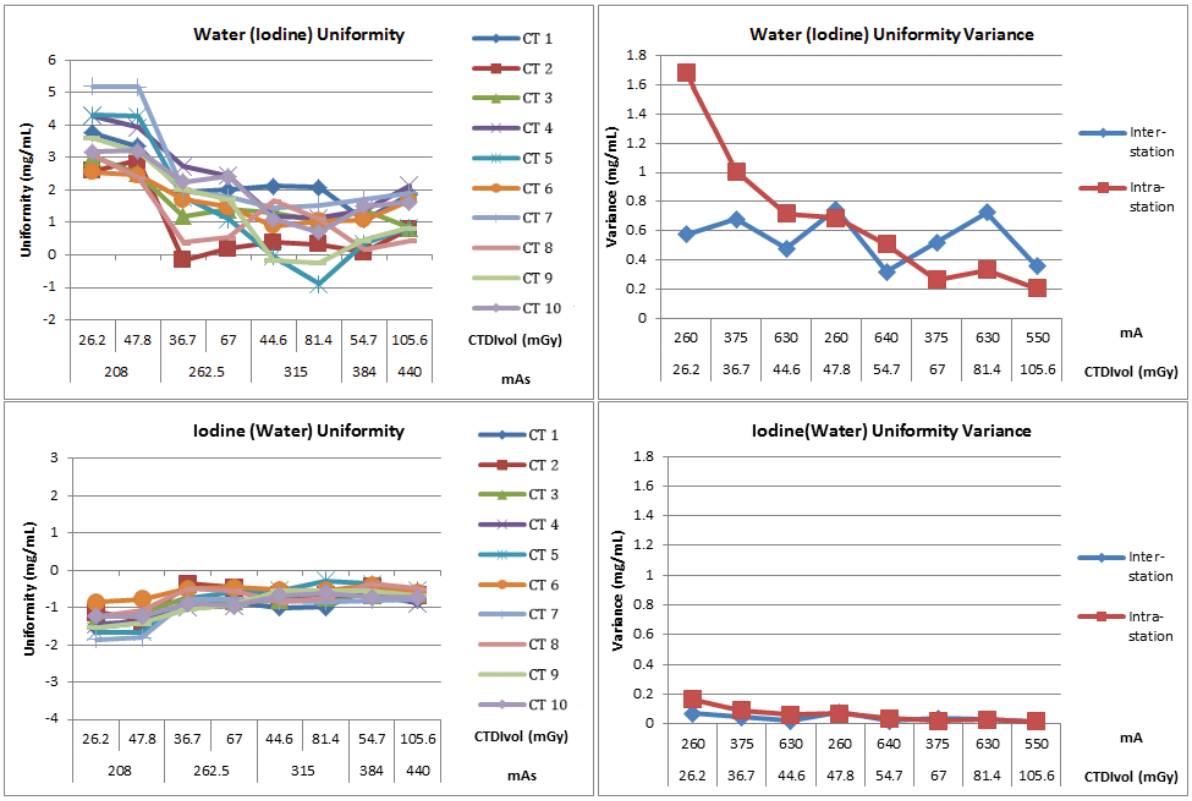

Figure 6.10: DEQC head phantom results for uniformity. Left: Uniformity trends sorted primarily by mAs and secondarily by $CTDI_{vol}$ for Water(Iodine) and Iodine(Water) material density reconstructions and displayed by scanner. Right: Uniformity inter- and intra-scanner variance trends sorted primarily by $CTDI_{vol}$ and secondarily by mA for Water(Iodine) and Iodine(Water) material density reconstructions.

Table 6.16: DEQC head phantom results for the effect of mAs on Uniformity based on linear mixed model analysis.

Dual-Energy Reconstruction	mAs effect on Uniformity
50 keV	384 >> 440 = 262.5 >> 315 >> 208
70 keV	208 >> 262.5 >> 440 = 384 >> 315
110 keV	208 >> 262.5 >> 440 > 384 > 315
140 keV	208 >> 262.5 > 440 >> 384 > 315
Water (Iodine)	208 >> 262.5 > 440 >> 384 = 315
Iodine (Water)	384 >> 440 = 315 > 262.5 >> 208

Legend		
>>	Significantly Different	P < 0.05
>	Not Significantly Different	0.05 < P < 0.9
=	Statistically Equivalent	P > 0.9

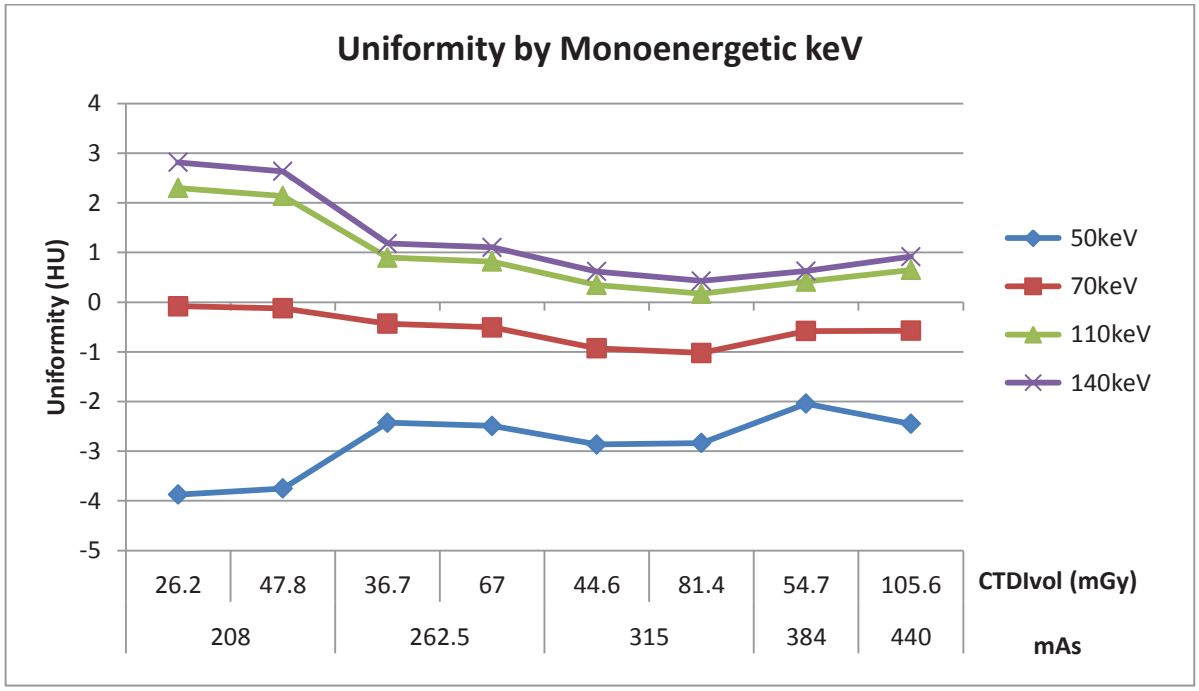

Figure 6.11: DEQC head phantom results for uniformity sorted primarily by mAs and secondarily by rotation time for 50, 70, 110 and 140 keV monoenergetic reconstructions.

6.3.2.3 Monoenergetic HU Stability

DEQC Body Phantom:

Monoenergetic HU Stability using the DEQC body phantom was found to be affected primarily by mAs and secondarily by $CTDI_{vol}$ for all monoenergetic reconstructions investigated (Figure 6.12). All visualizations are shown over a 30 HU range, however the minimum and maximum attenuation shown is specific to the reconstruction. Using vendor-provided elemental composition for the soft tissue rods and acquired NIST attenuation values, the predicted attenuation assuming a true monoenergetic acquisition was calculated. These values, shown as black lines, demonstrate the varied attenuations, and thus varied contrasts, supplied by monoenergetic imaging. For 110 and 140 keV reconstructions, the accuracy of the attenuation is improved with increased mAs. In this case, low mAs protocols overestimate the attenuation in the soft tissue rods. For 50 keV, protocols with increased mAs do increase the attenuation, however none of the protocols investigated provides an accurate attenuation. 70 keV monoenergetic reconstruction was invariant to changes in protocol and in general was within 5 HU of the predicted attenuation. Based on protocol and scanner variation, the range of possible attenuations provided by 50, 70, 110 and 140 keV reconstructions was 26 HU, 6 HU, 12 HU and 15 HU, respectively. Intra-scanner variance was primarily affected by $CTDI_{vol}$ and secondarily affected by mAs. Inter-scanner variance appeared to be equally affected by both parameters. In general, inter- and intra-scanner variances were on the same order of magnitude, however inter-scanner variance was occasionally greater than intra-scanner variance for 50 keV monoenergetic reconstruction.

Results of the linear mixed model analysis for the effect of the primary acquisition parameter, mAs, on monoenergetic HU stability in the DEQC body phantom can be seen in Table 6.17. Increasing mAs had a statistically significant effect on improving monoenergetic HU stability for both 110 and 140 keV. Results for 70 keV seem to indicate an optimal mAs of 182, however given the limited variability of the result with mAs, it is unlikely that this is clinically significant.

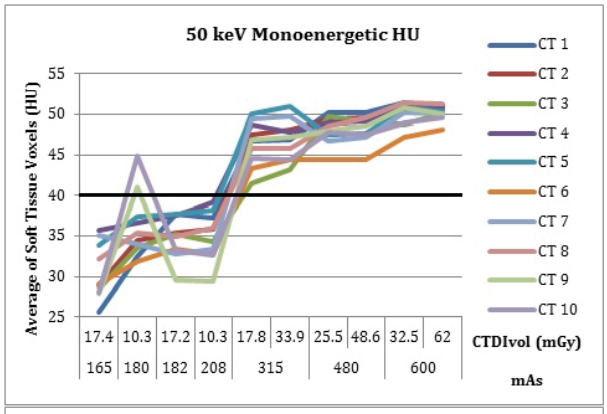
50 keV Monoenergetic HU
Average of Soft Tissue Voxels (HU)
55
50
45
40
35
30
25
CT 1
CT 2
CT 3
CT 4
CT 5
CT 6
CT 7
CT 8
CT 9
CT 10
17.4 10.3 17.2 10.3 17.8 33.9 25.5 48.6 32.5 62
CTDIvol (mGy)
165 180 182 208 315 480 600
mAs

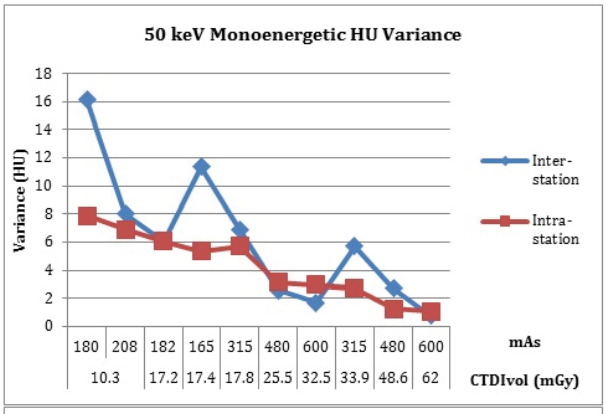
50 keV Monoenergetic HU Variance
Variance (HU)
18
16
14
12
10
8
6
4
2
0
Inter-station
Intra-station
180 208 182 165 315 480 600 315 480 600
mAs
10.3 17.2 17.4 17.8 25.5 32.5 33.9 48.6 62
CTDIvol (mGy)

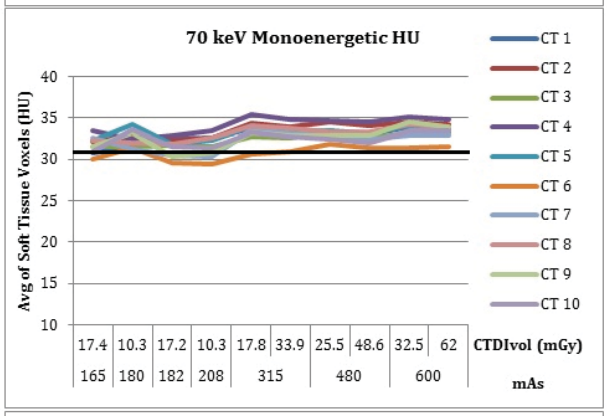
70 keV Monoenergetic HU
Avg of Soft Tissue Voxels (HU)
40
35
30
25
20
15
10
CT 1
CT 2
CT 3
CT 4
CT 5
CT 6
CT 7
CT 8
CT 9
CT 10
17.4 10.3 17.2 10.3 17.8 33.9 25.5 48.6 32.5 62
CTDIvol (mGy)
165 180 182 208 315 480 600
mAs

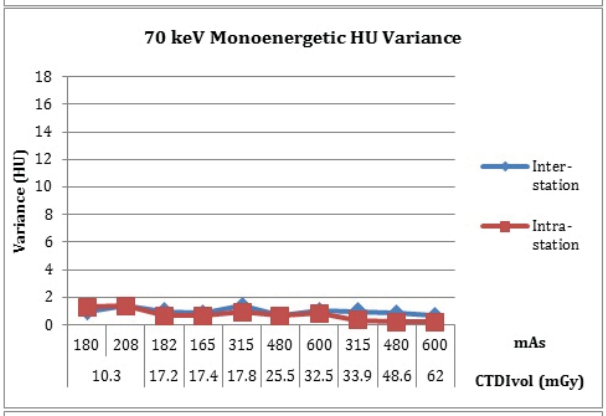
70 keV Monoenergetic HU Variance
Variance (HU)
18
16
14
12
10
8
6
4
2
0
Inter-station
Intra-station
180 208 182 165 315 480 600 315 480 600
mAs
10.3 17.2 17.4 17.8 25.5 32.5 33.9 48.6 62
CTDIvol (mGy)

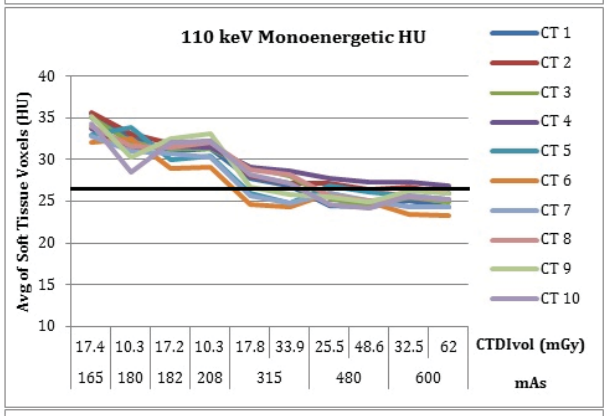
110 keV Monoenergetic HU
Avg of Soft Tissue Voxels (HU)
40
35
30
25
20
15
10
CT 1
CT 2
CT 3
CT 4
CT 5
CT 6
CT 7
CT 8
CT 9
CT 10
17.4 10.3 17.2 10.3 17.8 33.9 25.5 48.6 32.5 62
CTDIvol (mGy)
165 180 182 208 315 480 600
mAs

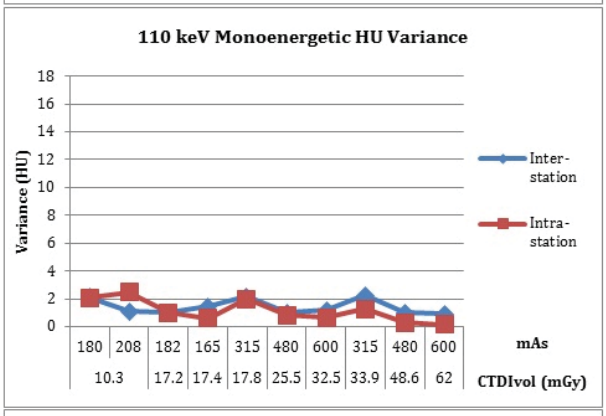
110 keV Monoenergetic HU Variance
Variance (HU)
18
16
14
12
10
8
6
4
2
0
Inter-station
Intra-station
180 208 182 165 315 480 600 315 480 600
mAs
10.3 17.2 17.4 17.8 25.5 32.5 33.9 48.6 62
CTDIvol (mGy)

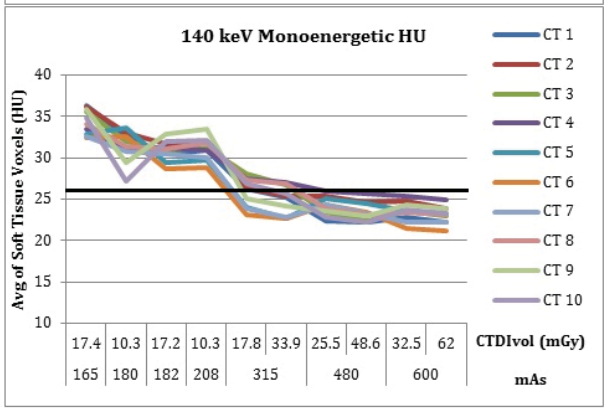
140 keV Monoenergetic HU
Avg of Soft Tissue Voxels (HU)
40
35
30
25
20
15
10
CT 1
CT 2
CT 3
CT 4
CT 5
CT 6
CT 7
CT 8
CT 9
CT 10
17.4 10.3 17.2 10.3 17.8 33.9 25.5 48.6 32.5 62
CTDIvol (mGy)
165 180 182 208 315 480 600
mAs

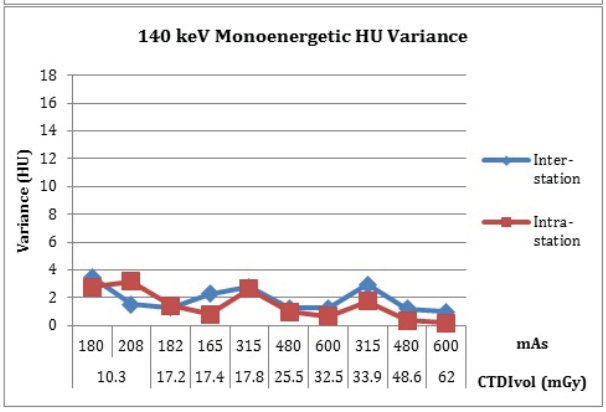
140 keV Monoenergetic HU Variance
Variance (HU)
18
16
14
12
10
8
6
4
2
0
Inter-station
Intra-station
180 208 182 165 315 480 600 315 480 600
mAs
10.3 17.2 17.4 17.8 25.5 32.5 33.9 48.6 62
CTDIvol (mGy)

Figure 6.12: DEQC body phantom results for monoenergetic HU stability. Left: Monoenergetic HU stability trends sorted primarily by mAs and secondarily by $CTDI_{vol}$ for 50, 70, 110 and 140 keV monoenergetic reconstructions and displayed by scanner. Calculated attenuations (using NIST values) based on vendor-provided elemental composition and true monoenergetic acquisition are shown in black. Right: Monoenergetic HU stability inter- and intra-scanner variance trends sorted primarily by $CTDI_{vol}$ and secondarily by mAs for 50, 70, 110, and 140 keV monoenergetic reconstructions.

Table 6.17: DEQC body phantom results for the effect of mAs on monoenergetic HU stability based on linear mixed model analysis.

Dual-Energy Reconstruction	mAs effect on Monoenergetic HU Stability
50 keV	600 >> 480 >> 315 >> 180 >> 182 = 208 >> 165
70 keV	600 >> 315 >> 480 >> 180 >> 165 = 208 > 182
110 keV	165 >> 180 > 208 > 182 >> 315 >> 480 >600
140 keV	165 >> 180 > 208 = 182 >> 315 >> 480 >> 600

Legend		
>>	Significantly Different	P < 0.05
>	Not Significantly Different	0.05 < P < 0.9
=	Statistically Equivalent	P > 0.9

Investigation of trends in monoenergetic HU stability by mAs and monoenergetic keV show the effect of lower mAs protocols on the utility of monoenergetic imaging. Protocols using 208mAs and below result in monoenergetic images with fixed attenuation, and thus fixed contrast, across all monoenergetic energies. Protocols using 315mAs and above provide variable attenuation, and thus variable contrast, across monoenergetic energy values. This variable contrast is one of the added benefits provided by DECT. By altering the keV of the monoenergetic reconstruction, the relative influence of photoelectric and Compton processes is modulated and the relative contrast of high-Z materials can be either enhanced or diminished. This ability has been shown to be particularly useful in the improvement of iodine contrast compared to SECT (41,62,107).

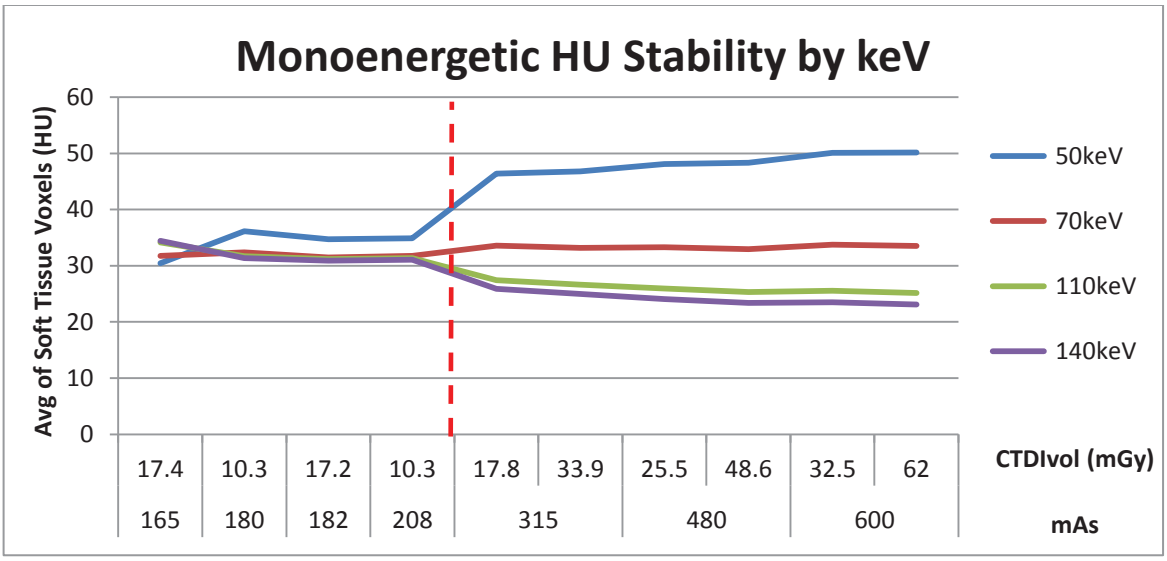

Figure 6.13: DEQC body phantom results for monoenergetic HU stability trends sorted primarily by mAs and secondarily by $CTDI_{vol}$ for 50, 70, 110 and 140 keV monoenergetic reconstructions. The dashed red line indicates a potential mAs cutoff for optimum efficiency of monoenergetic visualizations.

DEQC Head Phantom:

Monoenergetic HU Stability using the DEQC head phantom was found to be affected primarily by mA and secondarily by $CTDI_{vol}$ for all monoenergetic reconstructions investigated (Figure 6.14). Similar to uniformity results from the DEQC phantom, CT 6 appears to deviate from the rest of the scanner population. All visualizations are shown using a 16 HU range, however the minimum and maximum attenuation shown is specific to the reconstruction. Using vendor-provided elemental composition for the soft tissue rods and acquired NIST attenuation values, the predicted attenuation assuming a true monoenergetic acquisition was calculated. These values, shown as black lines, demonstrate the variable attenuation, and thus variable contrast, supplied by monoenergetic imaging. For 110 and 140 keV reconstructions, the reconstruction attenuation decreases as mA increases. This trend is reversed at the highest mA value

investigated. Tube current (mA) values under 630mA appear to be fairly invariant to mA changes. Two potential explanations for this pattern include: 1) attenuation does in fact decrease with increasing mA, and the 640mA acquisition represents an unexpected change in this pattern; 2) attenuation is stable as mA changes, and that the 630mA acquisitions represent an unexpected change in this pattern. The correct interpretation of these results is unclear at this point. 70 keV monoenergetic reconstruction follows a similar pattern to 110 and 140 keV, however to a much lesser extent with all results falling between 31 and 36 HU. 50 keV monoenergetic reconstructions show a similar pattern but inverted, with the 630mA acquisitions resulting in higher attenuations than expected and the 640mA protocol resulting in lower attenuations. Based on protocol and scanner variation, the range of possible attenuations provided by 50, 70, 110 and 140 keV reconstructions was 9 HU, 5 HU, 7 HU and 8 HU, respectively.

Inter- and intra-scanner variance were primarily affected by mA and secondarily affected by $CTDI_{vol}$. Variance for 50 keV monoenergetic reconstructions decreased with increasing mA while variance for 110 and 140 keV increased with increasing mA. Variance for 70 keV monoenergetic reconstructions was fairly stable across all mA values investigated. Inter-scanner variance was considerably higher than intra-scanner variance for 50 keV monoenergetic reconstructions acquired using protocols with lower than 630mA.

Results of the linear mixed model analysis for the effect of the primary acquisition parameter, mA, on monoenergetic HU stability in the DEQC head phantom can be seen in Table 6.18. Attenuation was found to be statistically significantly different for all mA values investigated using 110 or 140 keV reconstructions.

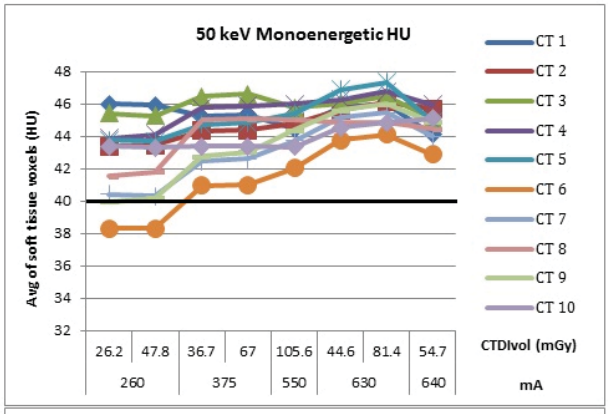
50 keV Monoenergetic HU
Avg of soft tissue voxels (HU)
CT 1
CT 2
CT 3
CT 4
CT 5
CT 6
CT 7
CT 8
CT 9
CT 10
26.2 47.8 36.7 67 105.6 44.6 81.4 54.7
260 375 550 630 640
CTDIvol (mGy)
mA

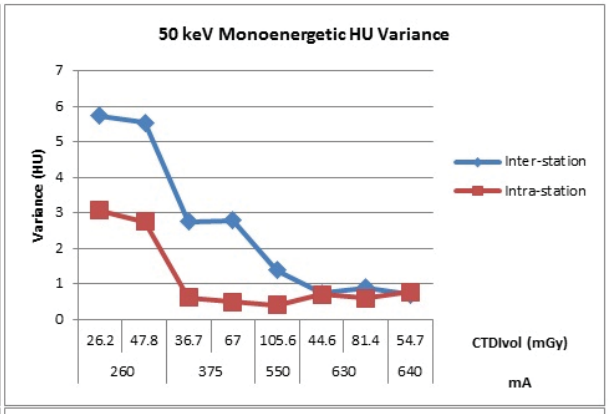
50 keV Monoenergetic HU Variance
Variance (HU)
Inter-station
Intra-station
26.2 47.8 36.7 67 105.6 44.6 81.4 54.7
260 375 550 630 640
CTDIvol (mGy)
mA

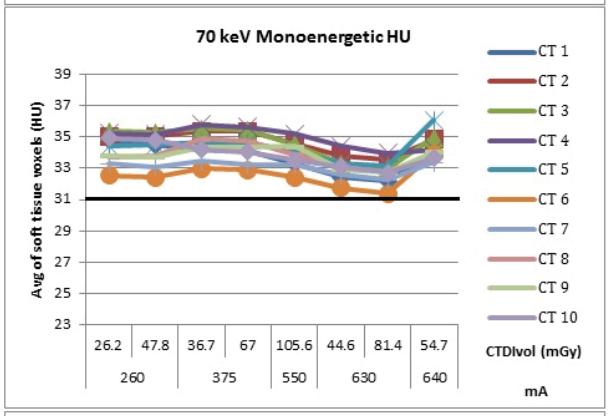
70 keV Monoenergetic HU
Avg of soft tissue voxels (HU)
CT 1
CT 2
CT 3
CT 4
CT 5
CT 6
CT 7
CT 8
CT 9
CT 10
26.2 47.8 36.7 67 105.6 44.6 81.4 54.7
260 375 550 630 640
CTDIvol (mGy)
mA

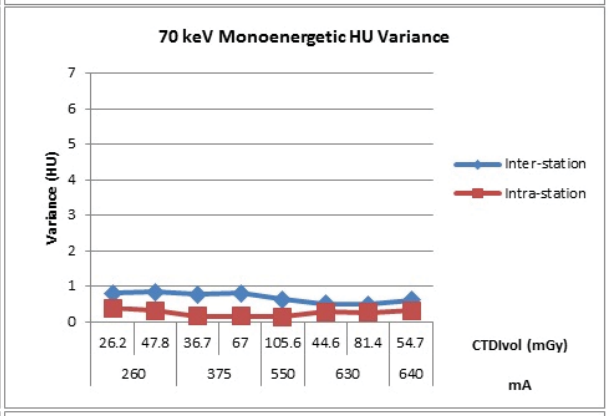
70 keV Monoenergetic HU Variance
Variance (HU)
Inter-station
Intra-station
26.2 47.8 36.7 67 105.6 44.6 81.4 54.7
260 375 550 630 640
CTDIvol (mGy)
mA

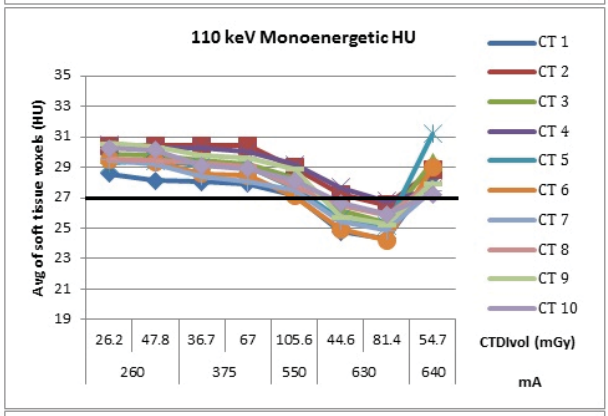
110 keV Monoenergetic HU
Avg of soft tissue voxels (HU)
CT 1
CT 2
CT 3
CT 4
CT 5
CT 6
CT 7
CT 8
CT 9
CT 10
26.2 47.8 36.7 67 105.6 44.6 81.4 54.7
260 375 550 630 640
CTDIvol (mGy)
mA

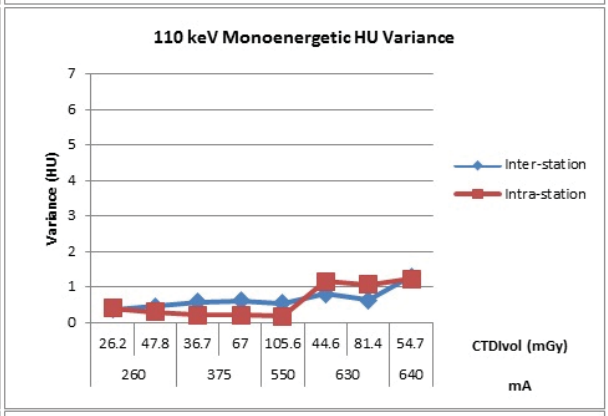
110 keV Monoenergetic HU Variance
Variance (HU)
Inter-station
Intra-station
26.2 47.8 36.7 67 105.6 44.6 81.4 54.7
260 375 550 630 640
CTDIvol (mGy)
mA

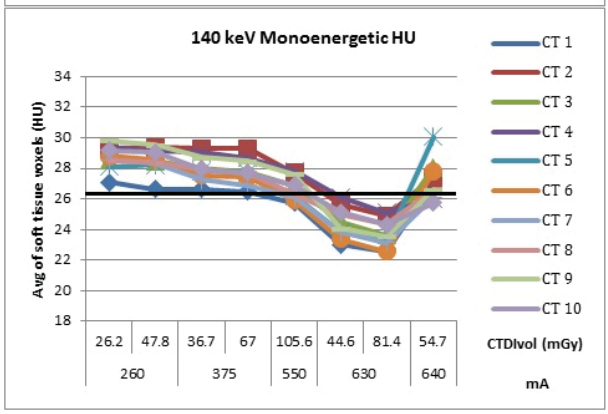
140 keV Monoenergetic HU
Avg of soft tissue voxels (HU)
CT 1
CT 2
CT 3
CT 4
CT 5
CT 6
CT 7
CT 8
CT 9
CT 10
26.2 47.8 36.7 67 105.6 44.6 81.4 54.7
260 375 550 630 640
CTDIvol (mGy)
mA

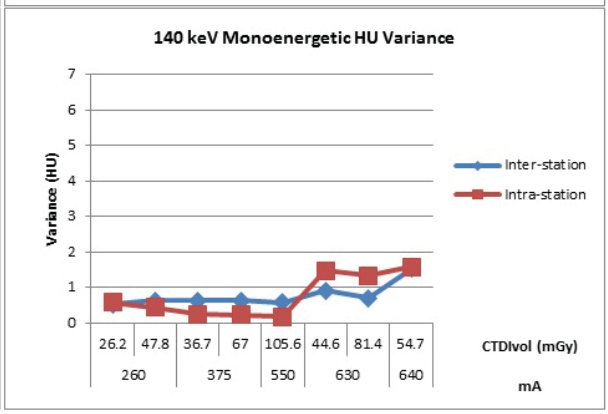
140 keV Monoenergetic HU Variance
Variance (HU)
Inter-station
Intra-station
26.2 47.8 36.7 67 105.6 44.6 81.4 54.7
260 375 550 630 640
CTDIvol (mGy)
mA

Figure 6.14: DEQC head phantom results for monoenergetic HU stability. Left: Monoenergetic HU stability trends sorted primarily by mA and secondarily by $CTDI_{vol}$ for 50, 70, 110 and 140 keV monoenergetic reconstructions and displayed by scanner. Calculated attenuations (using NIST values) based on vendor-provided elemental composition and true monoenergetic acquisition are shown in black. Right: Monoenergetic HU stability inter- and intra-scanner variance trends sorted primarily by mA and secondarily by $CTDI_{vol}$ for 50, 70, 110, and 140 keV monoenergetic reconstructions.

Table 6.18: DEQC head phantom results for the effect of mA on monoenergetic HU stability based on linear mixed model analysis.

Dual-Energy Reconstruction	mA effect on Iodine Accuracy
50 keV	630 >> 640 > 550 > 375 >> 260
70 keV	375 >> 640 = 260 >> 550 >> 630
110 keV	260 >> 375 >> 640 >> 550 >> 630
140 keV	260 >> 375 >> 640 >> 550 >> 630

Legend		
>>	Significantly Different	P < 0.05
>	Not Significantly Different	0.05 < P < 0.9
=	Statistically Equivalent	P > 0.9

Investigation of trends in monoenergetic HU stability by mA and monoenergetic keV show relatively stable attenuation response compared to the dramatic effect seen in the DEQC body phantom. Attenuation with respect to keV of the monoenergetic reconstruction was most variable (largest range) for 630mA protocols.

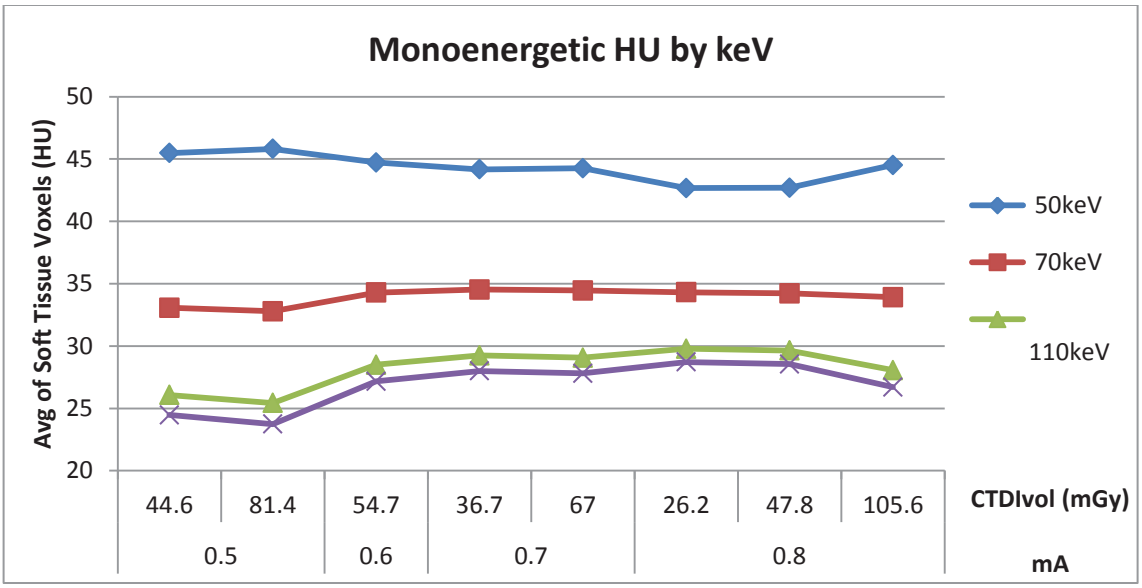

Figure 6.15: DEQC head phantom results for monoenergetic HU stability trends sorted primarily by mA and secondarily by $CTDI_{vol}$ for 50, 70, 110 and 140 keV monoenergetic reconstructions.

6.3.2.4 Noise

DEQC Body Phantom:

Noise using the DEQC body phantom was found to be affected solely by $CTDI_{vol}$ for all dual-energy reconstructions investigated (Figure 6.16, Figure 6.17). As expected, noise was greatest for 50 keV monoenergetic reconstructions. Unexpectedly, 110 and 140 keV reconstructions resulted in lower noise values than 70 keV for all $CTDI_{vol}$ values investigated. This effect is likely due to reduction in beam hardening artifacts at the higher monoenergetic reconstructions. Water(Iodine) reconstruction noise was higher than Iodine(Water) noise at all $CTDI_{vol}$ values investigated, however, direct comparison of these two noise values is inappropriate due to the large differences in the relative dynamic range of the two image types. In general, voxel values from water density images tend to span approximately 100 mg/mL, while voxel values from iodine density images tend to span approximately 20-25 mg/mL.

Results of the linear mixed model analysis for the effect of the primary acquisition parameter, $CTDI_{vol}$, on noise in the DEQC body phantom can be seen in Table 6.19. A statistically significant change in noise was seen for all incremental $CTDI_{vol}$ increases over 2 mGy for all dual-energy reconstructions.

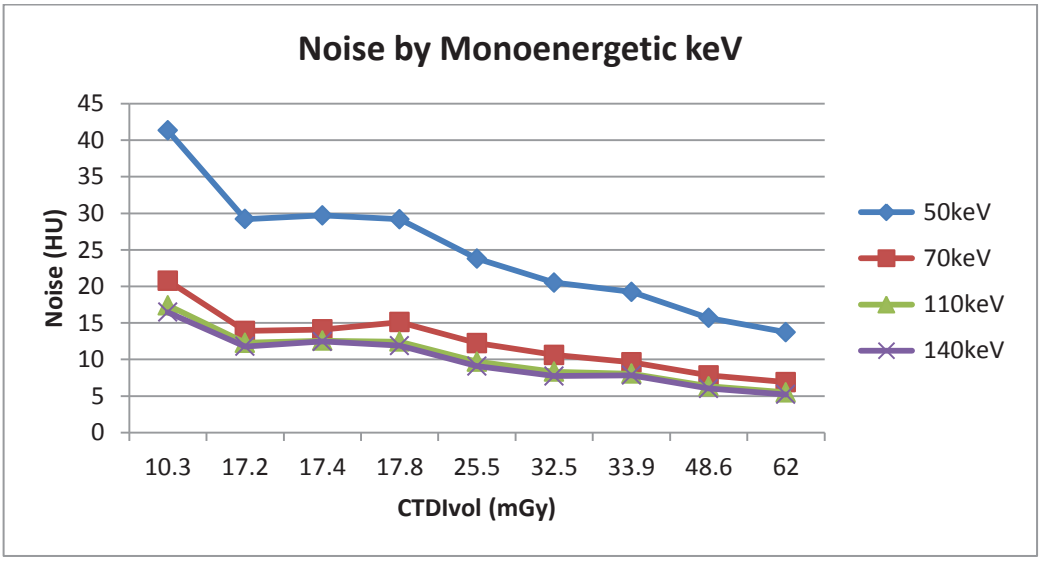

Figure 6.16: DEQC body phantom results for noise trends sorted by $CTDI_{vol}$ for 50, 70, 110 and 140 keV monoenergetic reconstructions.

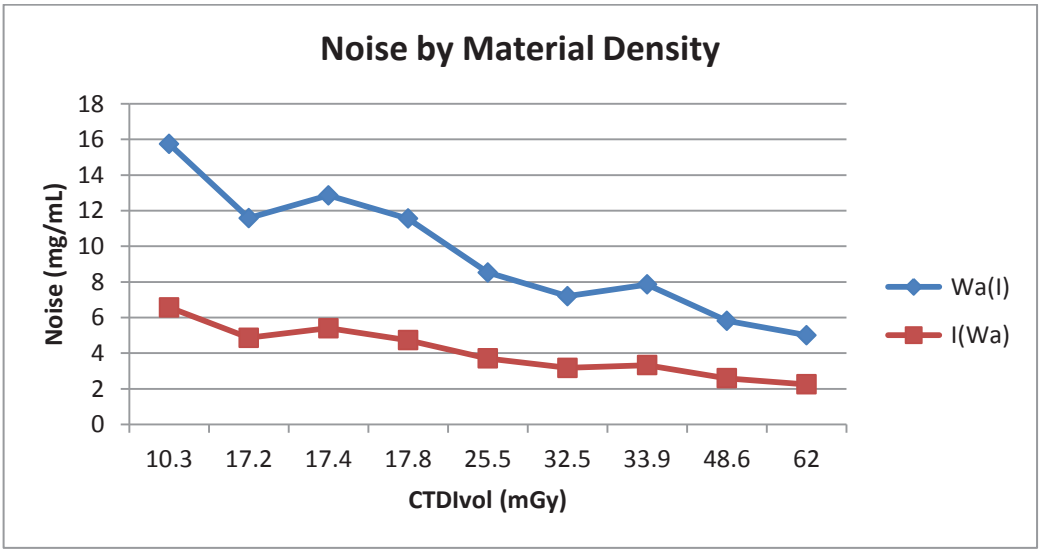

Figure 6.17: DEQC body phantom results for noise trends sorted by $CTDI_{vol}$ for Water(Iodine) and Iodine(Water) material density reconstructions.

Table 6.19: DEQC body phantom results for the effect of $CTDI_{vol}$ on noise based on linear mixed model analysis.

Dual-Energy Reconstruction	$CTDI_{vol}$ effect on Noise
50 keV	10.3 >> 17.4 > 17.8 = 17.2 >> 25.5 >> 32.5 >> 33.9 >> 48.6 >> 62
70 keV	10.3 >> 17.8 >> 17.4 > 17.2 >> 25.5 >> 32.5 >> 33.9 >> 48.6 >> 62
110 keV	10.3 >> 17.4 = 17.8 > 17.2 >> 25.5 >> 32.5 >> 33.9 >> 48.6 >> 62
140 keV	10.3 >> 17.4 >> 17.8 = 17.2 >> 25.5 >> 33.9 = 32.5 >> 48.6 >> 62
Water (Iodine)	10.3 >> 17.4 >> 17.8 = 17.2 >> 33.9 >> 32.5 >> 48.6 >> 62
Iodine (Water)	10.3 >> 17.4 >> 17.2 > 17.8 >> 25.5 >> 33.9 >> 32.5 >> 48.6 >> 62

Legend		
>>	Significantly Different	P < 0.05
>	Not Significantly Different	0.05 < P < 0.9
=	Statistically Equivalent	P > 0.9

DEQC Head Phantom:

Noise using the DEQC head phantom was found to be affected solely by $CTDI_{vol}$ for all dual-energy reconstructions investigated (Figure 6.18, Figure 6.19). As expected based on the literature, noise was lowest for 70 keV monoenergetic reconstructions with higher keV reconstructions resulting in slightly higher noise and 50 keV reconstructions resulting in the greatest amount of noise. This represents a change in the noise pattern for higher keV reconstructions relative to the DEQC body phantom, where the reduction in beam hardening likely played a larger role due to the greater size of the phantom. Water(Iodine) reconstruction noise was higher than Iodine(Water) noise at all $CTDI_{vol}$ values investigated, however, given the large differences in the relative dynamic range of the two image types, direct comparison of these two noise values is inappropriate.

Results of the linear mixed model analysis for the effect of the primary acquisition parameter, $CTDI_{vol}$, on noise in the DEQC body phantom can be seen in Table 6.20. Statistically significant changes in noise were found across all dual-energy reconstructions for each $CTDI_{vol}$ investigated except the 36.7 and 47.8 mGy protocols.

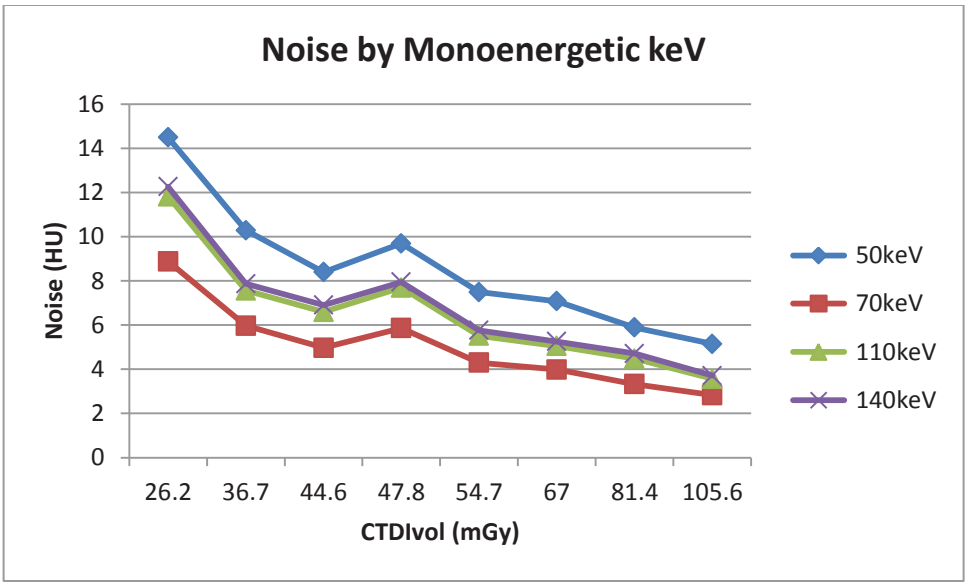

Figure 6.18: DEQC head phantom results for noise trends sorted by $CTDI_{vol}$ for 50, 70, 110 and 140 keV monoenergetic reconstructions.

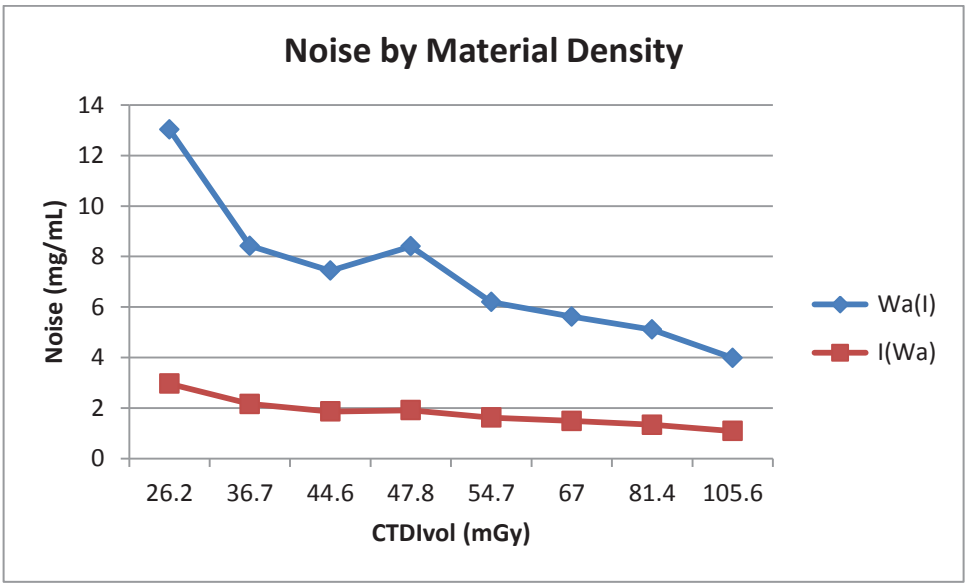

Figure 6.19: DEQC head phantom results for noise trends sorted by $CTDI_{vol}$ for Water(Iodine) and Iodine(Water) material density reconstructions.

Table 6.20: DEQC head phantom results for the effect of $CTDI_{vol}$ on noise based on linear mixed model analysis.

Dual-Energy Reconstruction	$CTDI_{vol}$ effect on Noise
50 keV	26.2 >> 36.7 >> 47.8 >> 44.6 >> 54.7 >> 67 >> 81.4 >> 105.6
70 keV	26.2 >> 36.7 > 47.8 >> 44.6 >> 54.7 >> 67 >> 81.4 >> 105.6
110 keV	26.2 >> 47.8 > 36.7 >> 44.6 >> 54.7 >> 67 >> 81.4 >> 105.6
140 keV	26.2 >> 47.8 > 36.7 >> 44.6 >> 54.7 >> 67 >> 81.4 >> 105.6
Water (Iodine)	26.2 >> 36.7 = 47.8 >> 44.6 >> 54.7 >> 67 >> 81.4 >> 105.6
Iodine (Water)	26.2 >> 36.7 >> 47.8 > 44.6 >> 54.7 >> 67 >> 81.4 >> 105.6

Legend		
>>	Significantly Different	P < 0.05
>	Not Significantly Different	0.05 < P < 0.9
=	Statistically Equivalent	P > 0.9

6.3.3 Recommendations on Clinical Implementation of DEQC Program

Although a scan protocol covering the full ranges of multiple parameters is vital for the full characterization of a system, long term collection of such data for QC purposes is impractical. In order to develop a long-term quality control program suitable for clinical implementation, a streamlined protocol was developed based on the results from the first 13 weeks of analysis (Table 6.21). Given the similarity of the DEQC head and DEQC body results, and the time required to setup and scan both phantoms, the finalized DEQC program limited data collection and analysis to only the DEQC body phantom. Protocol acquisitions were limited to a more clinical $CTDI_{vol}$ range of 17.2 to 33.9 mGy, while maintaining those acquisitions necessary to separate out effects due to $CTDI_{vol}$ and rotation time. Two such groups remained: approximately 33 mGy at 0.5 and 1.0sec rotation times, and approximately 17.5 mGy at 0.5, 0.6 and 0.7sec rotation times.

A large dataset will be needed in order to determine the baseline values and tolerances necessary for the establishment of a true DECT quality control program. Streamlining the DEQC program from two phantoms with a combined 18 acquisitions to

one phantom with 6 acquisitions allowed more consistent and frequent data collection. In addition, by sampling only the data sets previously acquired from the earlier version, data collection prior to the implementation of this finalized DEQC program could also contribute to future analysis, increasing the size and scope of the data set. This finalized DEQC program is currently established in the clinic and at the point of this publication has collected 35 weekly or bi-weekly DEQC exams on 10 dual-energy CT systems, for a total of 350 DEQC exams.

Table 6.21: Final recommendations for the clinically implementable dual-energy quality control protocol. All acquisitions performed in helical mode, using a 40 mm beam width, Large Body SFOV, 42 cm DFOV and standard reconstruction filter.

Group	GSI-Preset	Pitch	Rot (s)	mA	Img Thk (mm)	Interval	$CTDI_{vol}$	Extent	# Imgs
1	**GSI-1**	0.516	0.5	630	5	5	33.9	S10-I10	5
2	**GSI-5**	0.984	1	600	5	5	32.5	S10-I10	5
3	**GSI-10**	0.984	0.8	600	5	5	25.5	S10-I10	5
4	**GSI-1**	0.984	0.5	630	5	5	17.8	S10-I10	5
5	**GSI-54**	0.516	0.6	275	5	5	17.4	S10-I10	5
6	**GSI-48**	0.516	0.7	260	5	5	17.2	S10-I10	5

6.4 Discussion

While many studies have been performed to evaluate the effect of dual-energy acquisition and processing on noise (41,42,48,63,107), iodine accuracy (42,56,106,114–118) and the stability and accuracy of the attenuations derived from the monoenergetic reconstructions (61), few have investigated the impact of acquisition parameters and none have investigated long term trends in these values. This study sought to investigate the relationship of various acquisition parameters to values important to the quantitative clinical use of dual-energy CT such as iodine accuracy, uniformity, noise and the stability of the attenuations derived from monoenergetic reconstructions. The end goal was to create an

efficient and pertinent DEQC program for clinical implementation and long term data collection.

6.4.1 Iodine Accuracy

Iodine accuracy was found to be primarily affected by protocol mAs with increasing values leading to improved iodine accuracy and decreased intra- and inter-scanner variances. At low mAs values in the DEQC body phantom, iodine accuracy was found to be overestimated for the 2 mg/mL rod, underestimated for the 5 mg/mL rod, and the 15 mg/mL rod remained generally unaffected by protocol variation. While the differences in iodine concentration could certainly play a role, this effect is likely also influenced by differences in location and local environment between the three iodine rods. For both the DEQC body and DEQC head phantom, iodine accuracies converged to a -5% measurement error. Given that independent verification of the concentration of iodine within the rods could not be performed, it is possible that the error is due to incorrect fabrication. The iodine rods are also based on a 0 HU epoxy resin solid water containing a range of elements not limited to hydrogen and oxygen, which may affect the results of the water/iodine material decomposition.

6.4.2 Uniformity

Uniformity measures using the DEQC body phantom were primarily affected by rotation time, however the direction of the effect was dependent on the dual-energy reconstruction. For 50 keV and Iodine(Water) reconstructions, increased rotation time led to lower and improved uniformity values, while in 110 keV, 140 keV and Water(Iodine) reconstructions it led to higher and degraded uniformity. 70 keV uniformity was not affected by increased rotation time, however, it was consistently elevated. Given that these data were collected using a fast-kVp switching technique, one might assume that faster rotation

times would affect the efficiency of the kVp waveform and lead to reduced spectral separation. However, longer rotation times seem to adversely affect uniformity in both the 110 and 140 keV reconstructions. Given the consistently elevated uniformity result for the 70 keV reconstruction, it is likely that some factor outside protocol variation is in play. If an offset were applied to the data to correct for the elevated 70 keV results, 110 and 140 keV uniformity would improve with increasing rotation time and 50 keV would initially improve but then worsen as it overshoots the 0 HU goal. This result would be more consistent with current understanding of the potential effect of rotation time on uniformity measures. This "offset" in the uniformity results could be due to a number of outside factors, however, the most likely factor is phantom design. Based on the local environment of the central soft tissue rod used to evaluate uniformity, it is likely that these measurements might be affected by beam hardening or photon starvation caused by the influence of the 198 and 334 HU calcium rods. This would cause a consistent reduction in the CT number of the central soft tissue rod and thus an elevation in the uniformity value. This hypothesis could be evaluated by replacing all non-soft tissue rods by solid water rods and repeating the measurement. For all dual-energy reconstructions investigated, intra-scanner variance was always equal to or greater than inter-scanner variance, which indicated that uniformity would not be a concern for repeat scanning on varied scanners.

Uniformity measures using the DEQC head phantom were primarily affected by mAs rather than rotation time. This reduced dependence on rotation time is likely due to the reduction in phantom size from the DEQC body phantom to the DEQC head phantom. For all dual-energy reconstructions, increased mAs led to similar or improved uniformity. Uniformity measures for 50 keV reconstructions were much improved from the DEQC body phantom with a reduction in maximum uniformity value from 18 HU for the DEQC body to 5.2 HU for the DEQC head phantom. Of note in the DEQC head phantom uniformity data is the consistently higher uniformity values at 50 keV for CT6 compared to the rest of the

scanner population. Daily single-energy quality control data, which is based on an in-house QC program and measures uniformity in a similarly sized 22 cm diameter phantom (123), showed passing values for uniformity over the complete duration of this study. This finding highlights the serious need for a quality control program designed specifically to monitor the dual-energy capabilities and specific reconstructions available on these scanners.

6.4.3 Monoenergetic HU Stability

Monoenergetic attenuation (HU) results using the DEQC body phantom were dramatically affected by mAs. Protocols with less than 315mAs resulted in similar attenuation measures across all monoenergetic reconstructions investigated. One of the greatest advantages of dual-energy CT over single-energy CT is the variable contrast based on reconstructed keV that is derived from the dual-energy data. In order to acquire dual-energy data, both the 80kVp and 140kVp beams must penetrate through the patient in sufficient quantities to be reconstructed into an image. In the case of the DEQC body phantom, protocols below 315mAs did not provide sufficient tube output to result in adequate photon collection at the detector. Having limited 80kVp data to draw from, the material decomposition process is highly affected, resulting in fixed attenuation across all monoenergetic reconstructions. Since this fixed attenuation is tied to over-attenuation of the 80kVp beam, the mAs limit for this effect will be phantom (or patient) size dependent.

Due to this fixed attenuation at low mAs values, attenuation results varied widely with acquisition protocol resulting in attenuation ranges of 25 HU, 6 HU, 12 HU and 17 HU for 50, 70, 110 and 140 keV reconstructions, respectively. By constraining protocols to only those with mAs of 315 and above, the attenuation ranges were reduced to 10 HU (61% reduction), 5 HU (20% reduction), 6 HU (53% reduction) and 7 HU (54% reduction). These results are within 1 HU of the attenuation ranges found using the DEQC head phantom

where no attenuation discontinuity was identified, potentially indicating stable response due to adequate 80kVp penetration.

Inter-scanner variance was greater than intra-scanner variance for measures of monoenergetic HU stability for 50 keV reconstructions using both the DEQC body and DEQC head phantoms. 50 keV monoenergetic reconstructions are routinely used to increase the conspicuity of iodine (62). Given the high inter-scanner variance relative to the intra-scanner variance, it is recommended that patients requiring repeat measures be limited to a single scanner or imaged using a higher mAs protocol for increased repeatability.

6.4.4 Noise

Noise values improved with increasing selected $CTDI_{vol}$ for both the DEQC body and DEQC head phantom, as expected. Although several papers have shown optimal noise values at 65-77 keV (41,42,48,63,107), data for the DEQC body phantom resulted in lowest noise in the 110 and 140 keV reconstructions. Given the large size of the phantom and the highly heterogeneous environment, it is likely this effect is due to enhanced correction of beam hardening artifacts at the higher keV reconstructions. Data for the DEQC head phantom does not show improved noise values for the 110 and 140 keV reconstructions relative to 70 keV, likely due to the lesser extent of beam hardening in a smaller phantom.

6.4.5 Differences in DEQC Body and DEQC Head Phantom Results

In general, the DEQC head phantom provided more stable and improved results over the DEQC body phantom. Iodine accuracy results for the DEQC head phantom showed 60% improvement in iodine accuracy relative to the DEQC body phantom. While the DEQC body phantom provided inconsistent results on the effect of protocol mAs on

uniformity, the DEQC head phantom provided consistent improvement in measured uniformity with increasing protocol mAs. In addition, the uniformity for 50 keV monoenergetic reconstructions was vastly improved from a maximum value of 18 HU in the DEQC body phantom to 5 HU in the DEQC head phantom. Monoenergetic HU stability results were dramatically improved in the DEQC head phantom due to the lack of over-attenuation of the 80kVp beam. After eliminating those protocols with inadequate transmission, the results for attenuation (HU) range across protocols were similar for both phantoms.

In general, both inter- and intra-scanner variances for all test metrics evaluated were lower in the DEQC head phantom than in the DEQC body phantom. Comparing the DEQC head phantom results to those of the DEQC body phantom, there was a reduction in the dependence on rotation time for both the uniformity and monoenergetic HU stability metrics. Given the smaller size and uniform shape of the DEQC head phantom, the effect on the fast-kVp switching waveform, and thus the material decomposition process is likely less pronounced.

6.4.6 Impact of Results on Intracranial Lesion Characterization

While this project's primary aim was to characterize the response of the DECT scanner and develop a long-term, clinically-implementable quality control program, it also served as validation for the comparison of data collected over time as part of the intracranial lesion research projects. Iodine accuracy for the DEQC head phantom was measured used two iodine rods; one at 2 mg/mL and a second at 5 mg/mL. When imaged using a 120kVp single-energy protocol, these rods have attenuations of 51 HU and 128 HU. This attenuation range is very similar to the attenuation range of intracranial lesions investigated in Chapters 4 and 5. Iodine accuracy for these rods resulted in maximum percent errors of 8 and 6% for the 2 mg/mL and 5 mg/mL rods respectively (Figure 6.5).

Presented as a difference measure instead of a percentage, this translates to maximum errors of 0.15 and 0.3 mg/mL. This, coupled with inter- and intra-scanner variances of under 0.05 mg/mL indicates that iodine concentration measurements are consistent among scanners and over time (at least for several months). Given that all basis material reconstructions are linearly correlated (a calcium/water material density pair is derived from an iodine/water material density pair), these iodine density data also validate the comparison of calcium and water density data collected over time. Direct measure of the calcium and iron rods included in the DEQC head phantom was initially pursued, however use of a non-standard background material for these rods due to material engineering requirements made accuracy measures less straightforward.

Monoenergetic HU stability measurements for the DEQC head phantom resulted in relatively stable attenuation regardless of protocol for 70 keV reconstructions (Figure 6.14). The maximum attenuation range, based on either protocol variation on a single scanner, or scanner variation given a single protocol, was 2.9 HU, within the 3 HU matching of the matched model pairs in Chapter 4. Inter- and intra-scanner variances were found to be under 1 HU. These results support the comparison of the 68 keV monoenergetic data collected over several months as part of the intracranial lesion work.

Uniformity data collected using the DEQC head phantom resulted in uniformities of 2 HU, 2 mg/mL and 6 mg/mL for 70 keV, Iodine(Water) and Water(Iodine) reconstructions respectively (Figure 6.9, Figure 6.10). Results for the Water(Iodine) reconstruction were higher than that of the Iodine(Water) reconstruction, though given the difference in the dynamic range of these image types, the higher value for the Water(Iodine) reconstruction is reasonable. Inter- and intra-scanner variances were found to be below 0.3 HU, 0.2 mg/mL and 1.8 mg/mL for 70 keV, Iodine(Water) and Water(Iodine) respectively. Given that these uniformity errors are minimal, it is unlikely that uniformity errors would affect lesion model data. This is especially likely given that none of the lesion models were

evaluated close to the center of the phantom and instead were positioned midway between the phantom center and periphery (Figure 4.2).

The DEQC head phantom results for iodine accuracy, uniformity and monoenergetic HU stability all resulted in low inter- and intra-scanner variance for the 70 keV, Iodine(Water) and Water(Iodine) reconstructions. This provides independent support for the high inter- and intra-canner correlations found in Chapter 4. Coefficients of variation (CV) were found to be approximately 5% for inter-scanner and 4% for intra-scanner correlations, respectively (Table 4.23), supporting the comparison of results from both different time points and different scanners.

While rod size was not varied as part of the DEQC head phantom, rotation time and selected $CTDI_{vol}$ were identified as sources of variability, similar to the results of inter-method, inter-scanner and intra-scanner correlations investigated in Chapter 4. Results of the DEQC head phantom also indicated mAs as a major parameter affecting multiple test metrics. No analysis was performed based on variation in protocol mAs for the intracranial lesion work, however for the protocols investigated, mAs monotonically increased with selected $CTDI_{vol}$ for a given pitch. This would indicate that analysis by mAs would provide similar results to analysis by selected $CTDI_{vol}$. Given that the use of fixed GSI-presets does not allow for independent investigation of these two parameters, it is possible that variation in mAs may explain the relatively low success of the power fits for determining the appropriate $CTDI_{vol}$ for 90% differentiation accuracy based on lesion attenuation.

In all cases, results of the DEQC head phantom support the comparison of intracranial lesion data collected over the course of several months. The results show low inter- and intra-scanner variability, potentially opening this method for intracranial differentiation and classification to repeat measures on separate scanners. Iodine accuracy, uniformity and monoenergetic HU stability measures using the DEQC head phantom were all significantly improved compared to DEQC body phantom results. Given

the difference in effective diameter of the DEQC head phantom (22 cm diameter) and the biologically relevant brain phantom used in Chapters 4 and 5 (14 cm by 18 cm for an effective diameter of 16 cm), it is likely that the smaller phantom size would lead to even more stable results than those of the DEQC head phantom.

6.4.7 Limitations

Phantom design was heavily influenced by the desire to include the evaluation of a wide range of material rods and test metrics. As a consequence, several aspects of the phantom design may impact the results. First, in order to include relevant material rods, the size of the DEQC head phantom was increased to 22 cm, larger than the approximately 17 cm diameter of the typical human head (124). Second, the profile of the DEQC head phantom was simplified to a circle, enabling easy insertion and removal from the DEQC body phantom. Third, the DEQC head phantom was not designed with anthropomorphic features like a skull, which would influence its applicability to patient scans. Due to its size and shape, the DEQC head phantom was imaged on a stand on the CT table instead of in a head holder, which would better approximate clinical imaging. For both the DEQC head and DEQC body phantoms, material rods were fixed to a single location. Although an attempt was made to optimize the rod layout to minimize the effect of beam hardening on the evaluation of test metrics, it is likely that test metric results were influenced by both a rod's location and local environment. This is especially true for noise, which was evaluated within a single centrally located rod and not over a larger or more representative portion of the phantom. Iodine accuracy was assessed using a material decomposition of pure iodine and water, although the rods were fabricated by adding iodobenzene (C_6H_5I) to a 0 HU epoxy resin material. This discrepancy between the fabrication materials and the basis materials for the material decomposition may influence the accuracy of the iodine concentration results.

In addition to the phantoms, analysis was heavily limited due to the inability to independently investigate acquisition parameters due to the use of fixed GSI-presets. This is the current reality of dual-energy acquisition using the GE DECT system and while complicating advanced analysis, it does force the quality control program to mimic clinical care. The method to determine primary and secondary trends in test metrics was primarily based on visual assessment and would benefit from more rigorous statistical analysis. Finally, evaluation of iodine accuracy and monoenergetic HU stability both used nominal values that could not be independently validated. In the case of iodine accuracy, the true accuracy was derived from the stated iodine concentration by the rod manufacturer. Without some way to independently verify this, errors in iodine accuracy could potentially be due to errors in rod fabrication. In the case of monoenergetic HU stability, the predicted attenuation added to the graphs was calculated assuming a true monoenergetic beam while DECT reconstructions represent virtual monoenergetic values based on the material decomposition results.

6.4.8 Future Work

Future work includes development of a dual-energy quality control process for dual-source dual-energy systems. In addition, investigation will continue into the effect of phantom (or patient) size on the mAs cutoff for static attenuation across monoenergetic reconstructions, as well as the creation of a more advanced and rigorous noise metric. A multivariate logistic model will be pursued to determine major sources of variability for test metrics based on all available acquisition parameters. Data will continue to be collected in order to determine baseline values and failure threshold criteria for the validation of long-term DECT scanner performance.

Chapter 7

Conclusions

7.1 Summary of Major Findings

In this dissertation we have explored the application of dual-energy CT to the differentiation of intracranial calcification and hemorrhage. Currently, single-energy CT is able to positively identify intracranial lesions of over 100 HU as calcification, however, lesions below this cut off are impossible to identify using this technique. We have shown using a basic agar-gel based physics model (Chapter 3) that calcium, present in calcification, and iron, present in hemorrhage have distinct enough spectral attenuation curves to be differentiable using dual-energy CT over the attenuation range of interest.

Next, this method was expanded to better replicate the imaging environment of the head and to evaluate a range of lesion sizes and locations (Chapter 4). A spectrally equivalent brain material was created to mimic the spectral attenuation properties of brain matter and an anthropomorphic phantom was used to mimic the shape and attenuation of the skull. A range of protocol variations ($CTDI_{vol}$, image thickness and reconstruction filter) were used to elucidate the optimal acquisition and reconstruction parameters for this method. While the initial goal was to create optimized protocols for each lesion size and location, general trends were identified that influenced differentiation accuracy regardless of these lesion specific parameters. Based on the protocol variations investigated, differentiation accuracy increased with selected $CTDI_{vol}$ and image thickness. No effect was observed based on changes in reconstruction filter. Although these factors were the only parameters varied directly, due to the fixed nature of the GSI-presets available on the GE 750HD scanner, a further parameter, rotation time, was found to affect differentiation accuracy based on inter-method and inter-study correlation measurements. Rotation times

of 0.5sec, in particular, were found to adversely affect both inter- and intra-scanner correlation and should therefore be avoided.

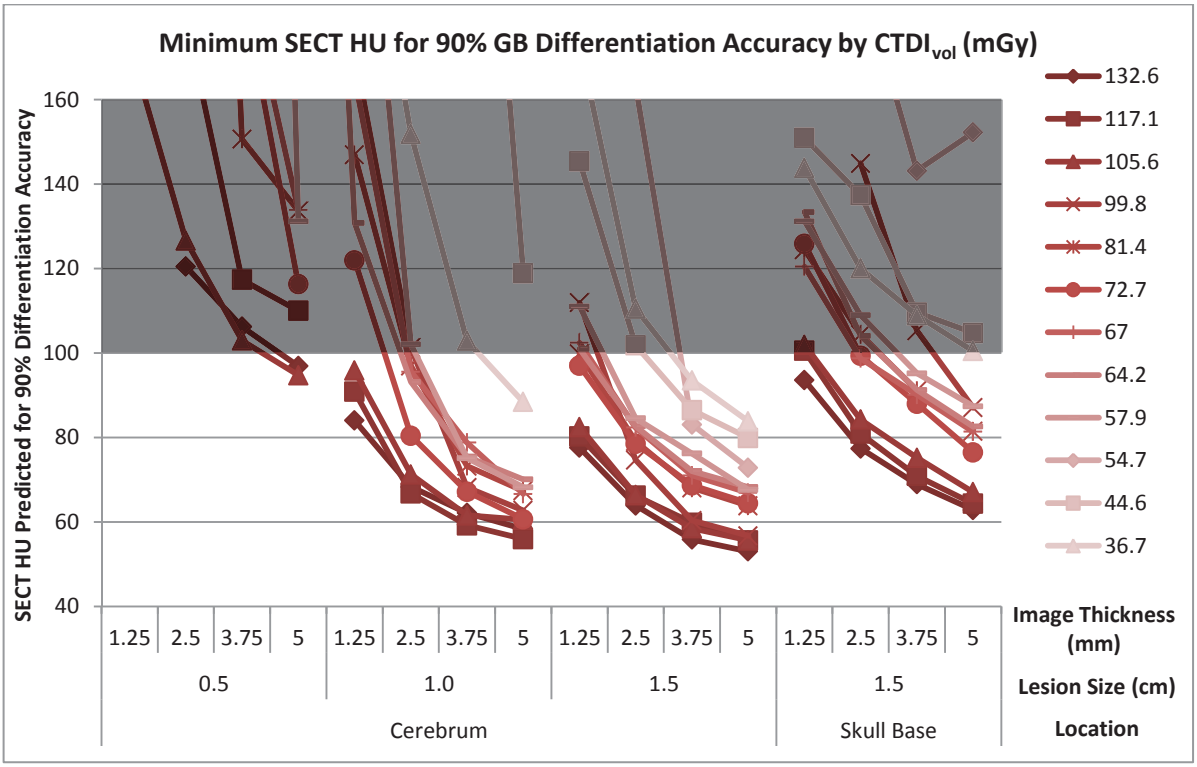

Figure 7.1: Graphical representation of lesion attenuation (HU) necessary for 90% GB differentiation accuracy by acquisition parameters (Table 4.15). The un-shaded region represents $CTDI_{vol}$ and image thickness values allow 90% differentiation accuracy under the current clinical limit of 100 HU imposed by SECT.

The effect of selected $CTDI_{vol}$ and image thickness on differentiation accuracy can be seen in Figure 7.1 (reproduction of Figure 4.33 for convenience) which shows the SECT attenuation (HU) necessary to achieve 90% differentiation accuracy using geometric bisector analysis. The shaded region represents differentiation currently available using single-energy CT, while the un-shaded region represents additional differentiation ability using dual-energy CT. Assuming a 132.6 mGy $CTDI_{vol}$, a standard filter and 5 mm thick

images, 90% differentiation accuracy using the geometric bisector method would be possible down to approximately 60 HU, 55 HU and 70 HU for 1.0 cm cerebrum, 1.5 cm cerebrum and 1.5 cm skull base lesions respectively (Figure 7.2).

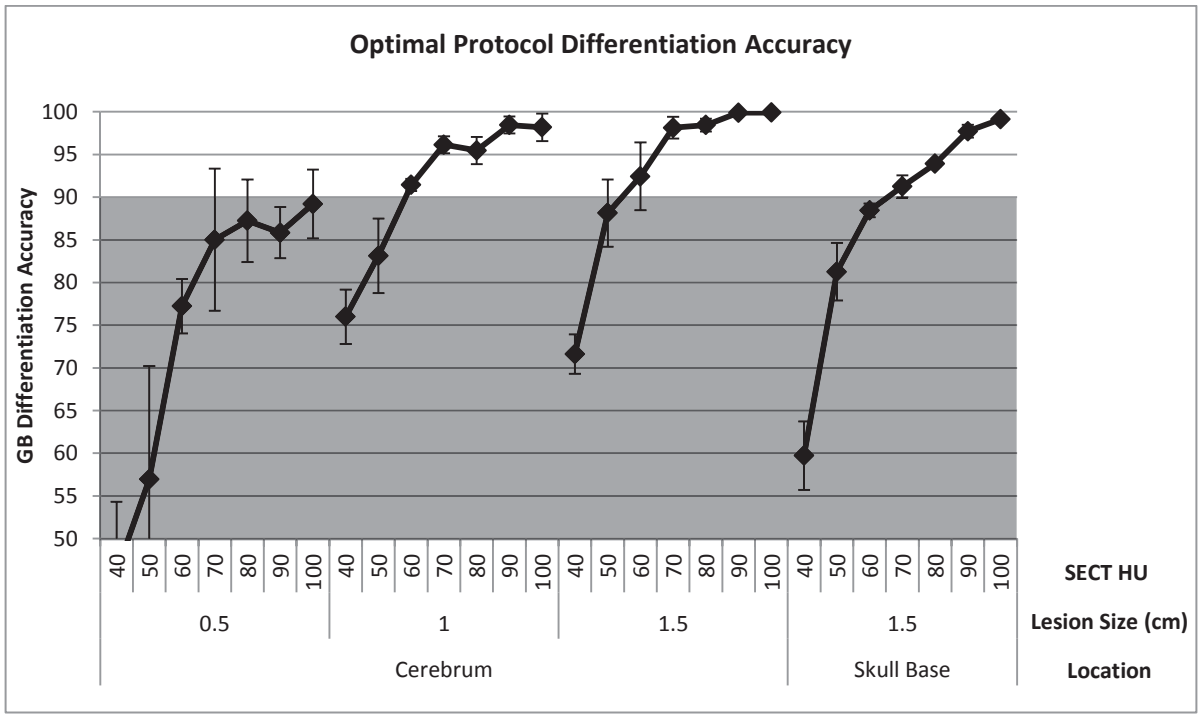

Figure 7.2: Accuracy of intracranial lesion differentiation using geometric bisector method with 132.6 mGy $CTDI_{vol}$, 5 mm image thickness and standard filter. Error bars represent one SD of the variation over the three studies collected.

Based on these differentiation results, an experiment was pursued to assess the ability of dual-energy CT to classify unknown intracranial lesions using the geometric bisector method (Chapter 5). Based on the results of the earlier differentiation project, and current clinical parameters, a three tier protocol with fixed image thickness, fixed filter and three separate $CTDI_{vol}$ values was designed. The $CTDI_{vol}$ values represented the current routine brain protocol $CTDI_{vol}$ value, the maximum value available on the CT scanner, and a midpoint value. All lesion models, except for 0.5 cm calcifications in the cerebrum, resulted

in increased classification ability beyond that of single-energy CT. These results support our hypothesis that DECT could be used to differentiate (and subsequently classify) intracranial calcification and hemorrhage below the attenuation level possible using SECT.

7.2 Comments on Clinical Implementation

Several methods were investigated based on their ability to differentiate, and later classify, intracranial hemorrhage and calcification. Although more simplistic, the geometric bisector method was found to be as effective, if not more so, than the competing advanced statistical methods (Gaussian mixture model method, support vector machine method, and probability distribution method). This effect was seen for both differentiation and classification studies. Analysis of the generalizability of the original lesion and acquisition specific geometric bisector plane solution (Chapter 4.2.5.5), identified two major sources of variability: small lesions under 0.5 cm diameter and lesions in the skull base. The ability to use a generalized geometric bisector plane solution that has no dependence on acquisition and reconstruction parameters will allow the radiologist more freedom to prescribe protocol parameters on a case by case basis.

In addition, high correlation was seen between 68 keV attenuation and single-energy CT attenuation for all lesion models investigated. Correlation was less optimal in the skull base, likely due to increased beam hardening in that region of the brain. These results indicate that a 68 keV reconstruction could be used for lesion attenuation measures instead of a separate single-energy acquisition. By removing the necessity for a separate single-energy acquisition, the total dose to the patient may be reduced by limiting the exam to the dual-energy acquisition, or the dose of the dual-energy acquisition could be increased, thus increasing the quality and accuracy of the exam.

While inter- and intra-scanner correlations were not assessed for intracranial classification, results for the intracranial differentiation studies yielded coefficients of

variation (CV) under 5% in both cases once major sources of variability were removed. For the geometric bisector method, inter-scanner variance was higher than intra-scanner variance, potentially indicating that repeat measures should be performed on the same scanner. Since the difference between inter-scanner and intra-scanner correlation was approximately 1.3%, the clinical impact of this effect would likely be minimal. These conclusions are supported by the dual-energy quality control program results (Chapter 6), indicating low inter- and intra-scanner variances in the DEQC head phantom across all test metrics. Accurate and consistent quantitative results were observed for iodine accuracy, uniformity and monoenergetic HU across a wide range of GSI-presets, further supporting the inter-comparability of collected project data.

7.3 Limitations and Future Directions

The investigation of intracranial lesion classification using dual-energy CT has led to several unresolved questions. First, lesion classification results for 0.5 cm and 1.0 cm cerebrum lesions do not provide sufficient information to state the lesion size limitations of this method. Further investigation would require the creation of intermediate size models, the evaluation of which would not be possible without modification of this phantom. Furthermore, since neither heterogeneity nor cross contamination between the lesion types were investigated as part of our phantom model, the usefulness of this method for heterogeneous or mixed lesions cannot currently be confirmed. Further investigation using various levels of heterogeneity or differing mixture ratios of calcification and hemorrhage may provide further insight. Finally, display field of view remained constant throughout this study. Reduction in DFOV from 25 cm to 12 cm may improve classification confidence for smaller lesions by increasing sample size, reducing partial volume effect and increasing ease of ROI placement.

The dual-energy quality control program will be generalized to include dual-source dual-energy CT systems. In addition, further investigation of the effect of phantom size on the mAs required for variable attenuation and contrast (when using variable keV monoenergetic reconstruction options) is warranted. A multivariate logistic model will be pursued to statistically determine major sources of variability in DEQC test metrics based on all acquisition parameters investigated. DEQC data collection will continue in order to determine the baseline and failure threshold criteria necessary for validation of long-term DECT scanner performance.

In conclusion, these studies into the characterization of intracranial lesions have supported the hypothesis that DECT could be used to differentiate, and further classify, intracranial calcification and hemorrhage below the attenuation level possible using SECT. Chapter 3 (Specific Aim 1) supports the idea that calcium, associated with calcification, and the iron, associated with hemorrhage, have distinct enough attenuation curves to allow for differentiation of these two lesion types using dual-energy CT. Chapter 4 (Specific Aim 2) verified these differentiation results for various size and location lesions using a more biologically relevant and spectrally equivalent phantom model resulting in recommended acquisition parameters and analysis models for optimal differentiation accuracy. Chapter 5 (Specific Aim 3) validated the protocol recommendations and analysis methods developed in Chapter 4 by showing dual-energy CT's ability to classify unknown lesions below the 100 HU cutoff imposed by SECT. Finally, Chapter 6 (Specific Aim 4) established the effect of protocol acquisition parameters on a number of DEQC test metrics, as well as the inter- and intra-scanner variance in these metrics, allowing both validation of the collected research data and assessment of the validity of repeat measures in patients. Together these findings establish the added benefit of dual-energy CT evaluation for intracranial lesion characterization and provide justification for future clinical evaluation in patients.

Chapter 8

Appendix

This chapter is based upon:

JL Nute, LG Le Roux, AG Chandler, V Baladandayuthapani, D Schellingerhout, DD Cody. Differentiation of low-attenuation intracranial hemorrhage and calcification using dual-energy computed tomography in a phantom system. Invest Radiol. 2015; 50(1): 9-16. doi: 10.1097/RLI.0000000000000089

8.1 Gaussian Mixture Model Formulation

The basic data collected from our experiments had a three dimensional structure with the x-axis defined as the dual-energy CT water density, the y-axis defined as the dual-energy CT calcium density, and the z-axis defined as the SECT attenuation (HU). Our basic scientific question of characterizing this three-dimensional data cloud into distinct (sub-) populations corresponding to water and calcium can be construed as a clustering problem i.e. at each HU we wish to identify how well these distinct clusters are separated. Visually inspecting the data we found that at lower HU these clusters are not very well separated but the distinction increases with SECT attenuation (HU) levels and we would like accurately quantify the uncertainty of this process. The most commonly used clustering algorithms are mixture models (125). Mixture models are a common statistical tool for clustering and allow properties of multiple subpopulations (distributions) to be statistically inferred from pooled-population data. Gassuian mixture models (GMM) are a special case of mixture models and

was chosen for this study because of its ease of interpretation and to take advantage of the 3D and potentially overlapping nature of the data collected. The basic GMM can be expressed concisely as:

Equation 15

$$P(X) = \sum_{k=1}^{K} p_k \, N(\mu_k, \Sigma_k)$$

where P(X) represents the joint distribution of the 3-D water/calcium/HU data, K is number of mixture components, p_k is the mixture weights/prior probability and $N(\mu_k, \Sigma_k)$ represents the Gaussian (normal) density with mean μ_k and variance-covariance matrix Σ_k corresponding to the cluster k respectively. All of these quantities are treated as unknown parameters and are estimated by the data as detailed below.

8.2 GMM Fitting and Analysis

We used MATLAB Statistics Toolbox™ software, and specifically the *gmdistribution* class to fit an unsupervised GMM analysis using a 50% training set, 50% validation set approach. GMM analysis uses an expectation maximization(EM) algorithm (126) to iteratively fit two potentially overlapping Gaussian distributions to the combined hemorrhage-calcification model pair data and consists of two steps: the Expectation (E) step which calculates the expected values for the membership weights of each data point as functions of the mixture weights p_k and the maximization (M) step which uses the membership weights obtained from the E step, and recomputes the distribution of the Gaussian distributions μ_k and $\Sigma_k$respectively (127). This procedure is repeated iteratively until convergence is achieved.

Posterior probability calculations

Once these distributions are optimally estimated using the EM algorithm, the analysis provides for each voxel the probability that the voxel belongs to the hemorrhage cluster and (vice-versa) the probability that the voxel belongs to the calcification cluster which is calculated using the Bayes theorem as:

Equation 16 $$P = Prob(Voxel|Cluster) = Prob(Cluster|Voxel)Prob(Voxel)$$

where the probabilities on the right-hand side are calculated using the (weighted) ratio of the Gaussian densities corresponding to each cluster estimated via the EM algorithm. An example plot of these posterior probabilities for one HU pair is show in Figure 8.1. Voxels were assigned to a cluster if their probability of belonging to a cluster (P) exceeded a median probability threshold of 50%. The voxel identities predicted by the GMM were then compared to the true voxel identities and the true hemorrhage and true calcification values were calculated. The accuracy with which the GMM differentiated the calcification gel model from the hemorrhage gel model was then calculated as the sum of the true hemorrhage and calcification values divided by the total number of voxels in the two gel model data sets. Because of the stochastic nature of iterative approaches such as GMM analysis, the method was repeated over 1,000 runs for each matched model pair to assess the stability of model configurations. Each run used a different starting point randomly selected as part of the gmdistribution.fit function. Any runs whose final log likelihood value differed from that of the median results by my more than 3 standard deviations were presumed to be influenced by local minima (128), and were removed from the results. The analysis was repeated with new initial values until there were 1,000 successful runs for each matched model pair. The accuracy was calculated for each

successful run, and then the mean and standard deviation of the accuracy was calculated for the 1,000 runs of each attenuation matched model pair.

To determine whether the initial random separation of data into training and validation sets affected the accuracy results, the random selection, as well as the 1,000-GMM-run analysis, was repeated 10 times for each SECT attenuation-matched model pair. For each matched model pair, the 10 random splits were found to yield identical results (data not shown), indicating the random separation of the data into training and validation data sets did not affect the final GMM accuracy results.

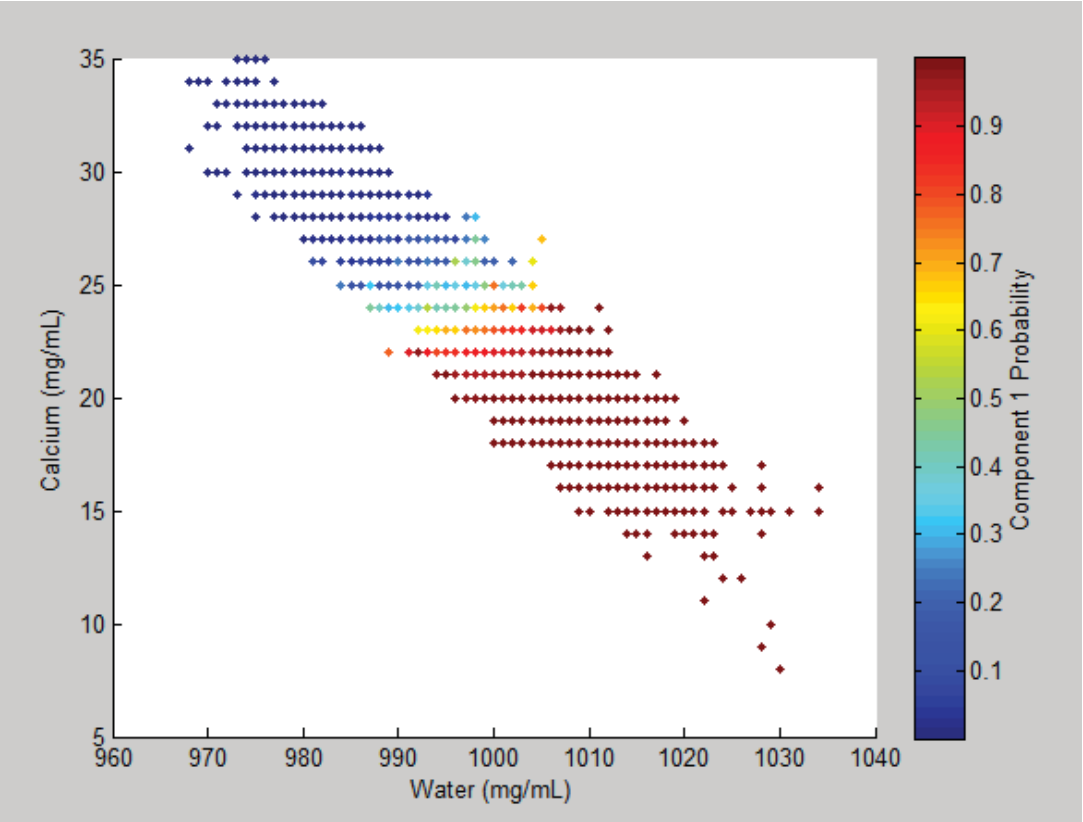

Figure 8.1: Posterior probabilities for the calcification cluster based on the GMM results of the 50 HU matched model pair. Red indicates a very high probability the voxel is calcification, while blue indicates a very low probability.

References

1. Haacke E, Reichenbach J. Susceptibility Weighted Imaging in MRI. Hoboken, NJ: Wiley-Blackwell; 2011.

2. Go JL, Zee CS. Unique CT imaging advantages. Hemorrhage and calcification. Neuroimaging Clin. N. Am. 1998 Aug 1;8(3):541–58.

3. Makariou E, Patsalides A. Intracranial calcifications. Appl Radiol. 2009;38(11):48–60.

4. Raychaudhuri R, Batjer HH, Awad IA. Intracranial cavernous angioma: a practical review of clinical and biological aspects. Surg. Neurol. 2005 Apr;63(4):319–28; discussion 328.

5. Khurana V. Cavernous malformation (cavernoma) [Internet]. 2011 [cited 2014 Sep 5]. Available from: http://www.brain-aneurysm.com/cm.html

6. Shinagare AB, Guo M, Hatabu H, Krajewski KM, Andriole K, Van den Abbeele AD, DiPiro PJ, Nishino M. Incidence of pulmonary embolism in oncologic outpatients at a tertiary cancer center. Cancer. 2011 Aug 15;117(16):3860–6.

7. Thaler J, Ay C, Pabinger I. Venous thromboembolism in cancer patients - risk scores and recent randomised controlled trials. J. Thromb. Haemost. 2012 Dec;108(6):1042–8.

8. Blom JW, Vanderschoot JPM, Oostindiër MJ, Osanto S, Van Der Meer FJM, Rosendaal FR. Incidence of venous thrombosis in a large cohort of 66 329 cancer patients: Results of a record linkage study. J. Thromb. Haemost. 2006;4(3):529–35.

9. Heit JA, Silverstein M, Mohr D, Petterson T, O'Fallon W, Melton L 3rd. Risk Factors for Deep Vein Thrombosis and Pulmonary Embolism: A Population-Based Case-Control Study. Arch. Intern. Med. 2000;160(6):809–15.

10. Brandes AA, Scelzi E, Salmistraro G, Ermani M, Carollo C, Berti F, Zampieri P, Baiocchi C, Fiorentino M V. Incidence and risk of thromboembolism during treatment of high-grade gliomas: A prospective study. Eur. J. Cancer. 1997;33(10):1592–6.

11. Perry SL, Bohlin C, Reardon DA, Desjardins A, Friedman AH, Friedman HS, Vredenburgh JJ. Tinzaparin prophylaxis against venous thromboembolic complications in brain tumor patients. J. Neurooncol. 2009;95(1):129–34.

12. Pan E, Tsai J, Mitchell S. Retrospective study of venous thromboembolic and intracerebral hemorrhagic events in glioblastoma patients. Anticancer Res. 2009;29(10):4309–13.

13. Keime-Guibert F, Napolitano M, Delattre J-Y. Neurological complications of radiotherapy and chemotherapy. J. Neurol. 1998 Oct 1;245(11):695–708.

14. Niwa T, Aida N, Takahara T, Kwee TC, Fujita K, Shishikura A, Miyata D, Inoue T. Imaging and clinical characteristics of children with multiple foci of microsusceptibility changes in the brain on susceptibility-weighted MRI. Pediatr. Radiol. 2010 Oct;40(10):1657–62.

15. Singer R. Vascular malformations of the central nervous system [Internet]. 2001. Available from: www.uptodate.com

16. Francis CW. Prevention of venous thromboembolism in hospitalized patients with cancer. J. Clin. Oncol. 2009 Oct 10;27(29):4874–80.

17. Cohen AT, Tapson VF, Bergmann J-F, Goldhaber SZ, Kakkar AK, Deslandes B, Huang W, Zayaruzny M, Emery L, Anderson FA. Venous thromboembolism risk and prophylaxis in the acute hospital care setting (ENDORSE study): a multinational cross-sectional study. Lancet. 2008 Feb 2;371(9610):387–94.

18. Zwicker JI, Rojan A, Campigotto F, Rehman N, Funches R, Connolly G, Webster J, Aggarwal A, Mobarek D, Faselis C, Neuberg D, Rickles FR, Wun T, Streiff MB, Khorana AA. Pattern of frequent but nontargeted pharmacologic thromboprophylaxis for hospitalized patients with cancer at academic medical centers: a prospective, cross-sectional, multicenter study. J. Clin. Oncol. 2014 Jun 10;32(17):1792–6.

19. Beauregard K, Carper K. Outpatient Prescription Anticoagulants Utilization and Expeditures for the U.S. Civilian Noninstitutionalized Population Age 18 and Older, for 2007. Med. Expend. Panel Surv. Agency Healthc. Res. Qual. 2009;1–5.

20. Gupta RK, Rao SB, Jain R, Pal L, Kumar R, Venkatesh SK, Rathore RKS. Differentiation of Calcification from Chronic Hemorrhage with Corrected Gradient Echo Phase Imaging. J. Comput. Assist. Tomogr. 2001 Sep;25(5):698–704.

21. Zhu WZ, Qi JP, Zhan CJ, Shu HG, Zhang L, Wang CY, Xia LM, Hu JW, Feng DY. Magnetic resonance susceptibility weighted imaging in detecting intracranial calcification and hemorrhage. Chin. Med. J. (Engl). 2008 Oct;121(20):2021–5.

22. Kalender WA, Perman WH, Vetter JR, Klotz E. Evaluation of a prototype dual-energy computed tomographic apparatus. I. Phantom studies. Med. Phys. American Association of Physicists in Medicine; 1986 May 1;13(3):334–9.

23. Chiro G Di, Brooks RA, Kessler RM, Johnston GS, Jones AE, Herdt JR, Sheridan WT. Tissue signatures with dual-energy computed tomography. Radiology. 1979;131(2):521–3.

24. Genant HK, Boyd D. Quantitative bone mineral analysis using dual energy computed tomography. Invest. Radiol. 1977;12(6):545–51.

25. Millner MR, McDavid WD, Waggener RG, Dennis MJ, Payne WH, Sank VJ. Extraction of information from CT scans at different energies. Med. Phys. 1979;6(1):70–1.

26. Graser A, Johnson TRC, Hecht EM, Becker CR, Leidecker C, Staehler M, Stief CG, Hildebrandt H, Godoy MCB, Finn ME, Stepansky F, Reiser MF, Macari M. Dual-energy CT in patients suspected of having renal masses: can virtual nonenhanced images replace true nonenhanced images? Radiology. 2009 Aug;252(2):433–40.

27. Flohr TG, McCollough CH, Bruder H, Petersilka M, Gruber K, Süß C, Grasruck M, Stierstorfer K, Krauss B, Raupach R, Primak AN, Küttner A, Achenbach S, Becker C, Kopp A, Ohnesorge BM. First performance evaluation of a dual-source CT (DSCT) system. Eur. Radiol. 2006;16(2):256–68.

28. Primak AN, Ramirez Giraldo JC, Liu X, Yu L, McCollough CH. Improved dual-energy material discrimination for dual-source CT by means of additional spectral filtration. Med. Phys. 2009;36(4):1359–69.

29. Langan DA. Gemstone spectral imaging: GE white paper. 2008.

30. Krauss B, Grant KL, Schmidt BT, Flohr TG. The Importance of Spectral Separation. Invest. Radiol. 2015;50(2):114–8.

31. Gordic S, Morsbach F, Schmidt B, Allmendinger T, Flohr T, Husarik D, Baumueller S, Raupach R, Stolzmann P, Leschka S, Frauenfelder T, Alkadhi H. Ultralow-Dose Chest Computed Tomography for Pulmonary Nodule Detection: First Performance Evaluation of Single Energy Scanning With Spectral Shaping. Invest. Radiol. 2014;49(7):465–73.

32. Meinel FG, Canstein C, Schoepf UJ, Sedlmaier M, Schmidt B, Harris BS, Flohr TG, De Cecco CN. Image quality and radiation dose of low tube voltage 3rd generation dual-source coronary CT angiography in obese patients: A phantom study. Eur. Radiol. 2014;24(7):1643–50.

33. Jackson J, Okerlund D. Revolution Cardiac CT : The Comprehensive Solution for Cardiovascular Imaging, GE White Paper. 2015.

34. Web of Science [Internet]. Available from: apps.webofknowledge.com

35. Fletcher JG, Takahashi N, Hartman R, Guimaraes L, Huprich JE, Hough DM, Yu L, McCollough CH. Dual-energy and dual-source CT: is there a role in the abdomen and pelvis? Radiol. Clin. North Am. 2009 Jan;47(1):41–57.

36. Johnson TRC, Krauss B, Sedlmair M, Grasruck M, Bruder H, Morhard D, Fink C, Weckbach S, Lenhard M, Schmidt B, Flohr T, Reiser MF, Becker CR. Material differentiation by dual energy CT: initial experience. Eur. Radiol. 2007 Jun;17(6):1510–7.

37. Kaza RK, Platt JF, Megibow AJ. Dual-energy CT of the urinary tract. Abdom. Imaging. 2013 Feb;38(1):167–79.

38. Park J, Chandarana H, MacAri M, Megibow AJ. Dual-energy computed tomography applications in uroradiology. Curr. Urol. Rep. 2012;13(1):55–62.

39. Mobberley SD, Fuld MK, Sieren JP, Primak AN, Hoffman EA. Scatter correction associated with dedicated dual-source ct hardware improves accuracy of lung air measures. Acad. Radiol. 2013;20(11):1334–43.

40. Silva AC, Morse BG, Hara AK, Paden RG, Hongo N, Pavlicek W. Dual-energy (spectral) CT: applications in abdominal imaging. Radiographics. Radiological Society of North America; 2011 Jul 8;31(4):1031–46; discussion 1047–50.

41. Matsumoto K, Jinzaki M, Tanami Y, Ueno A, Yamada M, Kuribayashi S. Virtual monochromatic spectral imaging with fast kilovoltage switching: improved image quality as compared with that obtained with conventional 120-kVp CT. Radiology. 2011;259(1):257–62.

42. Zhang D, Li X, Liu B. Objective characterization of GE discovery CT750 HD scanner: gemstone spectral imaging mode. Med. Phys. 2011;38(3):1178–88.

43. Li B, Yadava G, Hsieh J. Quantification of head and body CTDI(VOL) of dual-energy x-ray CT with fast-kVp switching. Med. Phys. 2011;38(5):2595–601.

44. Cai X, Zhou Q, Yu J, Xian Z, Feng Y, Yang W, Mo X. Impact of reduced-radiation dual-energy protocols using 320-detector row computed tomography for analyzing urinary calculus components: initial in vitro evaluation. Urology. 2014 Oct;84(4):760–5.

45. Tatsugami F, Higaki T, Kiguchi M, Tsushima S, Taniguchi A, Kaichi Y, Yamagami T, Awai K. Measurement of Electron Density and Effective Atomic Number by Dual-Energy Scan Using a 320-Detector Computed Tomography Scanner with Raw Data-Based. J. Comput. Assist. Tomogr. 2014;38(6):824–7.

46. Kalra MK, Maher MM, Toth TL, Schmidt B, Westerman BL, Morgan HT, Saini S. Techniques and applications of automatic tube current modulation for CT. Radiology. Radiological Society of North America; 2004 Dec 1;233(3):649–57.

47. Vrtiska TJ, Takahashi N, Fletcher JG, Hartman RP, Yu L, Kawashima A. Genitourinary applications of dual-energy CT. Am. J. Roentgenol. 2010;194(6):1434–42.

48. Lin XZ, Miao F, Li JY, Dong HP, Shen Y, Chen KM. High-definition CT Gemstone spectral imaging of the brain: initial results of selecting optimal monochromatic image for beam-hardening artifacts and image noise reduction. J. Comput. Assist. Tomogr. 2011;35(2):294–7.

49. Zou Y, Silver MD. Analysis of Fast kV-switching in Dual Energy CT using a Pre-reconstruction Decomposition Technique. Proc. SPIE. 2008. p. 691313–12.

50. Wu X, Langan D a., Xu D, Benson TM, Pack JD, Schmitz AM, Tkaczyk EJ, Leverentz J, Licato P. Monochromatic CT image representation via fast switching dual kVp. Proc. SPIE. 2009;7258:725845–9.

51. Alvarez RE, Macovski A. Energy-selective reconstructions in X-ray computerized tomography. Phys. Med. Biol. 1976;21(5):733–44.

52. Stolzmann P, Leschka S, Scheffel H, Rentsch K, Baumüller S, Desbiolles L, Schmidt B, Marincek B, Alkadhi H. Characterization of urinary stones with dual-energy CT: improved differentiation using a tin filter. Invest. Radiol. 2010;45(1):1–6.

53. Lv P, Lin XZ, Li J, Li W, Chen K. Differentiation of small hepatic hemangioma from small hepatocellular carcinoma: recently introduced spectral CT method. Radiology. 2011;259(3):720–9.

54. Kaza RK, Caoili EM, Cohan RH, Platt JF. Distinguishing enhancing from nonenhancing renal lesions with fast kilovoltage-switching dual-energy CT. Am. J. Roentgenol. 2011;197(6):1375–81.

55. Ho LM, Marin D, Neville AM, Barnhart HX, Gupta RT, Paulson EK, Boll DT. Characterization of adrenal nodules with dual-energy CT: Can virtual unenhanced attenuation values replace true unenhanced attenuation values? Am. J. Roentgenol. 2012;198(4):840–5.

56. Chandarana H, Megibow AJ, Cohen BA, Srinivasan R, Kim D, Leidecker C, Macari M. Iodine quantification with dual-energy CT: phantom study and preliminary experience with renal masses. Am. J. Roentgenol. American Roentgen Ray Society; 2011 Jun 23;196(6):W693–700.

57. Takahashi N, Hartman RP, Vrtiska TJ, Kawashima A, Primak AN, Dzyubak OP, Mandrekar JN, Fletcher JG, McCollough CH. Dual-energy CT iodine-subtraction virtual unenhanced technique to detect urinary stones in an iodine-filled collecting system: A phantom study. Am. J. Roentgenol. 2008;190(5):1169–73.

58. Stolzmann P, Scheffel H, Frauenfelder T, Schertler T, Desbiolles L, Leschka S, Marincek B, Alkadhi H. Dual Source CT: Detecting Urinary Stones by Spiral Dual Energy Computed Tomography With Virtual Non-Enhanced Images. Siemens Somat. Sess. 2007;49–51.

59. Takeuchi M, Kawai T, Ito M, Ogawa M, Ohashi K, Hara M, Shibamoto Y. Split-bolus CT-urography using dual-energy CT: Feasibility, image quality and dose reduction. Eur. J. Radiol. 2012;81(11):3160–5.

60. Lehmann LA, Alvarez RE, Macovski A, Brody WR, Pelc NJ, Riederer SJ, Hall AL. Generalized image combinations in dual KVP digital radiography. Med. Phys. 1981;8(5):659–67.

61. Goodsitt MM, Christodoulou EG, Larson SC. Accuracies of the synthesized monochromatic CT numbers and effective atomic numbers obtained with a rapid kVp switching dual energy CT scanner. Med. Phys. 2011;38(4):2222–32.

62. Yuan R, Shuman WP, Earls JP, Hague CJ, Mumtaz HA, Scott-Moncrieff A, Ellis JD, Mayo JR, Leipsic JA. Reduced iodine load at CT pulmonary angiography with dual-

energy monochromatic imaging: comparison with standard CT pulmonary angiography--a prospective randomized trial. Radiology. 2012 Jan 1;262(1):290–7.

63. Yamada Y, Jinzaki M, Tanami Y, Abe T, Kuribayashi S. Virtual monochromatic spectral imaging for the evaluation of hypovascular hepatic metastases: the optimal monochromatic level with fast kilovoltage switching dual-energy computed tomography. Invest. Radiol. 2012;47(5):292–8.

64. Yu L, Primak AN, Liu X, McCollough CH. Image quality optimization and evaluation of linearly mixed images in dual-source, dual-energy CT. Med. Phys. 2009;36(3):1019–24.

65. Li M, Zheng X, Li J, Yang Y, Lu C, Xu H, Yu B, Xiao L, Zhang G, Hua Y. Dual-Energy Computed Tomography Imaging of Thyroid Nodule Specimens. Invest. Radiol. 2012;47(1):58–64.

66. Maturen KE, Kaza RK, Liu PS, Quint LE, Khalatbari SH, Platt JF. “Sweet Spot” for endoleak detection: optimizing contrast to noise using low keV reconstructions from fast-switch kVp dual-energy CT. J. Comput. Assist. Tomogr. 2012;36(1):83–7.

67. Wu HW, Cheng JJ, Li JY, Yin Y, Hua J, Xu JR. Pulmonary Embolism Detection and Characterization Through Quantitative Iodine-Based Material Decomposition Images With Spectral Computed Tomography Imaging. Invest. Radiol. 2012;47(1):85–91.

68. Geyer LL, Scherr M, Körner M, Wirth S, Deak P, Reiser MF, Linsenmaier U. Imaging of acute pulmonary embolism using a dual energy CT system with rapid kVp switching: Initial results. Eur. J. Radiol. 2012;81(12):3711–8.

69. Ruzsics B, Lee H, Powers ER, Flohr TG, Costello P, Schoepf UJ. Myocardial ischemia diagnosed by dual-energy computed tomography: Correlation with single-photon emission computed tomography. Circulation. 2008;117(9):1244–5.

70. Ruzsics B, Lee H, Zwerner PL, Gebregziabher M, Costello P, Schoepf UJ. Dual-energy CT of the heart for diagnosing coronary artery stenosis and myocardial ischemia-initial experience. Eur. Radiol. 2008;18(11):2414–24.

71. Kumar R, Wang ZJ, Forsythe C, Fu Y, Chen YY, Yeh BM. Dual energy CT monitoring of the renal corticomedullary sodium gradient in swine. Eur. J. Radiol. 2012;81(3):423–9.

72. Phan CM, Yoo AJ, Hirsch JA, Nogueira RG, Gupta R. Differentiation of hemorrhage from iodinated contrast in different intracranial compartments using dual-energy head CT. Am. J. Neuroradiol. 2012;33(6):1088–94.

73. Gupta R, Phan CM, Leidecker C, Brady TJ, Hirsch JA, Nogueira RG, Yoo AJ. Evaluation of dual-energy CT for differentiating intracerebral hemorrhage from iodinated contrast material staining. Radiology. 2010;257(1):205–11.

74. Gronemeyer SA, Langston JW, Hanna SL, Langston JW. MR imaging detection of calcified intracranial lesions and differentiation from iron-laden lesions. J. Magn. Reson. Imaging. 1992;2(3):271–6.

75. Yamada N, Imakita S, Nishimura T, Takamiya M, Naito H. Evaluation of the susceptibility effect on gradient echo phase images in vivo: A sequential study of intracerebral hematoma. J. Magn. Reson. Imaging. 1992;10(4):559–71.

76. Gumus K, Koc G, Doganay S, Gorkem SB, Dogan MS, Canpolat M, Coskun A, Bilgen M. Susceptibility-Based Differentiation of Intracranial Calcification and Hemorrhage in Pediatric Patients. J. Child Neurol. 2014;

77. Berberat J, Grobholz R, Boxheimer L, Rogers S, Remonda L, Roelcke U. Differentiation between calcification and hemorrhage in brain tumors using susceptibility-weighted imaging: a pilot study. Am. J. Roentgenol. American Roentgen Ray Society; 2014 Apr 24;202(4):847–50.

78. Chen W, Zhu W, Kovanlikaya I, Kovanlikaya A, Liu T, Wang S, Salustri C, Wang Y. Intracranial calcifications and hemorrhages: characterization with quantitative susceptibility mapping. Radiology. 2014 Feb;270(2):496–505.

79. Schweser F, Deistung A, Lehr BW, Reichenbach JR. Differentiation between diamagnetic and paramagnetic cerebral lesions based on magnetic susceptibility mapping. Med. Phys. American Association of Physicists in Medicine; 2010 Sep 7;37(10):5165–78.

80. Kaaouana T, de Rochefort L, Samaille T, Thiery N, Dufouil C, Delmaire C, Dormont D, Chupin M. 2D harmonic filtering of MR phase images in multicenter clinical setting: Toward a magnetic signature of cerebral microbleeds. Neuroimage. 2014;104:287–300.

81. Deistung A, Schweser F, Wiestler B, Abello M, Roethke M, Sahm F, Wick W, Nagel AM, Heiland S, Schlemmer HP, Bendszus M, Reichenbach JR, Radbruch A. Quantitative Susceptibility Mapping Differentiates between Blood Depositions and Calcifications in Patients with Glioblastoma. PLoS One. 2013;8(3).

82. Yamada N, Imakita S, Sakuma T, Takamiya M. Intracranial calcification on gradient-echo phase image: depiction of diamagnetic susceptibility. Radiology. 1996;198(1):171–8.

83. Haacke EM, Liu S, Buch S, Zheng W, Wu D, Ye Y. Quantitative susceptibility mapping: current status and future directions. J. Magn. Reson. Imaging. Elsevier Inc.; 2015 Jan;33(1):1–25.

84. Wu Z, Mittal S, Kish K, Yu Y, Hu J, Haacke EM. Identification of calcification with MRI using susceptibility-weighted imaging: A case study. J. Magn. Reson. Imaging. 2009;29(1):177–82.

85. Tsuruda J, Bradley W. MR detection of intracranial calcification: a phantom study. Am. J. Neuroradiol. 1987;8(6):1049–55.

86. Haacke E. Magnetic resonance imaging: physical principles and sequence design. New York: Wiley; 1999.

87. Hagberg GE, Welch EB, Greiser A. The sign convention for phase values on different vendor systems: Definition and implications for susceptibility-weighted imaging. J. Magn. Reson. Imaging. 2010;28(2):297–300.

88. Cheng AL, Batool S, McCreary CR, Lauzon ML, Frayne R, Goyal M, Smith EE. Susceptibility-weighted imaging is more reliable than T2*-weighted gradient-recalled echo mri for detecting microbleeds. Stroke. 2013;44(10):2782–6.

89. Zulfiqar M, Dumrongpisutikul N, Intrapiromkul J, Yousem DM. Detection of intratumoral calcification in oligodendrogliomas by susceptibility-weighted MR imaging. Am. J. Neuroradiol. 2012;33(5):858–64.

90. Hayashida Y, Kakeda S, Hiai Y, Ide S, Ogasawara A, Ooki H, Watanabe K, Nishimura J, Ohnari N, Korogi Y. Diagnosis of intracranial hemorrhagic lesions: comparison between 3D-SWAN (3D T2*-weighted imaging with multi-echo acquisition) and 2D-T2*-weighted imaging. Acta radiol. 2014;55(2):201–7.

91. Haacke EM, Mittal S, Wu Z, Neelavalli J, Cheng Y-CN. Susceptibility-weighted imaging: technical aspects and clinical applications, part 1. Am. J. Neuroradiol. 2009 Jan;30(1):19–30.

92. Tijssen MPM, Hofman PAM, Stadler AAR, Van Zwam W, De Graaf R, Van Oostenbrugge RJ, Klotz E, Wildberger JE, Postma AA. The role of dual energy CT in differentiating between brain haemorrhage and contrast medium after mechanical revascularisation in acute ischaemic stroke. Eur. Radiol. 2014;24(4):834–40.

93. Knöß N, Hoffmann B, Krauss B, Heller M, Biederer J. Dual energy computed tomography of lung nodules: Differentiation of iodine and calcium in artificial pulmonary nodules in vitro. Eur. J. Radiol. 2011;80(3):e516–9.

94. Mongan J, Rathnayake S, Fu Y, Wang R, Jones EF, Gao D-W, Yeh BM. In Vivo Differentiation of Complementary Contrast Media at Dual-Energy CT. Radiology. 2012;265(1):267–72.

95. Primak AN, Fletcher JG, Vrtiska TJ, Dzyubak OP, Lieske JC, Jackson ME, Williams JC, McCollough CH. Noninvasive Differentiation of Uric Acid versus Non-Uric Acid Kidney Stones Using Dual-Energy CT. Acad. Radiol. 2007;14(12):1441–7.

96. Wisenbaugh ES, Paden RG, Silva AC, Humphreys MR. Dual-energy vs conventional computed tomography in determining stone composition. Urology. 2014;83(6):1243–7.

97. Heye T, Nelson RC, Ho LM, Marin D, Boll DT. Dual-energy CT applications in the abdomen. Am. J. Roentgenol. 2012;199(5 Suppl):S64–70.

98. Shi JW, Dai HZ, Shen L, Xu DF. Dual-energy CT: clinical application in differentiating an adrenal adenoma from a metastasis. Acta radiol. 2014;55(4):505–12.

99. Alvarez RE, Macovski A. Energy-selective reconstructions in X-ray computerized tomography. Phys. Med. Biol. 1976 Sep 1;21(5):733–44.

100. Everitt BS, Landau S, Leese M SD. Cluster Analysis. 5th ed. West Sussex, UK: John Wiley & Sons, Ltd; 2011.

101. Gaussian Mixture Models - MATLAB & Simulink [Internet]. [cited 2014 Sep 9]. Available from: http://www.mathworks.com/help/stats/gaussian-mixture-models.html

102. Simard JM, Garcia-Bengochea F, Ballinger WE, Mickle JP, Quisling RG. Cavernous angioma: A review of 126 collected and 12 new clinical cases. Neurosurgery. 1986 Feb;18(2):162–72.

103. Ramina R, Ingunza W, Vonofakos D. Cystic cerebral cavernous angioma with dense calcification. Case report. J. Neurosurg. Journal of Neurosurgery Publishing Group; 1980 Feb 7;52(2):259–62.

104. DW H, Lemeshow S. Applied logistic regression. 2nd ed. John Wiley & Sons, Ltd; 2000.

105. Cody DD, Pfieffer D, McNitt-Gray MF, Ruckdeschel TG, Strauss KJ. Computed Tomography: Quality Control Manual. 2012.

106. Yu L, Leng S, McCollough CH. Dual-energy CT-based monochromatic imaging. Am. J. Roentgenol. 2012;199(5 Suppl):S9–15.

107. Yu L, Christner JA, Leng S, Wang J, Fletcher JG, McCollough CH. Virtual monochromatic imaging in dual-source dual-energy CT: Radiation dose and image quality. Med. Phys. 2011;38(12):6371–9.

108. Pomerantz SR, Kamalian S, Zhang D, Gupta R, Rapalino O, Sahani D V., Lev MH. Virtual Monochromatic Reconstruction of Dual-Energy Unenhanced Head CT at 65-75 keV Maximizes Image Quality Compared with Conventional Polychromatic CT. Radiology. 2012;266(1):318–25.

109. Lee YH, Park KK, Song H-T, Kim S, Suh J-S. Metal artefact reduction in gemstone spectral imaging dual-energy CT with and without metal artefact reduction software. Eur. Radiol. 2012 Jun;22(6):1331–40.

110. Bamberg F, Dierks A, Nikolaou K, Reiser MF, Becker CR, Johnson TRC. Metal artifact reduction by dual energy computed tomography using monoenergetic extrapolation. Eur. Radiol. 2011 Jul;21(7):1424–9.

111. Zhou C, Zhao YE, Luo S, Shi H, Li L, Zheng L, Zhang LJ, Lu G. Monoenergetic imaging of dual-energy CT reduces artifacts from implanted metal orthopedic devices in patients with factures. Acad. Radiol. 2011 Oct;18(10):1252–7.

112. Lewis M, Reid K, Toms AP. Reducing the effects of metal artefact using high keV monoenergetic reconstruction of dual energy CT (DECT) in hip replacements. Skeletal Radiol. 2013 Feb;42(2):275–82.

113. Meinel FG, Bischoff B, Zhang Q, Bamberg F, Reiser MF, Johnson TRC. Metal Artifact Reduction by Dual-Energy Computed Tomography Using Energetic Extrapolation: A Systematically Optimized Protocol. Invest. Radiol. 2012;47(7):406–14.

114. Feuerlein S, Heye TJ, Bashir MR, Boll DT. Iodine Quantification Using Dual-Energy Multidetector Computed Tomography Imaging: phantom study assessing the impact of iterative reconstruction schemes and patient habitus on accuracy. Invest. Radiol. 2012;47(11):656–61.

115. Koonce JD, Vliegenthart R, Schoepf UJ, Schmidt B, Wahlquist AE, Nietert PJ, Bastarrika G, Flohr TG, Meinel FG. Accuracy of dual-energy computed tomography for the measurement of iodine concentration using cardiac CT protocols: Validation in a phantom model. Eur. Radiol. 2014;24(2):512–8.

116. Karlo C, Lauber A, Götti RP, Baumüller S, Stolzmann P, Scheffel H, Desbiolles L, Schmidt B, Marincek B, Alkadhi H, Leschka S. Dual-energy CT with tin filter technology for the discrimination of renal lesion proxies containing blood, protein, and contrast-agent. An experimental phantom study. Eur. Radiol. 2011;21(2):385–92.

117. Kawai T, Takeuchi M, Hara M, Ohashi K, Suzuki H, Yamada K, Sugimura Y, Shibamoto Y. Accuracy of iodine removal using dual-energy CT with or without a tin filter: an experimental phantom study. Acta radiol. 2013;54(8):954–60.

118. Matsuda I, Akahane M, Sato J, Katsura M, Kiryu S, Yoshioka N, Kunimatsu A, Ino K, Ohtomo K. Precision of the measurement of CT numbers: Comparison of dual-energy CT spectral imaging with fast kVp switching and conventional CT with phantoms. Jpn. J. Radiol. 2012;30(1):34–9.

119. Kenneth R. Castleman, Digital image processing. Upper Saddle River, NJ: Prentice Hall Press; 1996.

120. Jain A, Dubes R. Algorithms for clustering data. Englewood Cliffs, NJ: Prentice Hall Press; 1988.

121. Grangeat P. Mathematical framework of cone beam 3D reconstruction via the first derivative of the Radon transform: Mathematical Methods in Tomography. Math. methods Tomogr. Springer Berlin Heidelberb; 1991.

122. Crowder M, Hand D. Analysis of repeated measures. CRC Press; 1990.

123. Nute JL, Rong J, Stevens DM, Darensbourg BJ, Cheng J, Wei W, Hobbs BP, Cody DD. Evaluation of over 100 scanner-years of computed tomography daily quality control data. Med. Phys. 2013 May;40(5):051908.

124. Bushby KM, Cole T, Matthews JN, Goodship JA. Centiles for adult head circumference. Arch. Dis. Child. 1992 Oct;67(10):1286–7.

125. McLachlan G, Peel D. Finite mixture models. 2004.

126. Yu G, Sapiro G, Mallat S. Solving inverse problems with piecewise linear estimators: From gaussian mixture models to structured sparsity. IEEE Trans. Image Process. 2012;21(5):2481–99.

127. Dempster A, Laird N, Rubin D. Maximum likelihood from incomplete data via the EM algorithm. J. R. Stat. Soc. 1977;39(1):1–38.

128. Ruppert D. Statistics and data analysis for financial engineering. 2010.

Vita

Jessica Nute was born in Norfolk, Virginia on May 12, 1983, the daughter of Lorraine Madeline Nute and Marshall Raymond Nute. After graduating from Kempsville High School, Virginia Beach, Virginia, she entered University of Virginia in 2001. She double majored in Physics and Astronomy receiving Bachelor of Arts degrees in both subjects in May of 2005. In August of 2007 she entered Duke University where she pursued research on the reliability of positron emission tomography standard uptake values and received a Masters in Medical Physics in May of 2009. In August of 2009, Jessica entered The University of Texas Graduate School of Biomedical Sciences at Houston to pursue a Ph.D. in Medical Physics. As part of her research work, she was a research assistant at The University of Texas MD Anderson Cancer Center in the Department of Imaging Physics and worked at the Center for Advanced Biomedical Imaging. Her research interests included computed tomography, dual-energy computed tomography, phantom design, protocol development and quality control. Jessica's goal is to pursue these research interests at an academic medical center while developing her skills in clinical medical physics with the goal of obtaining ABR certification in Diagnostic Medical Physics.

Permanent Contact Information:

JLNute@gmail.com